NASA CONTRACTOR REPORT

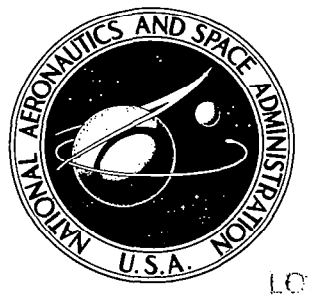

NASA CR-
c.1

NASA CR-814

SPACE RADIATION EQUIVALENCE FOR EFFECTS ON TRANSISTORS

by R. R. Brown and W. E. Horne

Prepared by
THE BOEING COMPANY
Seattle, Wash.
for Goddard Space Flight Center

NATIONAL AERONAUTICS AND SPACE ADMINISTRATION • WASHINGTON, D. C. • JULY 1967

NASA CR-814

SPACE RADIATION EQUIVALENCE FOR EFFECTS ON TRANSISTORS

By R. R. Brown and W. E. Horne

The appendix, the six-month report was issued by Originator as D2-84088-1 and final report as D2-84088-2.

Prepared under Contract No. NAS 5-9578 by
THE BOEING COMPANY
Seattle, Wash.

for Goddard Space Flight Center

NATIONAL AERONAUTICS AND SPACE ADMINISTRATION

For sale by the Clearinghouse for Federal Scientific and Technical Information
Springfield, Virginia 22151 – CFSTI price $3.00

ABSTRACT

This document constitutes the final progress report for NASA Goddard Contract NAS 5-9578. Included is a description of the results and conclusions of research conducted during the period of May 15, 1965, through November 15, 1966. Experimental testing and data analysis were directed toward accomplishing the main objective which was the establishment of valid space radiation equivalences for permanent displacement damage to transistors. Research was conducted essentially in accordance with the program plan as outlined in the Boeing technical proposal document D2-90619, "Space Radiation Equivalence for Effects on Transistors," January 1965.

Detailed progress for the period of May 15 through November 15, 1965, was reported in the Six-Month Progress Report (Reference 1). That report describes the selection and electrical characterization of transistors, the preparation and performance of electron tests of energies 0.5, 1, and 2 Mev, and the preliminary analysis of electron data.

This final report describes irradiation tests of 10 types of npn and pnp silicon transistors at proton energies of 1, 20, and 100 Mev and a Co^{60} gamma-ray exposure test. The results of these tests and the previously described electron tests are described not only in terms of their effects on transistor parameters, but also in terms of radiation equivalences for permanent displacement damage. Displacement effects were observed to dominate proton damage; however, low level exposures of electrons (typical of space mission) cause nonlinear damage which is not attributable to either displacement or temporary surface channeling effects. The energy dependences for both proton and electron displacement damage, as well as damage constants, have been obtained for the 10 transistor types tested. Nonlinear damage was identified and preliminary characterization was made. The feasibility of using Co^{60} gamma-ray sources to simulate radiation effects of electrons and protons was also assessed in terms of linear and nonlinear damage.

ACKNOWLEDGMENTS

In addition to the authors and technical supervisors, the following personnel have made significant contributions to the research performed under Contract NAS 5-9578.

Chalmers R. Brittain	Analysis and Processing of Test Data
Eugene L. McCafferty	Modification and Servicing of the Computer Program for Damage Analysis
Loren D. Milliman	
Richard F. Seiler	Director of the Accelerator Facilities and Development of the 20-Mev Proton Capability
Edward D. Sullivan	Assembly of Test Equipment and Acquisition of Test Data
Sally H. Schairer	Processing of Curve Tracer Photographs on the Benson Lehner Model Oscar F Oscillogram Reader

KEY WORDS

Base transit time
Co^{60} gamma rays
Computer analysis
Damage constants
Electrons
Nonlinear damage
Normalization of damage
Protons
Permanent linear damage
Radiation equivalence
Recombination currents
Transistors

TABLE OF CONTENTS

LIST OF ILLUSTRATIONS

LIST OF ILLUSTRATIONS (Continued)

LIST OF ILLUSTRATIONS (Continued)

LIST OF ILLUSTRATIONS (Continued)

LIST OF ILLUSTRATIONS (Continued)

LIST OF TABLES

1.0 INTRODUCTION

1.1 NEEDS

The general needs that relate to space mission vulnerability of electron systems include the ability to:

1. Extrapolate from laboratory-simulated radiation tests to space mission performance;
2. Extrapolate from performance on an inflight test to other space mission conditions;
3. Generalize from radiation effects on a limited number of transistors to the effects on many types; and
4. Develop techniques to allow standardization in qualification testing of new devices.

The results of the one-year effort of this research study were intended to be the accomplishment of specific goals that would represent a significant step toward an organized effort to ultimately satisfy the needs.

1.2 PROGRAM DESCRIPTION

The specific objective of the program was the establishment of valid space radiation equivalences for permanent damage to silicon transistors. The phrase, radiation equivalence for permanent damage, expresses the relative effectiveness of different types and energies of radiation for producing an equivalent amount of permanent damage.

Reliable silicon transistors of specified constructions and designs were selected for radiation effects testing, and 40 of each type were procured. The 10 types represent two of each of five construction designs: npn and pnp diffused planar, npn and pnp epitaxial planar, and npn epitaxial mesa. All of these transistors were electrically characterized before and after radiation exposure. Selected devices were also characterized during irradiation. In addition to obtaining oscillograms of common-emitter characteristic curves, the following electrical

parameters were measured: d.c. and small-signal a.c. common-emitter current gain, saturation voltages, breakdown voltage, leakage current, current as a function of base-emitter voltage, base transit time, alpha cut-off frequency, gain-bandwidth frequency, and transition capacitances.

Charged particle irradiation of transistors was performed using electrons of energies of approximately 0.5, 1, and 2 Mev and protons of energies of approximately 1, 20, and 100 Mev. These tests were used to establish displacement equivalences for permanent damage for significant radiation components of the Van Allen space environment. The possibility of obtaining gamma-ray equivalence for permanent damage was also experimentally studied in order to assess the practicality of using Co^{60} facilities for simulation testing of space radiation effects.

Text fixtures were wired for remote selection of transistors and subsequent dynamic recording of transistor curve traces during the irradiation tests. Transistor ambient temperatures were monitored during exposure and measurement. Careful dosimetry was also performed to determine valid exposure fluences.

Results of changes in transistor parameters measured on the automatic transistor tester were analyzed by hand, and data from oscillograms of transistor curve traces were computer analyzed to show not only the dependence of radiation damage on particle fluence but also on radiation type and particle energy. Radiation equivalences for permanent displacement damage, normalized to transistor base transit time, were determined for charged particle radiation used in the test program. The results of this study were also compared with data obtained in earlier Boeing studies using other particle energies. Data is presented whenever practical in a form that is suited to the needs of design engineers.

1.3 SUMMARY OF RESULTS

Proton and electron equivalences for linear damage to transistors were successfully obtained allowing for the determination of the energy dependence of the effects of atomic displacements. The importance of energy dependence of nonlinear damage was identified for electron effects on transistors, and a

preliminary characterization was made of this effect. The feasibility of using Co^{60} gamma facilities for simulation of the effects of electrons and protons was assessed in terms of both linear displacement damage and nonlinear ionization damage.

Proton displacement equivalences were obtained from linear damage observed for changes in BV_{CBO}, $V_{CE}(sat)$, $V_{BE}(sat)$, I_{CBO}, and h_{FE}^{-1}. Electron displacement equivalences were obtained from linear damage observed primarily from changes of $V_{CE}(sat)$ and h_{FE}^{-1} at very high electron exposures.

Displacement equivalences indicated fairly consistent agreement among the ten transistor types tested (npn and pnp). Good correlation was generally obtained between equivalences for permanent changes in h_{FE}^{-1}, $V_{CE}(sat)$, and I_{CBO}. Displacement damage constants from transit time normalization were fairly consistent for the proton tests, and agreement between devices of the same construction was generally quite close. Nonlinear damage, however, was observed to exceed linear damage for low exposures to electrons. The resulting electron damage constants did not agree as closely as the proton damage constants, particularly for the pnp devices. Proton displacement equivalences (linear damage) yielded energy dependence for damage that was correlatable with theory above 10 Mev and with solar cell data below 10 Mev. Inherent shielding by transistor cans caused protons of incident energies between 14 and 17 Mev to be significantly more effective for displacement damage. Energy dependence for proton damage, in agreement with solar cell results, increased more rapidly with increased energy than predicted by theory.

Co^{60} gamma-ray test results indicated that simulation feasibility for space radiation effects is limited. Although Co^{60} gamma rays can be useful in simulating nonlinear damage to I_{CBO} and h_{FE} characteristic of electron exposure, only at exposures in excess of 10^8 R can they be used to simulate proton displacement damage to current gains, and even then the simulation is partial.

Preliminary identification of the nonlinear damage (not temporary surface effects due to channeling or inversion layers) was obtained for the electron and

gamma-ray tests. Various characteristics of nonlinear damage were observed, such as its dominance at low radiation exposures and low emitter currents, its tendency to saturate at high exposures (allowing for a separation of linear and nonlinear damage), its dependence on ionization rather than displacement effects, and its correlation with increases of base-emitter recombination current. Recommendations include further extension of the studies of nonlinear damage to provide effective radiation equivalences for electron damage.

2.0 DETAILED DISCUSSION OF PROGRESS

After all transistors needed for this study were procured and characterized electrically, a schedule for experimental testing was established. The accelerator facilities were modified for electron and proton irradiation tests. Both the transistors to be studied and the necessary test fixtures were prepared. Seven separate radiation exposure tests were conducted; these included irradiation of transistors at three electron and three proton energies, as well as an irradiation by Co^{60} gamma rays. During the tests, both radiation flux and transistor degradation were monitored dynamically. Following the tests, all transistors were recharacterized electrically. Hand analysis on data obtained passively, as well as computer analysis of transistor characteristic curves, was performed. Radiation equivalences for displacement effects were obtained, the feasibility of simulating proton and electron effects with gamma rays was studied, and nonlinear damage was identified.

2.1 TRANSISTOR PREPARATION

Transistors of selected types were procured and characterized in preparation for the radiation exposure tests.

2.1.1 Selection of Transistors

Ten registered types of silicon transistors were selected for radiation effects testing. Information which identifies those specific devices is listed in Table 1. Frequency, f, shown in the table can be related to effective base width, as indicated in Section 2.7.1. Transistor selection was made on the basis of reliability and present utilization for missile and space vehicle electronic circuitry. These transistor types also represent three classes of design—epitaxial mesa, diffused planar, and epitaxial planar. Both npn and pnp semiconductor constructions were considered in order to permit a comparison to be made between radiation equivalences obtained from transistors with p- and n-type base regions. Two different registered transistors of each of the same class of construction designs (e.g., npn diffused planar) were selected in order to investigate the validity of extending radiation

Table 1. Transistor Types Studied

Construction	Transistor Identification		Manufacturer	Typical Initial Parameters		
	Design	Registration Number		h_{FE}	I_{CBO} (na)	f (Mc)
npn	Diffused planar	2N1613	Fairchild	45	0.33	95
npn	Diffused planar	2N1711	Fairchild	190	0.11	150
npn	Epitaxial planar	2N2538	Raytheon	75	9.93	415
npn	Epitaxial planar	2N2219	Fairchild	100	0.06	440
npn	Epitaxial mesa	2N743	Texas Instruments	35	2.42	440
npn	Epitaxial mesa	2N834	Motorola	95	13.30	415
pnp	Diffused planar	2N2303	Fairchild	140	0.20	125
pnp	Diffused planar	2N1132	Raytheon	60	0.10	400
pnp	Epitaxial planar	2N2801	Motorola	95	0.35	325
pnp	Epitaxial planar	2N2411	Texas Instruments	90	0.90	350

equivalence information to other transistor types of the same construction design.

Forty transistors of each type (400 total) were procured with the specification that transistors of the same type be of the same batch number and manufacture date in order to give more assurance that the semiconductor batch, the construction details, and the surface conditions are the same (Reference 1). Thus, comparisons can be made between transistors irradiated with different types of radiation with a greater assurance of no marked differences in the devices themselves.

2.1.2 Characterization of Sensitive Parameters

Transistor parameters which are radiation sensitive were measured with specialized equipment prior to radiation exposure. Parameters which control radiation sensitivity were also measured in order to provide data for analytically normalizing the degradation of current gain for different transistors. Careful procedures were employed both during instrument calibration and data acquisition. Equipment and techniques used in electrical characterization were described in great detail in the 6-month progress report (Reference 1), and only a short summary is contained here.

2.1.3 Measurement of Radiation-Sensitive Parameters

Values of radiation-sensitive parameters were measured by the use of a Fairchild Series 500 automatic transistor tester, a Tektronix Model 575 transistor curve tracer, and a measurement circuit for current as a function of base-emitter voltage.

The Fairchild Series 500 transistor tester was programmed to automatically perform 16 transistor measurements in sequence with direct digital readout. The following transistor parameters were measured: d. c. common-emitter current gain, h_{FE}, at a collector bias of 10 volts and currents of 10, 50, 100, and 500 μa, 1, 2, 5, and 10 ma; V_{CE}(sat) at 2 and 10 ma collector currents (with a gain of 2); V_{BE}(sat) at 2 and 10 ma collector current (with a gain of 2); BV_{CBO} at 100 μa; and I_{CBO} at V_{CB} = 10 volts. The measured values were then read out sequentially in the order, top to bottom and left to right, as shown in Table 2.

Table 2. A Typical Fairchild Series 500 Data Sheet

DEVICE TYPE: 2N1613 DEVICE NUMBER: 1

DATE: 10 August 1965 TIME: 1305 PARTICLE FLUENCE: 0

I_C (ma)	V_{BE}(on) (volts)	BV_{CBO} (volts)	h_{FE} (V_C = 10 volts)	V_{CE}(sat) (volts)	V_{BE}(sat) (volts)	I_{CBO}(na) (V_{CB} = 10 volts)
0.01	0.518					
0.05	0.545					
0.10	0.562	118				
0.50	0.602					
1.0	0.620					
2.0	0.638		44.8	0.078	0.652	
5.0	0.663		---	---	---	
10.0	0.689		52.7	0.103	0.727	
						0.33

During these measurements, the ambient temperature was maintained at 27±1°C. The actual temperature (within 0.05°C) was recorded on the data sheets at the time of measurement readout. The transistors were handled with insulated pincers rather than fingers in order to assure temperature stability. Data and time were recorded on each data sheet with an automatic time stamp. To verify instrument repeatability, control transistors were measured periodically and the values were compared with standard values obtained earlier.

A Tektronix Model 575 curve tracer was used in this study to display a family of transistor common-emitter characteristic curves. A typical oscillogram of a set of transistor common-emitter characteristic curves taken before irradiation is shown in Figure 1(a). The ordinate represents collector current, I_C. The abscissa represents collector voltage, V_C. A family of base-current curves is shown. Serial identification numbering on the face of the oscillogram is used to key punch the picture heading card and data cards at the oscillogram reader facility. Figure 1(b) shows the back of the oscillogram. Listed is pertinent data recorded at the time the picture was taken. This includes the I_B current per step, particle fluence, temperature, etc. This data was used as input information for a transistor damage-plotting program used on a SRU 1107 computer.

A measurement circuit for base turn-on voltage was also assembled to obtain I_B and I_C as a function of V_{BE} (Reference 1).

2.1.4 Measurement of Radiation-Control Parameters

Values of transistor parameters that are needed in order to determine radiation-control parameters were measured by the use of the following equipment: a General Radio Type 1607A transfer function and immittance bridge, a Tektronix 567 sampling oscilloscope, a Boonton capacity bridge, a specially designed base transit time circuit, and a Fairchild h_{fe} power gain tester Model 7515S.

Measurement techniques employed in obtaining control parameters from these instruments were described in great detail in the semiannual progress report (Reference 1). Values obtained from the test instruments included base transit time, t_b,

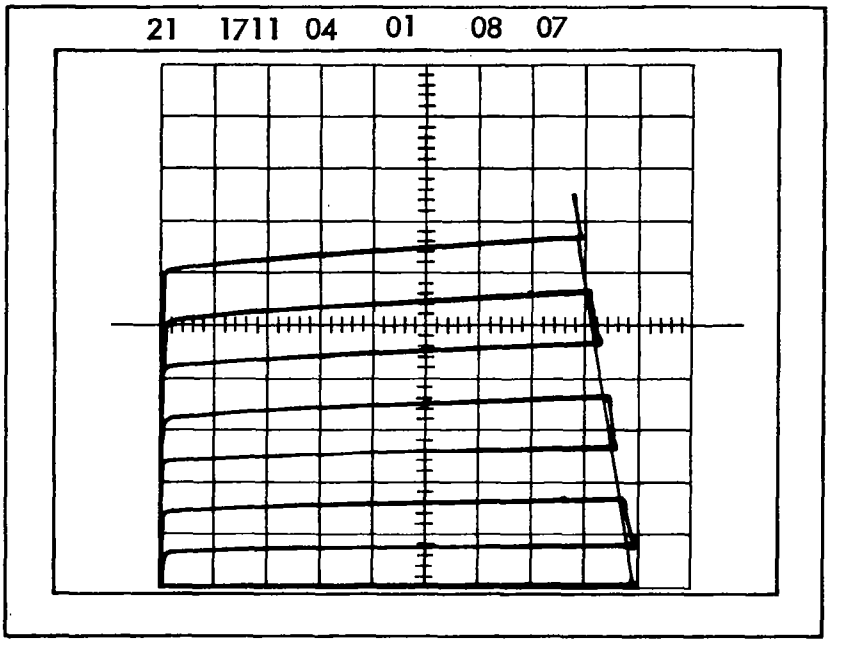

(a) FRONT VIEW

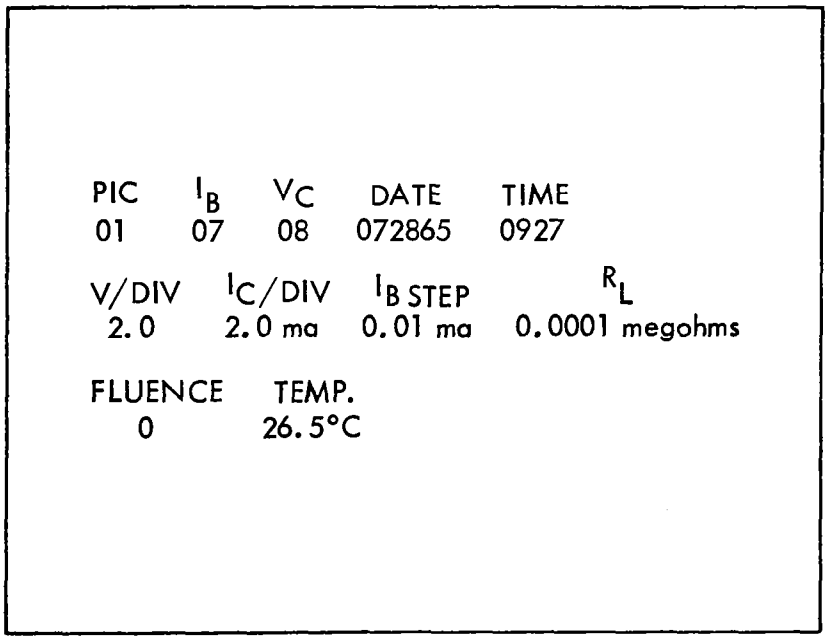

(b) BACK VIEW

Figure 1. Oscillogram of a Set of Characteristic Curves

and gain band width frequency, f_T. The use of these parameters in normalization of transistor damage and correction for variations in effective base width is described in Section 2.7.1.

2.2 TEST SCHEDULE

In order to simulate transistor damage for earth orbital missions, electrons of three energies and protons of three energies were selected for transistor irradiation. A gamma-ray test was also selected to assess the validity of space radiation simulation using a Co^{60} facility. Electron irradiation tests included energies of approximately 0.5, 1, and 2 Mev. Electrons of 0.5-Mev energy are representative of those present with high intensity in a shield-modified spectrum. Transistor inherent shielding was removed for the 0.5-Mev test. Electrons of 1-Mev energy can readily pass through the thickness of a transistor can, but suffer significant intensity and energy loss. Although the 1-Mev intensity in space is less than that for lower energy electrons, the displacement cross section is greater. Electrons of 2-Mev energy are representative of those high-energy electrons still having sufficient Van Allen intensity to be significant for transistor damage.

Proton irradiation tests included energies of 1, 20, and 100 Mev. Protons of 1.0-Mev energy are representative of those protons that degrade to low energy in passing through both inherent and vehicle skin shielding. Transistor inherent shielding was removed for the 1.0-Mev test. Protons of 20-Mev energy can readily pass through transistor inherent shielding but, in so doing, degrade to lower energies that are more effective for displacement damage. Transistors were irradiated at energies from 14 to 17 Mev, both with and without inherent shielding. Protons of 100 Mev are representative of those protons for which it is difficult to provide shielding, and they have the added feature of large inelastic reaction cross sections which lead to transmutations and secondary particle production.

All the irradiation tests performed are summarixed in Table 3. A total of 400 transistors were procured for this research program. The disposition of these devices is shown in Table 4. Selected transistors of each of the 10 transistor types

Table 3. Irradiation Test Schedule

Radiation Type	Nominal Energy (Mev)	Incident Energy (Mev)	Transistor Can	Energy on Silicon (Mev)	Source	Test Date	Test Number
Electrons	0.5	0.53	Off	0.53	Boeing Dynamitron	October 1965	23
	1	1.3	On	0.88 to 0.99	Boeing Dynamitron	September 1965	22
	2	2.0	On	1.55 to 1.68	Boeing Dynamitron	September 1965	21
Protons	1	1.0	Off	1.0	Boeing Dynamitron	November 1965	24
	20	14 to 17	Off On	14 to 17 7 to 14	$He^3(d, p)\ He^4$ reaction	May 1966	26
	100	100	On	100	Cyclotron	April 1966	27
Gamma Rays	Co^{60}	Co^{60}	On	Co^{60}	Boeing Co^{60} Facility	February 1966	25

Table 4. Disposition of Test Devices

Test	2N1613	2N1711	2N2538	2N2219	2N743	2N834	2N2303	2N1132	2N2801	2N2411
21 2.0-Mev Electron	4, 5, 6, 11	4, 5, 6, 11	4, 5, 6, 11	3, 4, 5, 6, 11	4, 5, 6, 11	4, 5, 6, 11	4, 5, 6, 11	4, 5, 6, 11	4, 5, 6, 11	4, 5, 6, 11
22 1.0-Mev Electron	10, 12, 13,	7, 8, 9, 10	3, 7, 8, 9	7, 8, 9, 10	7, 8, 9, 15	7, 8, 9, 10	7, 8, 9, 10	3, 7, 8, 9, 10	7, 8, 9, 10	7, 8, 9, 10
23 0.5-Mev Electron	7, 8, 9, 17	12, 13, 14, 17	10, 12, 13, 17	12, 13, 15, 17	3, 13, 14, 17	3, 12, 13, 15, 17	15, 16, 17, 18	12, 13, 14, 17	13, 15, 16, 17	12, 13, 14, 17
24 1.0-Mev Proton	2, 15, 19, 20	2, 15, 16, 19	2, 14, 15, 16, 19	2, 14, 16, 18	2, 12, 16, 18, 19	2, 14, 16, 18, 19	2, 12, 19, 20, 22	2, 15, 16, 19	2, 12, 18, 19	2, 15, 16, 18
25 Co^{60} Gamma	22, 23, 24 25	20, 21, 22, 23	20, 21, 22, 23	20, 21, 22, 23	20, 21, 22, 23	20, 21, 22, 23	23, 24, 25, 26	20, 21, 22, 23	20, 21, 22, 23	20, 21, 22, 23
26 20-Mev Proton	26, 28, 29, 40	25, 26, 27, 38	26, 27, 28, 29	25, 26, 27, 39	25, 26, 29	25, 27, 28, 29	21, 27, 28, 29, 30	24, 25, 27, 28	26, 27, 28,	25, 26, 27, 38
27 100-Mev Proton	30, 31, 32, 33, 34, 35, 36, 37, 38, 39	28, 29, 30, 31, 32, 33, 34, 35, 36, 37	31, 32, 33, 34, 35, 36, 37, 38, 39, 40	28, 29, 30, 31, 32, 33, 34, 36, 37, 38	30, 31, 32, 33, 34, 35, 36, 37, 38, 39	30, 31, 32, 33, 34, 35, 36, 37, 38, 39	31, 32, 33, 34, 35, 36, 37, 38, 39, 40	29, 30, 31, 32, 33, 34, 35, 36, 37, 38	30, 31, 32, 33, 34, 36, 37, 38, 39, 40	28, 29, 30, 31, 32, 33, 34, 35, 36, 37

served as controls for the tests. At least four of each transistor type were exposed for each test. At least nine of each type were exposed for the 100-Mev proton test. On each of the other tests, one of each transistor type was dynamically monitored by means of curve-tracer photographs taken during irradiation. At least three devices of each type were characterized by curve traces taken periodically (passive measurements) following each exposure run. At least three passive measurements were made during each test.

2.3 ELECTRON IRRADIATION TESTS

Electron irradiation of transistors was performed at energies as specified in Table 3 (nominal energies of 0.5, 1, and 2 Mev). These tests were performed at the Boeing Radiation Effects Laboratory using electrons obtained from a Dynamitron accelerator. Transistors were exposed, in an evacuated test chamber, to electrons that had been scattered through thin foils. The detailed description of the preparation, performance, and dosimetry analysis of those tests was described in the semiannual progress report (Reference 1).

2.4 PROTON IRRADIATION TESTS

Three proton irradiation tests of transistors were conducted at nominal energies of 1, 20, and 100 Mev (see Table 3).

2.4.1 1-Mev Proton Test

The test configuration, dosimetry, and test procedure for the 1-Mev proton test were essentially the same as for the electron tests.

Test Configuration

The same evacuated scattering chamber used in the electron tests (Reference 1) was also used for the 1-Mev proton test. Protons of energy 1.1 Mev were scattered through a 1-micron thick gold foil, resulting in uniform exposure of axially symmetric arrays of transistors to 1-Mev protons. Diagrams and photographs of the chamber and mounting dish were included in the earlier discussion of the electron tests. The

placement of transistors in the 1-Mev proton test array is shown in Figure 2.

Dosimetry

Dosimetry techniques for the 1-Mev proton test were similar to those discussed in detail for the electron tests. Experimental data were compared with theoretical values for Rutherford coulomb scattering. The results of field mapping, using a rotatable Faraday cup, are shown in Figure 3.

During the test, integrated current from a Faraday cup placed along the beam axis was used to calculate total beam current and, in conjunction with field mapping, was used to determine proton fluence at selected scattering angles. Total proton beam currents used during the test ranged from approximately 0.1 to 1.0 μa.

Test Procedure

The test procedure was the same as that employed in the previously discussed electron tests. After the transistor cases were removed and prior to irradiation, Tektronix 575 curve tracer oscillograms and Fairchild Series 500 measurements were obtained. Dynamic measurements were made on one device of each type during irradiation using a Tektronix 575 curve tracer. Periodic passive curve tracer measurements were also made on all transistors in air during and after the test. Ambient temperature was monitored during the test. After irradiation the transistors were again characterized on the Fairchild Series 500 test set.

2.4.2 20-Mev Proton Test

A capability to generate high-energy protons was developed at the Boeing Radiation Effects Laboratory. The technique used involved the exothermic $D^2(He^3, p)He^4$ reaction. This reaction can be used to obtain protons with energies up to 20 Mev.

Experimental Configuration

A diagram of the experimental arranagement is shown in Figure 4. Ionized He^3 was accelerated to an energy of 2 Mev, using the Dynamitron accelerator. A beam handling system was used to select $(He^3)^{++}$ ions and focus a beam through the entrance aperture, A, of the scattering chamber. The beam then impinged on a

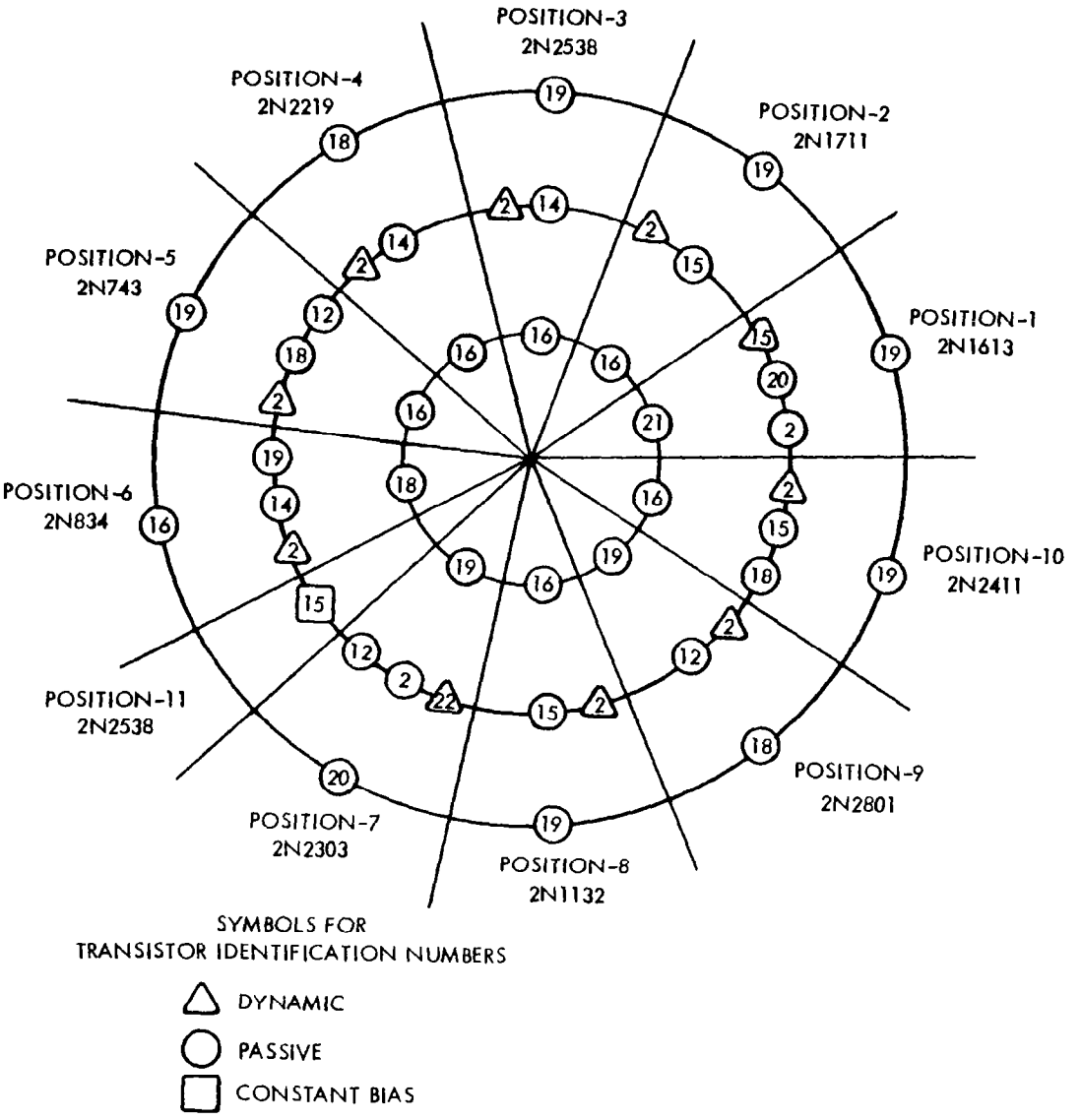

Figure 2. Transistor Array for the 1-Mev Proton Test

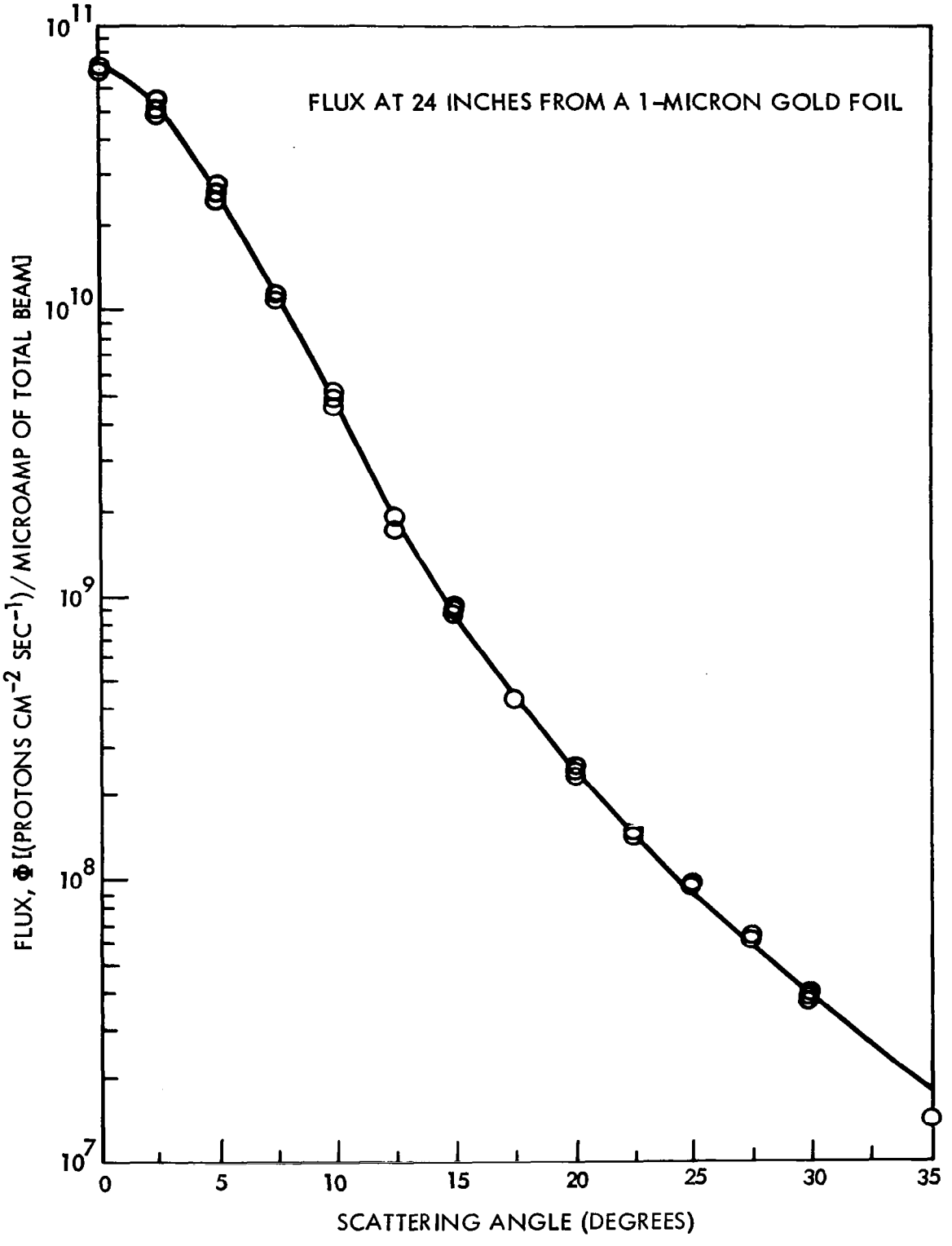

Figure 3. 1-Mev Proton Flux From a 1-Micron Gold Foil

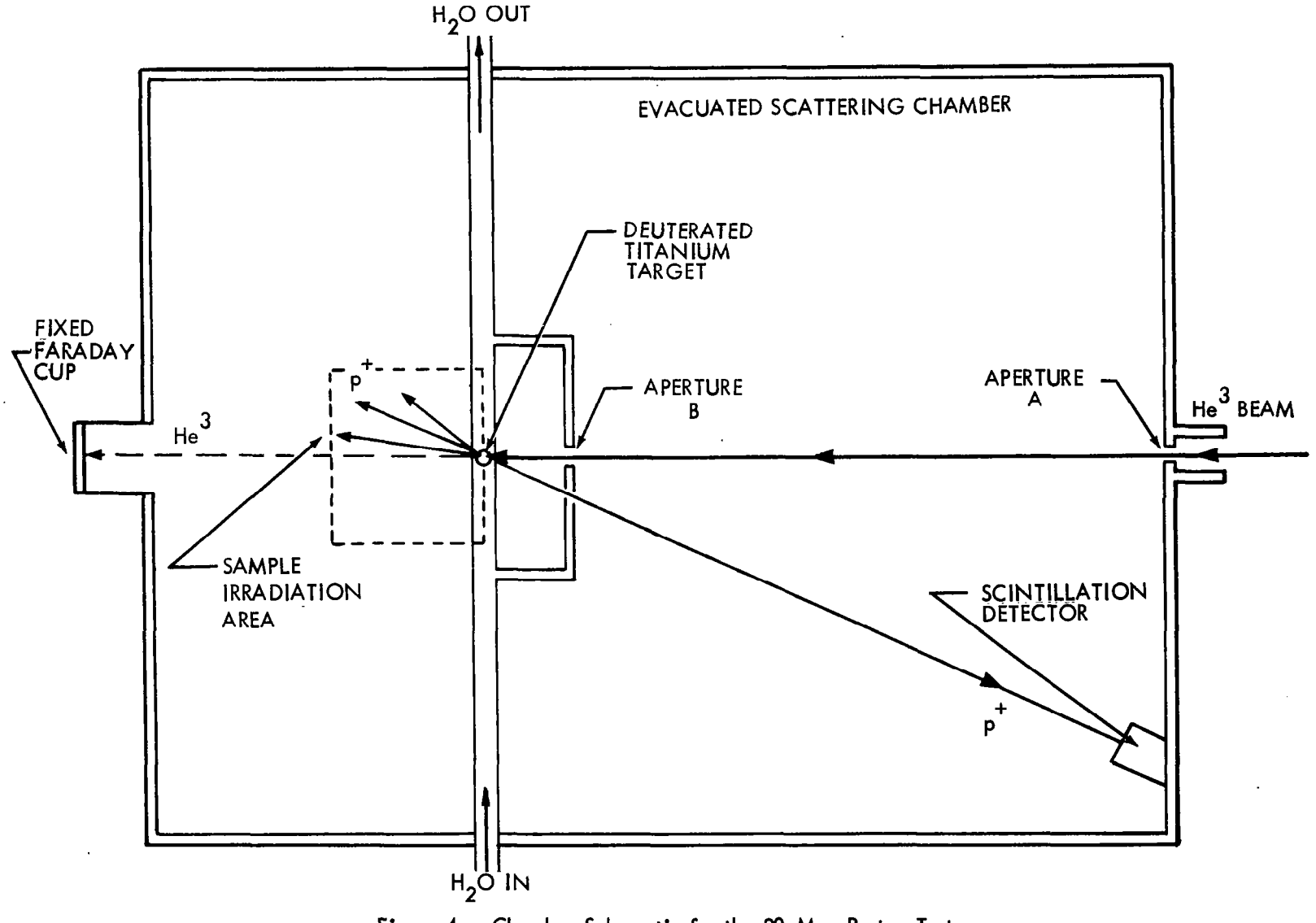

Figure 4. Chamber Schematic for the 20-Mev Proton Test

deuterated titanium target (3×10^4 angstroms thick) at an angle of 20 degrees with the plane of the target. A second aperture, B, placed in front of the target, acted as a shield to prevent the direct exposure of transistors by the He^3 beam. The shield of aperture B and the target mount were made of copper and cooled with circulating water. The Faraday cup at the rear of the chamber was used only to establish the total beam current before the target was moved into position. The scintillation counter in the front of the chamber served to monitor the high-energy proton yield from the target.

Details of the sample mount are illustrated in Figure 5. Transistors were placed at selected angles so that they were exposed to protons of energy 14 to 17 Mev. Since the energy of the protons would be seriously degraded by inherent shielding, most transistor cans were removed. However, the placement of thin shielding in front of these transistors was necessary in order to absorb scattered He^3 particles and secondary electrons. A diagram showing the geometry of the transistor array for the 20-Mev test is shown in Figure 6.

Dosimetry

The angular distribution of the proton flux for the 20-Mev test was determined from measurements obtained using a scintillation counter at a fixed angle of 165 degrees and a solid-state detector which was rotated through selected angles about the deuterated target.

An energy calibration of the solid-state detector was performed using a pulse height analyzer. The calibration was determined from the pulse height channel position for 5.5-Mev alpha particles (from Am^{241}), and linearity was assumed for 14- to 17-Mev proton energy deposition to pulse height for the detector. For incident 2-Mev He^3 ions, the proton energy as a function of angle from the beam axis is shown in Figure 7. This energy spread is predictable from the reaction kinetics and the fuct that the deuterated titanium targets which were used had a thickness comparable to the range of the He^3 ions.

A typical angular distribution for an incident He^3 energy of 2.0 Mev consists of a forward peaking with a minimum near 90 degrees and a back angle peak

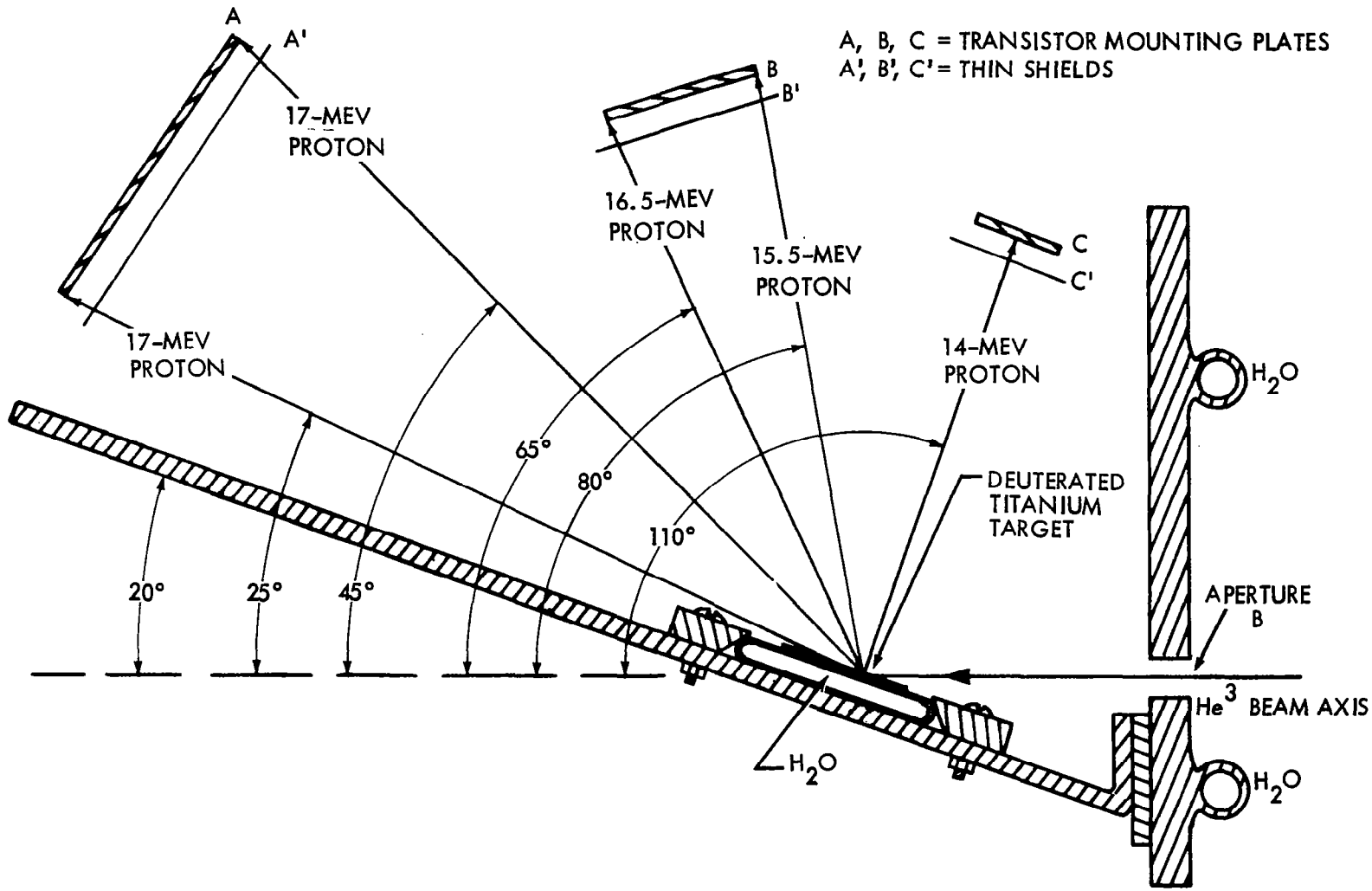

Figure 5. 20-Mev Proton Test Configuration

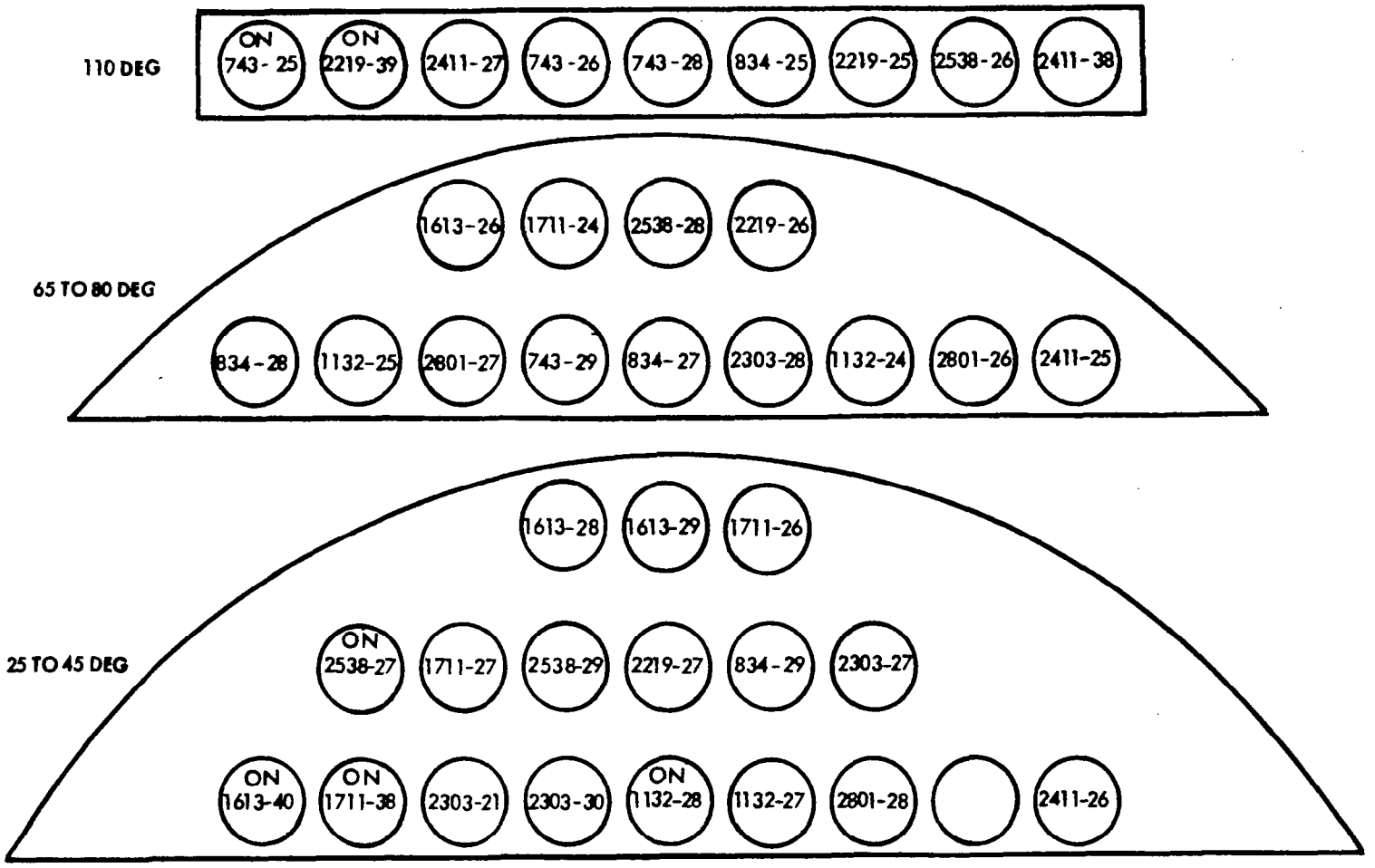

NOTE: "ON" INDICATES THE TRANSISTORS THAT RETAINED INHERENT CAN SHIELDING.

Figure 6. Transistor Array for the 20-Mev Proton Test

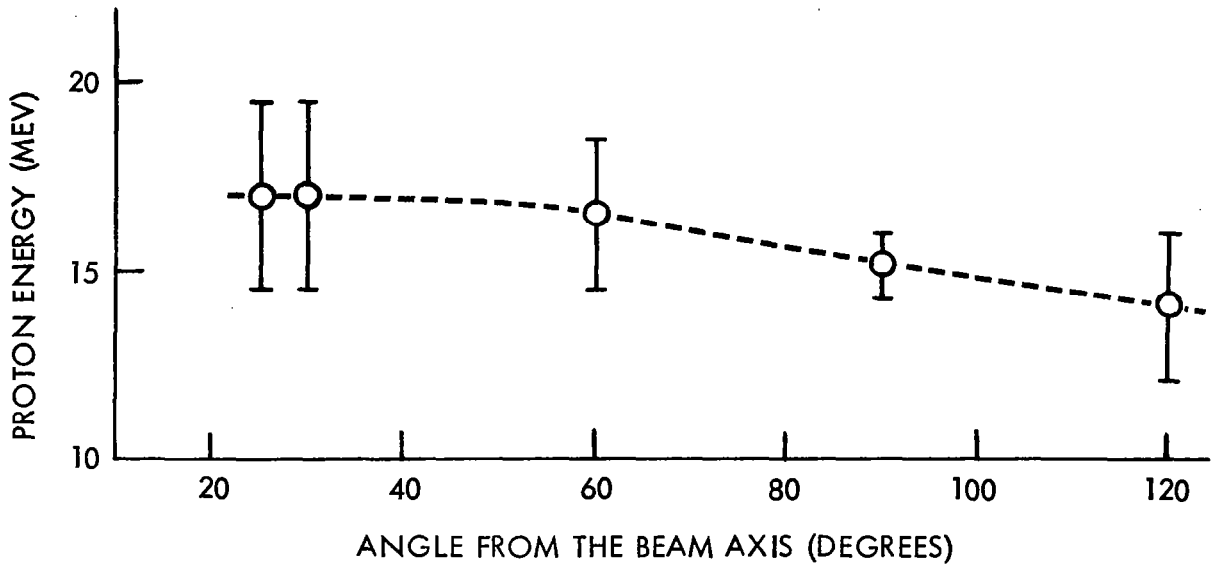

(a) ENERGY DISTRIBUTION

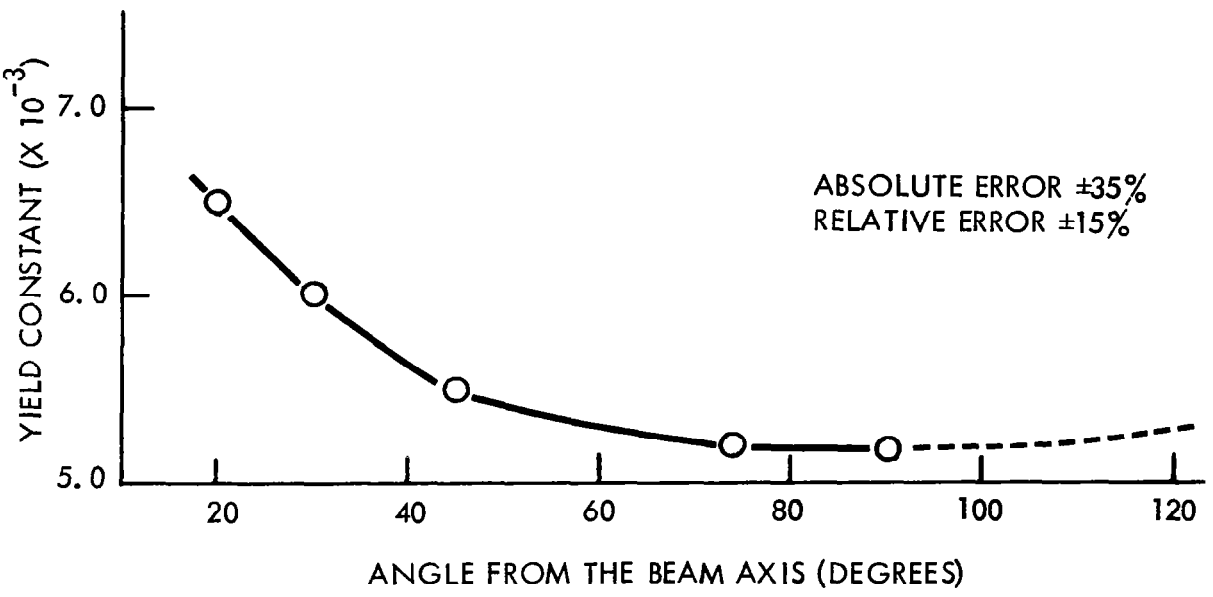

(b) YIELD

Figure 7. Angular Distributions From (He^3, p) Reaction

which is roughly half the height of the small angle maximum. Figure 7 also shows the angular distribution of proton yield over the field of interest. For the target configuration used in this experiment, the 30-degree yield was measured to be the same as the 165-degree yield.

To obtain proton flux, ϕ, at the transistor positions at selected angles, θ, the following relation was used:

$$\phi = Y G M(\theta)/r^2 \qquad (1)$$

where:

Y = count rate (scintillation counter)

G = geometric constant

r = distance (target to sample)

$M(\theta)$ = *angular anisotropy correction factor*

The calculated ratio of count rate of the solid-state detector to the scintillation counter was 4.1. The measured value was 4.8. Both values have associated errors —the former primarily from the measurement of the detector aperture diameters and the latter from measurements of the distance from the detector aperture to the target. The finite size of the beam spot on the target limits the validity of the r^{-2} dependence of Equation (1) for transistors mounted close to the target. If all sources of error are considered, the overall accuracy of the flux measurements is approximately ±35 percent.

In order to obtain exposure fluences for the transistors at specified times during the experiment, the count rate from the scintillation counter was monitored on a chart recorder and integrated numerically. The counts were then converted to fluence using Equation (1).

Experimental Procedure

Before irradiation, inherent shielding (can) was removed from most of the transistors before they were electrically characterized on the Tektronix curve tracer and the 500 semiconductor test set. During the irradiation test, one device of each type was monitored dynamically (beam on). Periodic passive (beam off and open to air) data was also obtained for all transistors using the curve tracer.

After irradiation, all devices were again characterized using both the curve tracer and automatic test set.

Sufficient warmup time was allowed on the measurement instruments before data was obtained, and periodic calibration checks of the equipment were also made. The ambient temperature of test devices was monitored during measurements, using a thermocouple mounted to a transistor can.

2.4.3 100-Mev Proton Test

Protons of 100-Mev energy were obtained using the synchrocyclotron available at the Foster Radiation Laboratory, McGill University, in Montreal, Canada.

Test Configuration

The cyclotron and its beam handling system is shown schematically in Figure 8. A 1/32-inch beryllium plate, located about 37 feet before the end of the accelerator beam tube, was used to scatter a proton beam of energy 100±0.1 Mev. The transistor mounting plates used in this test are shown in Figure 9 as they were attached to the end of the beam tube.

Test Dosimetry

The uniformity of the 100-Mev proton beam was determined by two methods. The beam was mapped using a Faraday cup and a collimating slit arrangement, shown schematically in Figure 10. In addition, activation foil analysis was performed.

In the first mapping, the collimating slit was moved across the field and the height of the beam transmitted was obtained from the fluorescent screen using closed circuit television. The current admitted to the Faraday cup was read on a Keithley 410 meter. The proton flux was calculated at each collimator position using Equation (2).

$$\phi = 6.25 \times 10^{18} \, I/W_c \, h \, (\text{proton cm}^{-2} \, \text{sec}^{-1}) \qquad (2)$$

where: I = Faraday cup current in amps

W_c = width of the collimating slit

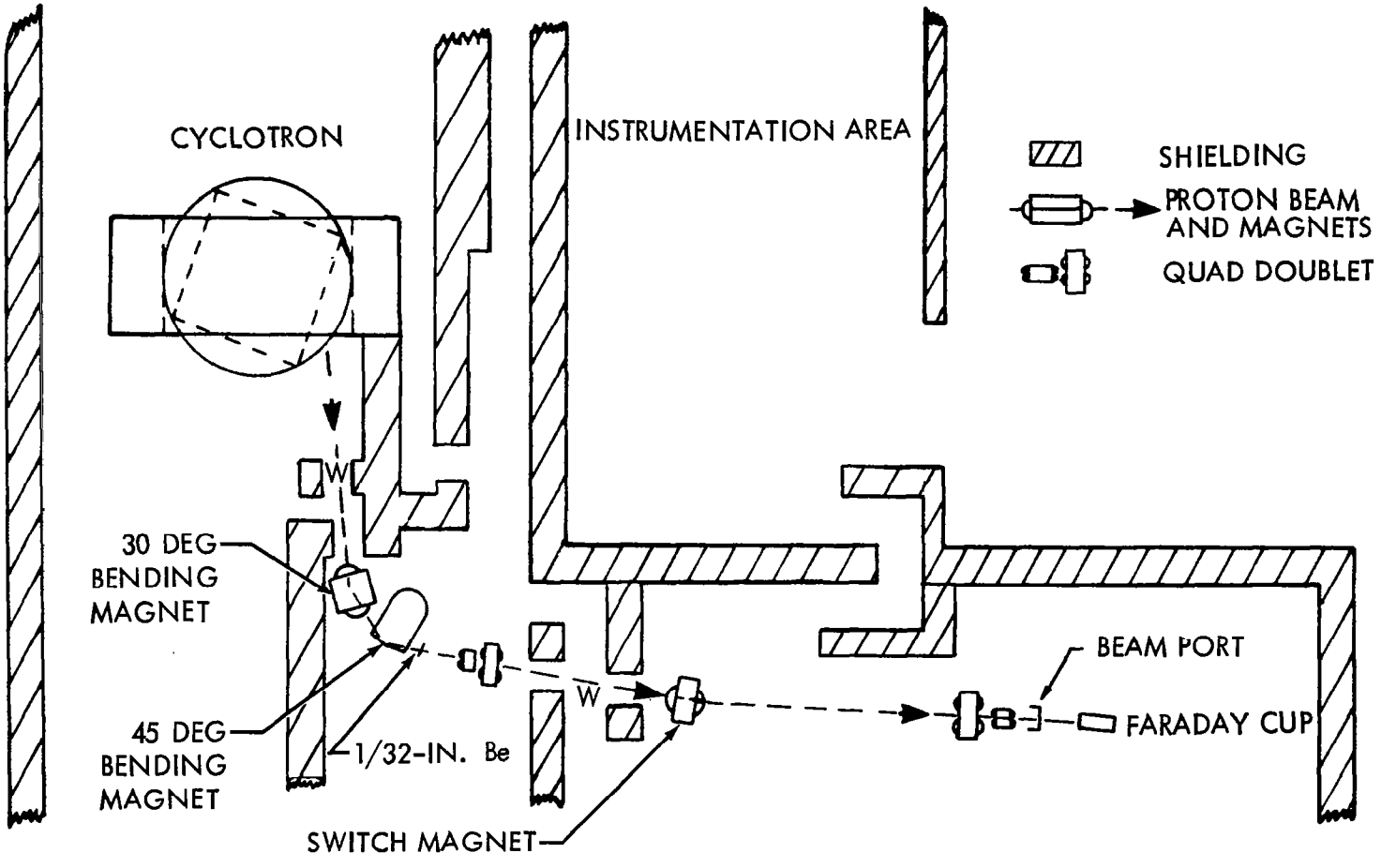

Figure 8. 100-Mev Proton Beam Handling System (McGill University)

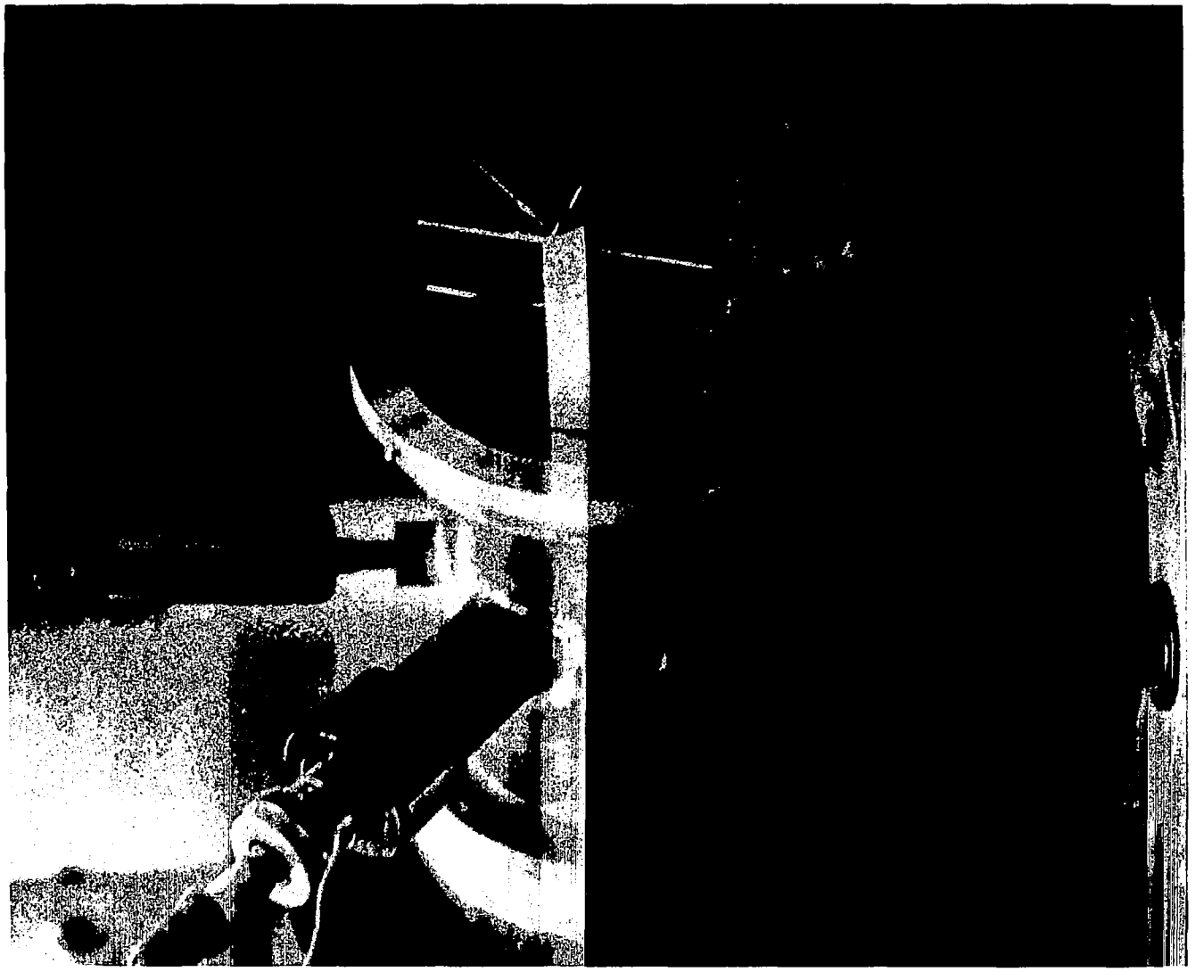

Figure 9. Transistor Mounting Plates

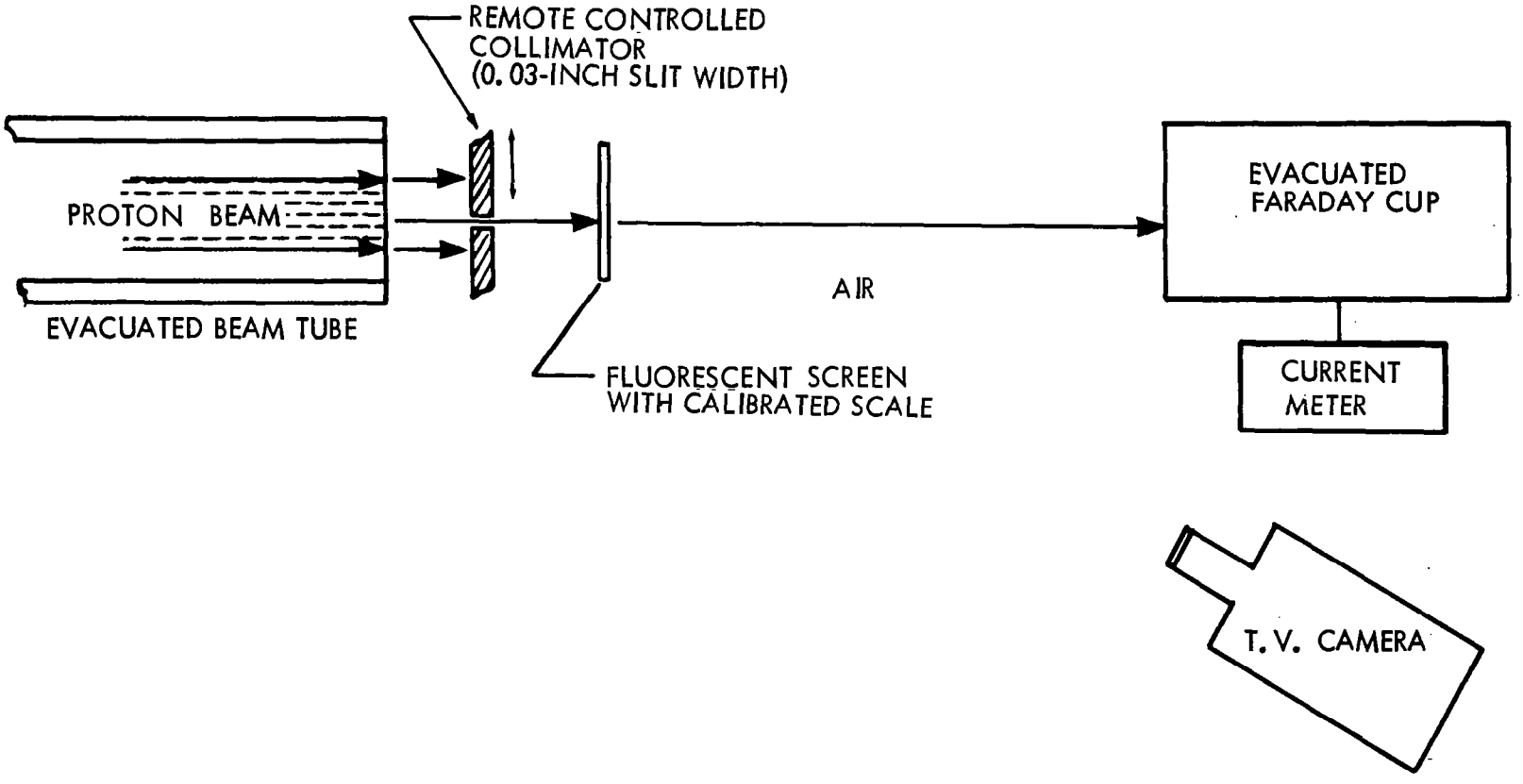

Figure 10. Mapping of the 100-Mev Proton Beam Profile

h = height of the transmitted beam.

The results of this mapping are shown in Figure 11.

The foil activation method served only as a cross-check of the Faraday cup mapping. Two polyethylene foils were placed in the beam, as shown in Figure 11. Measurements of the annihilation gamma activity of the foils indicated that 50.5 percent of the beam was concentrated inside the 2-cm diameter foil. Since the area of this foil constituted 49.5 percent of the total beam area, the activation foil results were in agreement with the Faraday cup mapping. The beam current was integrated during the test in order to calculate values of proton fluence. The exposure rate for the 100-Mev proton test was approximately 1.5×10^{10} protons cm^{-2} sec^{-1}. Transistor exposure data was obtained for fluences ranging from approximately 10^{11} to 10^{14} protons cm^{-2}.

Test Procedure

Four plates holding three transistors each were irradiated simultaneously, as shown in Figure 9. These devices were positioned in the beam in the working area designated in Figure 11. To average proton beam nonuniformities, transistor mounting plates were rotated periodically.

Before radiation exposure, data was obtained on all of the devices using a Tektronix 575 transistor curve tracer and a Fairchild Series 500 semiconductor test set at Boeing. Before and after irradiation, data was taken on all transistors using a 575 curve tracer at McGill University. During the radiation test, one device was monitored periodically during exposure using the curve tracer available at McGill University. After irradiation, all of the transistors were recharacterized at Boeing using a curve tracer and the automatic test set. Ambient temperatures were monitored at the time measurements were being made. Sufficient warmup time was allowed for the instruments, and calibration checks were made before measurements were taken.

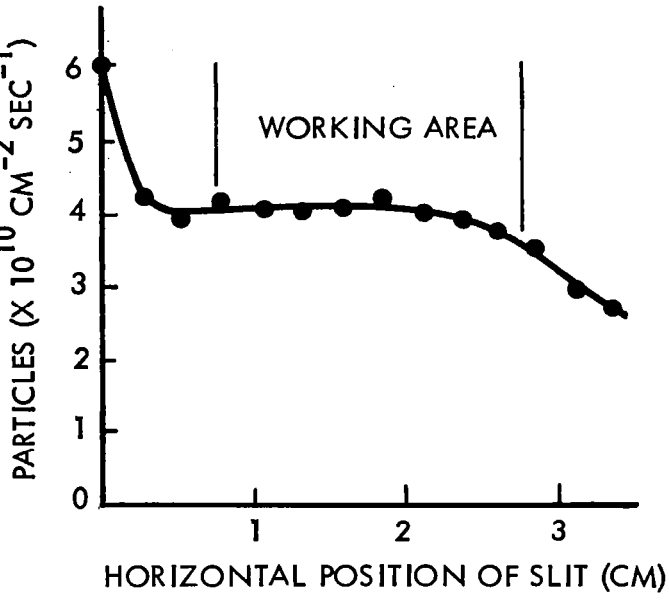

(a) FARADAY CUP MAPPING

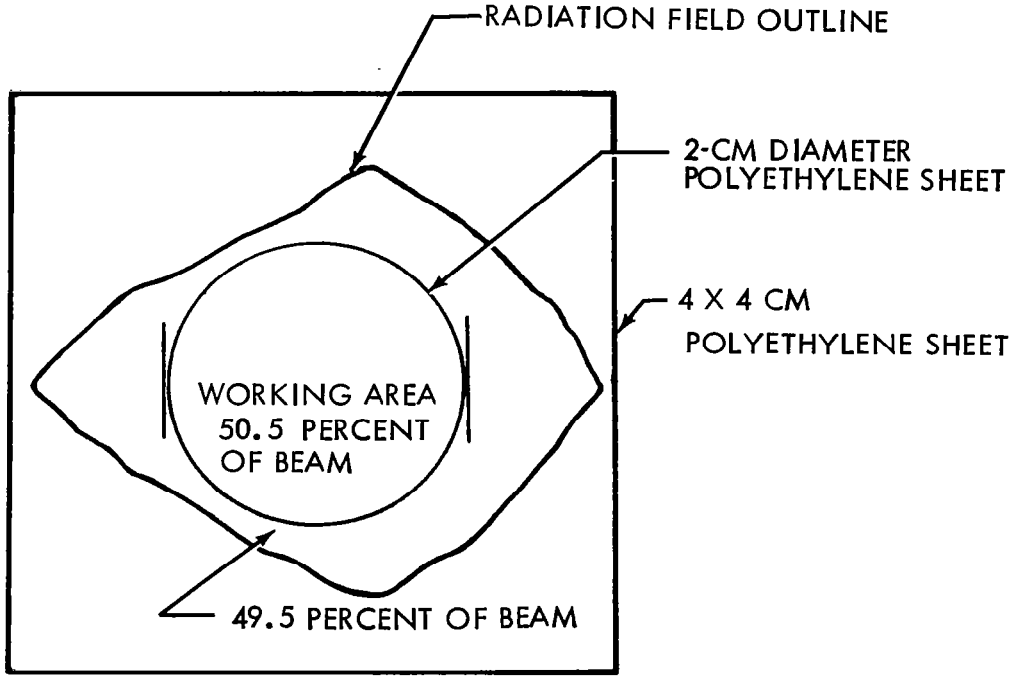

(b) ACTIVATION FOILS

Figure 11. Results of 100-Mev Proton Beam Mapping

2.5 Co^{60} GAMMA-RAY TEST

Co^{60} gamma-ray exposure was also performed on all the transistor types studied.

Experimental Configuration

Two experimental configurations were used during the Co^{60} gamma-ray exposure test. In the first configuration, shown in Figure 12, transistors were arranged in a circular array about a cylindrical source. The source was located in the Boeing Co^{60} Vault and raised into the center of the array by an elevator. In the second configuration, transistors were mounted on a cylindrical holder and lowered into the center of a cylindrical source array. The cylindrical source array was contained in a Gammacell 200, shown in Figure 13. The irradiation was carried out in air for both configurations. No electrical bias was applied to the devices during irradiation, except periodically when curve traces were obtained on selected devices.

Dosimetry

The radiation fields were mapped using cobalt glass chips. These chips were read, using a Beckman DU spectrophotometer, to a relative accuracy of about 5.0 percent and an absolute accuracy of about 10.0 percent. Exposure dose rates for the first configuration are shown in Figure 12. Exposure dose rates for the second configuration are shown in Table 5.

Experimental Procedure

Before the gamma-ray exposure test, all transistors were characterized on a Tektronix 575 curve tracer and a Fairchild Series 500 semiconductor test set. During and after the test, data was obtained from the transistors using both instruments.

In the first part of the test (using Configuration 1), two transistors of each type were irradiated at an exposure rate of approximately 3×10^4 R/hr to total exposure doses of approximately 6×10^5R. One device of each type was characterized during that radiation exposure using the curve tracer.

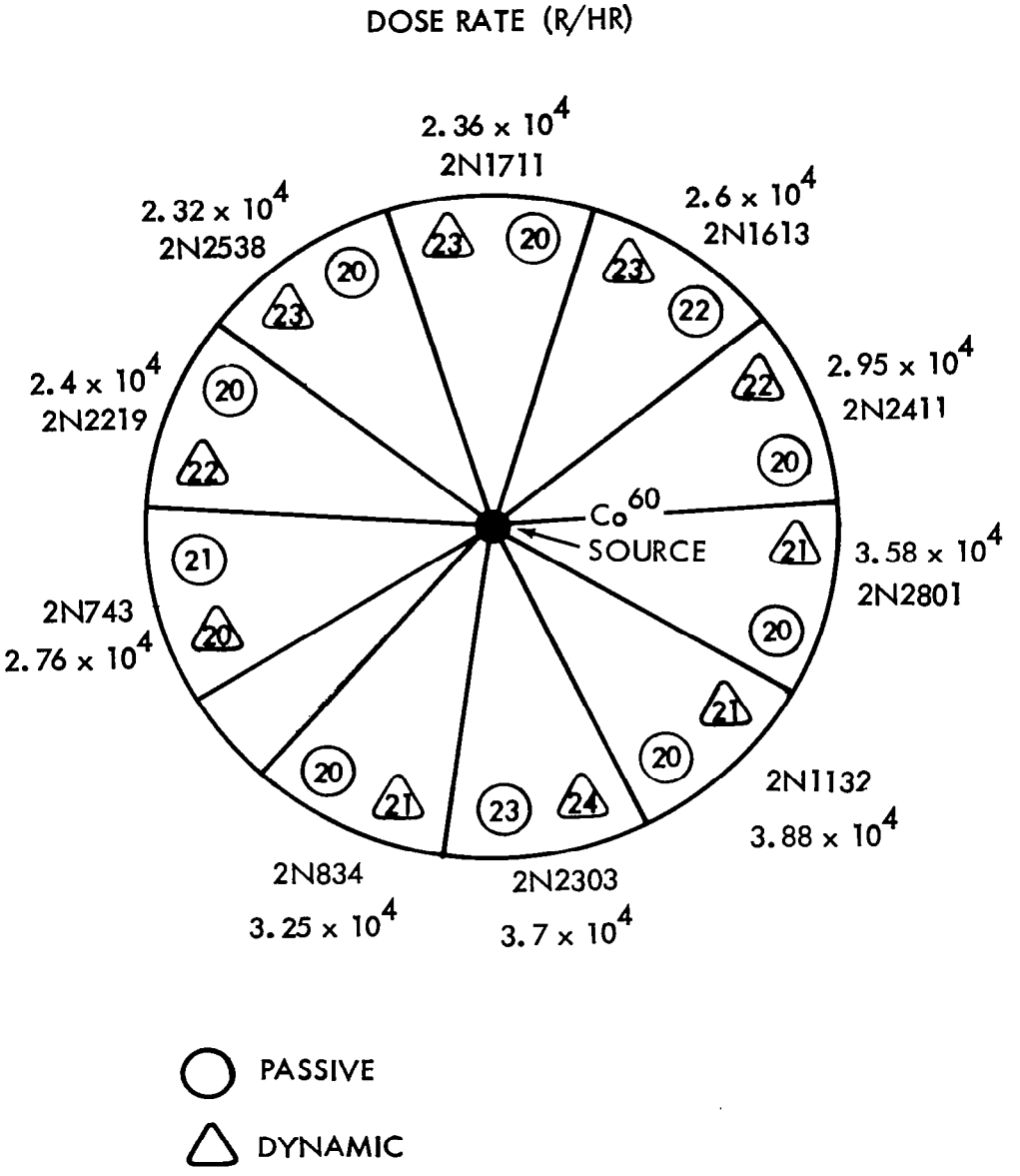

Figure 12. Transistor Array for Gamma-Radiation Test

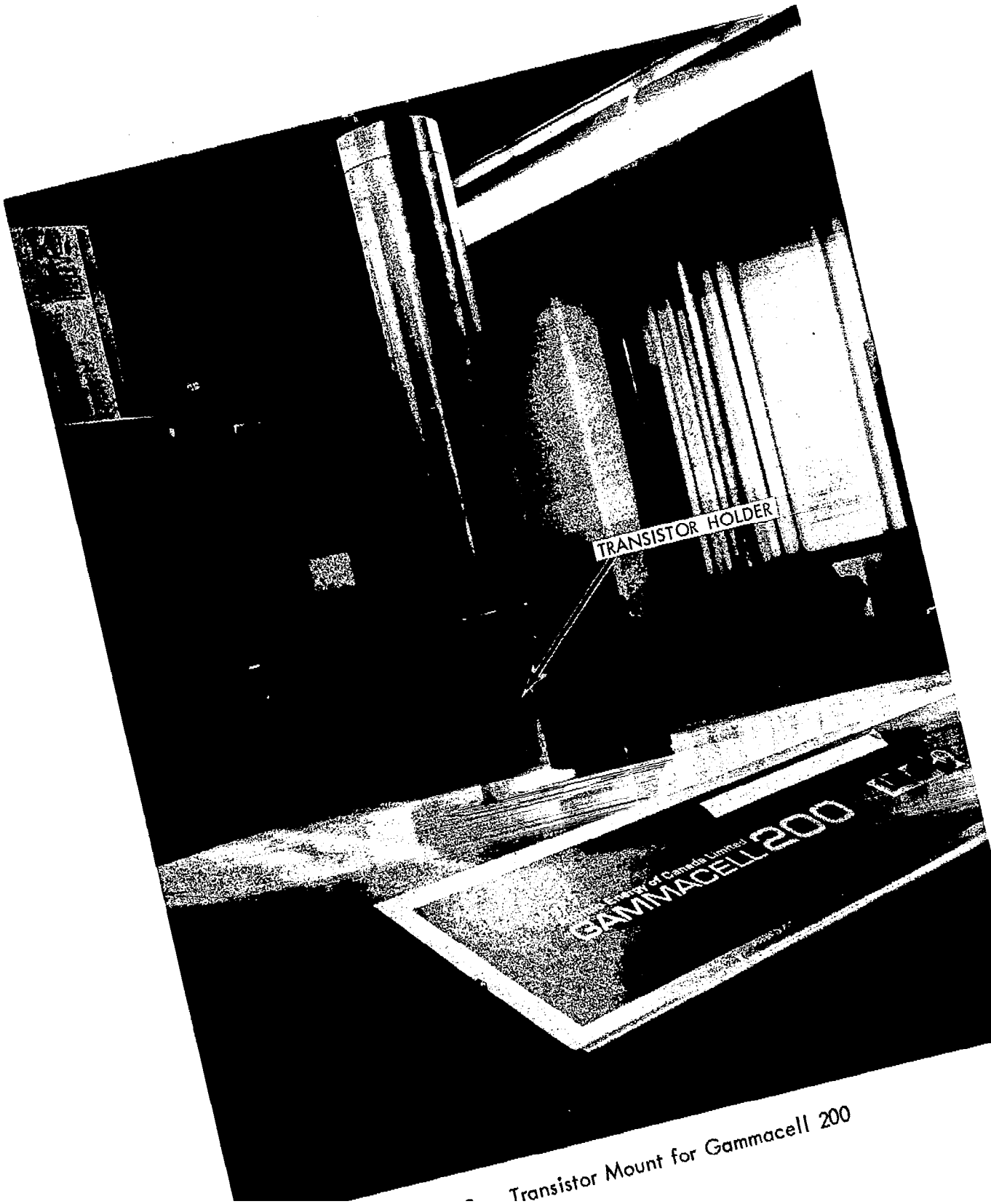

Transistor Mount for Gammacell 200

Table 5. Gammacell 200 Exposure Dose Rates

Transistor Type	Device No.	Dose Rate ($R\ hr^{-1}$)
2N1613	22	7.42×10^4
	23	6.95×10^4
	24	7.17×10^4
	25	6.56×10^4
2N1711	20	7.30×10^4
	21	6.63×10^4
	22	7.25×10^4
	23	6.85×10^4
2N2538	20	7.45×10^4
	21	7.10×10^4
	22	6.57×10^4
	23	6.90×10^4
2N2219	20	7.22×10^4
	21	7.32×10^4
	22	6.57×10^4
	23	6.95×10^4
2N743	20	6.90×10^4
	21	7.43×10^4
	22	7.15×10^4
	23	7.43×10^4
2N834	20	6.63×10^4
	21	6.75×10^4
	22	7.22×10^4
	23	7.43×10^4
2N2303	23	7.43×10^4
	24	6.90×10^4
	25	7.15×10^4
	26	6.62×10^4
2N1132	20	7.22×10^4
	21	6.57×10^4
	22	7.30×10^4
	23	6.85×10^4
2N2801	20	7.43×10^4
	21	6.95×10^4
	22	7.07×10^4
	23	6.53×10^4
2N2411	20	6.85×10^4
	21	6.63×10^4
	22	7.30×10^4
	23	6.53×10^4

In the second part of the test (Configuration 2), the two transistors of each type from Part 1, along with two additional unirradiated transistors of each type, were inserted into a gamma-ray field of approximately 7.5×10^4 R/hr. These devices were exposed to total doses of approximately 3×10^7 R.

Before each set of transistor measurements, the test instruments were allowed to warm up and calibration checks were made. The ambient temperature (room temperature) was monitored with a thermocouple during the measurements.

2.6 ANALYSIS OF TEST DATA

An analysis was performed on the effects of electrons, protons, and gamma rays on transistor parameters. The data which were analyzed included values of those radiation-sensitive parameters measured by use of the Fairchild Series 500 semiconductor tester, as well as oscillograms of transistor common-emitter characteristic curves made from the display of the Tektronix 575 curve tracer. Data values obtained passively from the semiconductor tester were analyzed by hand computation. Characteristic curves, obtained both passively and dynamically (during exposure), were analyzed by the use of a computer damage-plotting program.

2.6.1 Transistor Parameters Measured Passively

Selected values of radiation-sensitive transistor parameters, which were measured passively, have been analyzed in order to investigate the dependence of those parameters on electron fluence and energy.

The least radiation sensitive of the parameters which were studied was the breakdown voltage, BV_{CBO} (measured at a collector current of 100 μa). An average of the values of the percentage change in BV_{CBO} is shown in Table 6 for all seven irradiation tests. Most of the transistor types showed either no significant change (within the limits of precision) or an increase in breakdown voltage which does not appear to be a function of particle fluence. However, a decrease of breakdown voltage was observed for transistors of type 2N2538, and the decrease appeared to be a function of charged particle fluence. Dotted lines shown on

Table 6. Radiation-Induced Changes in BV_{CBO} at 100 μa

DEVICE TYPE	TYPICAL BV_{CBO} INITIAL CONTROL TRANSISTORS (VOLTS)	AVERAGE $\Delta(BV_{CBO})$ IN PERCENTAGE							APPARENT CHANGE WITH FLUENCE
		PROTON TESTS			ELECTRON TESTS			COBALT 60 GAMMA	
		1 MEV	20 MEV	100 MEV	2 MEV	1 MEV	0.53 MEV		
2N1613	118	4	5	5	7	10	9	3	None
2N1711	135	1 to 28	2 to 11	6	8	7	7	5	Possible Increase
2N2538	100	0 to -43	0	0 to -9	0 to -12	-1 to -17	1 to -25	1	Decrease
2N2219	82.7	1	5	3	1	6	8	7	None
2N743	63.9	0 to -49	1	1	0 to -10	0 to -5	0 to -8	0	Possible Decrease
2N834	81.2	0 to -58	-2	0 to -3	1	-4	-1	0	Possible Decrease
2N2303	70.8	0	1	-1	0	7	2	2	None
2N1132	82.9	7	3	7	12	9	9	3	None
2N2801	57.9	3	2	4	0 to 3	0 to 8	3	2	None
2N2411	57.7	1	1	3	0 to 6	0 to 4	2 to 7	0	None
APPROX. FLUENCE RANGE PARTICLES CM^{-2}		10^{10} to 10^{13}	10^{10} to 10^{12}	10^{12} to 10^{14}	10^{14} to 10^{16}	10^{14} to 10^{16}	10^{12} to 10^{16}	10^{11} to 10^{17}	

considerable scatter, there is indication of a strong dependence on both fluence and energy. Energies shown are those incident on the devices, some of which had inherent can shielding removed. Energy incident on the silicon can be calculated from shielding considerations (Tables 11 and 12 of Reference 1 and Section 2.7.3 of this document). Although BV_{CBO} was measured only at a current of 100 μa, from measurements of leakage current, I_{CBO}, as a function of reverse bias, V_{CB}, it was found that BV_{CBO} changes observed in Figure 14 are not attributable to a softening of the breakdown knee, but actually are due to changes in the threshold for breakdown voltage.

By assuming a linear dependence of $\Delta(BV_{CBO})$ on particle fluence (Figure 14), a crude indication of the relative order of effectiveness of electrons and protons of different energies is possible for later comparisons with radiation equivalences obtainable from other transistor parameters.

Saturation voltage, $V_{CE}(sat)$, measured at a current gain of 2 for collector currents of 2 and 10 ma, respectively, increased by over 100 percent for many of the exposed transistors. A strong dependence of the changes of $V_{CE}(sat)$ on charged particle fluence was observed for all 10 of the transistor types. All types tested yielded results similar to those shown in Figures 15, 16, and 17. The relative sensitivity of the 10 device types to proton exposure was, in general, similar to that observed for electrons, as shown in Figure 31 (for npn) and Figure 32 (for pnp) of the semiannual progress report (Reference 1).

Since the changes in $V_{CE}(sat)$ could be fitted, approximately, by a power law dependence on Φ, it was possible to obtain equivalence values or relative effectiveness for energy and particle types. A summary of radiation equivalences for $\Delta[V_{CE}(sat)]$, averaged over the 10 transistor types tested, is shown in Table 7. Values on the table indicate that one of the 1-Mev protons is approximately as effective as 15 of the 100-Mev protons or 4,500 of the 0.53-Mev electrons, etc. The energy dependence observed for $\Delta[V_{CE}(sat)]$ of all transistor types is similar to that observed for $\Delta(BV_{CBO})$ of transistor type 2N2538. (The 2N2538 was the only transistor type that showed a significant dependence of $\Delta(BV_{CBO})$ on fluence over the exposure ranges of this test program.)

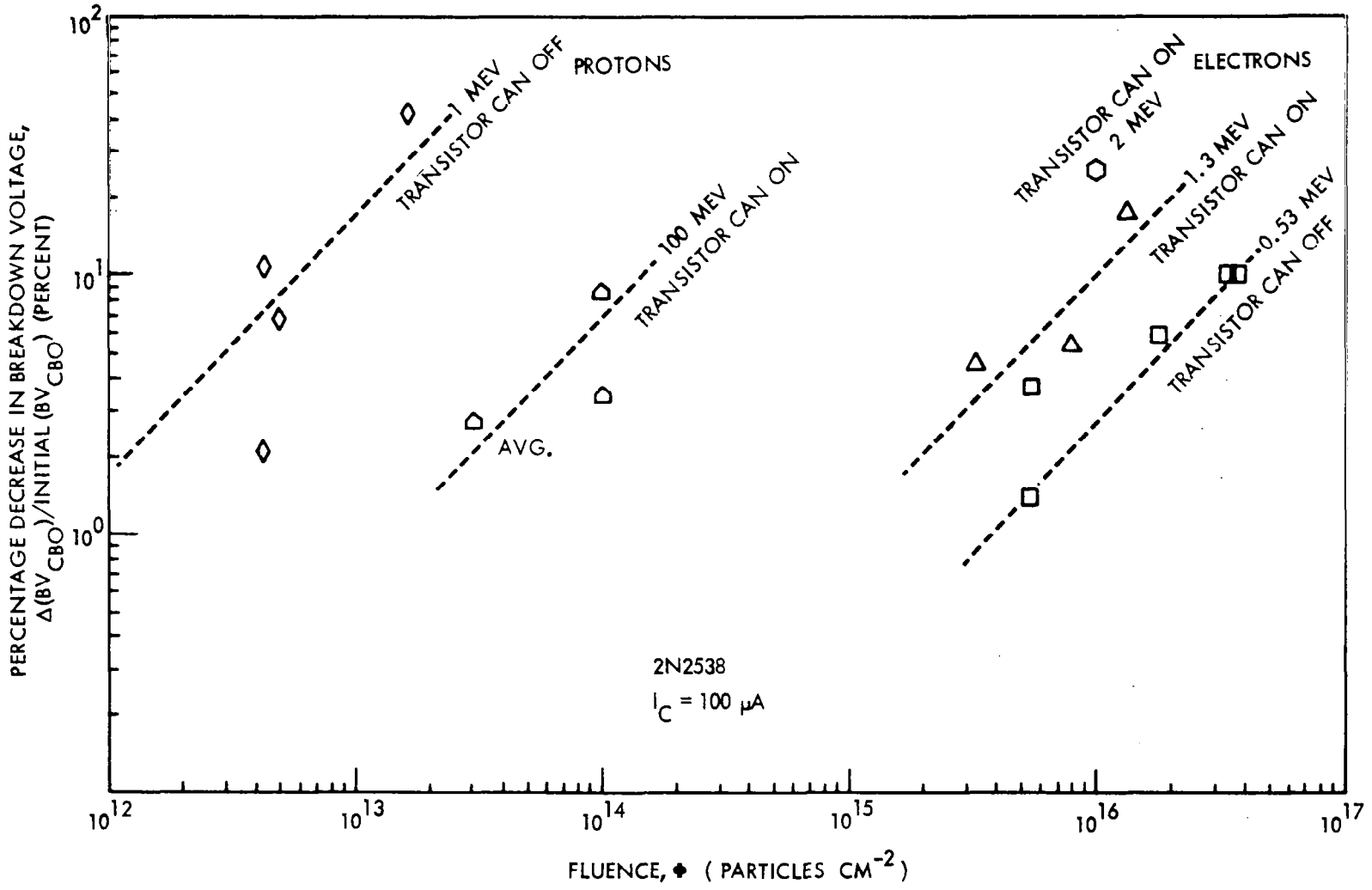

Figure 14. Dependence of $\Delta(BV_{CBO})$ on Charged Particle Fluence (2N2538)

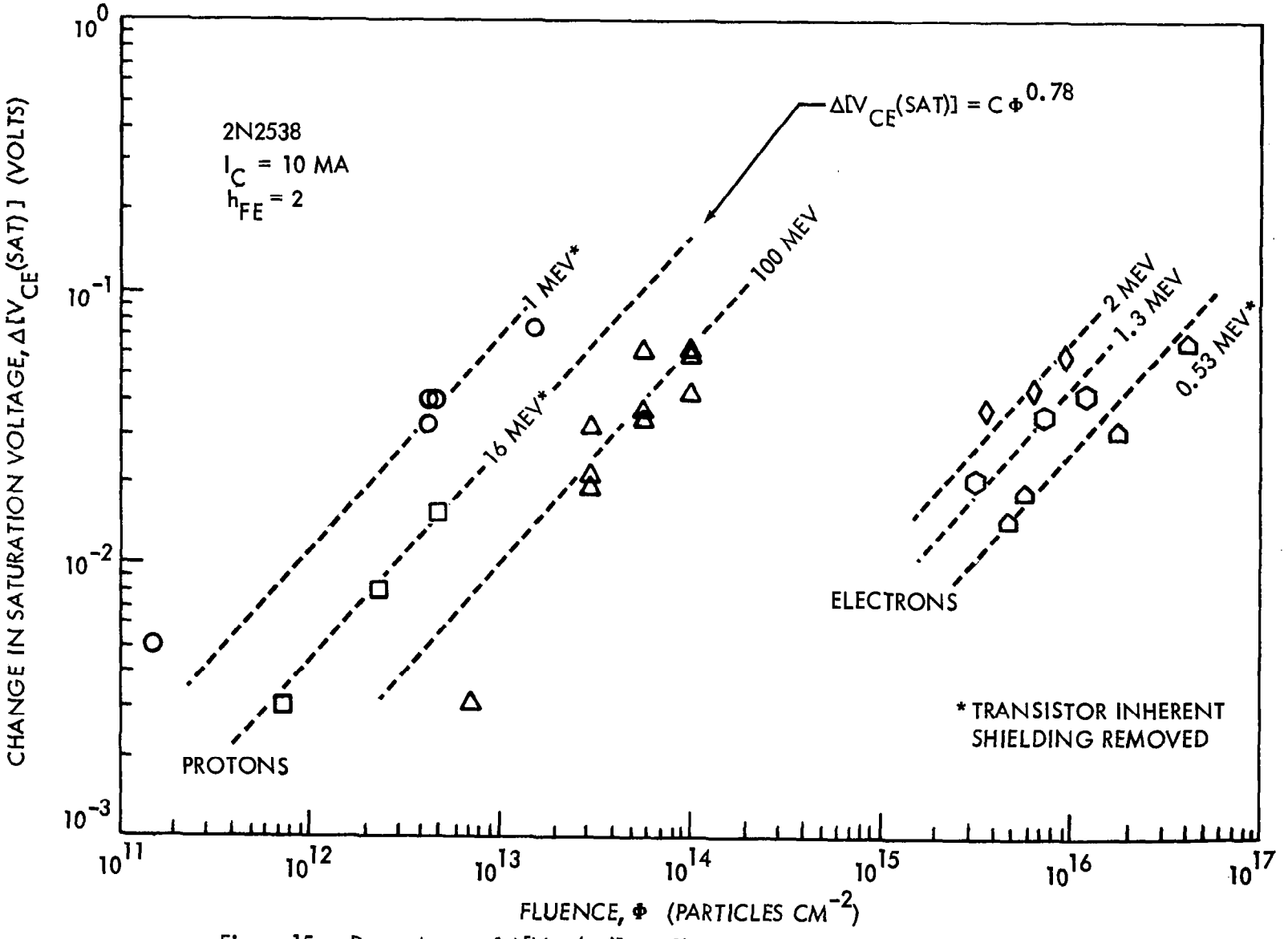

Figure 15. Dependence of $\Delta[V_{CE}(sat)]$ on Charged Particle Fluence (2N2538)

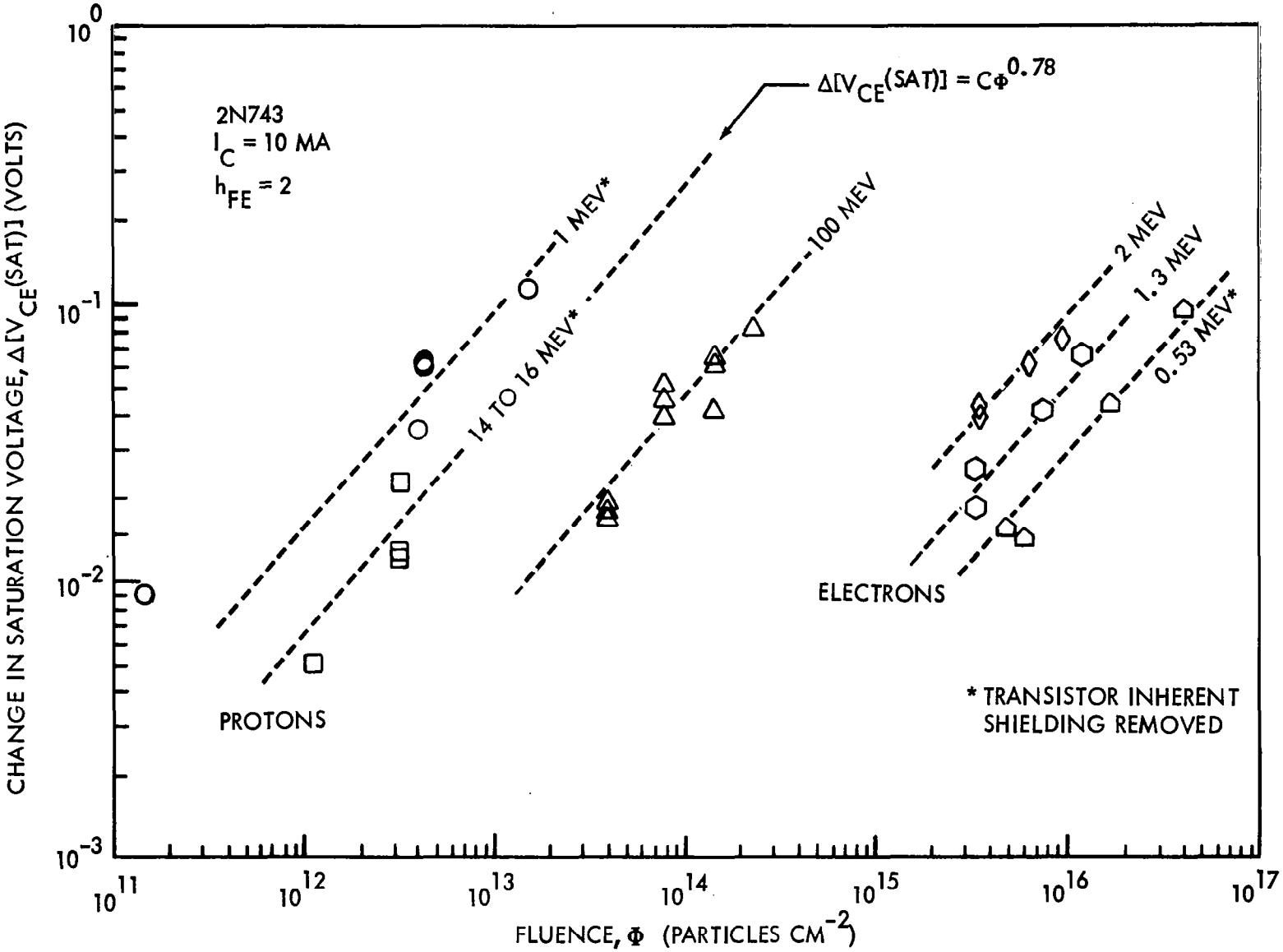

Figure 16. Dependence of $\Delta[V_{CE}(sat)]$ on Charged Particle Fluence (2N743)

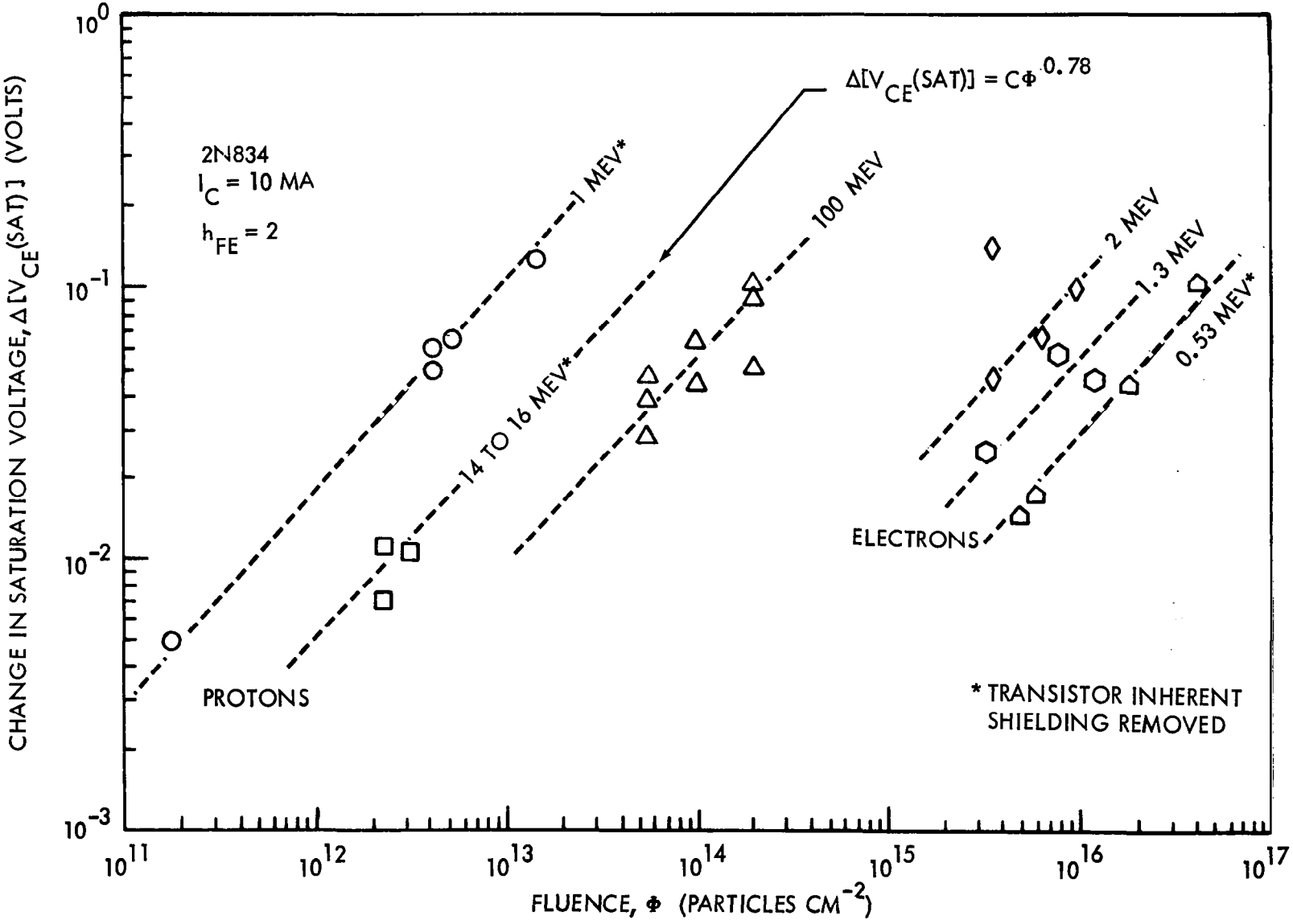

Figure 17. Dependence of $\Delta[V_{CE}(sat)]$ on Charged Particle Fluence (2N834)

Table 7. Charged Particle Equivalences for $\Delta[V_{CE}(sat)]$

Tests	Proton Tests (Mev)			Electron Tests (Mev)		
	1	20*	100	2**	1***	0.53
1-Mev Proton Can Off	1	3.0	1.5×10^{1}	1.1×10^{3}	2.3×10^{3}	4.5×10^{3}
20-Mev Proton Can Off	3.3×10^{-1}	1	5	3.8×10^{2}	7.5×10^{2}	1.5×10^{3}
100-Mev Proton	6.7×10^{-2}	2×10^{-1}	1	7.5×10^{1}	1.5×10^{2}	3×10^{2}
2-Mev Electron	9.1×10^{-4}	2.6×10^{-3}	1.3×10^{-2}	1	2	4
1-Mev Electron	4.3×10^{-4}	1.3×10^{-3}	6.7×10^{-3}	5×10^{-1}	1	2
0.53-Mev Electron Can Off	2.2×10^{-4}	6.7×10^{-4}	3.3×10^{-3}	2.5×10^{-1}	5×10^{-1}	1

* Energies 14 to 17 Mev on the silicon chip
** Energies 1.5 to 1.7 Mev on the silicon chip
*** Energies 0.8 to 1.0 Mev on the silicon chip

The observed changes in base-emitter saturation voltage, $V_{BE}(sat)$, were smaller than those observed for $V_{CE}(sat)$. However, $\Delta[V_{BE}(sat)]$ also shows a strong dependence on particle fluence, as shown in Figure 18. Charged particle equivalences obtained from changes in $V_{BE}(sat)$ are, in general, comparable to those summarized for $\Delta[V_{CE}(sat)]$ in Table 6.

Leakage current, I_{CBO} (measured at a collector-to-base reverse bias of 10 volts), was observed to show permanent increases for transistors exposed to charged particles. As described in Reference 1, $\Delta(I_{CBO})$, over a narrow range of high exposures studied using passive data from the electron tests, showed no evidence of a dependence on electron fluence. Figure 19 shows a comparison of initial- and final-leakage currents for the 2N2303 transistors irradiated in the electron tests. The diagonal line represents values for no change. This transistor type came closest to showing a dependence on the amount of electron exposure, but it also is the only transistor that showed such a wide variation in both initial and final values of leakage current. Five other transistor types (2N1132, 2N1613, 2N1711, 2N2219, and 2N2801) also showed large changes in leakage current but no obvious dependence on electron energy. Electron test data on these devices is shown in Figure 20, with the exception of the 2N1613 whose data point grouping was the same as the 2N1711. These devices, with the exception of the 2N1132, showed the same increase in I_{CBO} independent of initial value, which would indicate greater percentage increases for those of lower initial-leakage current. The remaining transistor types (2N743, 2N834, 2N2411, and 2N2538) showed only very small percentage increases in leakage current. The individual groupings of transistors shown in Figure 20 would indicate that transistor types with the highest initial values of leakage current generally would have the highest values of leakage current following an exposure (Reference 2) even as great as 10^{16} electrons/cm^2 (an exposure far in excess to that of a typical space mission). This fact was observed for all of the transistor types tested. Six types of transistors showed average changes of I_{CBO} of approximately an order of magnitude for the electron tests. However, four types of transistors (2N743, 2N834, 2N2411, and 2N2538) showed only small percentage changes; thus their initial and final leakage currents would necessarily conform to the results of the other six types.

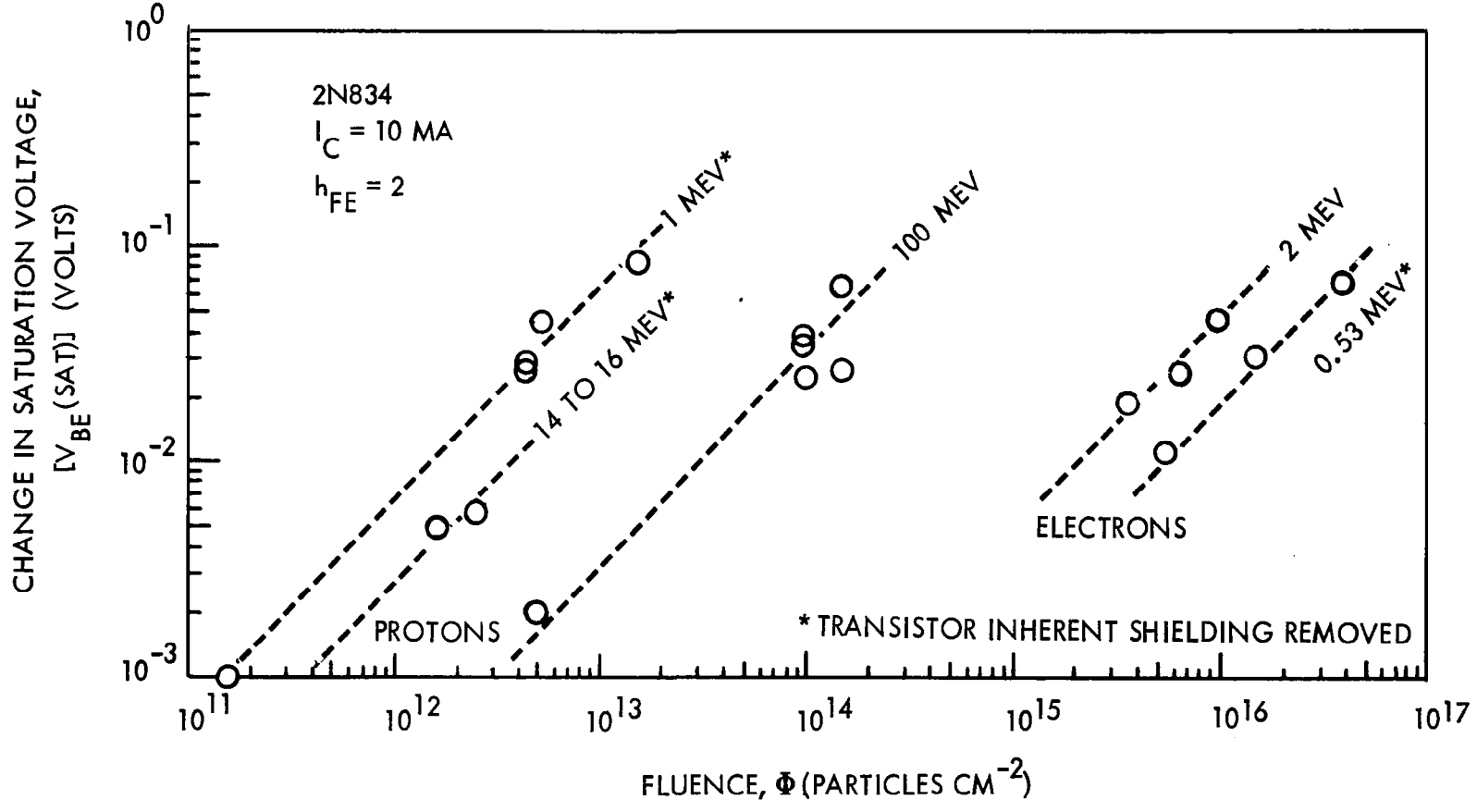

Figure 18. Dependence of Base-Emitter Saturation Voltage on Fluence

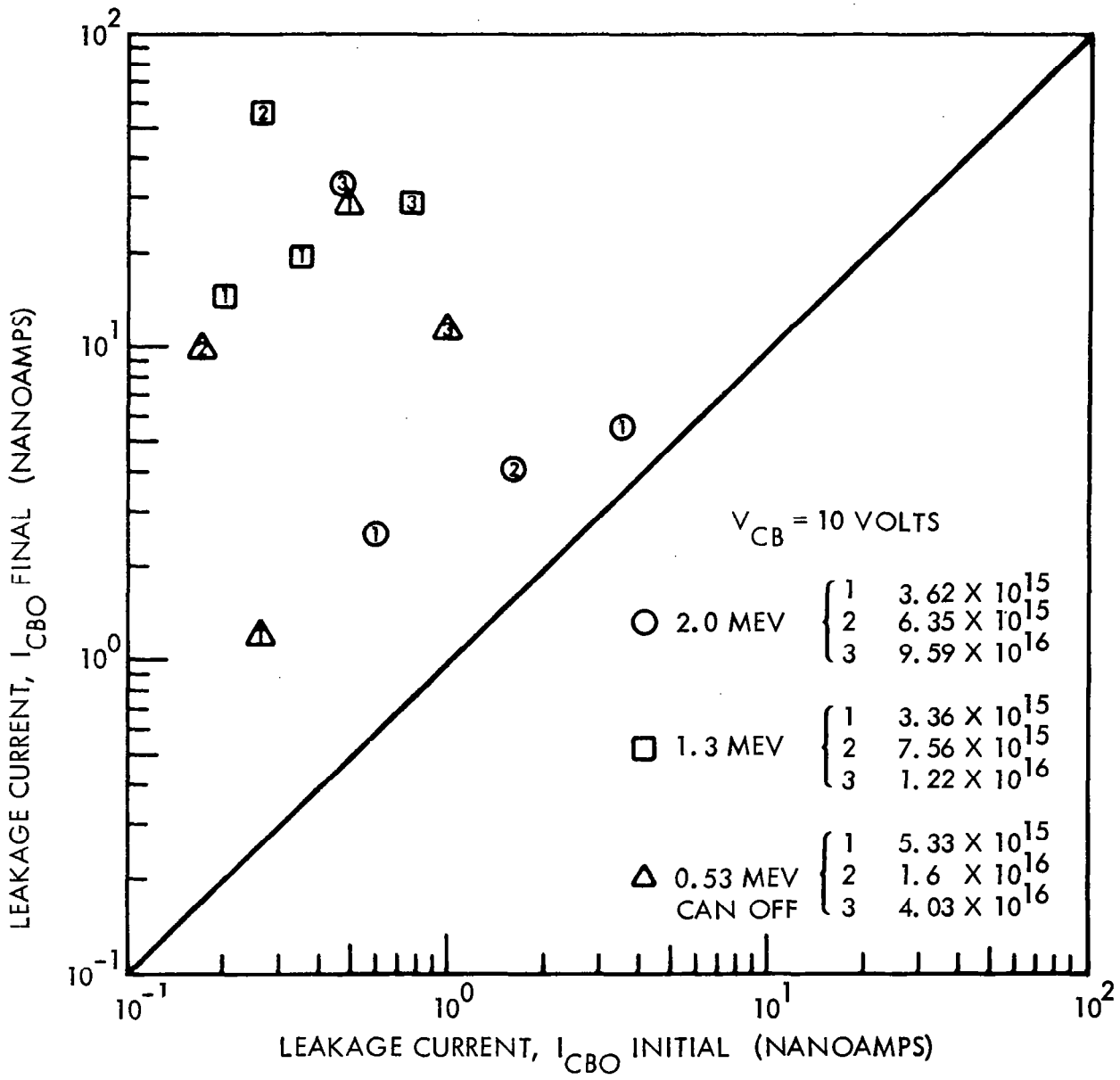

Figure 19. Electron-Induced Changes of I_{CBO} (2N2303)

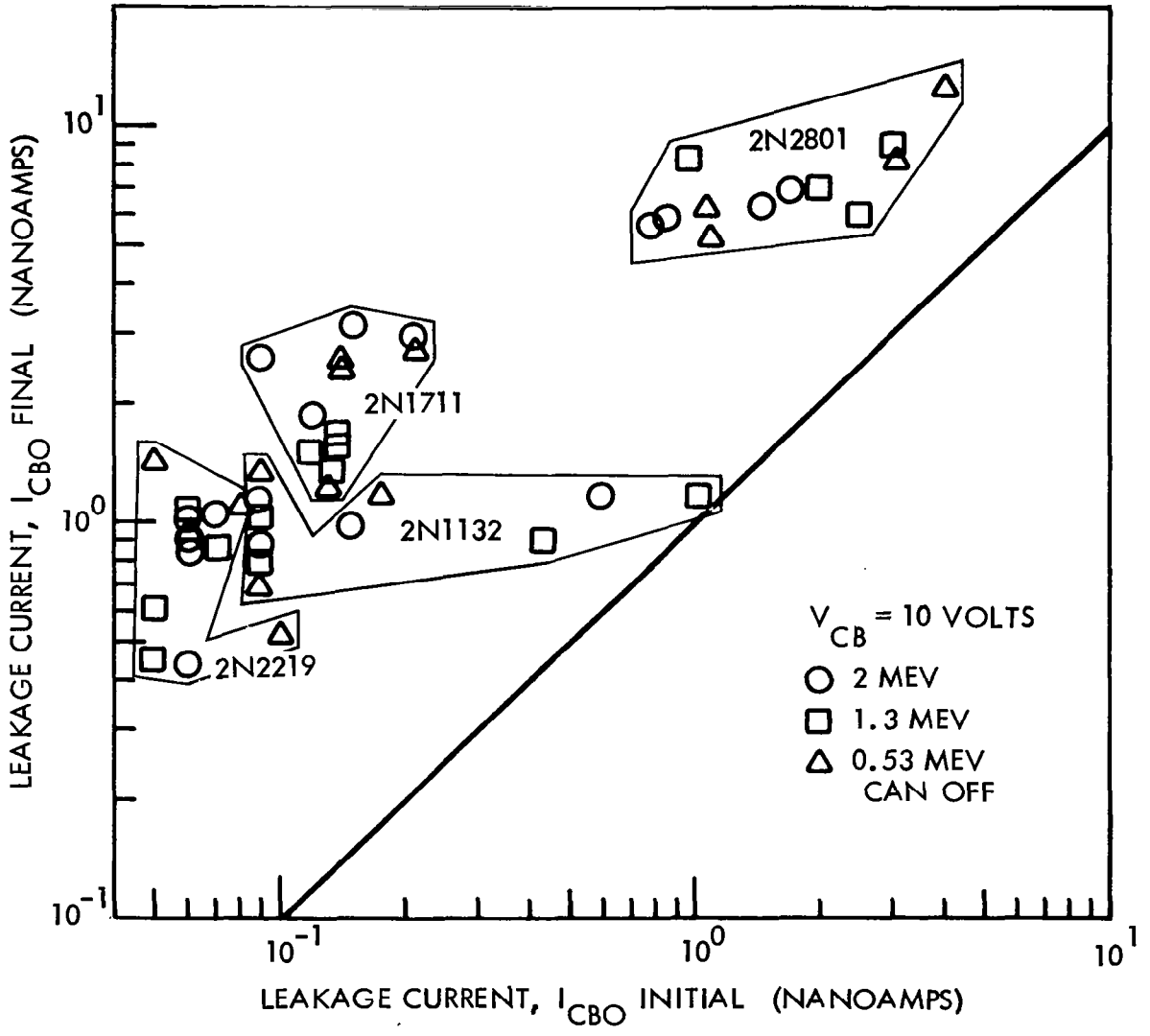

Figure 20. Electron-Induced Changes of I_{CBO}

Although detailed analysis of changes of I_{CBO} were performed only for collector voltages of 10 volts, the dependence of leakage current on voltage (measured on selected devices) was typical of the dependence before irradiation. Breakdown voltages (at 100 μamps), in general, showed very little change (plots as a function of current indicate a sharp breakdown rather than a softening of the breakdown knee for exposures up to 4.24×10^{12} 1-Mev protons/cm^2). Breakdown voltages after the irradiation tests all were in excess of the 10 volts used for I_{CBO} measurements.

In contrast to the electron tests, the results of proton exposure of transistors showed a very strong dependence of $\Delta(I_{CBO})$ not only on proton fluence, but on proton energy as well. Data on four transistor types is shown in Figures 21, 22, and 23. Since $\Delta(I_{CBO})$ could be approximately fitted by a linear dependence on proton fluence, it was possible to determine relative effectiveness of protons of different energies. Table 8 summarizes proton equivalences obtained for changes in I_{CBO}. These equivalence values compare roughly with those obtained in Table 7 for $\Delta[V_{CE}(sat)]$ and can be compared later to equivalence values related to common-emitter current gain, h_{FE} (see Section 2.7.2).

Table 8. Proton Equivalence for I_{CBO} Changes

Tests	Proton Tests (Mev)		
	1	20*	100
1-Mev Proton Can Off	1	2.5	1.1×10^{1}
20-Mev Proton Can Off	4.0×10^{-1}	1	5.0
100-Mev Proton	9.0×10^{-2}	2.0×10^{-1}	1

* Energies 14 to 17 Mev (see Section 2.5.2)

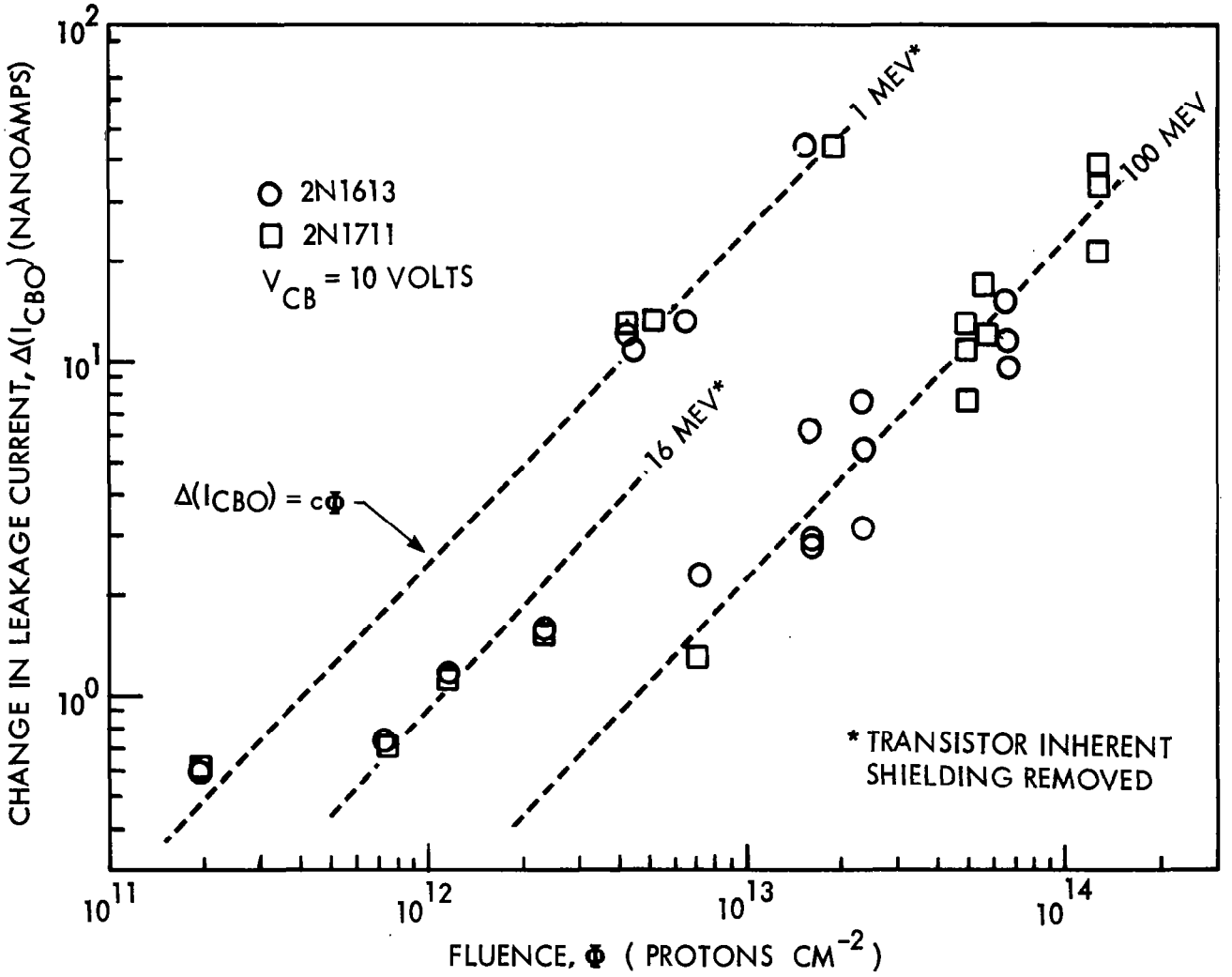

Figure 21. Dependence of $\Delta(I_{CBO})$ on Proton Fluence (2N1613 , 2N1711)

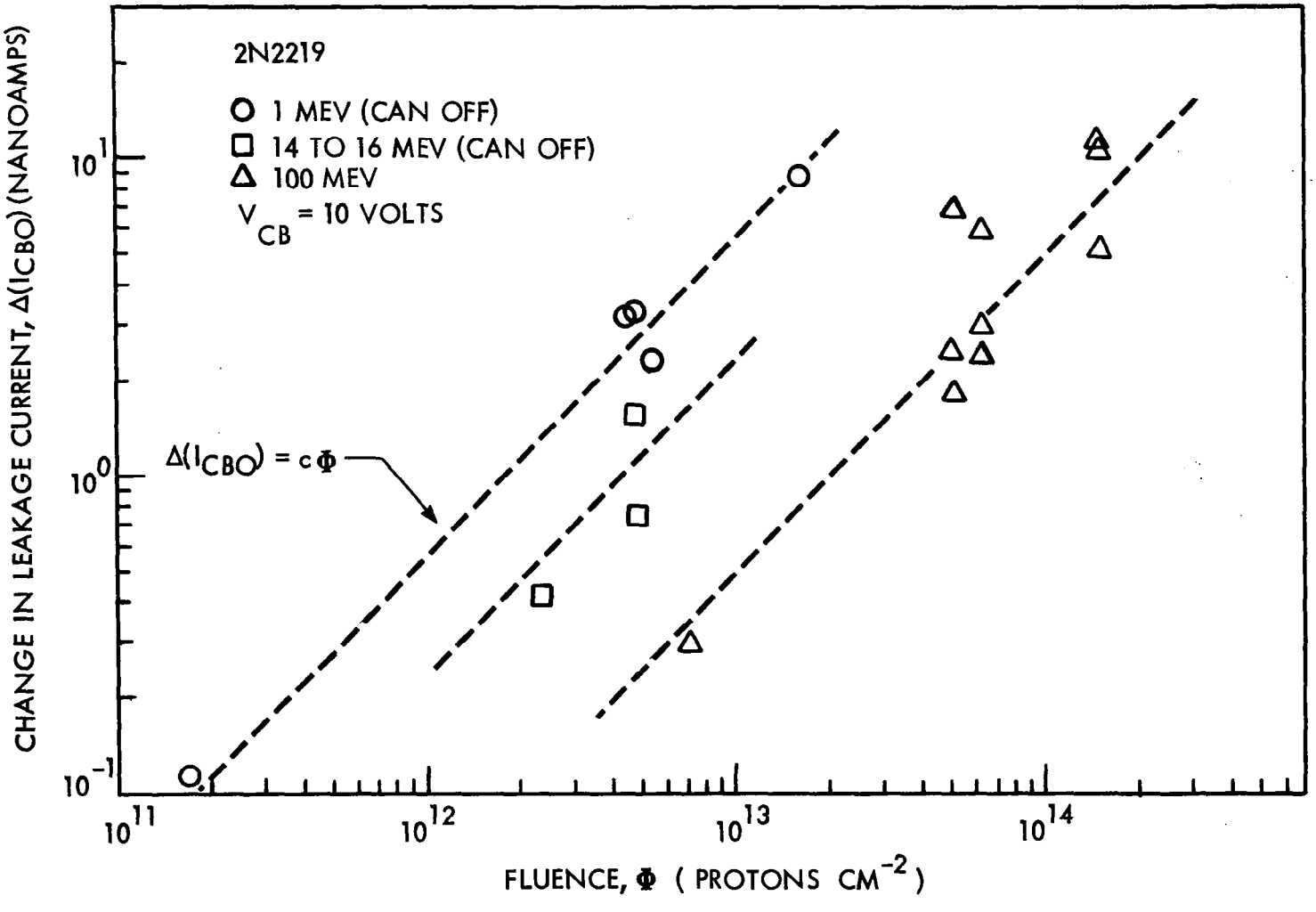

Figure 22. Dependence of $\Delta(I_{CBO})$ on Proton Fluence (2N2219)

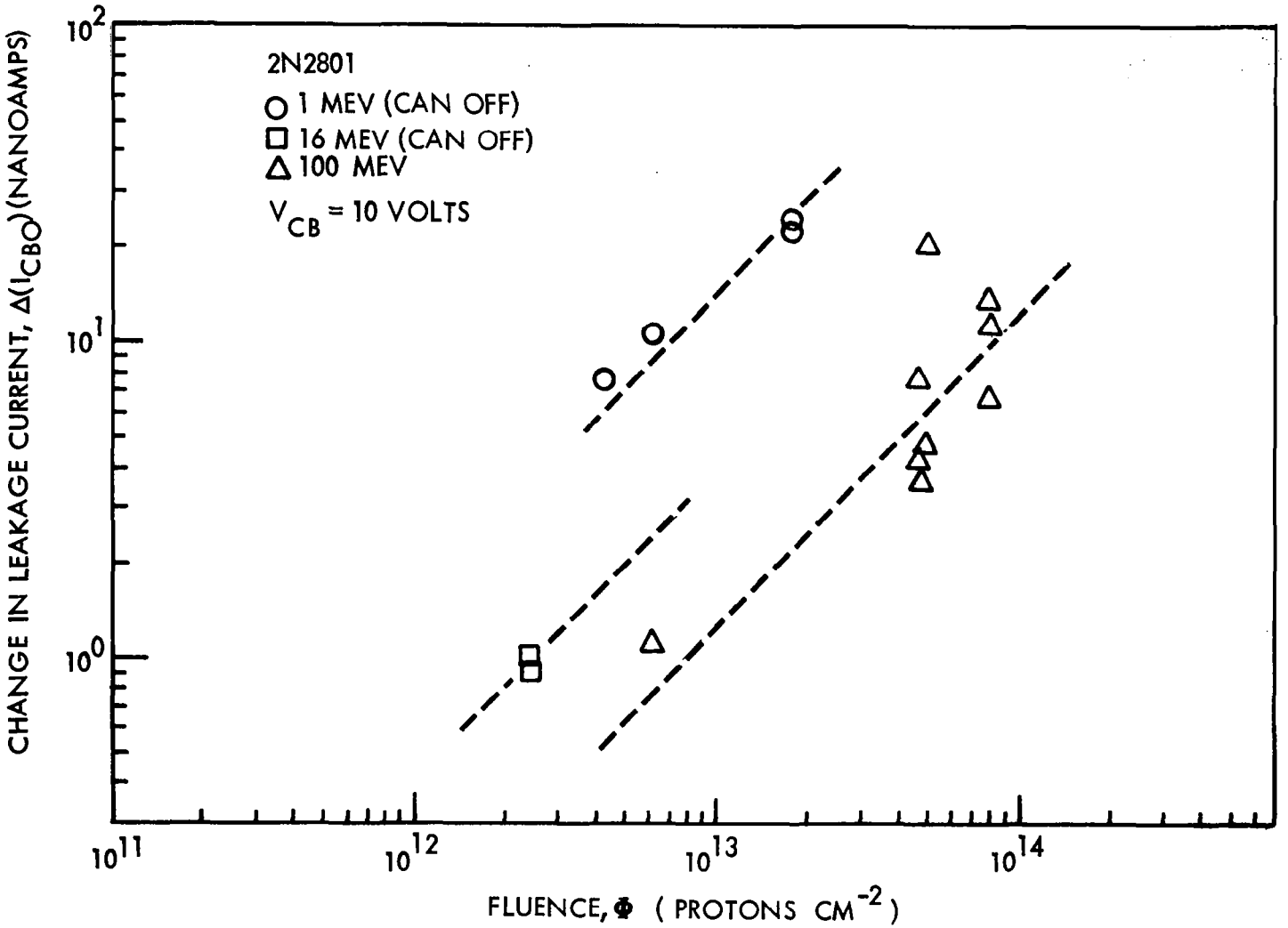

Figure 23. Dependence of $\Delta(I_{CBO})$ on Proton Fluence (2N2801)

The comparative permanency of these linear changes in $\Delta(I_{CBO})$ at room temperature (299°K) was verified by measuring I_{CBO} at selected time periods following radiation exposure. Data on 2N1613 devices are shown in Figure 24 for time periods of 5, 31, and 202 days after 1-Mev proton exposure. Figure 25 indicates that only slight annealing was observed for most of the transistor types after high-fluence proton exposure. However, a couple of the epitaxial mesa devices that showed anomalously large changes in leakage current at high exposures also showed pronounced recovery, as shown in Figure 26. (No biases were applied during or following exposure, except for measurements.) After those devices had recovered at room temperature, they more closely fitted a linear dependence on fluence which was similar to that shown in Figure 21, 22, and 23. The permanent components of proton-induced $\Delta(I_{CBO})$ provided information on proton equivalences (Table 8) similar to equivalences for $\Delta[V_{CE}(sat)]$ of Table 7.

Curves of collector current, I_C, as a function of base-emitter voltage, V_{BE}, were plotted from data obtained on the Fairchild transistor tester (e.g., Figure 27). According to the analysis of Easley (Reference 3) and Goben (Reference 4), one would expect I_C to decrease as the base transport factor decreases. The curve of Figure 27 might also be expected to appear as a straight line on a semi-log plot if the typical diode equation is valid.

$$I_C = I_o \left[\exp(qV_{BE}/kT) - 1\right] \qquad (3)$$

where:

q = electronic charge

k = Boltzmann's constant

T = absolute temperature

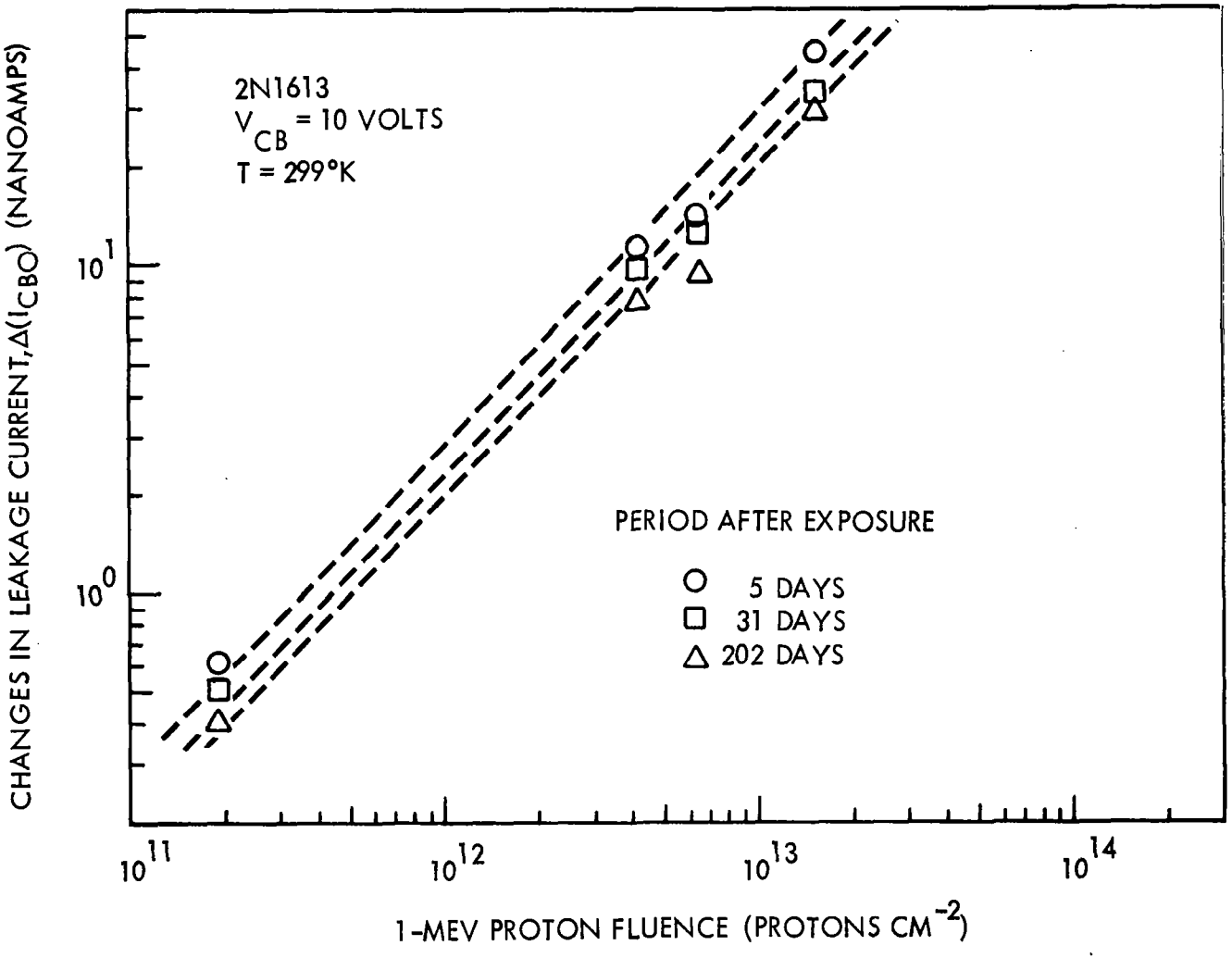

Figure 24. Slight Annealing of $\Delta(I_{CBO})$ (2N1613)

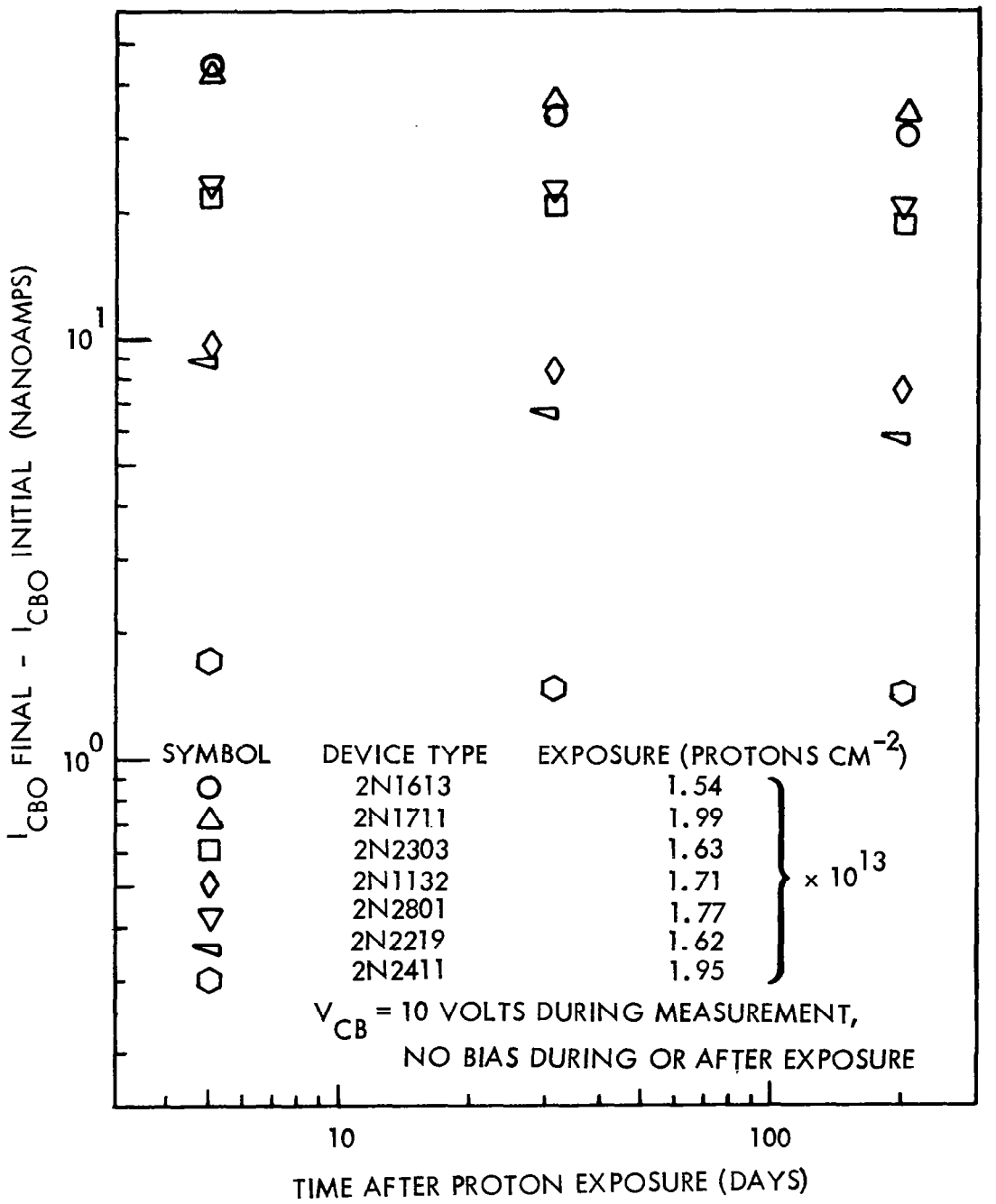

Figure 25. Slight Annealing of I_{CBO} After 1-Mev Proton Test

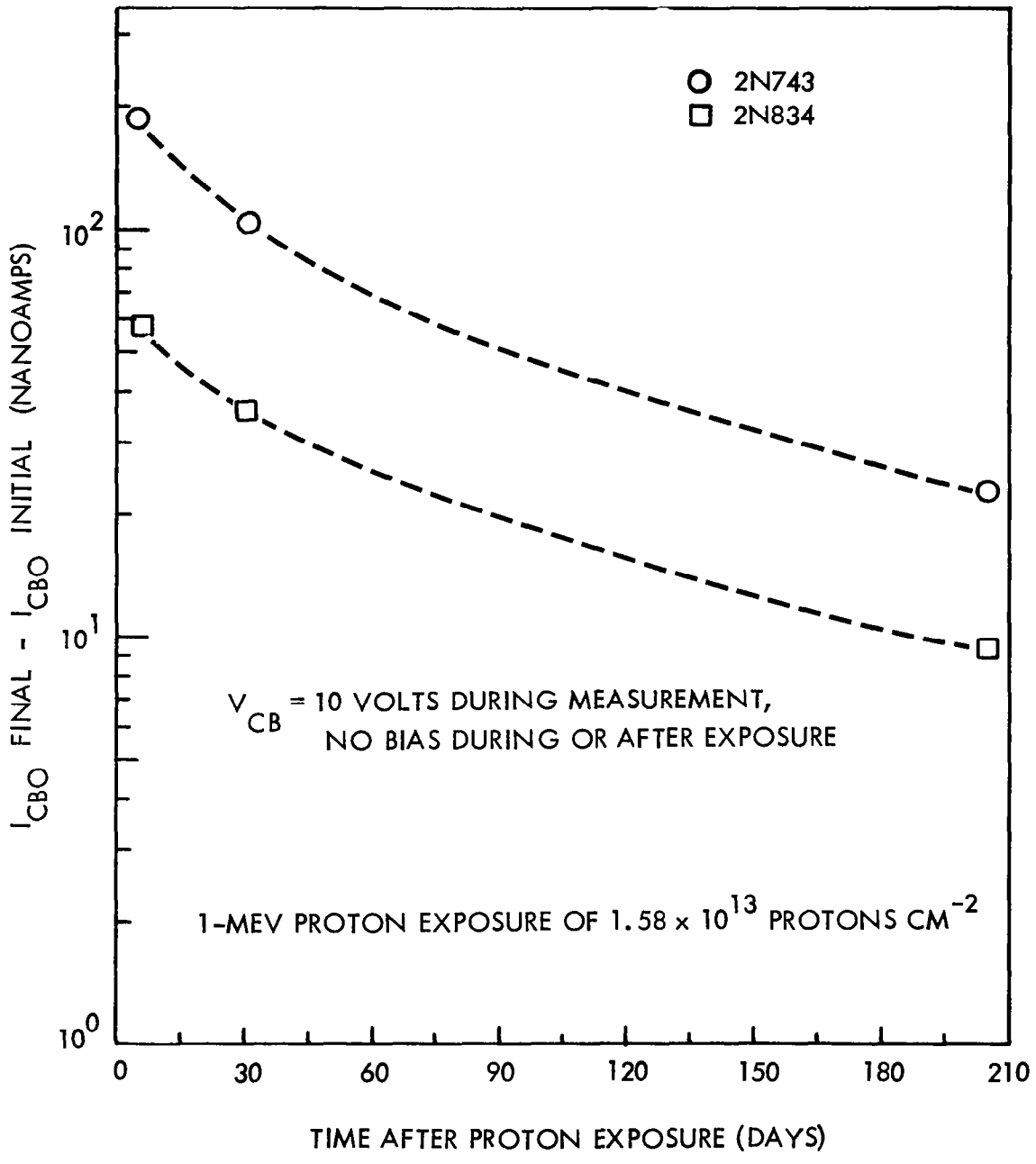

Figure 26. Annealing of I_{CBO} of Epitaxial Mesa Devices

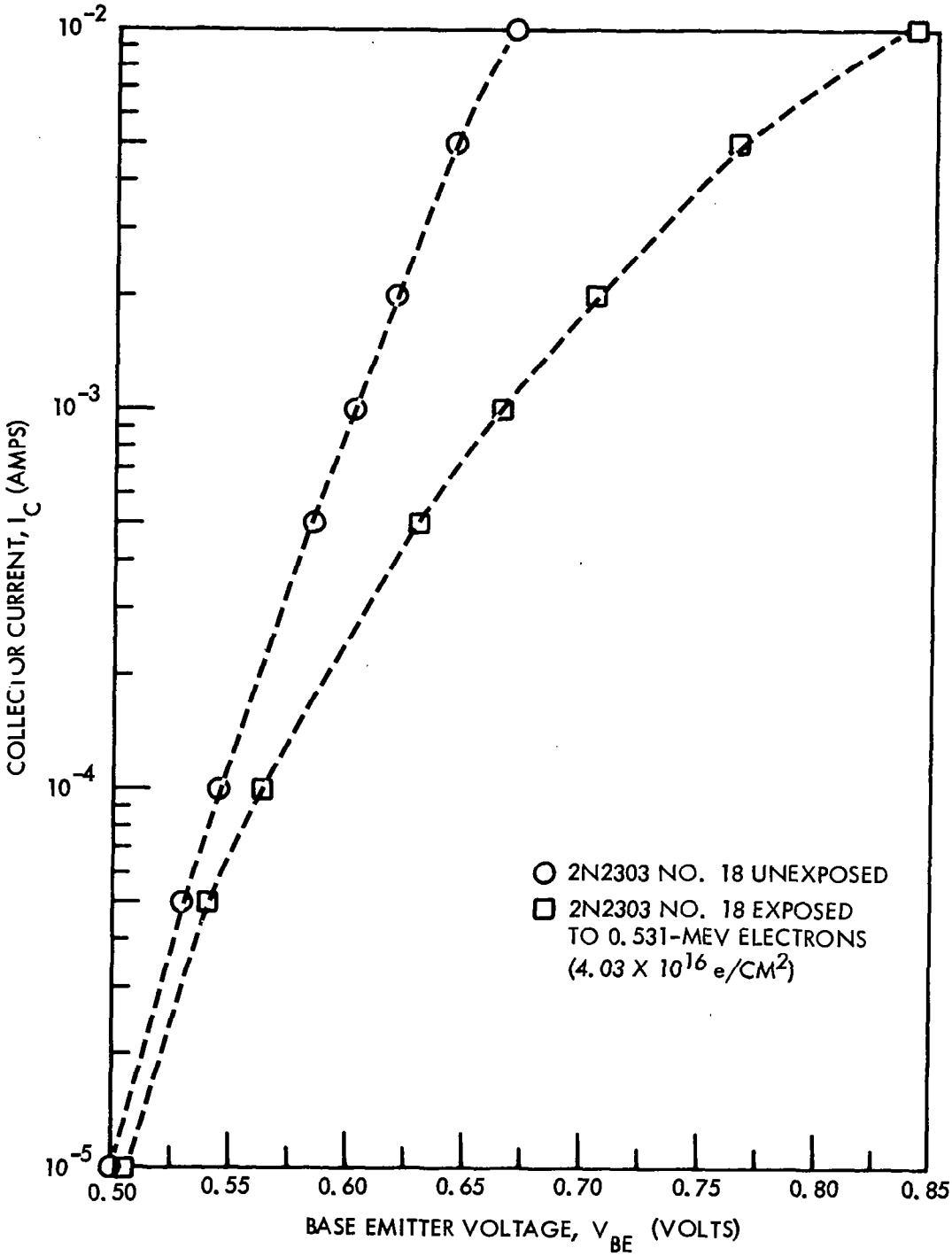

Figure 27. I_C Versus V_{BE} for 2N2303

The I_C curves, however, show a deviation from linear which, at high current, appears at first order to be due to a transverse voltage drop in the base sheet resistance and a fringing of the collector current due to the field set up by this voltage drop (Reference 5). It has been shown (References 6, 7, and 8) that transistor base current consists of the sums of components of recombination current originating in various regions of the device. Each of the base current components, $(I_B)_n$, approximately follows an exponential dependence on base-emitter voltage,

$$(I_B)_n \cong (I_o)_n \exp(qV_{BE}/nkT) \qquad (4)$$

where: $(I_o)_n$ = a constant dependent on physical properties of the device and is a function of radiation exposure. (In some cases I_o may depend on V_{BE}.)

n = a component number whose value at any specific value of V_{BE} depends on the region in which that component of recombination current originates.

The following components have been identified:

$n = 1.0$ component — recombination-generation current in the base region

$1 < n \leq 2$ component — recombination-generation at or near the surface and in the bulk of the emitter space-charge region

$2 < n \leq 4$ components — surface channel currents

In order to explore the usefulness of I_B versus V_{BE} data and to extend the range of current measurements, a simple circuit was assembled (Reference 1) to obtain accurate measurements of I_C as a function of V_{BE} to very low currents.

Figure 28 shows a "separated" curve of I_B versus V_{BE} that has been fitted to three components of base current with n values of 1, 1.5, and 2, respectively. Following an exposure of 2×10^7 R of Co^{60} gamma radiation, base recombination current was observed to increase, as indicated in Figure 29. Figure 30 shows the increase in base recombination current after the effects of secondary electrons generated by a Co^{60} gamma-ray exposure of 10^4 R. It is significant to note that the change in I_B at low levels is dominated by a component having $n \simeq 1.6$. This

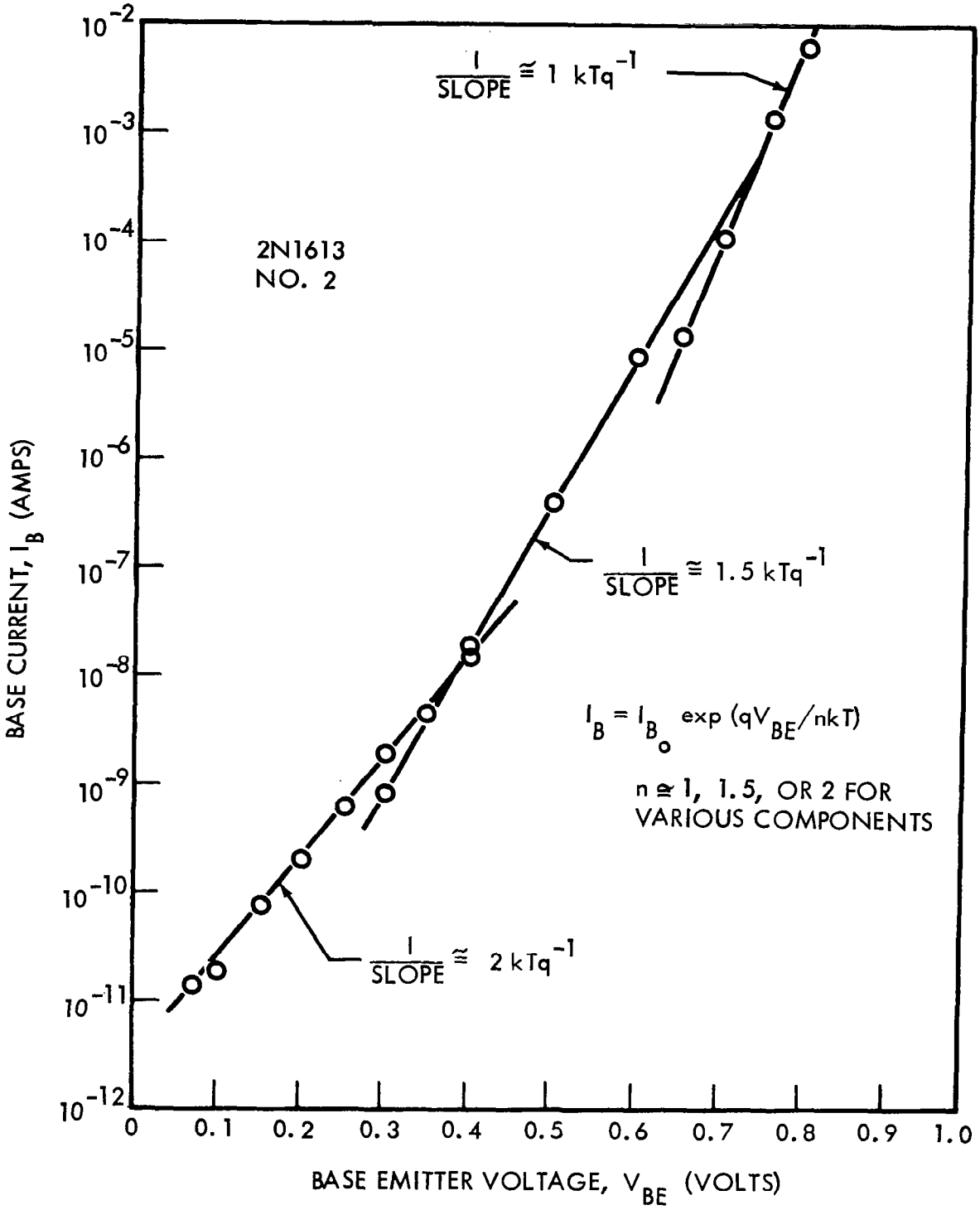

Figure 28. Components of I_B Versus V_{BE} (2N1613)

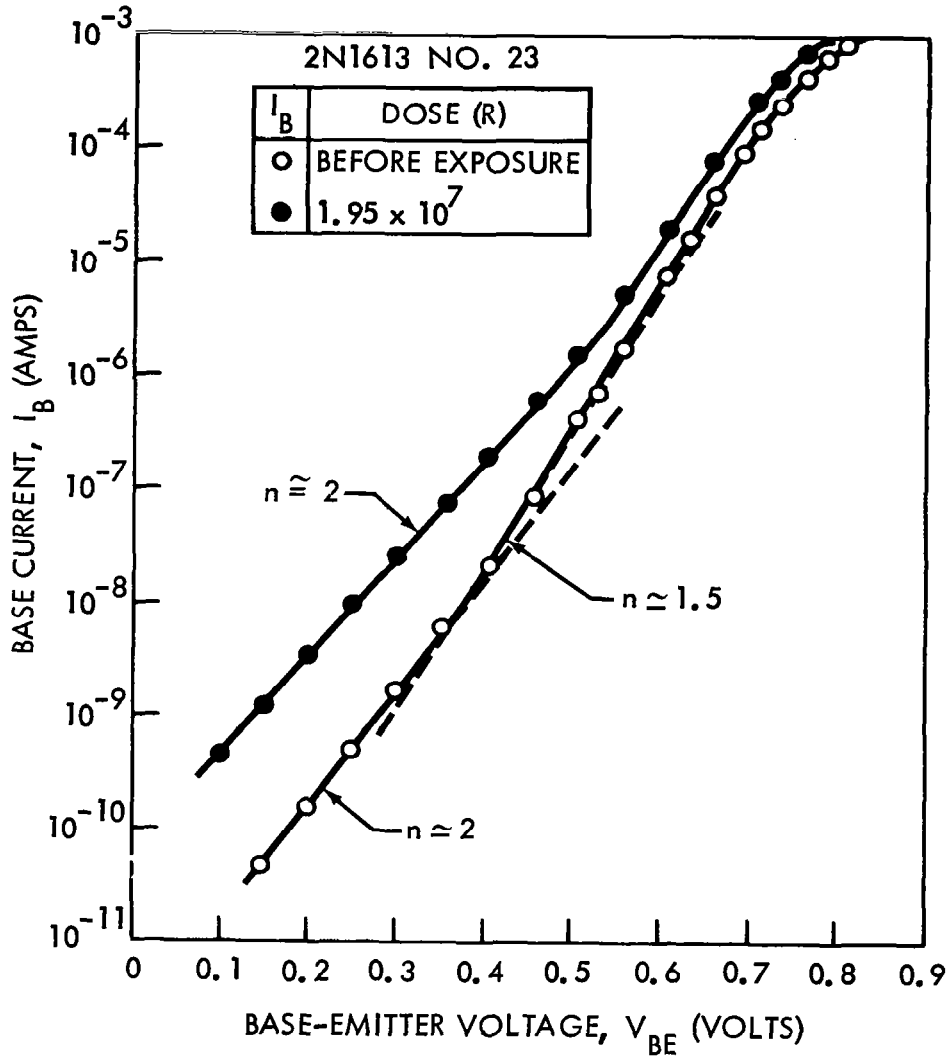

Figure 29. Radiation-Induced Change in I_B Versus V_{BE}

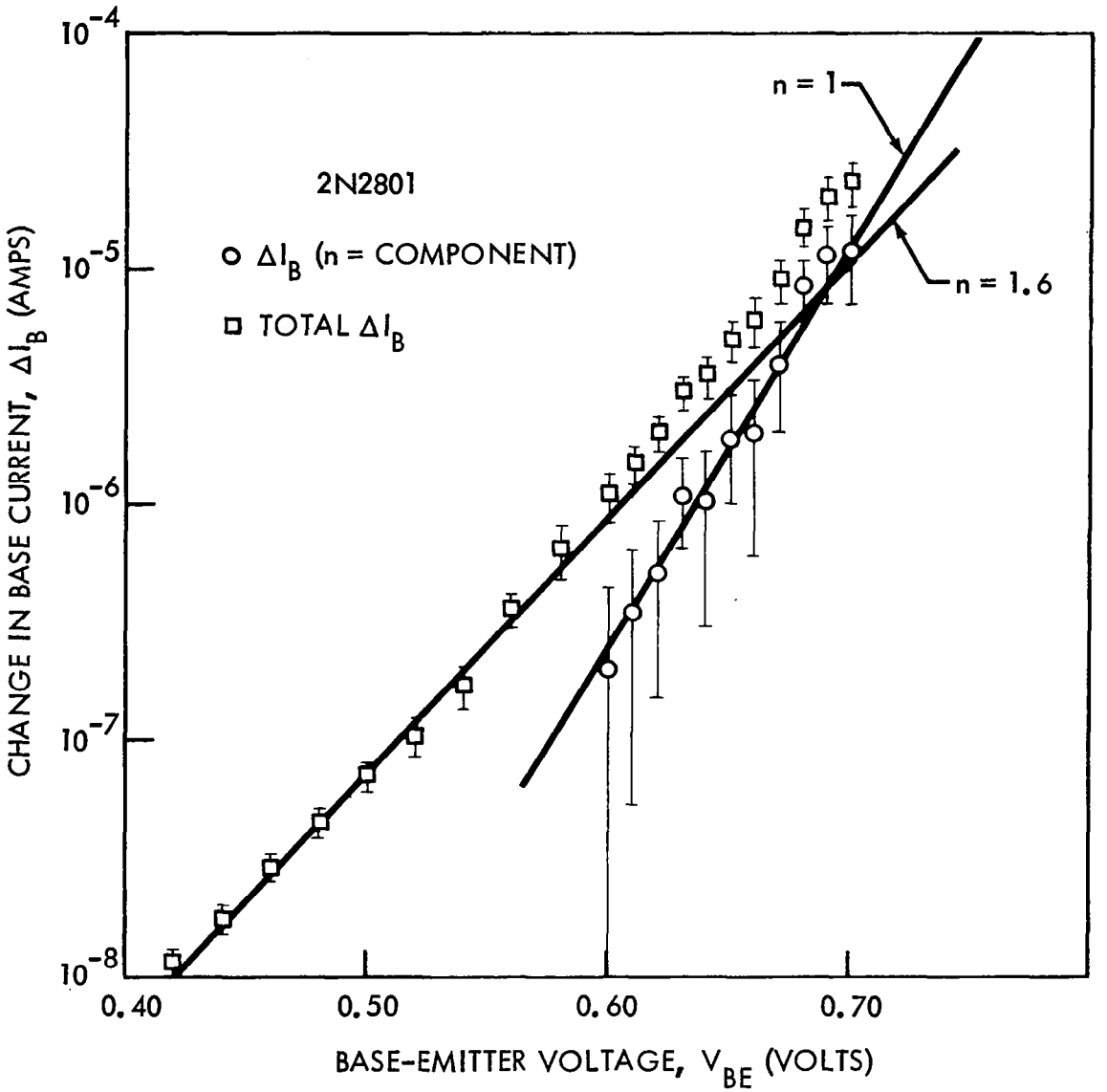

Figure 30. Change in I_B Versus V_{BE} After 10^4R Gamma Exposure

slope has been associated with the emitter depletion region rather than the base region.

As a supplementary study to this contract, a number of measurements were performed and reported at the annual IEEE Radiation Effects Symposium (Reference 9). Further discussion of analysis of this type of damage is also presented in Section 2.9.

2.6.2 Computer Analysis of Characteristic Curves

Data in the form of common-emitter characteristic curves were analyzed in detail using a transistor-damage-plotting program and an SRU 1107 computer (Reference 10). Raw data consisting of oscillograms of transistor d.c. characteristics (e.g., Figure 1) were taken by Polaroid camera from the display of a Tektronix 575 transistor curve tracer. Auxiliary information was fed to the computer on IBM cards (see Table 9 for example). As many as 20 dynamic pictures (taken during radiation exposure) were recorded on selected transistors. The raw data was transferred to IBM card form by the use of a Benson-Lehner Model Oscar F oscillogram reader. The reader can be used to measure trace amplitudes, apply calibrations, convert the data to engineering units, and automatically operate a card punch.

Card punch data was fed into the SRU 1107 computer along with computer option information. Several options were used for analysis and plotting of the characteristic curve information. The first option employed requested a replot of the IBM card input information into the form of I_C versus V_C plots, as was shown in Figure 1. Plots of this type were obtained from all transistors tested and were stored on microfilm. A microfilm reader was then used to screen for errors and thus guarantee that correct input data had been received and stored into the computer.

The second computer option exercised was to obtain plots of d.c. current gain, h_{FE}, as a function of emitter current and as a family of fluences. Included as examples of this option are copies of actual computer plots for an npn diffused planar device (Figures 31 and 32), an npn epitaxial planar device (Figures 33 and 34), and an epitaxial mesa device (Figure 35). Examples of this computer option for a pnp diffused planar (Figure 36) and a pnp epitaxial planar transistor (Figure 37)

Table 9. Keypunch Data Form

TEST HEADING CARD

Test	Transistor Type	Transistor No.	No. of Pictures	Batch No.	Case	Mfg.
23	16 13	08	4	4 36	ON	FC LD

PICTURE READING CARD

Picture No.	Date	Time	I_C/div (ma)	V_C/div (volts)	I_B/step	Load Resistor (megohms)	Fluence (electrons/cm^2)	Temperature (degrees absolute)
A1	07 27 65	14 56	2.0	2.0	.05	0.00 1	0.0	29 8.5
A2	09 28 65	13 07	2.0	2.0	.05	0.00 1	0.0	29 8.2
B	09 30 65	14 32	2.0	2.0	.05	0.00 1	5.04 E 14	29 9.7
C	09 30 65	23 35	2.0	2.0	.20	0.00 1	3.64 E 15	29 8.7
D	10 01 65	10 53	2.0	2.0	.50	0.00 1	1.82 E 16	29 8.2

U3 4266 3000

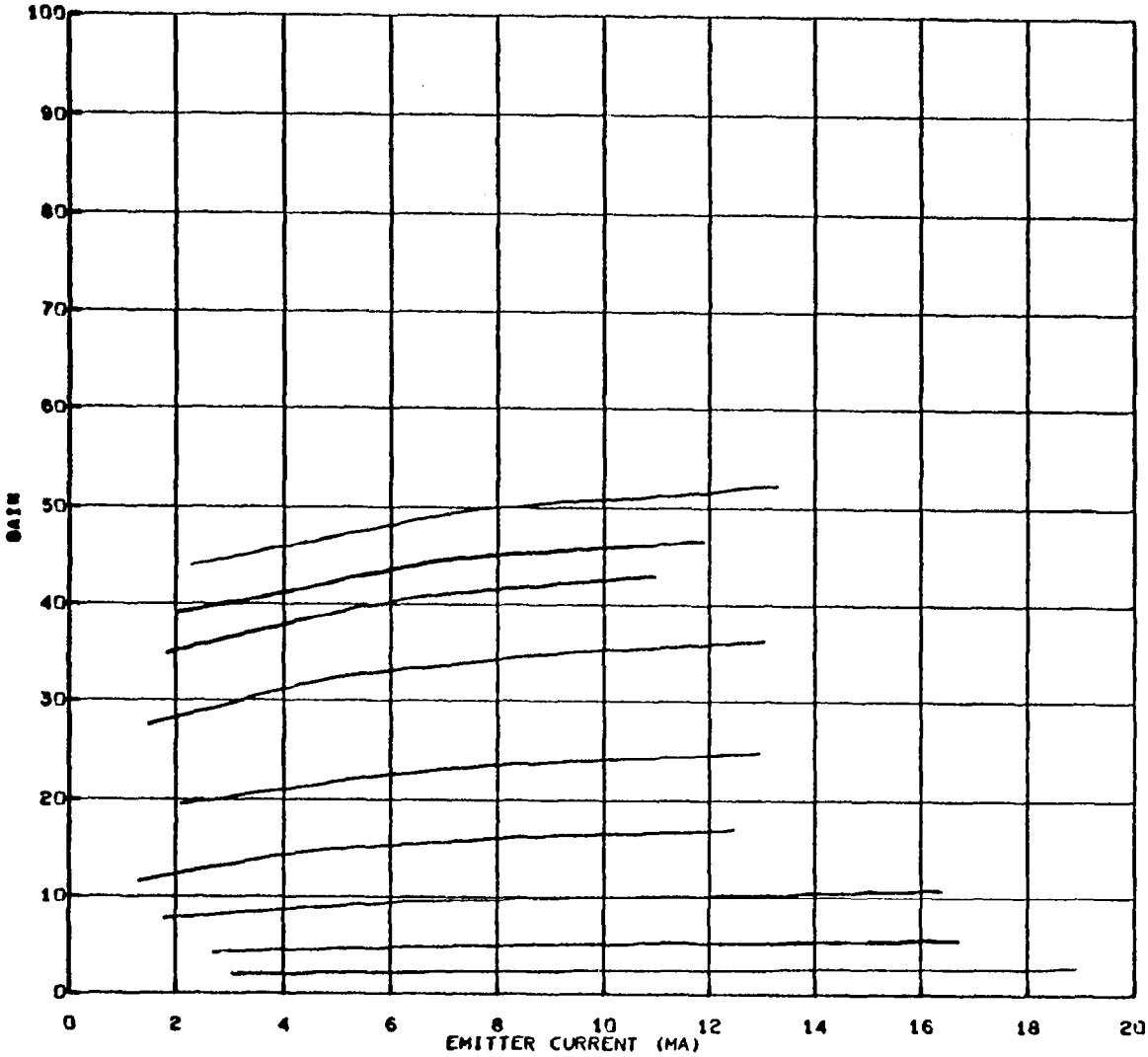

2N1613 TEST 24 POSITION 1 1.0 MEV PROTON IRRADIATION

DC GAIN VS. EMITTER CURRENT, FAMILY OF FLUENCES, COLLECTOR VOLTAGE = 10.0

TEST	TRANS.TYPE	TRANS.NO.	BATCH	MAKE	CUTOFF	NML.FREQ	CASE
24	1613	15	436	FCLD	92.89	94.14	OFF

PICTURE	FLUENCE	MAX. GAIN	MIN. GAIN
1	0.0	52.2	43.9
2	1.9+10	46.6	39.0
3	4.6+10	42.9	35.0
4	1.0+11	36.3	27.6
5	2.5+11	24.9	19.4
6	4.7+11	16.8	11.5
7	9.5+11	10.7	7.8
8	1.9+12	5.7	4.3
9	4.2+12	2.8	2.0

Figure 31. 2N1613 h_{FE} Versus I_E for 1-Mev Protons (High Gain)

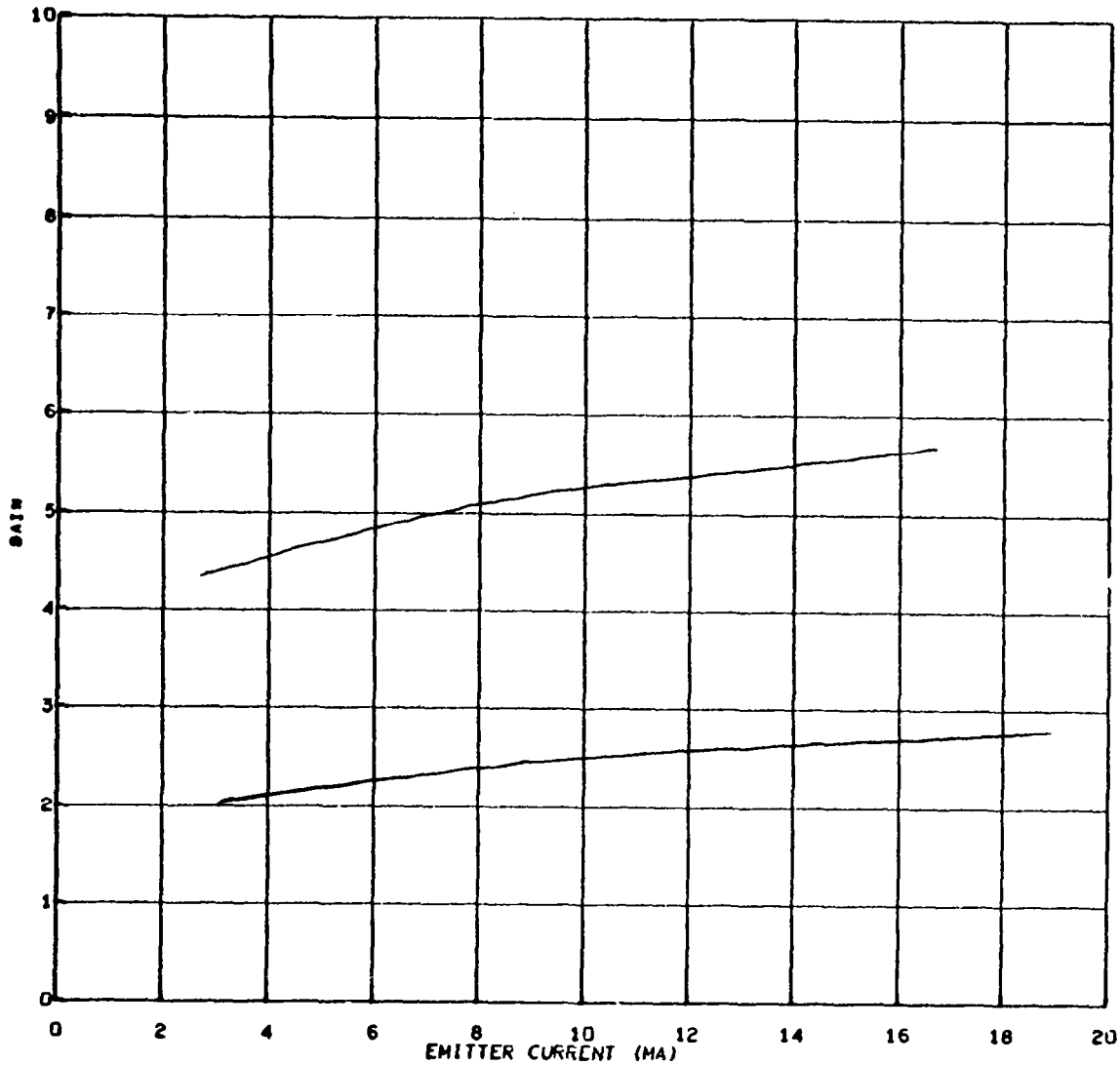

2N1613 TEST 24 POSITION 1 1.0 MEV PROTON IRRADIATION

DC GAIN VS. EMITTER CURRENT, FAMILY OF FLUENCES, COLLECTOR VOLTAGE = 10.0

TEST	TRANS.TYPE	TRANS.NO.	BATCH	MAKE	CUTOFF	NML.FREQ	CASE
24	1613	15	436	FCLD	92.89	94.14	OFF

PICTURE	FLUENCE	MAX. GAIN	MIN. GAIN
8	1.9+12	5.7	4.3
9	4.2+12	2.8	2.0

Figure 32. 2N1613 h_{FE} Versus I_E for 1-Mev Protons (Low Gain)

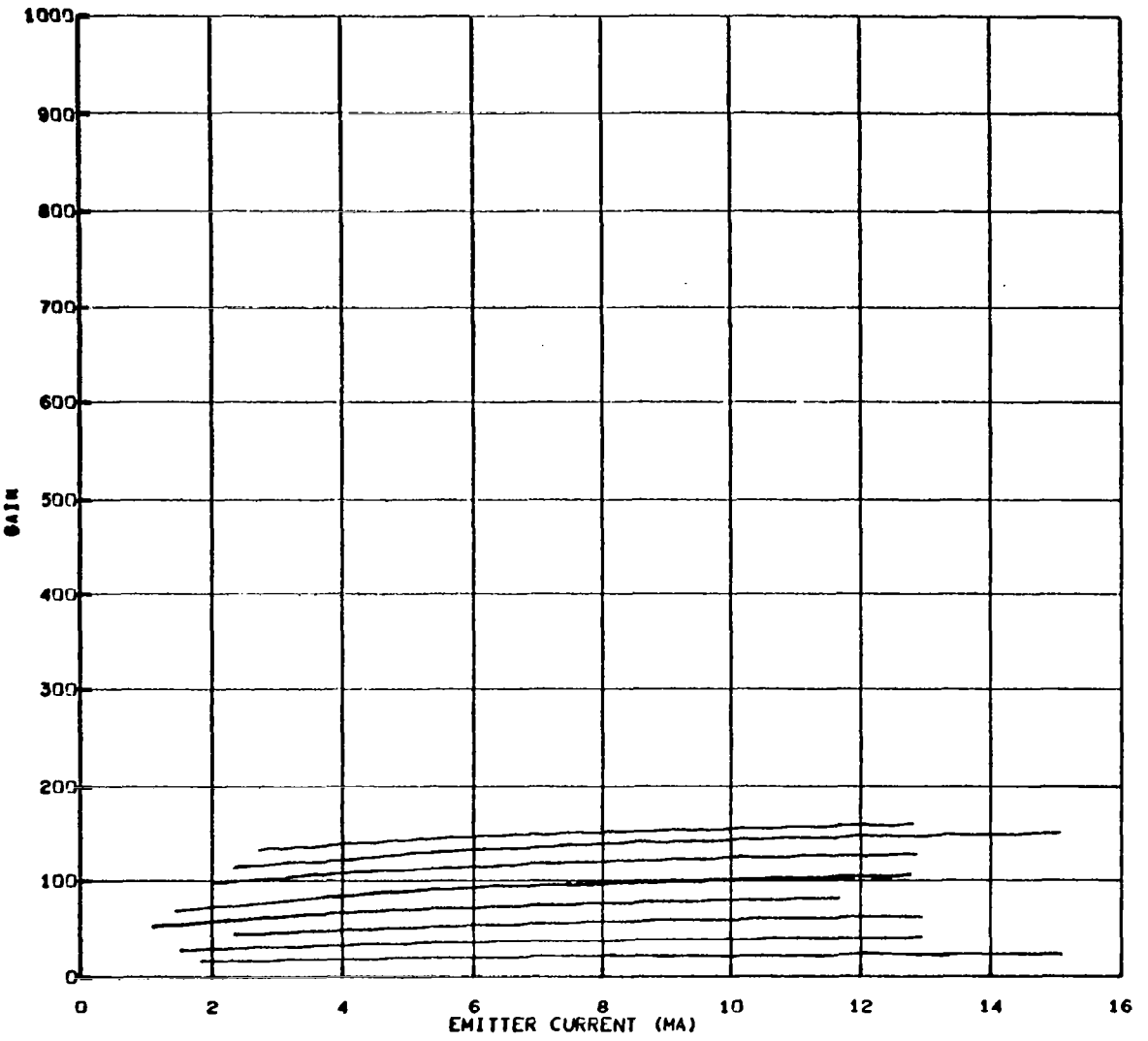

2N2219 TEST 24 POSITION 4 1.0 MEV PROTON IRRADIATION

DC GAIN VS. EMITTER CURRENT, FAMILY OF FLUENCES, COLLECTOR VOLTAGE = 10.0

TEST	TRANS.TYPE	TRANS.NO.	BATCH	MAKE	CUTOFF	NML.FREQ	CASE
24	2219	2	507	FCLD	555	439.49	OFF

PICTURE	FLUENCE	MAX. GAIN	MIN. GAIN
1	0.0	158.9	133.0
2	4.6+10	149.7	113.4
3	1.0+11	127.6	97.5
4	2.5+11	105.2	69.7
5	4.7+11	82.2	53.5
6	9.5+11	63.6	45.5
7	1.9+12	42.0	28.7
8	4.2+12	24.1	17.1

Figure 33. 2N2219 h_{FE} Versus I_E for 1-Mev Protons (High Gain)

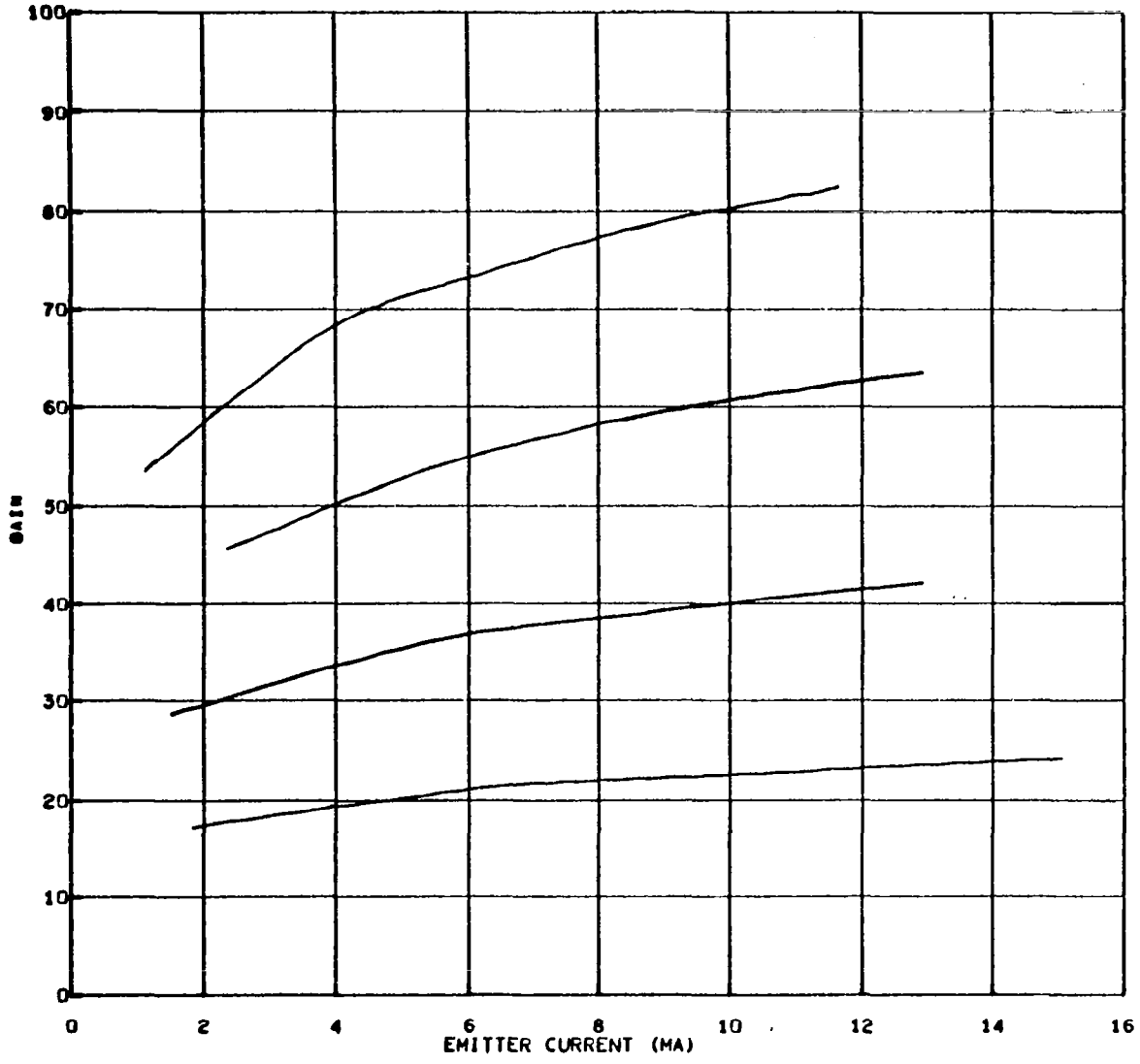

2N2219 TEST 24 POSITION 4 1.0 MEV PROTON IRRADIATION

DC GAIN VS. EMITTER CURRENT, FAMILY OF FLUENCES, COLLECTOR VOLTAGE = 10.0

TEST	TRANS.TYPE	TRANS.NO.	BATCH	MAKE	CUTOFF	NML.FREQ	CASE
24	2219	2	507	FCLD	555	439.49	OFF

PICTURE	FLUENCE	MAX. GAIN	MIN. GAIN
5	4.7+11	82.2	53.5
6	9.5+11	63.6	45.5
7	1.9+12	42.0	28.7
8	4.2+12	24.1	17.1

Figure 34. 2N2219 h_{FE} Versus I_E for 1-Mev Protons (Low Gain)

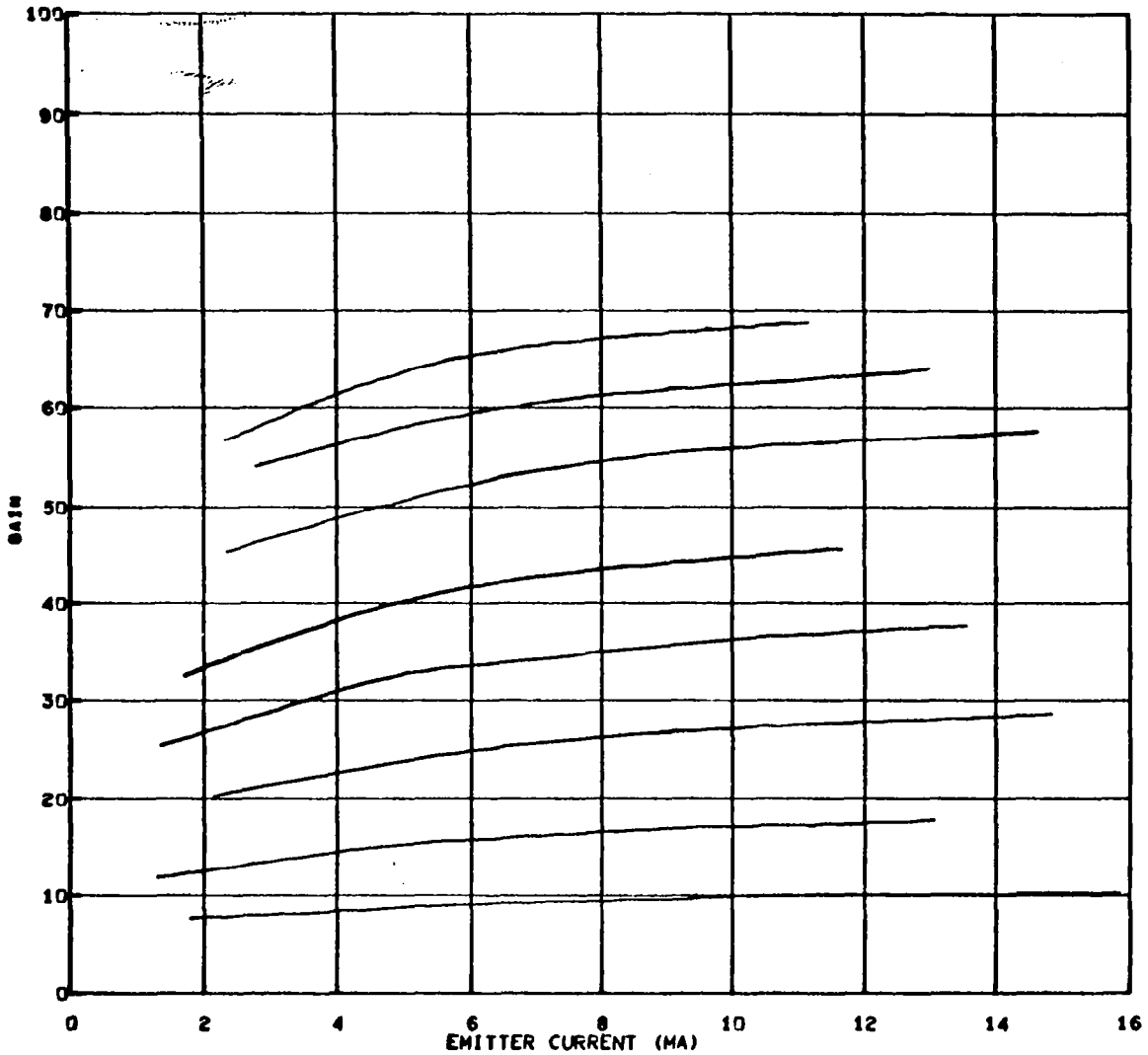

2N834 TEST 24 POSITION 6 1.0 MEV PROTON IRRADIATION

DC GAIN VS. EMITTER CURRENT, FAMILY OF FLUENCES, COLLECTOR VOLTAGE = 10.0

TEST	TRANS.TYPE	TRANS.NO.	BATCH	MAKE	CUTOFF	NML.FREQ	CASE
24	834	2	444	MTRA	364	413.08	OFF

PICTURE	FLUENCE	MAX. GAIN	MIN. GAIN
1	0.0	68.8	56.7
2	4.6+10	64.0	54.0
3	1.0+11	57.6	45.4
4	2.5+11	45.6	32.6
5	4.7+11	37.7	25.4
6	9.5+11	28.7	20.3
7	1.9+12	17.7	11.8
8	4.2+12	10.3	7.8

Figure 35. 2N834 h_{FE} Versus I_E for 1-Mev Protons

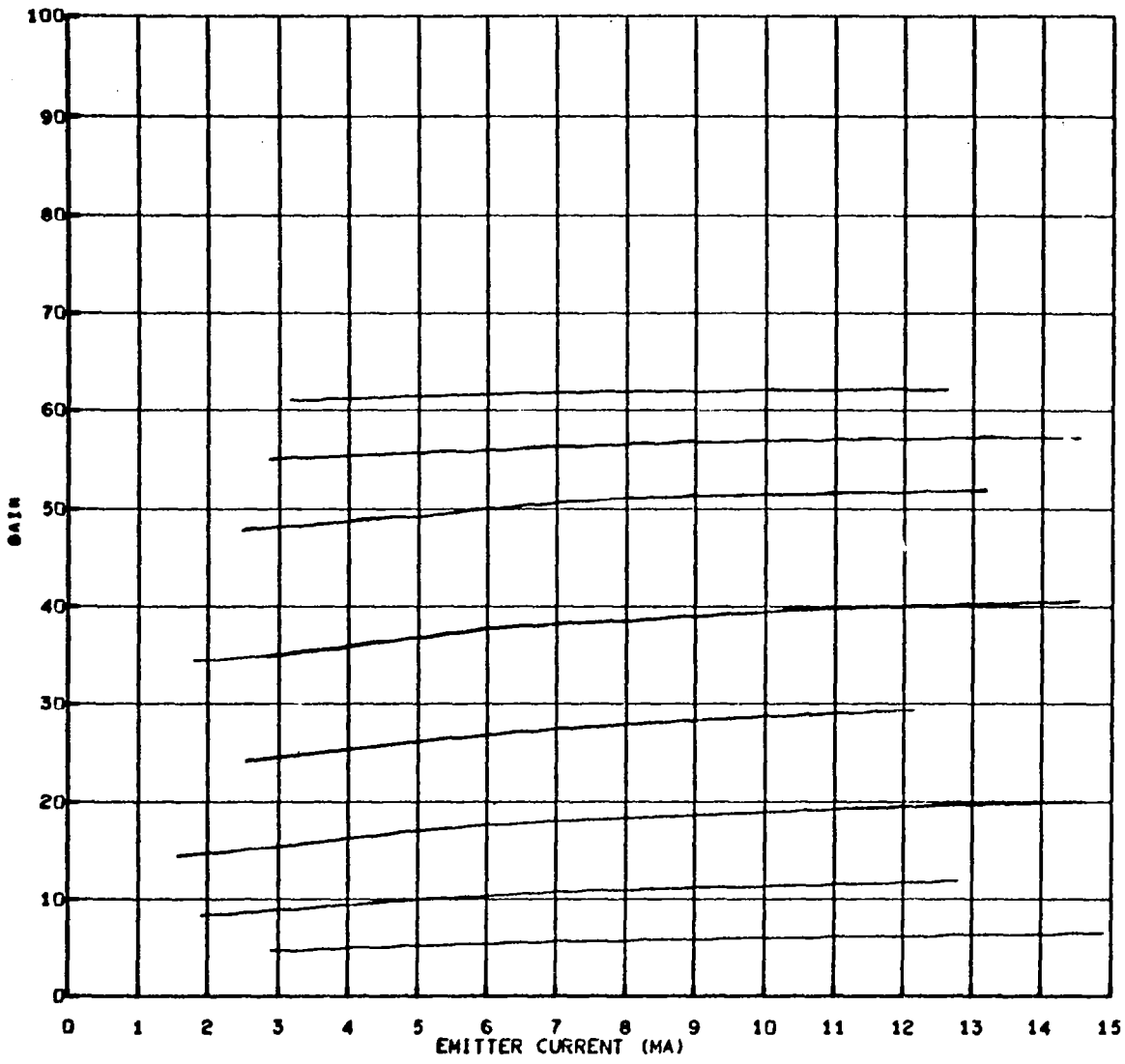

2N1132 TEST 24 POSITION 8 1.0 MEV PROTON IRRADIATION

DC GAIN VS. EMITTER CURRENT, FAMILY OF FLUENCES, COLLECTOR VOLTAGE = 10.0

TEST	TRANS.TYPE	TRANS.NO.	BATCH	MAKE	CUTOFF	NML.FREQ	CASE
24	1132	2	6511	RYTH	399.56	396.77	OFF

PICTURE	FLUENCE	MAX. GAIN	MIN. GAIN
1	0.0	62.3	61.0
2	4.6+10	57.3	55.1
3	1.0+11	51.9	47.8
4	2.5+11	40.5	34.4
5	4.7+11	29.3	24.1
6	9.5+11	19.9	14.3
7	1.9+12	11.8	8.4
8	4.2+12	6.4	4.7

Figure 36. 2N1132 h_{FE} Versus I_E for 1-Mev Protons

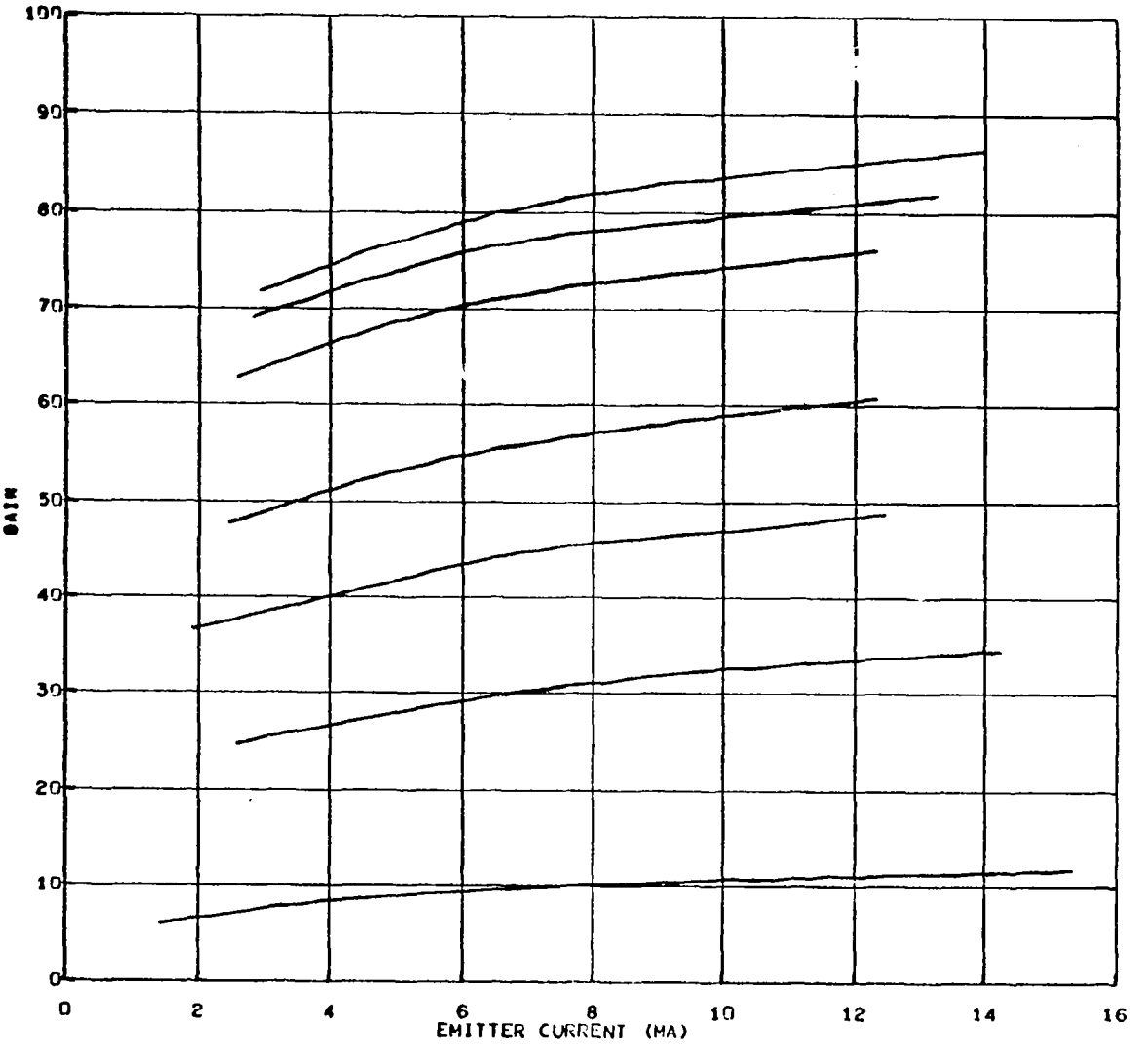

2N2801 TEST 24 POSITION 9 1.0 MEV PROTON IRRADIATION

DC GAIN VS. EMITTER CURRENT, FAMILY OF FLUENCES, COLLECTOR VOLTAGE = 10.0

TEST	TRANS.TYPE	TRANS.NO.	BATCH	MAKE	CUTOFF	NML.FREQ	CASE
24	2801	2	324	MTRA	388.92	324.26	OFF

PICTURE	FLUENCE	MAX. GAIN	MIN. GAIN
1	0.0	86.4	71.9
2	4.6+10	81.9	69.0
3	1.0+11	75.9	62.9
4	2.5+11	60.6	47.7
5	4.7+11	48.6	36.7
6	9.5+11	34.6	24.7
7	4.2+12	11.7	6.0

Figure 37. 2N2801 h_{FE} Versus I_E for 1-Mev Protons

are also shown for the 1-Mev proton tests. All of these transistors were measured dynamically during irradiation. Plots of h_{FE} versus Φ from transistors of type 2N2411 for an electron, a proton, and a gamma-ray test are shown in Figures 38, 39, and 40, respectively.

The third computer option selected for analysis of characteristic curve data was the plotting of h_{FE} versus particle fluence, Φ. This data was plotted for a family of three emitter currents. Figures 41 through 46 show copies of the actual computer plots of h_{FE} versus Φ for the 2N1711 transistors that were monitored dynamically. These figures include the 2-, 1-, and 0.5-Mev electron tests, the 1- and 20-Mev proton tests, and the Co^{60} gamma-ray test. Figure 47 shows typical h_{FE} versus Φ plots for 1 of the 10 transistors of type 2N1711 tested passively during the 100-Mev proton test. In general, only one or two exposure data points were obtained for each device in that test, but more devices were exposed than in the other tests. Figure 48 shows an h_{FE} versus Φ computer plot for a pnp device, 2N2801, irradiated in the 1-Mev proton test.

A fourth computer option that was exercised for this program was the plotting of changes in the inverse of common-emitter current gain, $\Delta(h_{FE}^{-1})$, versus particle fluence, Φ. It can be predicted from theory that $\Delta(h_{FE}^{-1})$ should be directly proportional to Φ if the only loss of current gain is that due to a reduction of base minority-carrier lifetime caused by atomic displacements.

The Webster equation, Equation (5), is a semiempirical expression relating h_{FE} to parameters of a minority-carrier injection-type transistor (Reference 11).

$$h_{FE}^{-1} = S A_s W/A_c D_b + W^2/2D_b\tau_b + W\sigma_b/L_e\sigma_e \qquad (5)$$

The first term of Equation (5) accounts for the loss of base current due to the surface recombination velocity, S, of the base region,

where:
- A_s = effective surface for recombination
- W = effective width of the base region
- A_c = area of the conduction path
- D_b = minority-carrier diffusion constant in the base

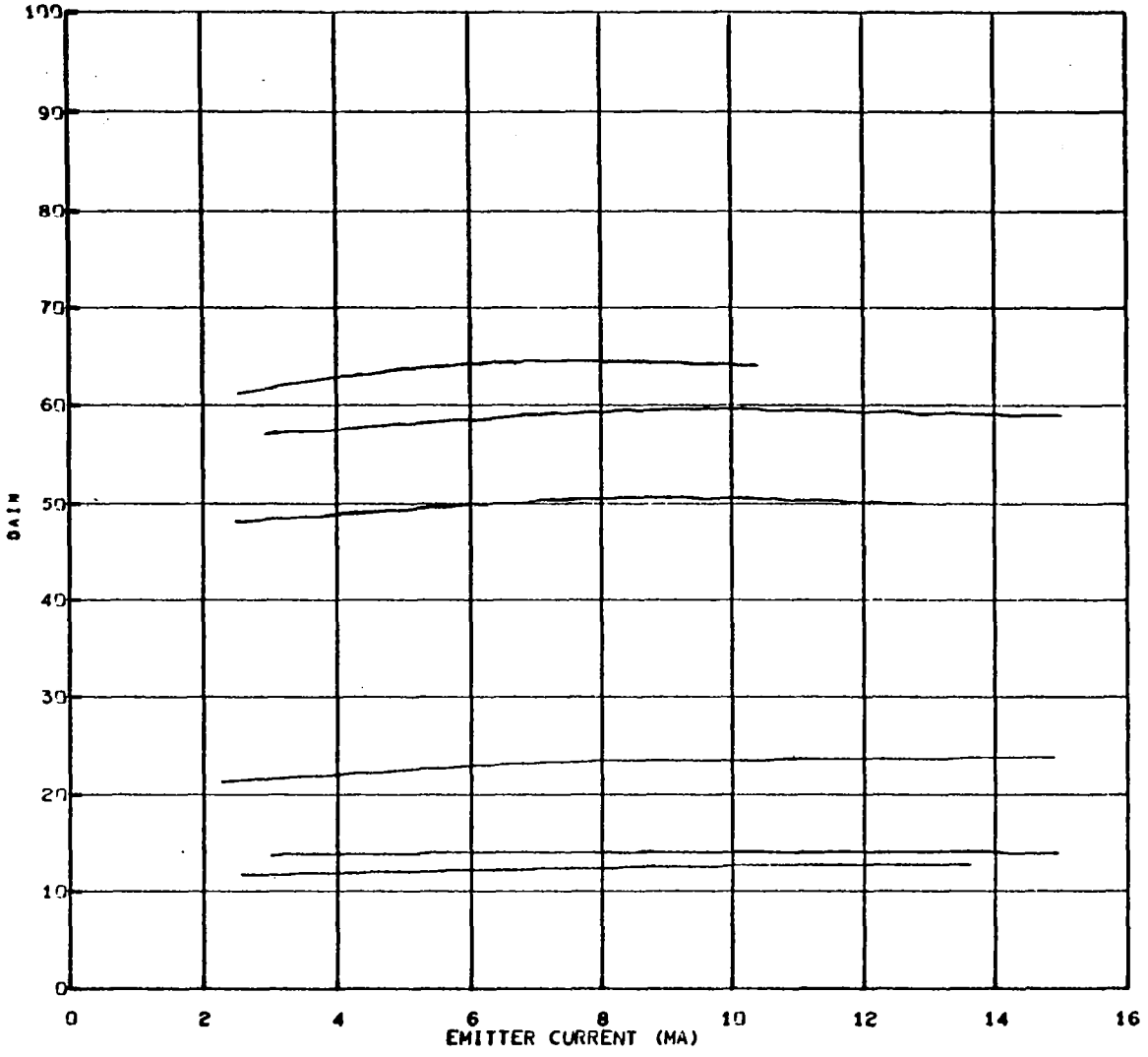

2N2411 TEST 21 POSITION 10 2. MEV ELECTRON IRRADIATION

DC GAIN VS. EMITTER CURRENT, FAMILY OF FLUENCES, COLLECTOR VOLTAGE = 10.0

TEST	TRANS.TYPE	TRANS.NO.	BATCH	MAKE	CUTOFF	NML.FREQ	CASE
21	2411	4	450A	TI	357.70	348.23	ON

PICTURE	FLUENCE	MAX. GAIN	MIN. GAIN
1	0.0	64.7	61.4
2	6.4+13	59.7	57.0
3	1.8+14	50.7	48.2
4	1.3+15	23.9	21.4
5	3.4+15	14.1	13.8
6	3.6+15	12.7	11.7

Figure 38. 2N2411 h_{FE} Versus I_E for 2-Mev Electrons

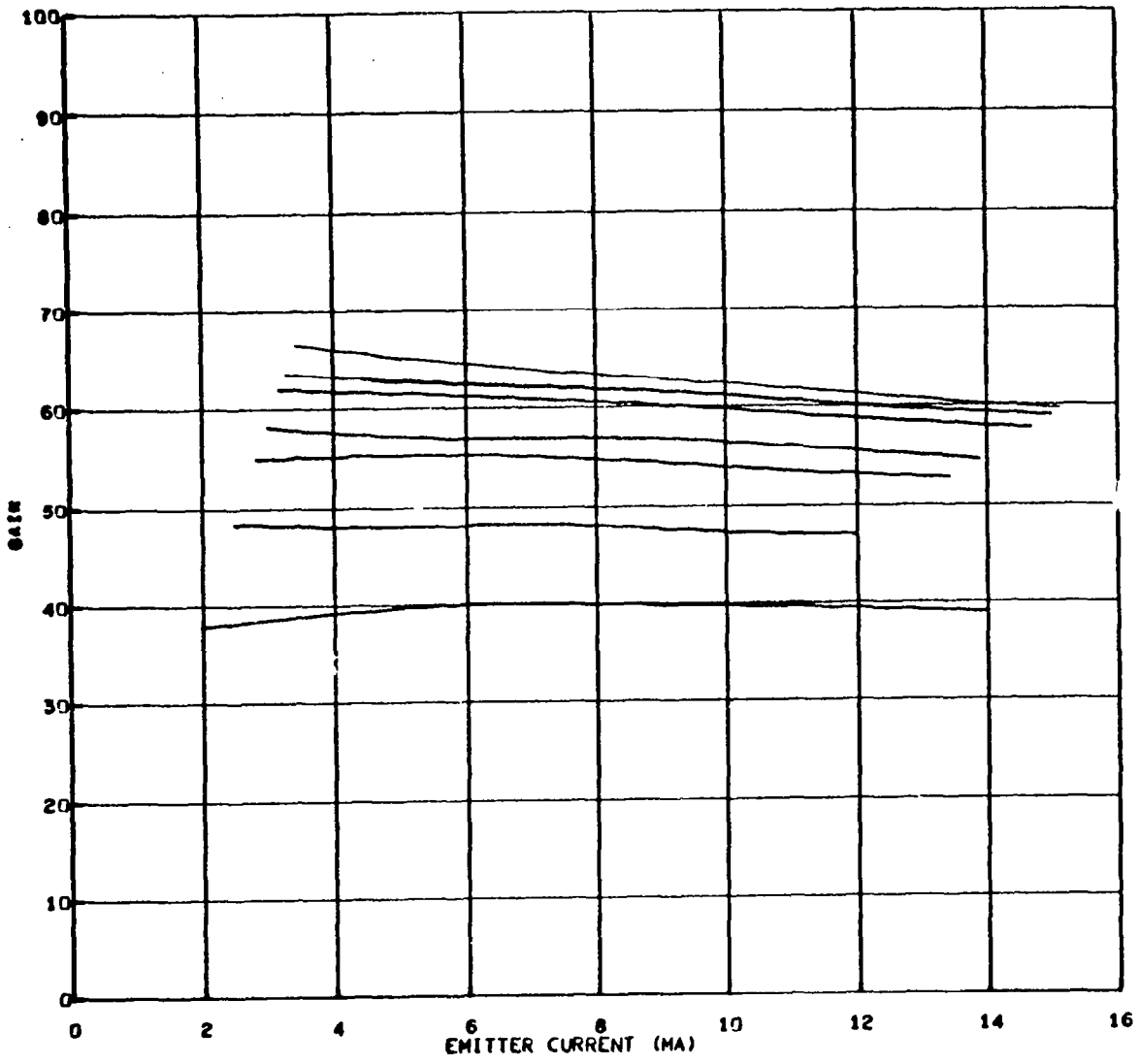

2N2411 TEST 24 POSITION 10 1.0 MEV PROTON IRRADIATION

DC GAIN VS. EMITTER CURRENT, FAMILY OF FLUENCES, COLLECTOR VOLTAGE = 10.0

TEST	TRANS.TYPE	TRANS.NO.	BATCH	MAKE	CUTOFF	NML.FREQ	CASE
24	2411	2	450A	TI	281.97	348.23	OFF

PICTURE	FLUENCE	MAX. GAIN	MIN. GAIN
1	0.0	66.7	59.8
2	4.6+10	63.7	59.1
3	1.0+11	62.1	57.9
4	2.5+11	58.3	54.7
5	4.7+11	55.3	52.8
6	9.5+11	48.4	47.0
7	1.9+12	40.2	38.0

Figure 39. 2N2411 h_{FE} Versus I_E for 1-Mev Protons

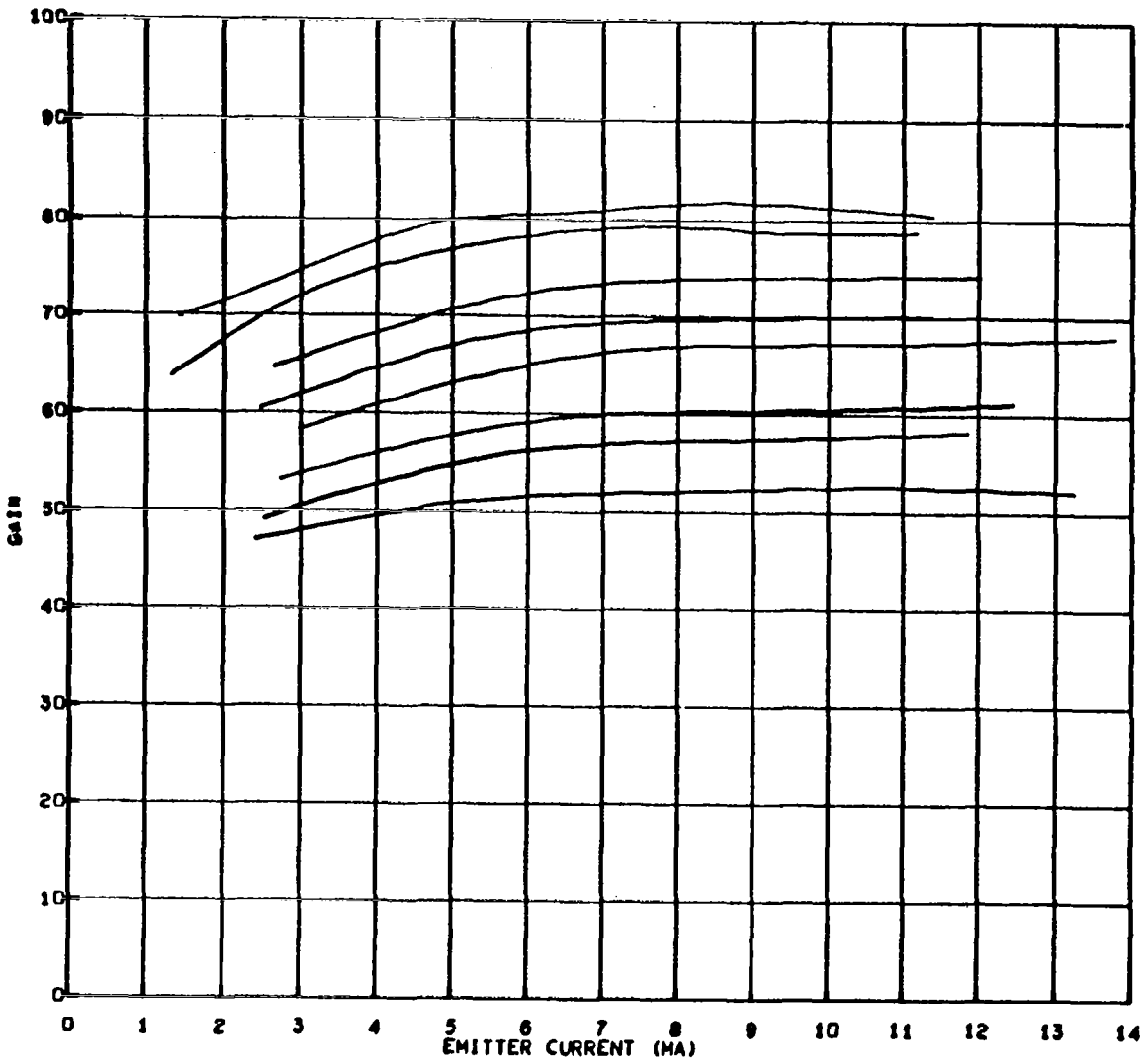

2N2411 TEST 25 COBALT 60 GAMMA IRRADIATION

DC GAIN VS. EMITTER CURRENT, FAMILY OF FLUENCES, COLLECTOR VOLTAGE = 10.0

TEST	TRANS.TYPE	TRANS.NO.	BATCH	MAKE	CUTOFF	NML.FREQ	CASE
25	2411	22	450A	TI	570	348.23	ON

PICTURE	FLUENCE	MAX. GAIN	MIN. GAIN
1	0.0	81.8	69.8
2	2.4+14	79.3	63.8
3	4.5+15	74.2	64.7
4	1.2+16	70.2	60.5
5	2.2+16	68.0	58.5
6	5.3+16	61.2	53.3
7	7.3+16	58.3	49.2
8	1.1+17	52.6	47.0

Figure 40. 2N2411 h_{FE} Versus I_E for Co^{60} Gamma Rays

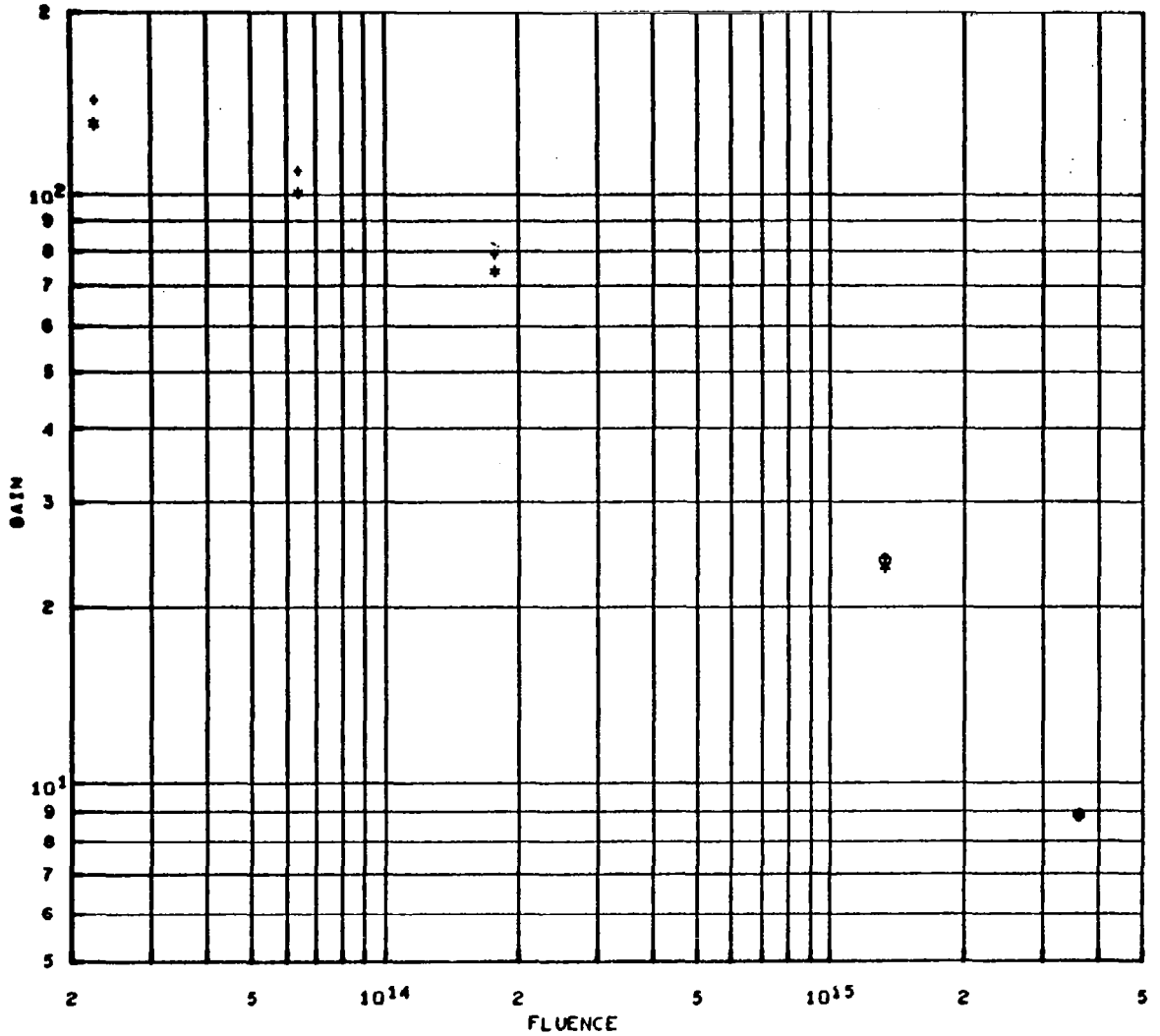

2N1711 TEST 21 POSITION 2 2. MEV ELECTRON IRRADIATION

DC GAIN VS. FLUENCE, FAMILY OF EMITTER CURRENTS, COLLECTOR VOLTAGE = 10.0

TEST	TRANS.TYPE	TRANS.NO.	DATCH	MAKE	CUTOFF	NML.FREQ	CASE
21	1711	4	513	FCLD	132.45	147.81	ON

SYMBOL	CURVE	CURRENT	MAX. GAIN	MIN. GAIN	NO DOSE GAIN
*	1	5.0	130.8	8.9	178.2
+	2	10.0	143.2	8.9	186.3
⊕	3	12.0	24.1	8.8	186.9

TABULATION OF ARRAY POINTS

CURVE 1		CURVE 2		CURVE 3	
FLUENCE	GAIN	FLUENCE	GAIN	FLUENCE	GAIN
2.25+13	130.8	2.25+13	143.2	1.32+15	24.1
6.37+13	100.3	6.37+13	109.6	3.62+15	8.8
1.76+14	73.9	1.76+14	78.9		
1.32+15	23.4	1.32+15	24.2		
3.62+15	8.9	3.62+15	8.9		

Figure 41. 2N1711 h_{FE} Versus Φ for 2-Mev Electron Test

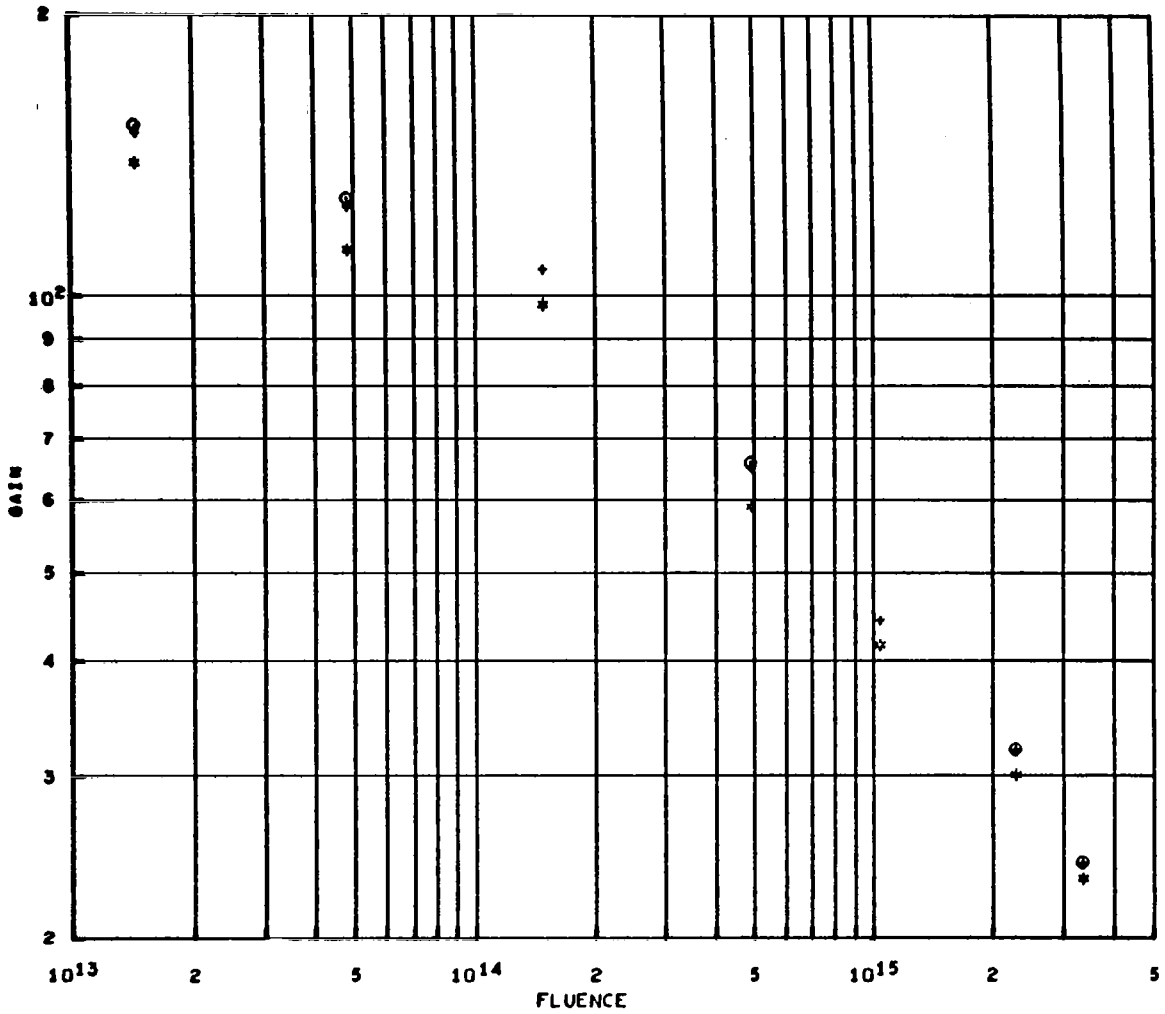

2N1711 TEST 22 POSITION 2 1.3 MEV ELECTRON IRRADIATION

DC GAIN VS. FLUENCE, FAMILY OF EMITTER CURRENTS, COLLECTOR VOLTAGE = 10.0

TEST	TRANS.TYPE	TRANS.NO.	BATCH	MAKE	CUTOFF	NML.FREQ	CASE
22	1711	8	513	FCLD	139.13	147.81	ON

SYMBOL	CURVE	CURRENT	MAX. GAIN	MIN. GAIN	NO DOSE GAIN
*	1	5.0	138.9	23.1	195.9
+	2	10.0	150.5	24.1	199.9
⊕	3	12.0	152.4	24.1	198.9

TABULATION OF ARRAY POINTS

CURVE 1		CURVE 2		CURVE 3	
FLUENCE	GAIN	FLUENCE	GAIN	FLUENCE	GAIN
1.44+13	138.9	1.44+13	150.5	1.44+13	152.4
4.80+13	111.9	4.80+13	125.2	4.80+13	127.6
1.47+14	97.7	1.47+14	107.0	4.88+14	65.7
4.88+14	58.8	4.88+14	64.8	2.27+15	31.9
1.04+15	41.6	1.04+15	44.3	3.36+15	24.1
2.27+15	30.0	2.27+15	31.8		
3.36+15	23.1	3.36+15	24.1		

Figure 42. 2N1711 h_{FE} Versus Φ for 1-Mev Electron Test

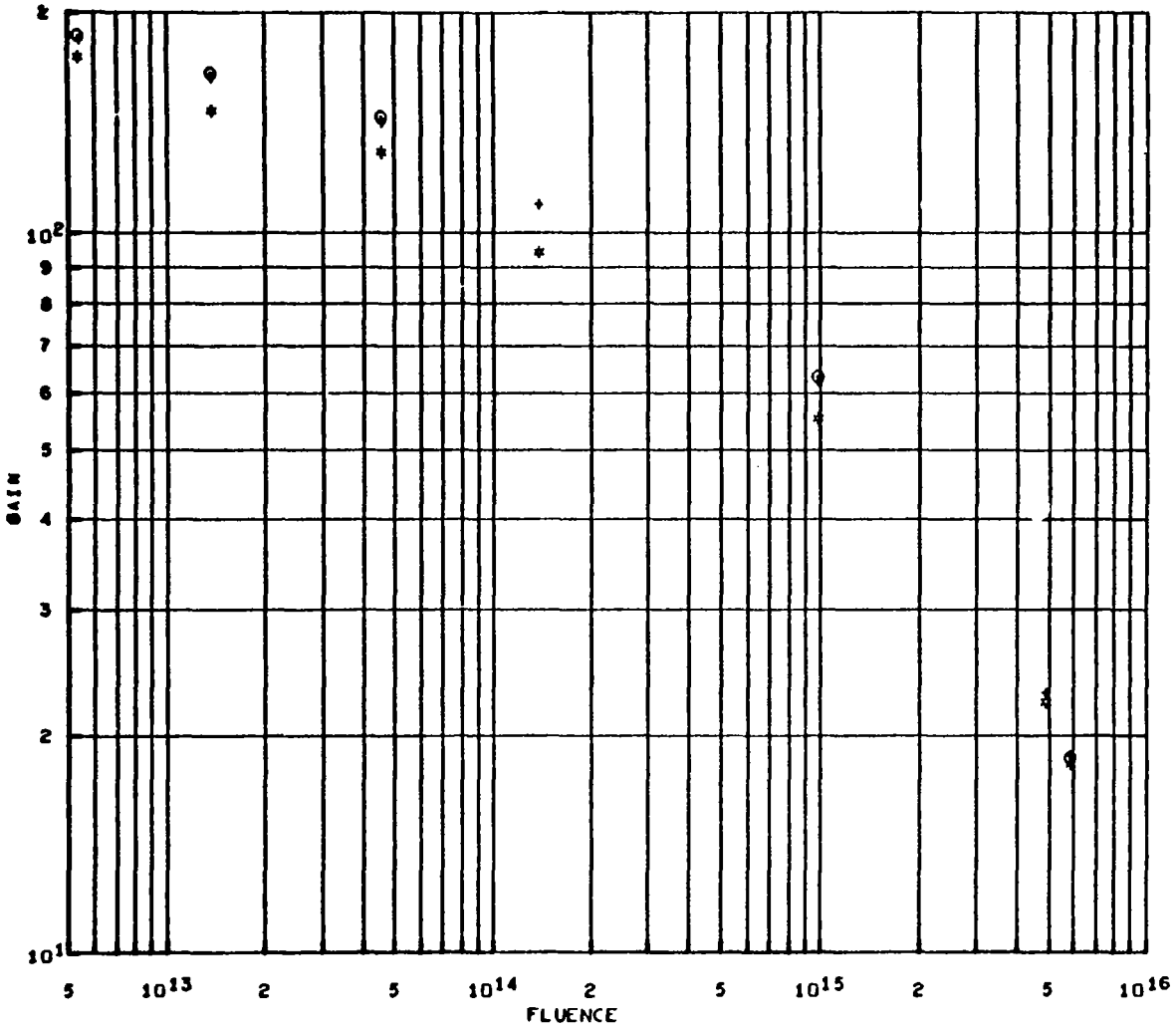

2N1711 TEST 23 POSITION 2 .53 MEV ELECTRON IRRADIATION

DC GAIN VS. FLUENCE, FAMILY OF EMITTER CURRENTS, COLLECTOR VOLTAGE = 10.0

TEST	TRANS.TYPE	TRANS.NO.	BATCH	MAKE	CUTOFF	NML.FREQ	CASE
23	1711	17	513	FCLD	149.85	147.81	OFF

SYMBOL	CURVE	CURRENT	MAX. GAIN	MIN. GAIN	NO DOSE GAIN
*	1	5.0	174.3	18.3	198.8
+	2	10.0	184.9	18.8	209.7
⊙	3	12.0	186.7	18.6	.0

TABULATION OF ARRAY POINTS

CURVE 1		CURVE 2		CURVE 3	
FLUENCE	GAIN	FLUENCE	GAIN	FLUENCE	GAIN
5.32+12	174.3	5.32+12	184.9	5.32+12	186.7
1.37+13	147.2	1.37+13	163.1	1.37+13	165.8
4.56+13	129.3	4.56+13	142.2	4.56+13	144.2
1.37+14	94.2	1.37+14	109.6	9.88+14	63.1
9.88+14	55.1	9.88+14	62.2	5.87+15	18.6
4.94+15	22.3	4.94+15	23.0		
5.87+15	18.3	5.87+15	18.8		

Figure 43. 2N1711 h_{FE} Versus Φ for 0.5-Mev Electron Test

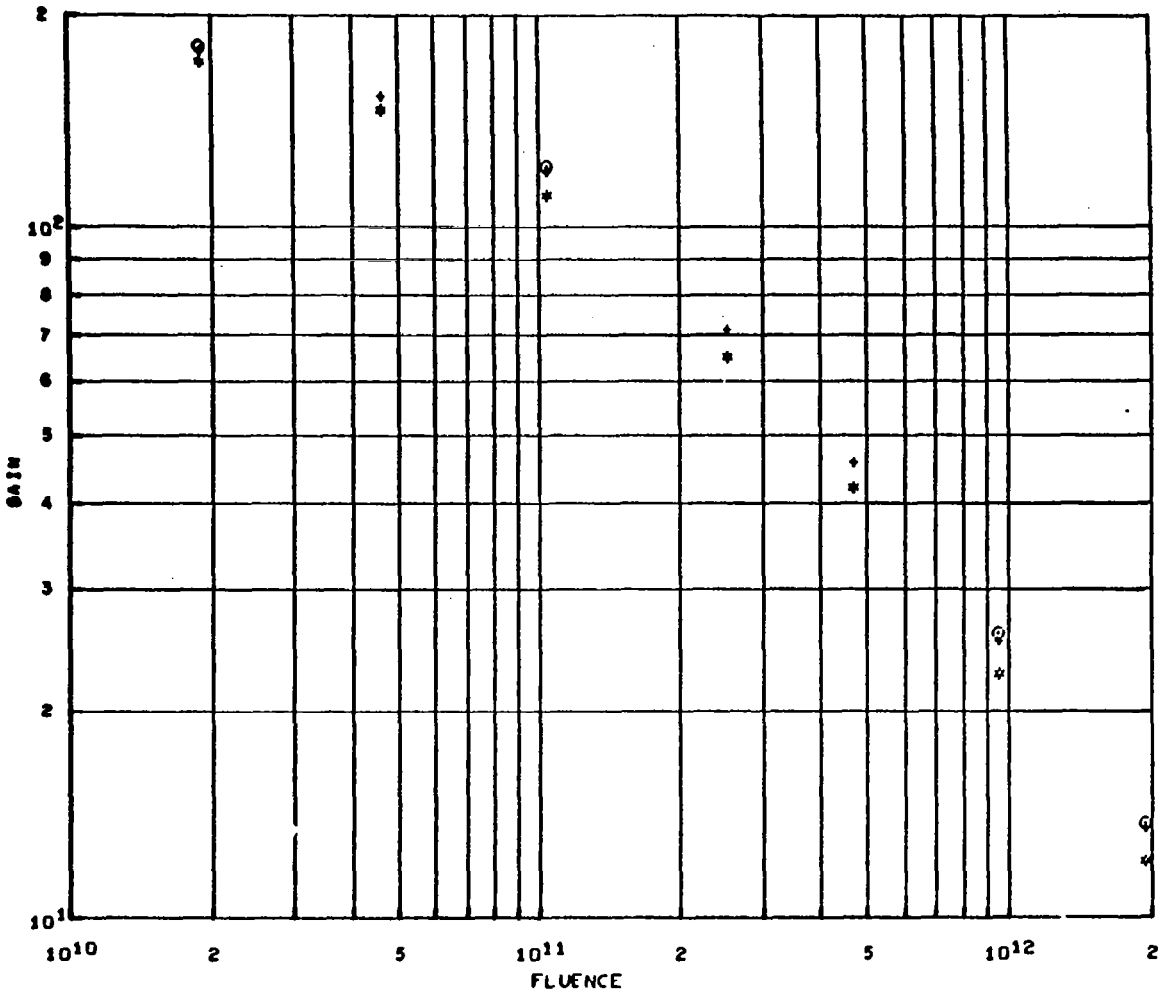

2N1711 TEST 24 POSITION 2 1.0 MEV PROTON IRRADIATION

DC GAIN VS. FLUENCE, FAMILY OF EMITTER CURRENTS, COLLECTOR VOLTAGE = 10.0

TEST	TRANS.TYPE	TRANS.NO.	BATCH	MAKE	CUTOFF	NML.FREQ	CASE
24	1711	2	513	FCLD	151.73	147.81	OFF

SYMBOL	CURVE	CURRENT	MAX. GAIN	MIN. GAIN	NO DOSE GAIN
*	1	5.0	172.1	12.1	194.1
+	2	10.0	179.9	13.4	203.3
⊕	3	12.0	181.0	13.6	205.4

TABULATION OF ARRAY POINTS

CURVE 1		CURVE 2		CURVE 3	
FLUENCE	GAIN	FLUENCE	GAIN	FLUENCE	GAIN
1.90+10	172.1	1.90+10	179.9	1.90+10	181.0
4.64+10	147.3	4.64+10	154.1	1.04+11	122.2
1.04+11	111.3	1.04+11	119.9	9.52+11	25.8
2.52+11	64.7	2.52+11	71.4	1.95+12	13.6
4.70+11	42.0	4.70+11	45.7		
9.52+11	22.6	9.52+11	25.2		
1.95+12	12.1	1.95+12	13.4		

Figure 44. 2N1711 h_{FE} Versus Φ for 1-Mev Proton Test

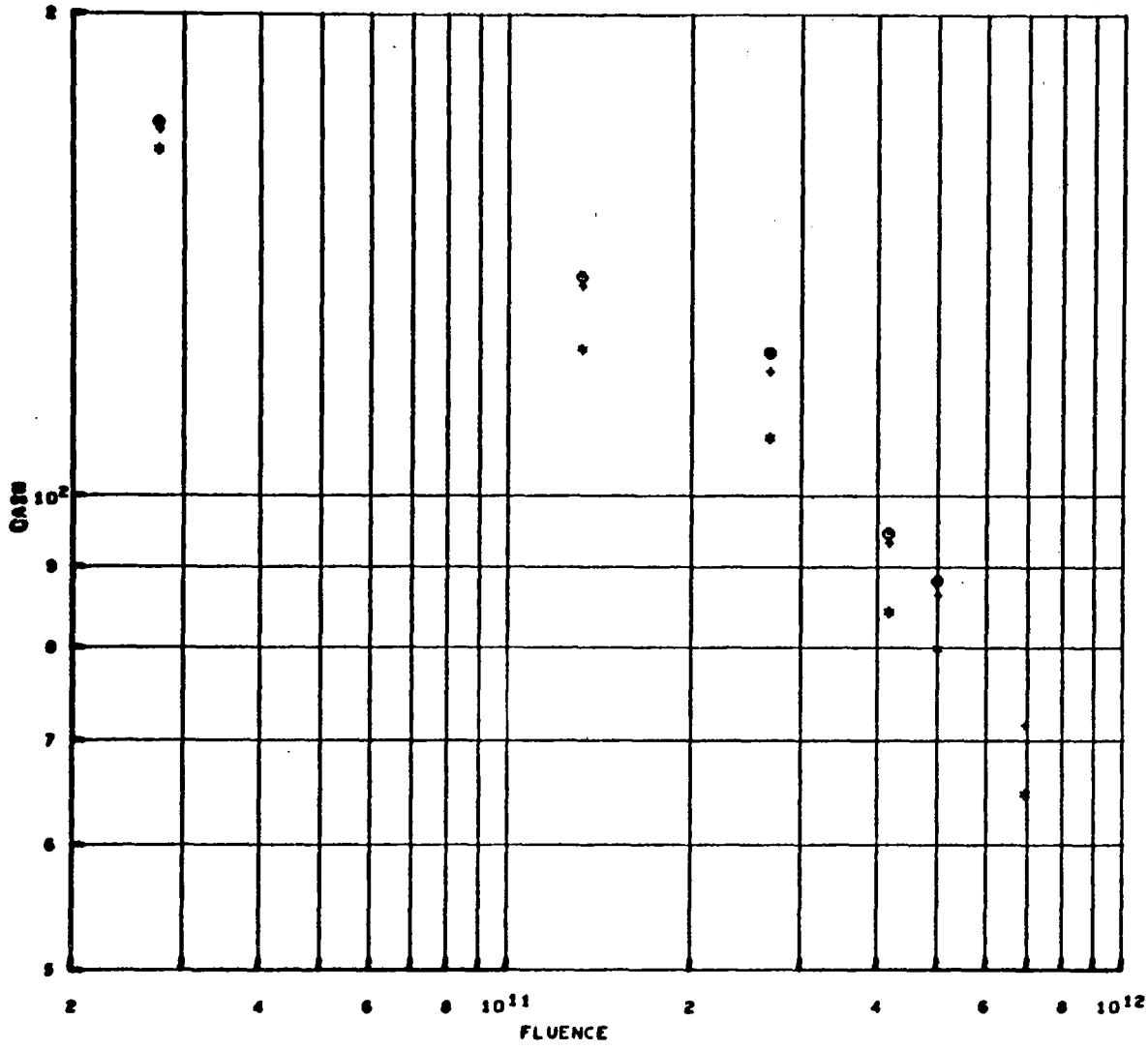

2N1711 TEST 26 20.0 MEV PROTON IRRADIATION

DC GAIN VS. FLUENCE, FAMILY OF EMITTER CURRENTS, COLLECTOR VOLTAGE = 10.0

TEST	TRANS.TYPE	TRANS.NO.	BATCH	MAKE	CUTOFF	NML.FREQ	CASE
26	1711	38	513	FCLD	175.00	147.81	ON

SYMBOL	CURVE	CURRENT	MAX. GAIN	MIN. GAIN	NO DOSE GAIN
*	1	5.0	164.7	64.6	182.4
+	2	10.0	169.9	71.6	191.0
⊙	3	12.0	171.6	88.1	193.3

TABULATION OF ARRAY POINTS

CURVE 1		CURVE 2		CURVE 3	
FLUENCE	GAIN	FLUENCE	GAIN	FLUENCE	GAIN
2.73+10	164.7	2.73+10	169.9	2.73+10	171.6
1.32+11	123.8	1.32+11	135.5	1.32+11	137.2
2.67+11	108.6	2.67+11	120.0	2.67+11	123.0
4.17+11	84.2	4.17+11	93.3	4.17+11	94.7
5.02+11	79.8	5.02+11	86.4	5.02+11	88.1
6.92+11	64.6	6.92+11	71.6		

Figure 45. 2N1711 h_{FE} Versus Φ for 20-Mev Proton Test

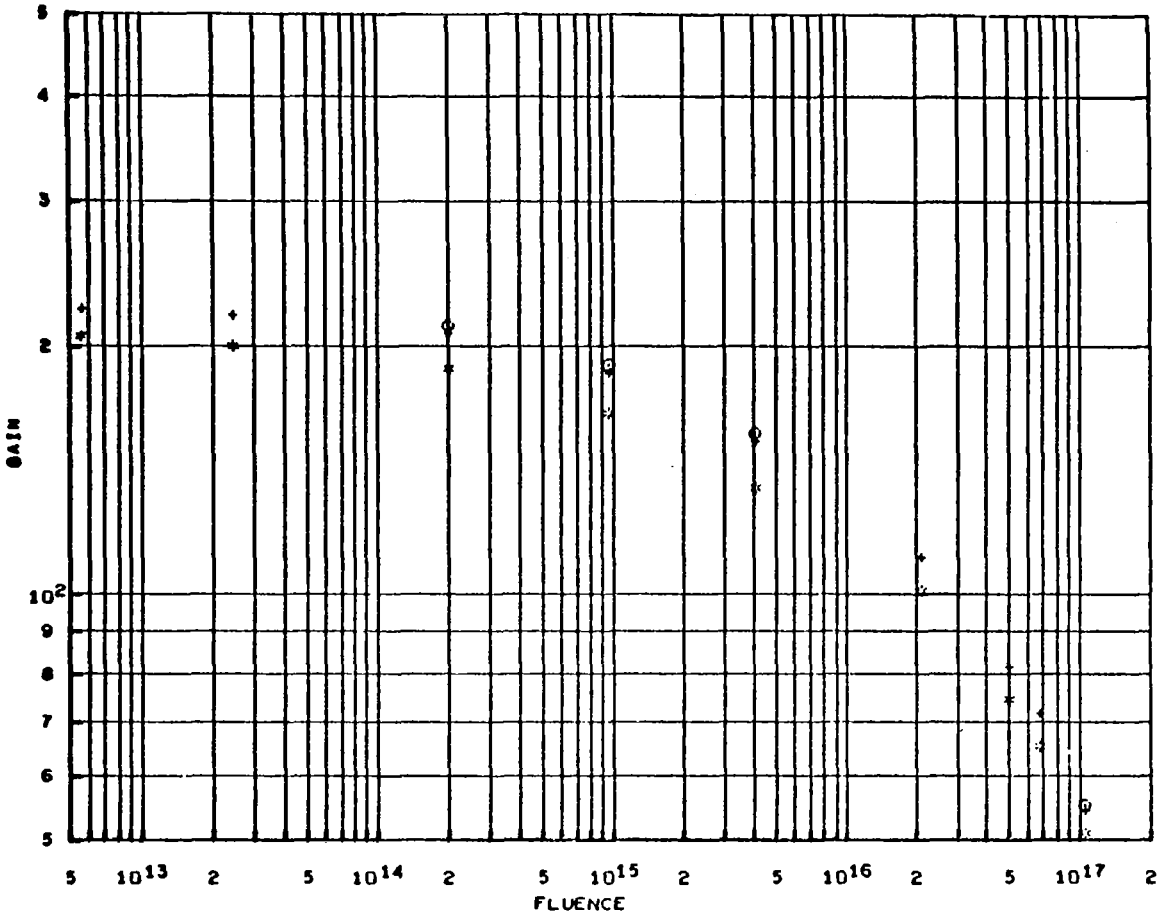

2N1711 TEST 25 COBALT 60 GAMMA IRRADIATION

DC GAIN VS. FLUENCE, FAMILY OF EMITTER CURRENTS, COLLECTOR VOLTAGE = 10.0

TEST	TRANS.TYPE	TRANS.NO.	BATCH	MAKE	CUTOFF	NML.FREQ	CASE
25	1711	23	513	FCLD	175.66	147.81	ON

SYMBOL	CURVE	CURRENT	MAX. GAIN	MIN. GAIN	NO DOSE GAIN
*	1	5.0	205.3	50.9	206.8
+	2	10.0	222.1	54.5	224.1
Φ	3	12.0	211.9	55.2	.0

TABULATION OF ARRAY POINTS

CURVE 1		CURVE 2		CURVE 3	
FLUENCE	GAIN	FLUENCE	GAIN	FLUENCE	GAIN
5.55+12	205.3	5.55+12	222.1	2.00+14	211.9
2.45+13	200.2	2.45+13	218.6	9.52+14	189.9
2.00+14	187.9	2.00+14	206.9	4.06+15	156.8
9.52+14	165.5	9.52+14	185.4	1.05+17	55.2
4.06+15	134.1	4.06+15	152.9		
2.09+16	100.9	2.09+16	110.7		
4.94+16	74.3	4.94+16	81.6		
6.79+16	65.1	6.79+16	71.5		
1.05+17	50.9	1.05+17	54.5		

Figure 46. 2N1711 h_{FE} Versus Φ for Co^{60} Gamma Test

The second term of Equation (5) accounts for the the loss of base current due to recombination of carriers in the bulk of the base region and is represented by the minority-carrier lifetime, τ_b. The third term of Equation (5) accounts for the emitter efficiency,

where: σ_b and σ_e = conductivities of the base and emitter regions, respectively

L_e = emitter diffusion length

In addition to those terms expressed in Equation (5), changes in current gain, particularly following radiation exposure, can result from losses of base current related to: 1) recombination in the base-emitter surface and/or bulk region, and 2) channeling of current caused by inversion layers on the surface at junctions between the transistor regions (base to emitter or base to collector).

If the loss in current gain following radiation exposure is caused only by the effect of atomic displacements on the bulk of the base region, then the reduced lifetime due to increased recombination can be related to reduced current gain by Equation (6):

$$\Delta(h_{FE}^{-1}) \cong (W^2/2D_b)\,\Delta(\tau_b^{-1}) \tag{6}$$

Initial values of minority-carrier lifetime can be related to the initial density of recombination sites, N_i:

$$\tau_{b_i}^{-1} = c_1 N_i \tag{7}$$

Atomic displacements create new defect sites, N_r, proportional to the amount of exposure fluence, Φ, of the displacement-type radiation.

$$\tau_{b_f}^{-1} = c_1 N_i + C_2 N_r \tag{8}$$

$$\Delta(\tau_b^{-1}) = \tau_{b_f}^{-1} - \tau_{b_i}^{-1} = c_2 N_r \tag{9}$$

$$\Delta(\tau_b^{-1}) = K_1 \Phi \tag{10}$$

From Equations (6) and (10) it follows that $\Delta(h_{FE}^{-1})$ should be proportional to the fluence if recombination sites resulting from defects produced by displacements within the bulk of the base region dominate the loss of current gain.

$$\Delta(h_{FE}^{-1}) \cong (W^2/2D_b) K_1 \Phi \tag{11}$$

Transistor damage, in agreement with Equation (11), was reported in 1958 by Easley (Reference 12) for neutron irradiation. The "linear" dependence of $\Delta(h_{FE}^{-1})$ on fluence, except at very low values of I_E, has consistently been observed for transistors irradiated in a neutron environment (Reference 13). The results of the present study illustrate cases where, for electron irradiation in particular, Equation (11) is not valid and "nonlinear" effects dominate. The nonlinear damage is identified in some detail in Section 2.9.

In order to study linear and nonlinear damage and to eventually determine equivalences for displacement damage, computer plots of $\Delta(h_{FE}^{-1})$ versus Φ were obtained. These plots were also determined from the oscillogram input data and were plotted as a family of emitter currents at a fixed collector voltage. Typical plots of $\Delta(h_{FE}^{-1})$ versus Φ are shown in Figures 49, 50, and 51 for the three proton tests having energies of 1, 20, and 100 Mev, respectively. Figures 49, 50, and 51 are for three different transistors, but all h_{FE} values were determined at an operating point of 10 volts collector voltage and a family of emitter currents (2, 10, and 12 ma). In each of the three curves it can be seen, by the slope on a log-log plot, that the data fits a linear damage relationship (Equation 11). In Figure 51, only two data points are shown for the 2N2538 transistor. One or two data points per device is typical of the 100-Mev proton test, where a large number of devices were tested passively. Figure 52 shows data on 2N743, No. 33, the only transistor monitored dynamically in the 100-Mev proton test.

Typical plots of $\Delta(h_{FE}^{-1})$ versus Φ are shown in Figures 53, 54, and 55 for the three electron tests, 2, 1, and 0.5 Mev, respectively. The nonlinear damage

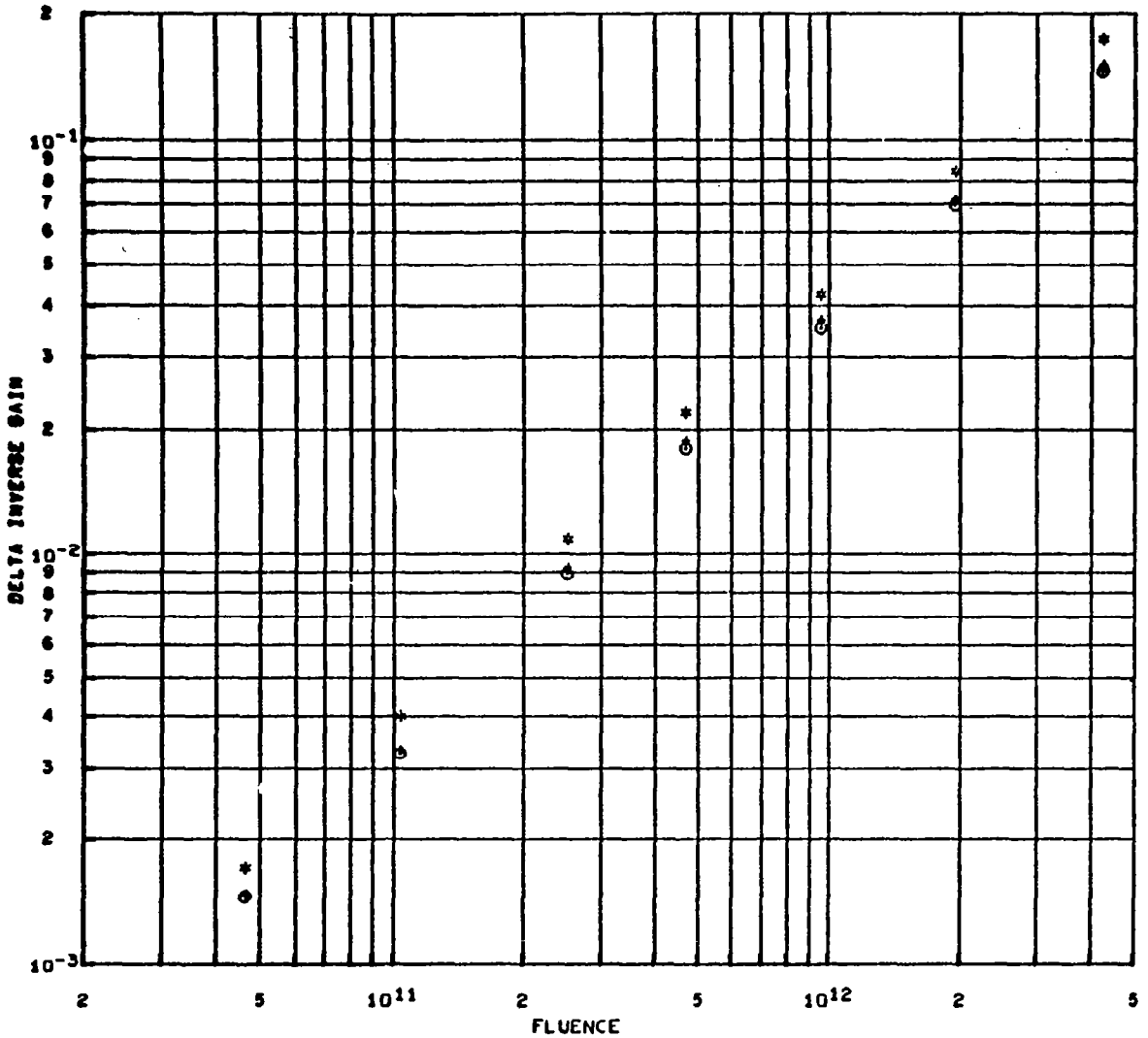

2N1132 TEST 24 POSITION 8 1.0 MEV PROTON IRRADIATION

DELTA INVERSE DC GAIN VS. FLUENCE, FAMILY OF EMITTER CURRENTS, COLLECTOR VOLTAGE = 10.0

TEST	TRANS.TYPE	TRANS.NO.	BATCH	MAKE	CUTOFF	NML.FREQ	CASE
24	1132	2	6511	RYTH	399.56	396.77	OFF

SYMBOL	CURVE	CURRENT	MAX. GAIN	MIN GAIN
*	1	5.0	.17502	.00170
+	2	10.0	.15040	.00147
⊕	3	12.0	.14527	.00146

TABULATION OF ARRAY POINTS

CURVE 1		CURVE 2		CURVE 3	
FLUENCE	INV.GAIN	FLUENCE	INV.GAIN	FLUENCE	INV.GAIN
4.64+10	.00170	4.64+10	.00147	4.64+10	.00146
1.04+11	.00401	1.04+11	.00331	1.04+11	.00327
2.52+11	.01083	2.52+11	.00922	2.52+11	.00890
4.70+11	.02195	4.70+11	.01873	4.70+11	.01802
9.52+11	.04240	9.52+11	.03684	9.52+11	.03540
1.95+12	.08422	1.95+12	.07222	1.95+12	.06957
4.24+12	.17502	4.24+12	.15040	4.24+12	.14527

Figure 49. $\Delta(h_{FE}^{-1})$ Versus Φ for 1-Mev Proton Test (2N1132)

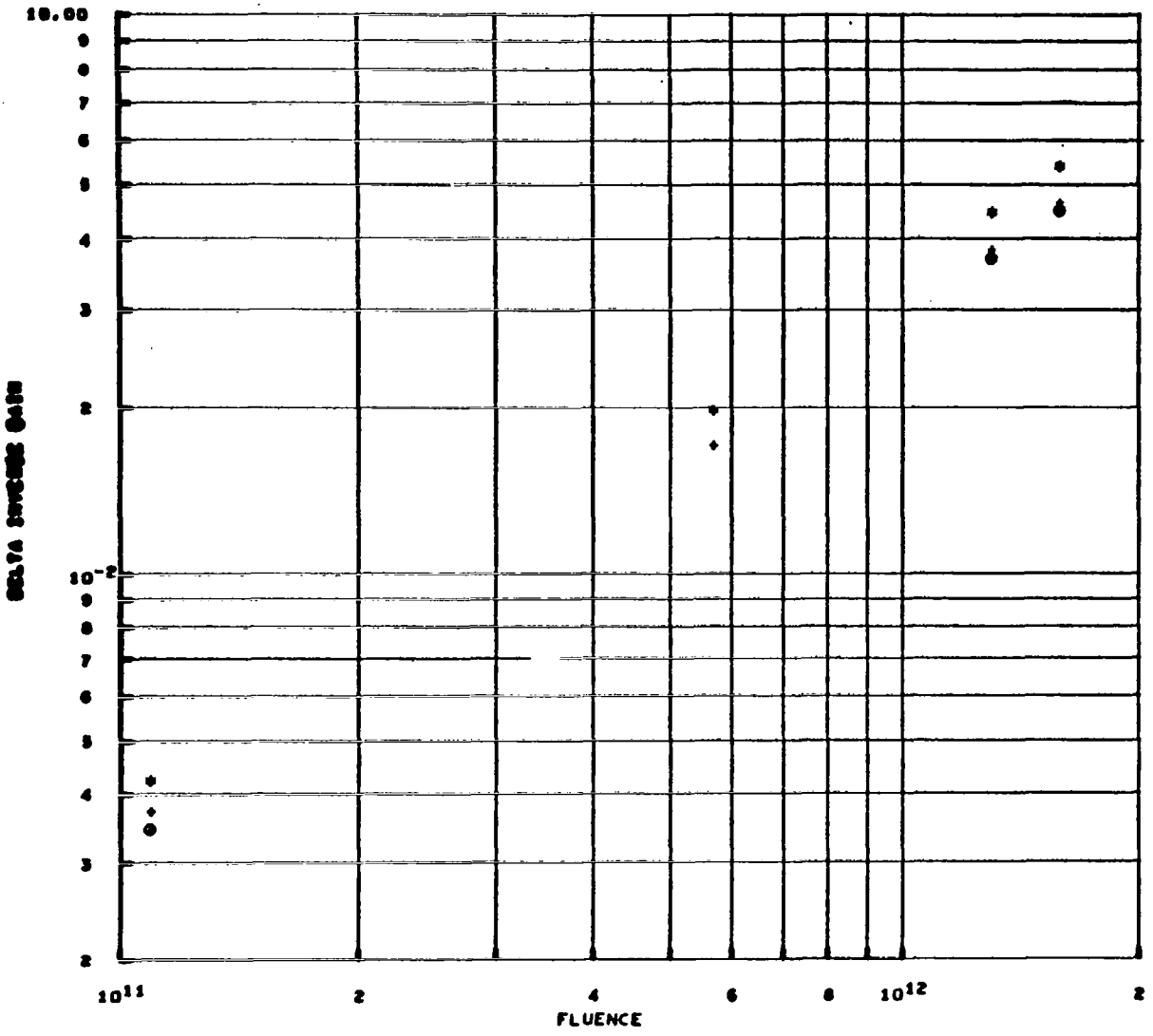

2N1613 TEST 26 20 MEV PROTON IRRADIATION

DELTA INVERSE DC GAIN VS. FLUENCE, FAMILY OF EMITTER CURRENTS, COLLECTOR VOLTAGE = 10.0

TEST	TRANS.TYPE	TRANS.NO.	BATCH	MAKE	CUTOFF	NML.FREQ	CASE
26	1613	26	436	FCLD	100.00	94.14	OFF

SYMBOL	CURVE	CURRENT	MAX. GAIN	MIN GAIN
*	1	5.0	.05383	.00420
+	2	10.0	.04655	.00372
●	3	12.0	.04468	.00344

TABULATION OF ARRAY POINTS

CURVE 1		CURVE 2		CURVE 3	
FLUENCE	INV.GAIN	FLUENCE	INV.GAIN	FLUENCE	INV.GAIN
1.09+11	.00420	1.09+11	.00372	1.09+11	.00344
5.69+11	.01966	5.69+11	.01714	1.30+12	.03696
1.30+12	.04445	1.30+12	.03849	1.59+12	.04468
1.59+12	.05383	1.59+12	.04655		

Figure 50. $\Delta(h_{FE}^{-1})$ Versus Φ for 20-Mev Proton Test (2N1613)

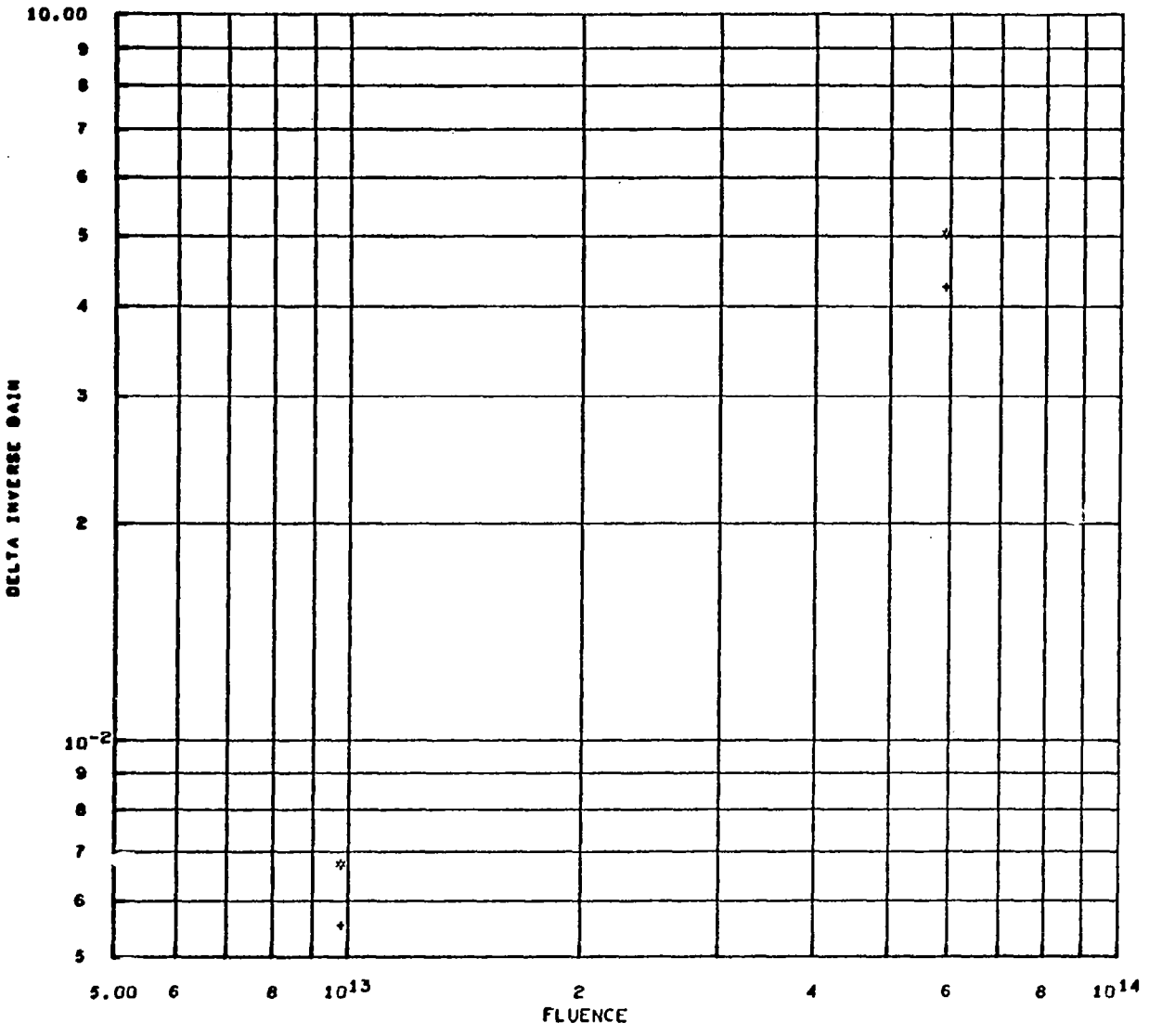

2N2538 TEST 27 60 SERIES 100.0 MEV PROTON IRRADIATION

DELTA INVERSE DC GAIN VS. FLUENCE, FAMILY OF EMITTER CURRENTS, COLLECTOR VOLTAGE = 10.0

TEST	TRANS.TYPE	TRANS.NO.	BATCH	MAKE	CUTOFF	NML.FREQ	CASE
27	2538	64	6525	RYTH	471.81	415.43	ON

SYMBOL	CURVE	CURRENT	MAX. GAIN	MIN GAIN
*	1	5.0	.05043	.00672
+	2	10.0	.04256	.00552
⊙	3	12.0	.00000	.00000

TABULATION OF ARRAY POINTS

CURVE 1		CURVE 2		CURVE 3	
FLUENCE	INV.GAIN	FLUENCE	INV.GAIN	FLUENCE	INV.GAIN
9.76+12	.00672	9.76+12	.00552		
5.92+13	.05043	5.92+13	.04256		

Figure 51. $\Delta(h_{FE}^{-1})$ Versus Φ for 100-Mev Proton Test (2N2538)

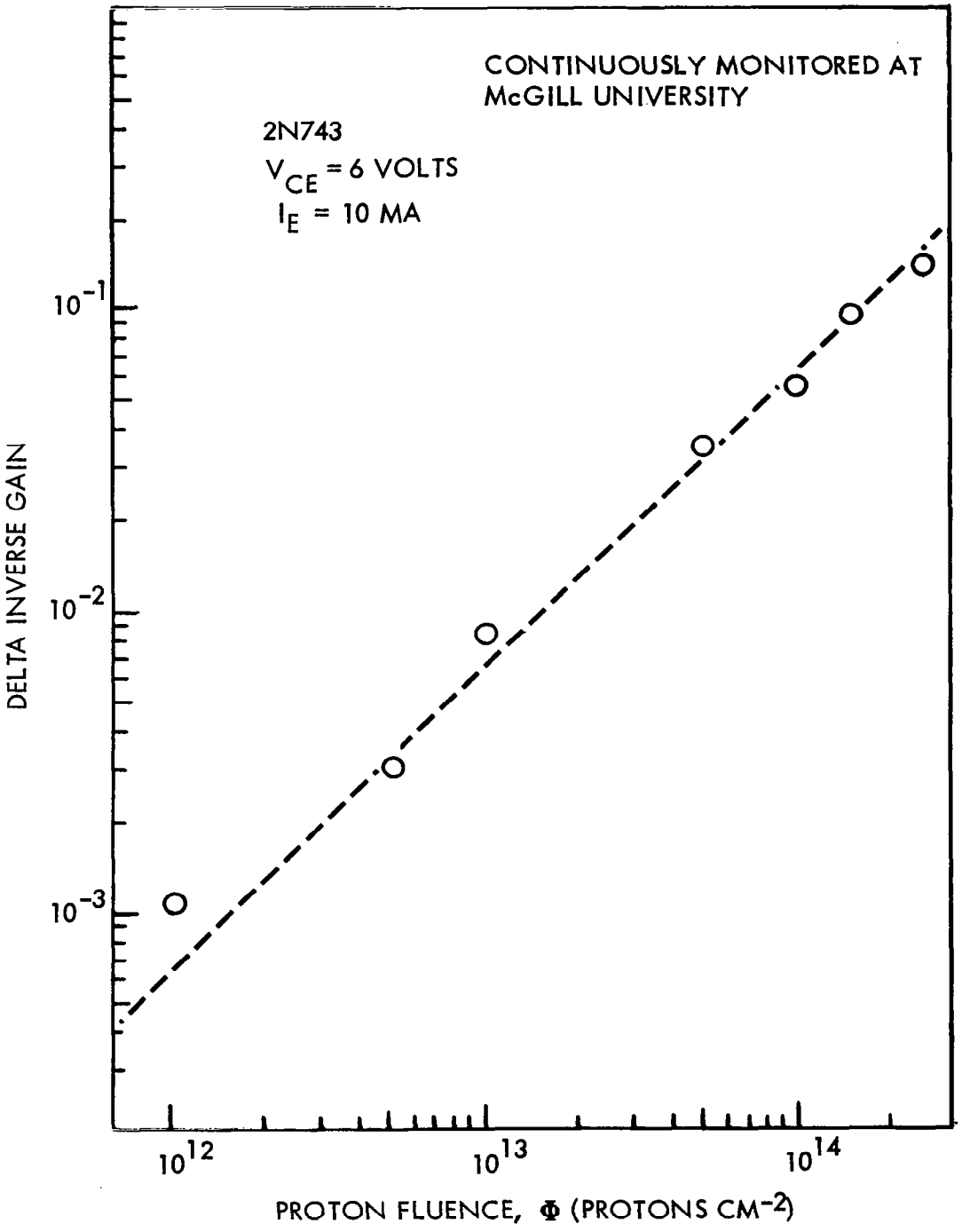

Figure 52. 2N743 $\Delta(h_{FE}^{-1})$ Versus Φ (100-Mev Protons)

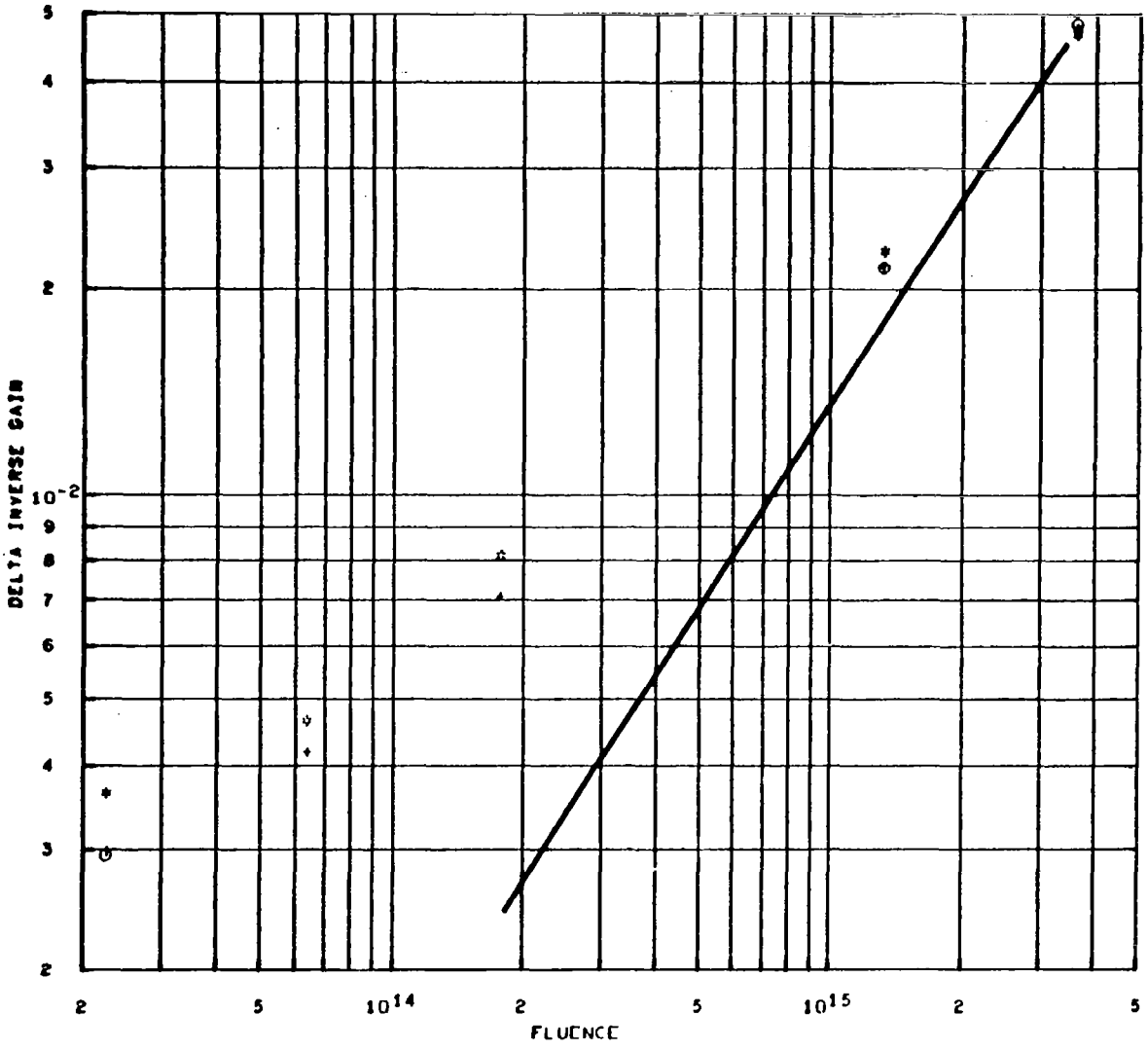

2N834 TEST 21 POSITION 6 2. MEV ELECTRON IRRADIATION

DELTA INVERSE DC GAIN VS. FLUENCE, FAMILY OF EMITTER CURRENTS, COLLECTOR VOLTAGE = 10.0

TEST	TRANS.TYPE	TRANS.NO.	BATCH	MAKE	CUTOFF	NML.FREQ	CASE
21	834	5	444	MTRA	452.59	413.08	ON

SYMBOL	CURVE	CURRENT	MAX. GAIN	MIN GAIN
*	1	5.0	.04690	.00362
+	2	10.0	.04778	.00298
⊙	3	12.0	.04849	.00294

TABULATION OF ARRAY POINTS

CURVE 1		CURVE 2		CURVE 3	
FLUENCE	INV.GAIN	FLUENCE	INV.GAIN	FLUENCE	INV.GAIN
2.25+13	.00362	2.25+13	.00298	2.25+13	.00294
6.37+13	.00466	6.37+13	.00418	1.32+15	.02157
1.76+14	.00812	1.76+14	.00709	3.62+15	.04849
1.32+15	.02286	1.32+15	.02169		
3.62+15	.04690	3.62+15	.04778		

Figure 53. $\Delta(h_{FE}^{-1})$ Versus Φ for 2-Mev Electron Test (2N834)

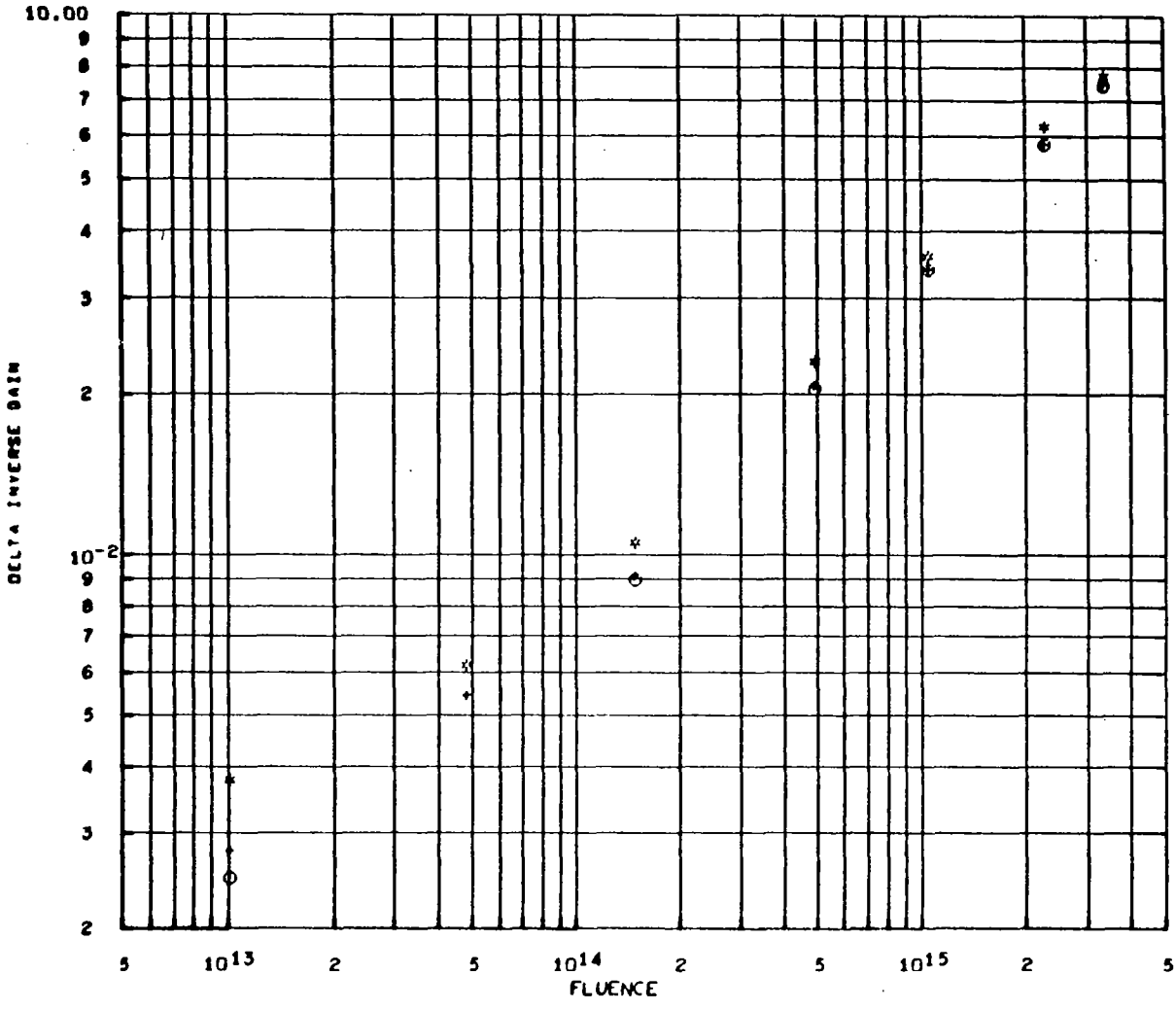

2N1613 TEST 22 POSITION 1 1.3 MEV ELECTRON IRRADIATION

DELTA INVERSE DC GAIN VS. FLUENCE, FAMILY OF EMITTER CURRENTS, COLLECTOR VOLTAGE = 10.0

TEST	TRANS.TYPE	TRANS.NO.	BATCH	MAKE	CUTOFF	NML.FREQ	CASE
22	1613	10	436	FCLD	86.98	94.14	ON

SYMBOL	CURVE	CURRENT	MAX. GAIN	MIN GAIN
*	1	5.0	.02783	.00377
+	2	10.0	.07509	.00277
⊕	3	12.0	.07481	.00248

TABULATION OF ARRAY POINTS

CURVE 1		CURVE 2		CURVE 3	
FLUENCE	INV.GAIN	FLUENCE	INV.GAIN	FLUENCE	INV.GAIN
1.00+13	.00377	1.00+13	.00277	1.00+13	.00248
4.80+13	.00620	4.80+13	.00542	1.47+14	.00897
1.47+14	.01056	1.47+14	.00912	4.88+14	.02049
4.88+14	.02310	4.88+14	.02074	1.04+15	.03416
1.04+15	.03620	1.04+15	.03405	2.27+15	.05819
2.27+15	.06295	2.27+15	.05832	3.36+15	.07481
3.36+15	.07783	3.36+15	.07509		

Figure 54. $\Delta(h_{FE}^{-1})$ Versus Φ for 1-Mev Electron Test (2N1613)

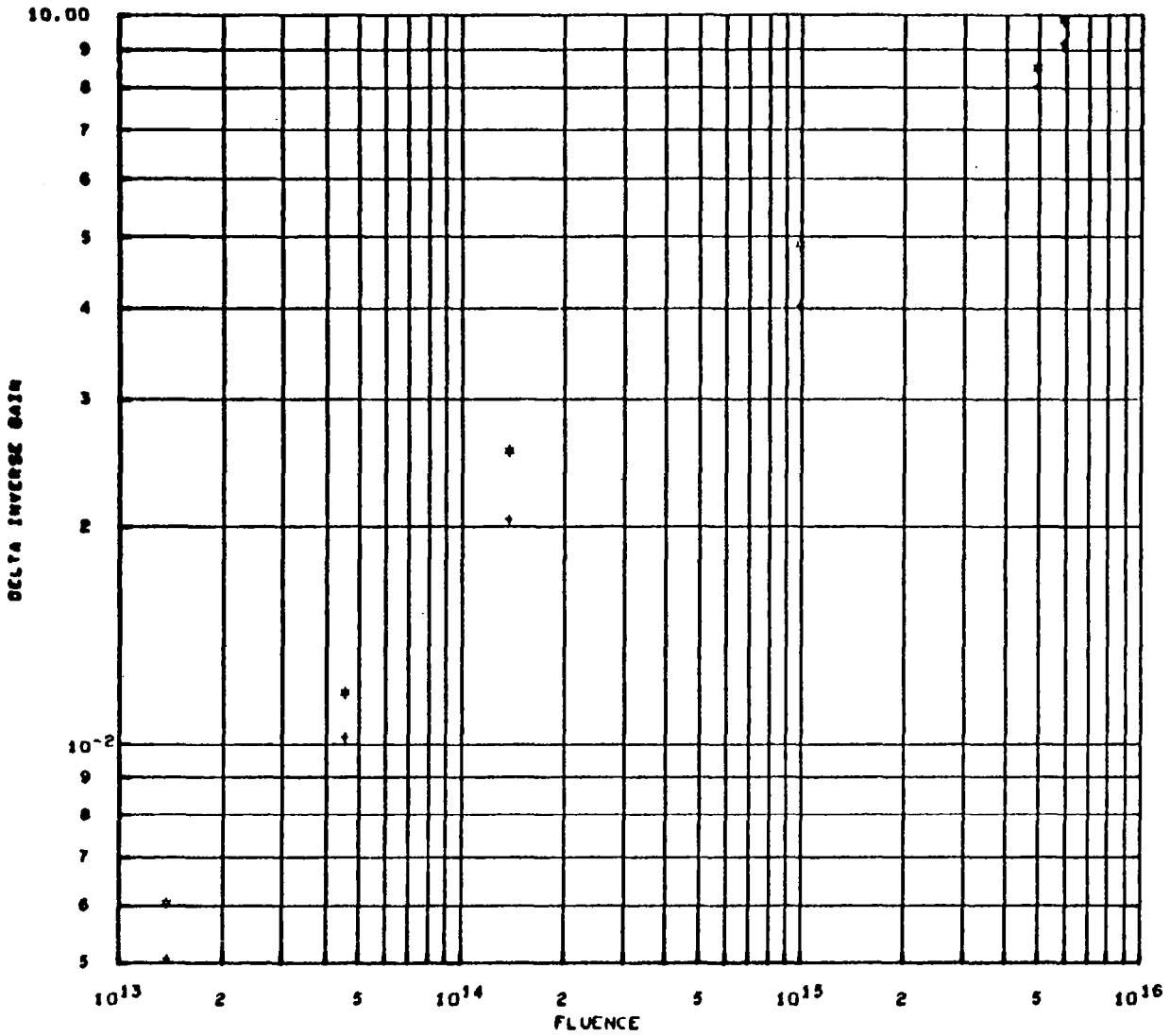

2N1132 TEST 23 POSITION 8 .53 MEV ELECTRON IRRADIATION

DELTA INVERSE DC GAIN VS. FLUENCE, FAMILY OF EMITTER CURRENTS, COLLECTOR VOLTAGE = 10.0

TEST	TRANS.TYPE	TRANS.NO.	DATCH	MAKE	CUTOFF	NML.FREQ	CASE
23	1132	14	6511	RYTH	336.66	396.77	OFF

SYMBOL	CURVE	CURRENT	MAX. GAIN	MIN GAIN
*	1	5.0	.09851	.00601
+	2	10.0	.09200	.00503
@	3	12.0	.00000	.00000

TABULATION OF ARRAY POINTS

CURVE 1		CURVE 2		CURVE 3	
FLUENCE	INV.GAIN	FLUENCE	INV.GAIN	FLUENCE	INV.GAIN
1.37+13	.00601	1.37+13	.00503		
4.56+13	.01182	4.56+13	.01026		
1.37+14	.02547	1.37+14	.02054		
9.88+14	.04901	9.88+14	.04036		
4.94+15	.08493	4.94+15	.08010		
5.87+15	.09851	5.87+15	.09200		

Figure 55. $\Delta(h_{FE}^{-1})$ Versus Φ for 0.5-Mev Electron Test (2N1132)

at the onset of damage is quite apparent. However, as radiation testing is continued to higher fluences, the curves tend to approach a linear dependence on Φ, as is shown in Figure 56 for a 2N1613 transistor which was tested passively. Passive test devices of all transistor types were, in general, tested to high enough electron exposures to obtain information on linear damage in order to eventually obtain displacement equivalences. In agreement with earlier work (Reference 14), it was also observed that nonlinear damage was generally more severe at lower values of emitter current, as shown in Figures 53, 54, and 55. Even greater nonlinear damage was observed in the gamma-ray test, as evidenced by Figure 57. In that test, very high values of fluence (photons cm^{-2}) were required in order to approach linear damage even though nonlinear damage was observed at rather low exposures. The significance of nonlinear damage in terms of gamma-ray effects and the feasibility of simulating space radiation with Co^{60} gamma sources is described in some detail in Section 2.8.

2.7 DISPLACEMENT EQUIVALENCES

Linear damage of transistor current gain was corrected for differences in effective base width by normalization to a common value of transit time or frequency. Linear regions of computer plots of normalized $\Delta(h_{FE}^{-1})$ as a function of Φ were used to obtain displacement equivalences for proton and electron effects. The influence of inherent transistor shielding was also considered. From the six charged particle tests performed under this contract and from several other tests (at other electron and proton energies performed either earlier or in conjunction with this program), the dependence of proton and electron displacement effects was evaluated as a function of particle energy. Finally, the electron and proton equivalence values, as well as those from other particle types, were compared with both experimental and theoretical data published by other investigators.

2.7.1 Control Parameters for Damage Normalization

Using Equation (11) and plots of linear damage, transistor displacement equivalences can be obtained provided groups of transistors of a particular type

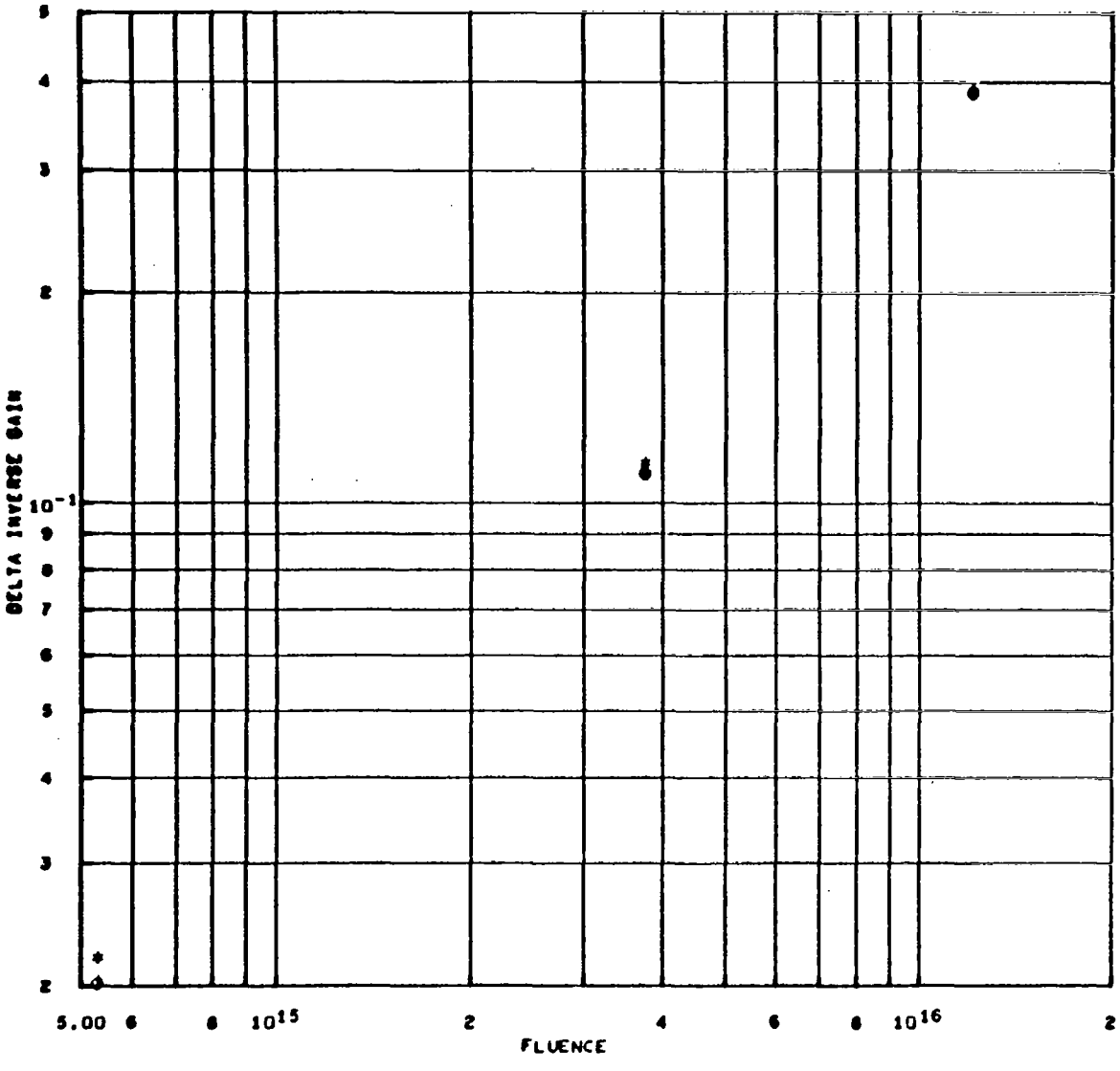

2N1613 TEST 22 POSITION 1 1.3 MEV ELECTRON IRRADIATION

DELTA INVERSE DC GAIN VS. FLUENCE, FAMILY OF EMITTER CURRENTS, COLLECTOR VOLTAGE = 10.0

TEST	TRANS.TYPE	TRANS.NO.	BATCH	MAKE	CUTOFF	NML.FREQ	CASE
22	1613	14	436	FCLD	81.95	94.14	ON

SYMBOL	CURVE	CURRENT	MAX. GAIN	MIN GAIN
*	1	5.0	.39051	.02192
+	2	10.0	.38504	.02044
0	3	12.0	.38561	.02011

TABULATION OF ARRAY POINTS

CURVE 1		CURVE 2		CURVE 3	
FLUENCE	INV.GAIN	FLUENCE	INV.GAIN	FLUENCE	INV.GAIN
5.32+14	.02192	5.32+14	.02044	5.32+14	.02011
3.77+15	.11403	3.77+15	.11061	3.77+15	.10984
1.22+16	.39051	1.22+16	.38504	1.22+16	.38561

Figure 56. 1-Mev Electron Linear Damage (High Exposure)

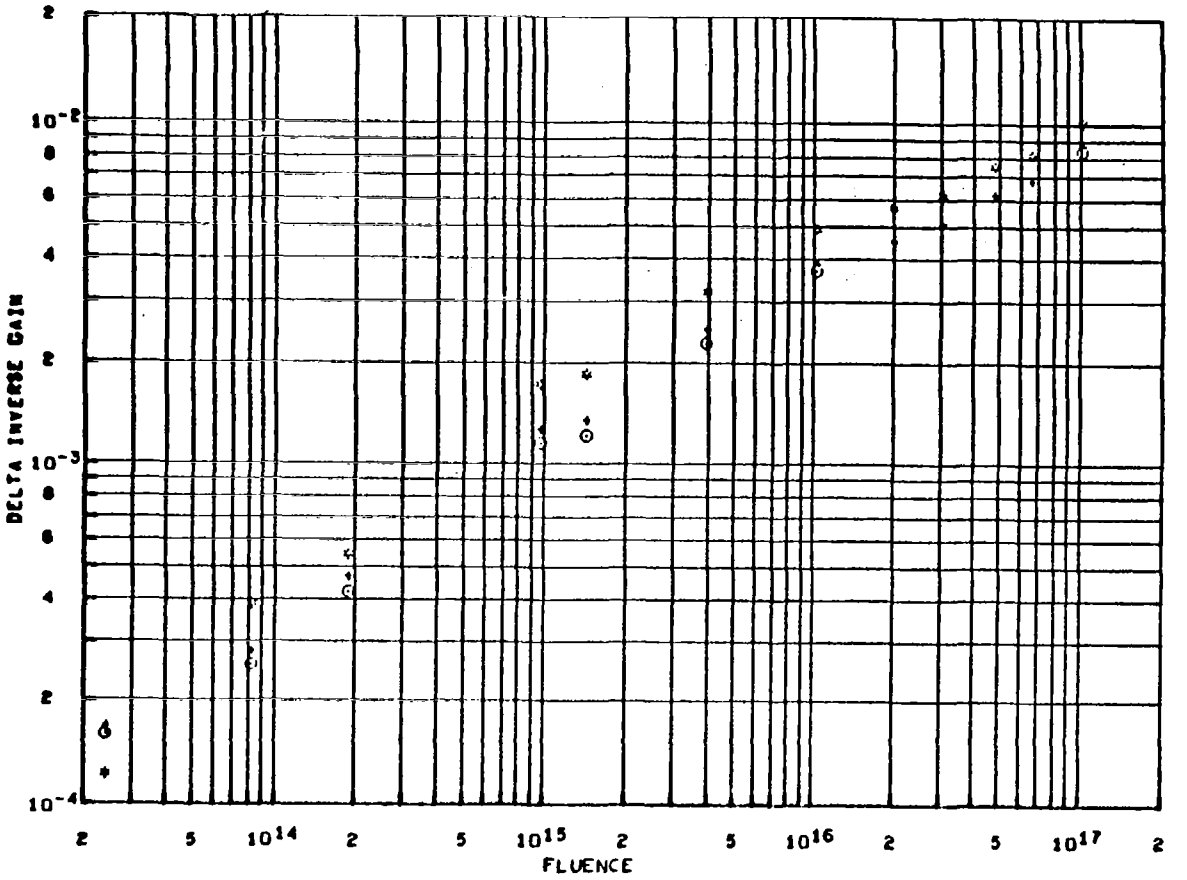

2N2219 TEST 25 COBALT 60 GAMMA IRRADIATION

DELTA INVERSE DC GAIN VS. FLUENCE, FAMILY OF EMITTER CURRENTS, COLLECTOR VOLTAGE = 10.0

TEST	TRANS.TYPE	TRANS.NO.	DATCH	MAKE	CUTOFF	NML.FREQ	CASE
25	2219	22	507	FCLD	340.56	439.49	

SYMBOL	CURVE	CURRENT	MAX. GAIN	MIN GAIN
*	1	5.0	.01007	.00012
+	2	10.0	.00870	.00017
⊙	3	12.0	.00829	.00016

TABULATION OF ARRAY POINTS

CURVE 1		CURVE 2		CURVE 3	
FLUENCE	INV.GAIN	FLUENCE	INV.GAIN	FLUENCE	INV.GAIN
2.37+13	.00012	2.37+13	.00017	2.37+13	.00016
8.29+13	.00039	8.29+13	.00028	8.29+13	.00026
1.88+14	.00054	1.88+14	.00047	1.88+14	.00042
9.68+14	.00172	9.68+14	.00126	9.68+14	.00115
1.44+15	.00186	1.44+15	.00134	1.44+15	.00121
3.94+15	.00322	3.94+15	.00250	3.94+15	.00226
1.03+16	.00488	1.03+16	.00390	1.03+16	.00369
2.01+16	.00566	2.01+16	.00452	1.01+17	.00829
3.03+16	.00620	3.03+16	.00511		
4.75+16	.00746	4.75+16	.00617		
6.54+16	.00818	6.54+16	.00679		
1.01+17	.01007	1.01+17	.00870		

Figure 57. $\Delta(h_{FE}^{-1})$ Versus Φ for Co^{60} Gamma Tests (2N2219)

can be corrected for differences in effective base width, W.

In the semiannual progress report (Reference 1), the equations were shown which relate W to alpha cutoff frequency, f_α, to current gain-bandwidth frequency, f_T, and to transit time, t_b. In summary (Reference 15):

$$t_b = W^2/2.43 D_{pb} \ln(N_{B'}/N_{BC}) \tag{12}$$

where: $N_{B'}$ = base impurity concentration at emitter junction
N_{BC} = background impurity concentration
D_{pb} = hole diffusion constant in base

$$f_\alpha^{-1} \simeq 2\pi \left[kTq^{-1} I_E^{-1} (C_{Te} + C_{Tc}) + t_b\right] \tag{13}$$

By plotting $(2\pi f_\alpha)^{-1}$ as a function of I_E^{-1}, terms of Equation (13) related to the emitter and collector transition capacities, C_{Te} and C_{Tc}, respectively, can be graphically separated out in order to obtain t_b.

The gain-bandwidth frequency, f_T, can be analyzed in the same manner as f_α; however, after the graphical separation, the term obtained is not t_b but t_b'.

$$f_T^{-1} = \alpha_o^{-1} K_\theta^{-1} f_\alpha^{-1} \tag{14}$$

where: α_o = grounded base current gain (low frequency)
K_θ = excess phase constant

$$t_b' = \alpha_o^{-1} K_\theta^{-1} t_b \tag{15}$$

α_o is usually close to unity so that

$$t_b' \cong K_\theta^{-1} t_b \tag{16}$$

No attempt was made to measure K_θ. It has been assumed that the variation of K_θ between transistors of the same type is small. However, this variation of K_θ could

become quite large between different types of transistors. K_θ is a result of built-in electric fields peculiar to the construction of the device and may vary between 0.5 and 1.0 with different constructions (Reference 16).

Transit frequencies were obtained from the measured values of transit time: time:

$$f = (2\pi t_b)^{-1} \tag{17}$$

$$f' = (2\pi t_b')^{-1} \tag{18}$$

These values were used to correct for differences in effective base width and to serve as a control parameter for normalization of $\Delta(h_{FE}^{-1})$ data on all transistors of a given type. It was important in the damage normalization process that the transit time information used be determined for the same values of emitter current that are being specified for the current gain analysis. Thus values of f on equivalence plots are for I_E = 10 ma where equivalences were determined.

Equation (19) follows from Equations (11) and (12):

$$\Delta(h_{FE}^{-1}) \cong c t_b \Phi \tag{19}$$

And thus from Equation (17)

$$f\Delta(h_{FE}^{-1}) \cong K_D \Phi \tag{20}$$

where K_D is the damage constant (for linear displacement effects).

In order to obtain normalized equivalence plots for several devices of one transistor type from the data presented for separate devices (from curves such as those shown in Figures 49 through 57), Equation (20) was multiplied by values of f_N^{-1}:

$$(f/f_N)\,\Delta(h_{FE}^{-1}) \cong K' \Phi \tag{21}$$

The f_N values for each of the transistor types were arbitrarily selected to be

approximately the average value of f or f' (of Equations 17 and 18) for the group of transistors of that type tested. The normalized damage constant, K', as defined by Equation (21), shows the relative sensitivity of each transistor type according to its typical frequency, f_N. Values of f_N are given in Table 10 for each transistor type.

Values of damage constants K' and K_D are shown in Table 10 for proton tests and in Table 11 for that high exposure region of the electron damage curves that follows a linear dependence on Φ.

2.7.2 Proton and Electron Equivalences

From Table 10 it is apparent that when all devices are corrected to one common effective base width (as is the case for K_D rather than K' values), device pairs of the same construction groups (e.g., the npn epitaxial planar) show very close agreement for displacement damage. For the electron damage constants, K_D, of Table 11, it is apparent that the npn devices (first 6 types listed) normalized together quite closely (within a factor of 3); however, considerable variation was observed in K_D for the four pnp transistor types. In particular, the pnp device 2N1132 showed consistently higher damage constants than did the npn devices.

Normalized equivalence plots were obtained by computer analysis using Equation (21) and values of f and f'. Figures 58 through 106 (one of the major goals of this contract) are the equivalence plots for all 10 transistor types tested in all 7 of the radiation exposure tests. The values of f_N used for each transistor type are indicated on each of the respective computer plots. The operational point chosen for representation of this data is an emitter current of 10 ma and a collector voltage of 10 volts (except for 2N743 transistors, which were presented at 10 ma and 5 volts).

Dotted linear lines (i.e., satisfying Equation 21) are shown on each of the plots as a guide to compare results with that anticipated from Equation (11). As already noted, the proton tests (except very close to threshold) obeyed a linear fit. The electron tests, in general, fitted linear damage only at high electron

Table 10. Transistor Damage Constants for Proton Tests

Freq. f_N (Mc)	Transistor Type	Test 24 1 Mev Can Off		Test 26 20 Mev (14 to 16 Mev) Can Off		Test 27 100 Mev	
		K' $(\text{protons/cm}^2)^{-1}$	K_D $\left(\frac{\text{Mc protons}}{\text{cm}^2}\right)^{-1}$	K' $(\text{protons/cm}^2)^{-1}$	K_D $\left(\frac{\text{Mc protons}}{\text{cm}^2}\right)^{-1}$	K' $(\text{protons/cm}^2)^{-1}$	K_D $\left(\frac{\text{Mc protons}}{\text{cm}^2}\right)^{-1}$
94.1	2N1613	9.1×10^{-14}	8.6×10^{-12}	3.3×10^{-14}	3.1×10^{-12}	7.1×10^{-15}	6.7×10^{-13}
147.8	2N1711	3.6×10^{-14}	5.3×10^{-12}	1.3×10^{-14}	1.9×10^{-12}	2.9×10^{-15}	4.3×10^{-13}
415.4	2N2538	9.1×10^{-15}	3.8×10^{-12}	3.3×10^{-15}	1.4×10^{-12}	7.1×10^{-16}	2.9×10^{-13}
439.5	2N2219	8.3×10^{-15}	3.6×10^{-12}	3.0×10^{-15}	1.6×10^{-12}	6.7×10^{-16}	2.9×10^{-13}
437.3	2N743	1.3×10^{-14}	5.6×10^{-12}	4.5×10^{-15}	2.0×10^{-12}	6.7×10^{-16}	2.9×10^{-13}
413.1	2N834	1.5×10^{-14}	6.2×10^{-12}	6.7×10^{-15}	2.8×10^{-12}	9.1×10^{-16}	3.8×10^{-13}
123.4	2N2303	5.6×10^{-14}	6.9×10^{-12}	2.2×10^{-14}	2.7×10^{-12}	3.7×10^{-15}	4.6×10^{-13}
396.8	2N1132	3.7×10^{-14}	1.5×10^{-11}	1.5×10^{-14}	6.0×10^{-12}	2.9×10^{-15}	1.2×10^{-12}
324.3	2N2801	2.7×10^{-14}	8.8×10^{-12}	1.1×10^{-14}	3.6×10^{-12}	2.2×10^{-15}	7.1×10^{-13}
348.2	2N2411	4.3×10^{-15}	1.5×10^{-12}	4.0×10^{-15}	1.4×10^{-12}	1.0×10^{-15}	3.5×10^{-13}

Table 11. Transistor Damage Constants for Electron Tests (Only for Linear Displacement Component)

Transistor Type	Test 21 2.0-Mev Incident on Thick and Thin Can Devices		Test 22 1.3-Mev Incident on Thick and Thin Can Devices		Test 23 0.53-Mev Can Off	
	K'	K_D	K'	K_D	K'	K_D
2N1613	5.6×10^{-17}	5.3×10^{-15}	2.0×10^{-17}	1.9×10^{-15}	1.7×10^{-17}	1.6×10^{-15}
2N1711	2.4×10^{-17}	3.5×10^{-15}	8.0×10^{-18}	1.2×10^{-15}	7.1×10^{-18}	1.0×10^{-15}
2N2538*	7.6×10^{-18}	3.2×10^{-15}	3.3×10^{-18}	1.4×10^{-15}	2.0×10^{-18}	8.3×10^{-16}
2N2219	4.5×10^{-18}	2.0×10^{-15}	2.0×10^{-18}	8.8×10^{-16}	1.8×10^{-18}	7.9×10^{-16}
2N743*	1.0×10^{-17}	4.4×10^{-15}	6.0×10^{-18}	2.6×10^{-15}	2.8×10^{-18}	1.2×10^{-15}
2N834*	1.4×10^{-17}	5.7×10^{-15}	8.3×10^{-18}	3.4×10^{-15}	3.2×10^{-18}	1.3×10^{-15}
2N2303	5.6×10^{-17}	6.9×10^{-15}	2.2×10^{-17}	2.7×10^{-15}	2.0×10^{-17}	2.4×10^{-15}
2N1132*	4.5×10^{-17}	1.8×10^{-14}	2.9×10^{-17}	1.2×10^{-14}	1.0×10^{-17}	4.0×10^{-15}
2N2801	2.9×10^{-18}	9.4×10^{-16}	1.3×10^{-17}	3.6×10^{-15}	7.6×10^{-18}	2.5×10^{-15}
2N2411*	1.4×10^{-17}	4.9×10^{-15}	7.7×10^{-18}	2.7×10^{-15}	2.7×10^{-18}	9.4×10^{-16}

* Thin can devices

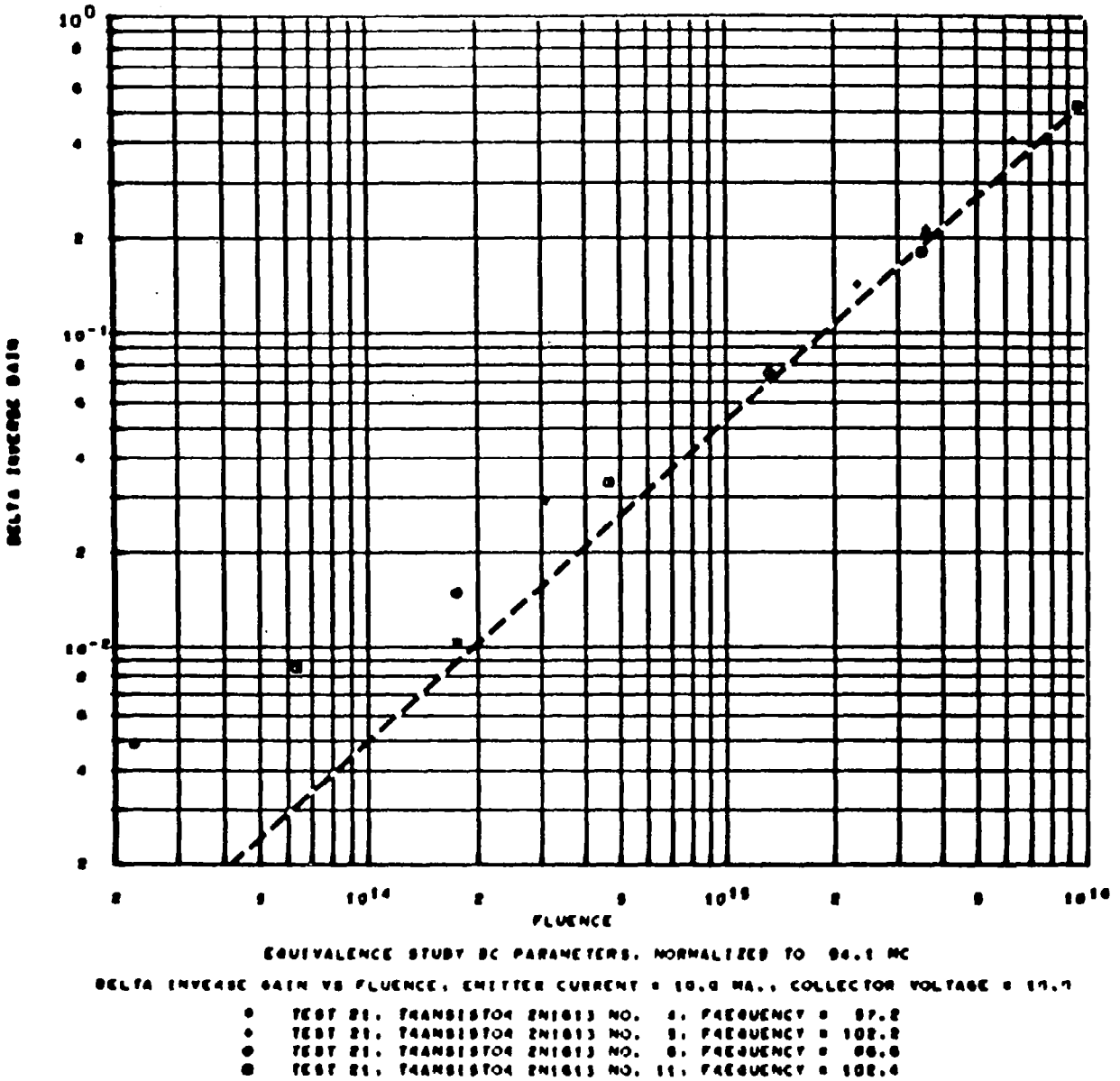

Figure 58. 2N1613 Equivalence Plot, Electron Test 21

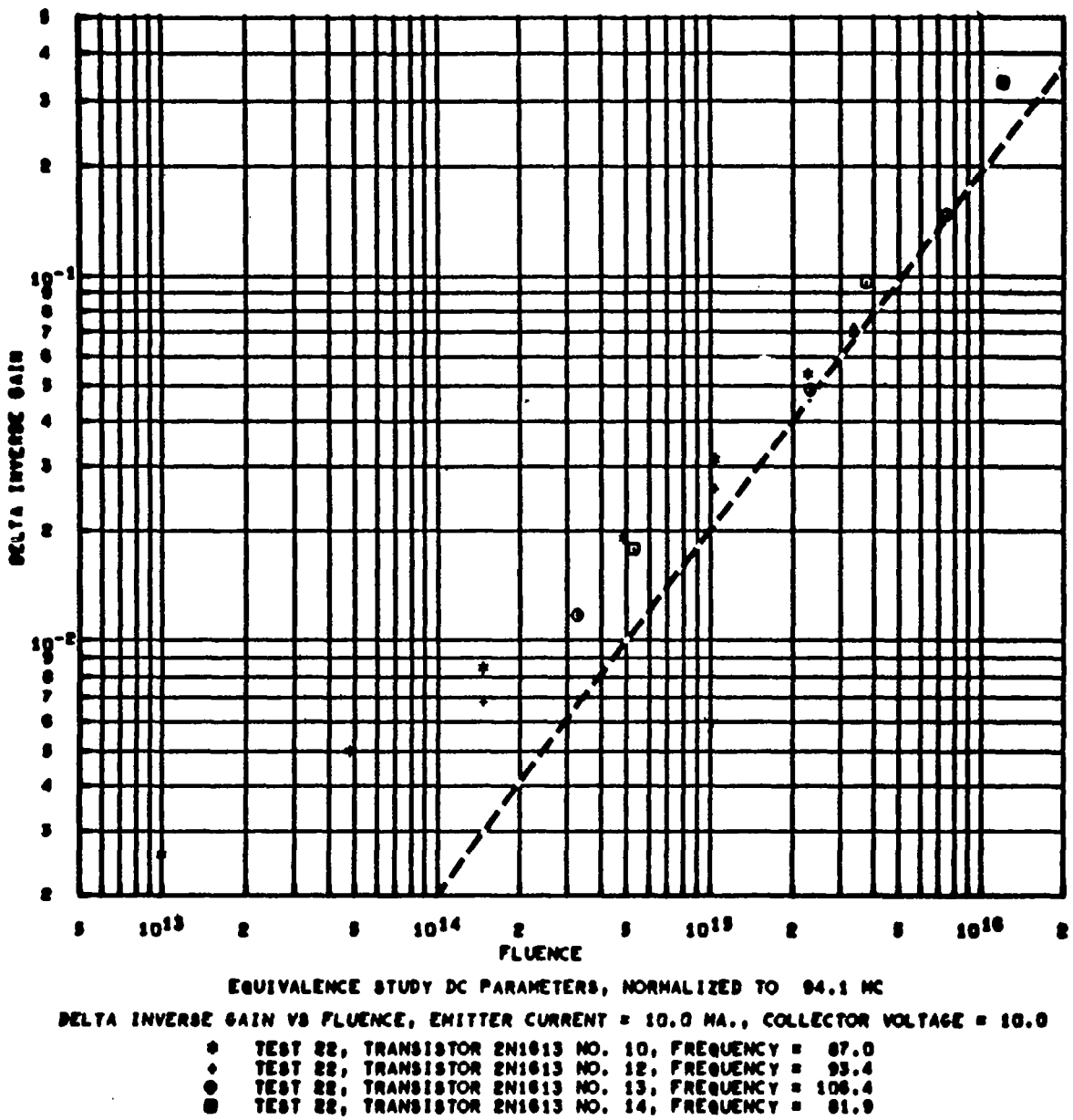

Figure 59. 2N1613 Equivalence Plot, Electron Test 22

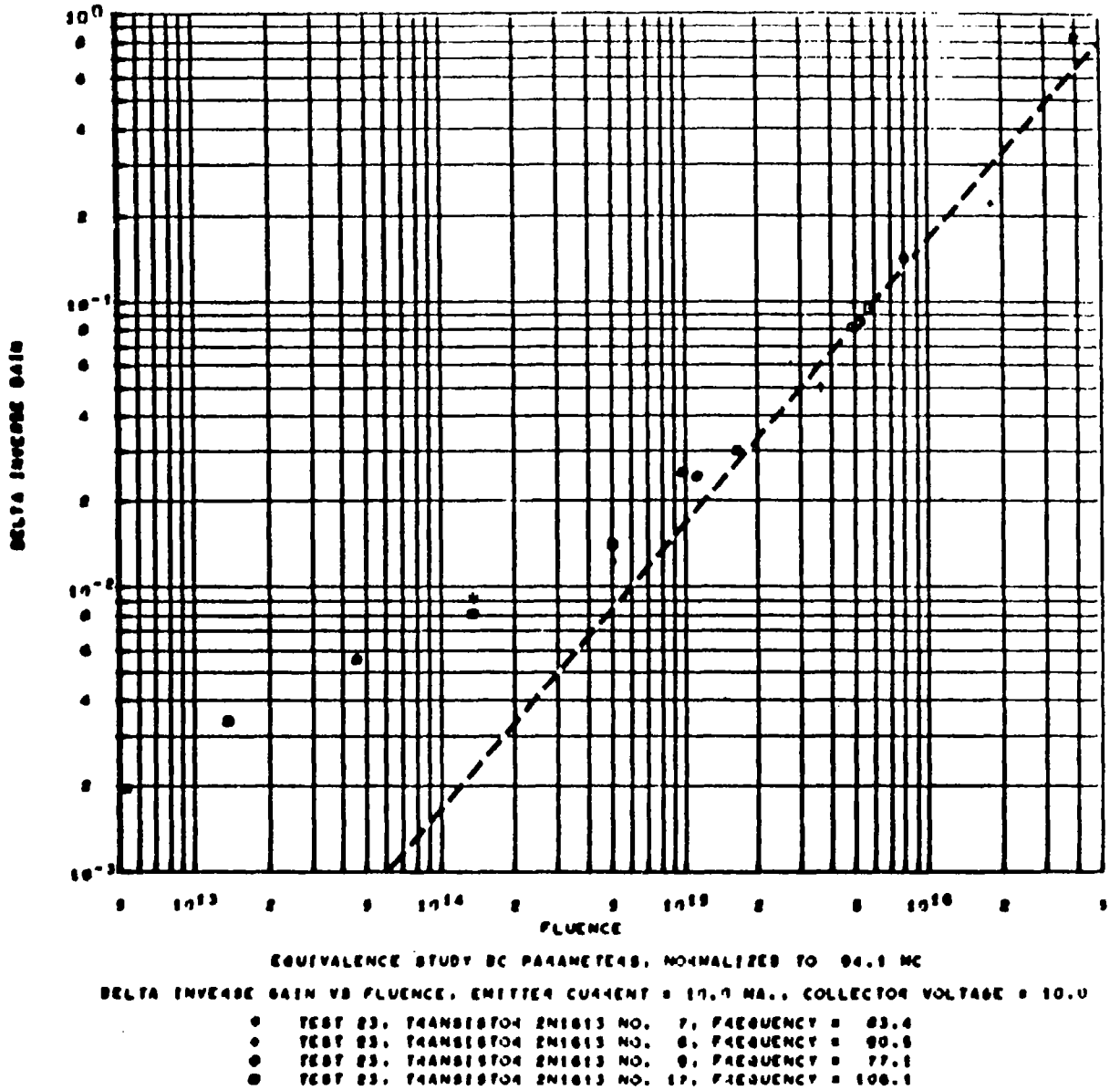

Figure 60. 2N1613 Equivalence Plot, Electron Test 23

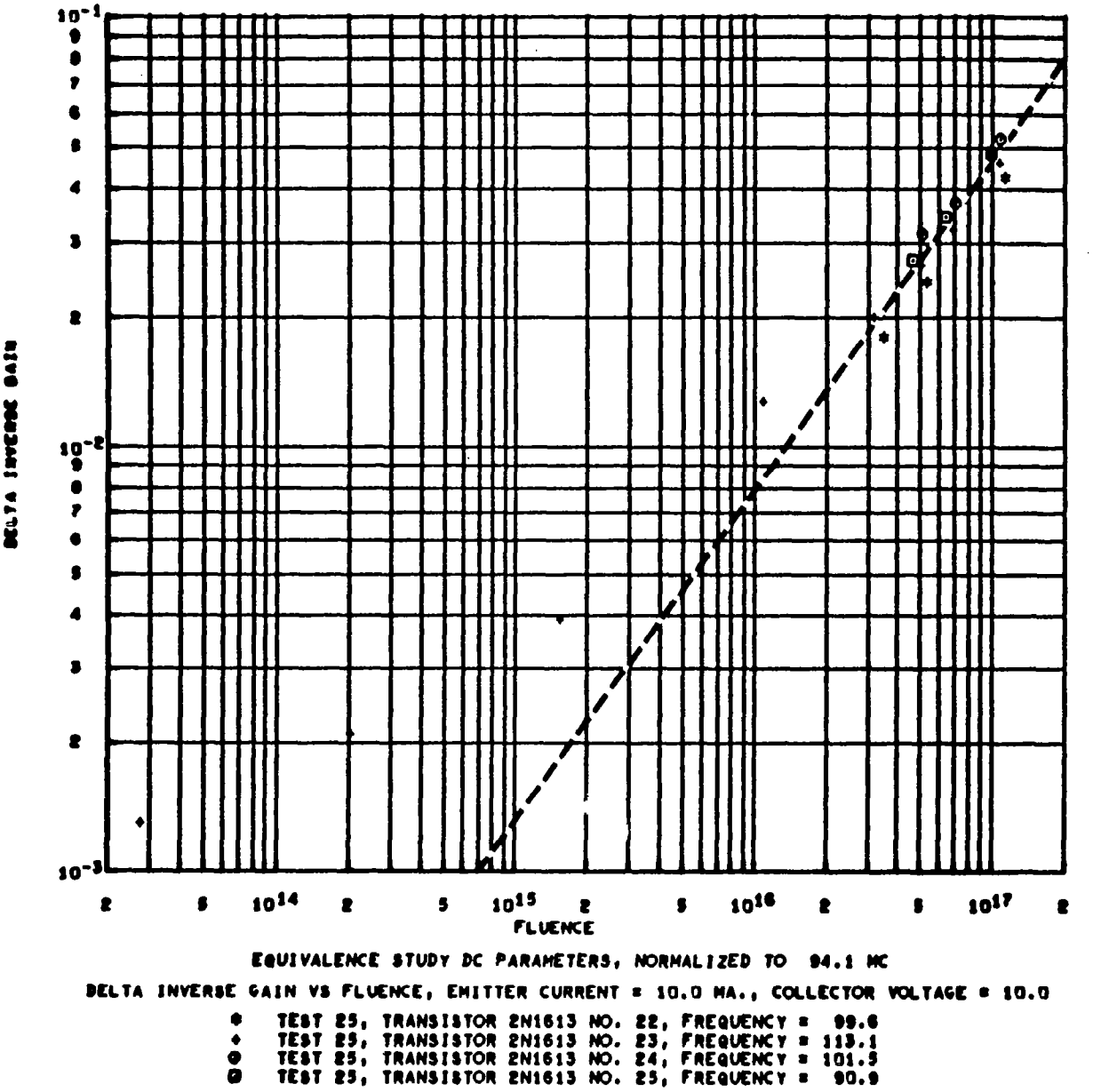

Figure 61. 2N1613 Equivalence Plot, Co^{60} Test

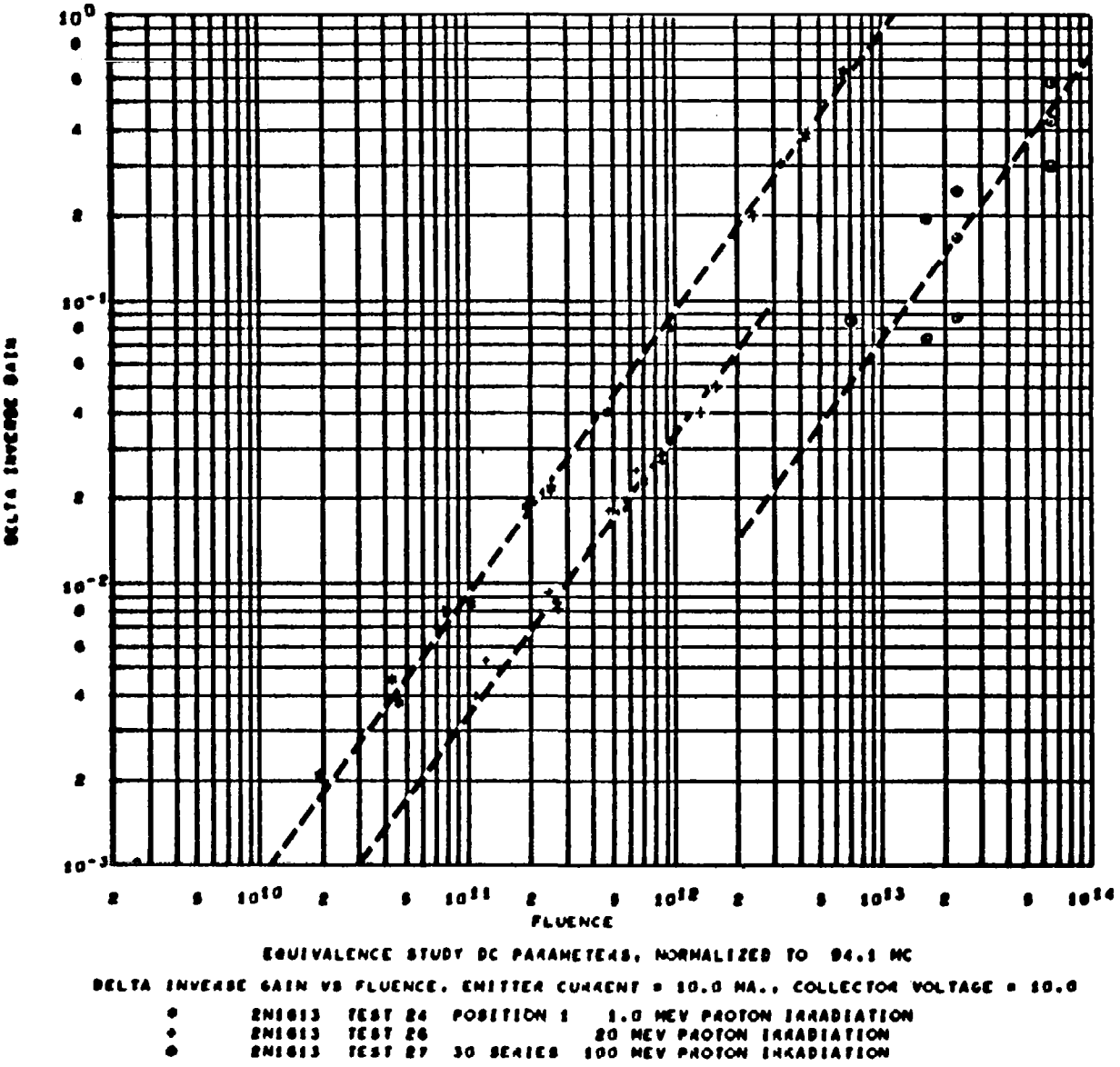

Figure 62. 2N1613 Equivalence Plot, Proton Tests

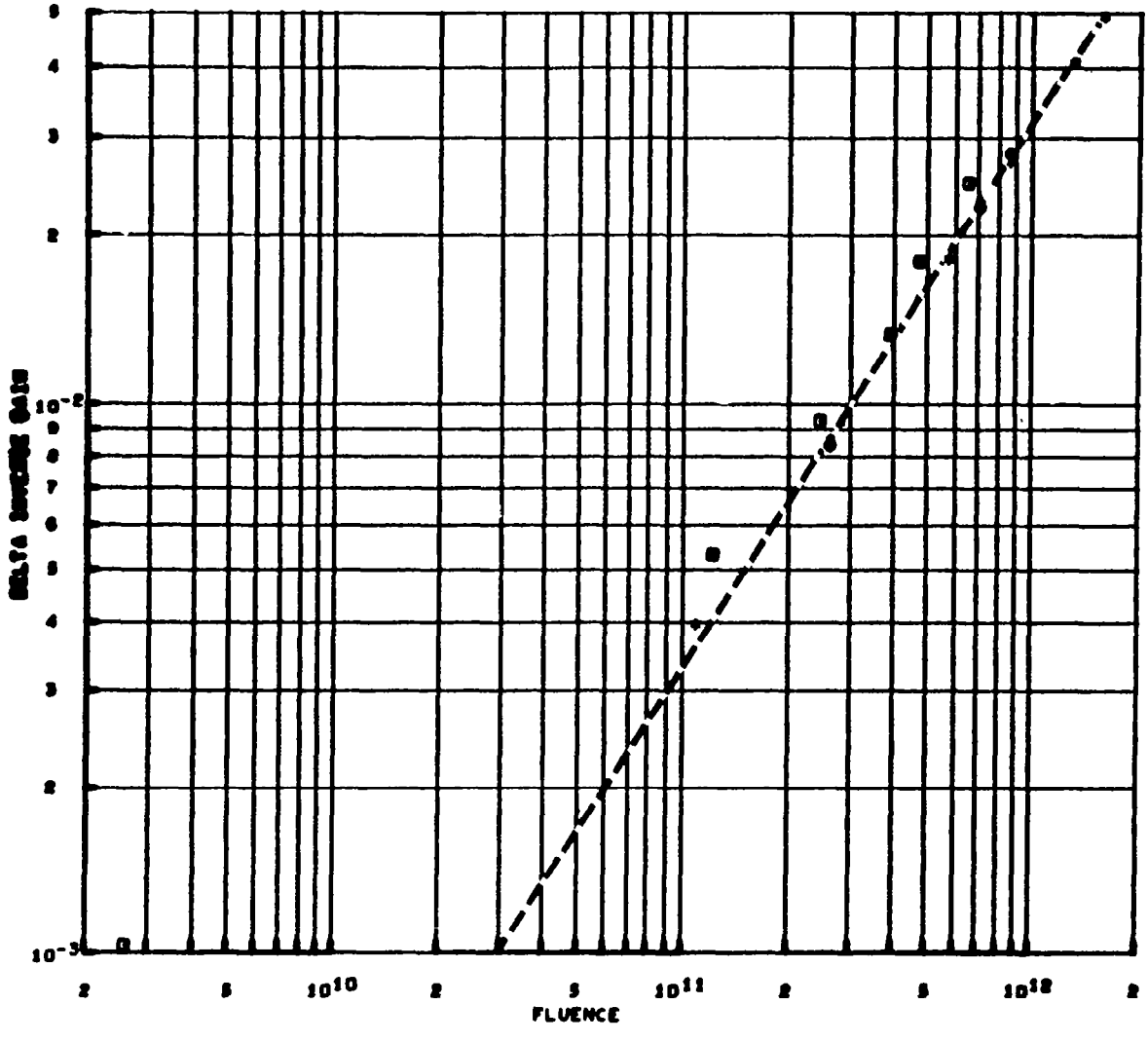

Figure 63. 2N1613 Equivalence Plot, Proton Test 26

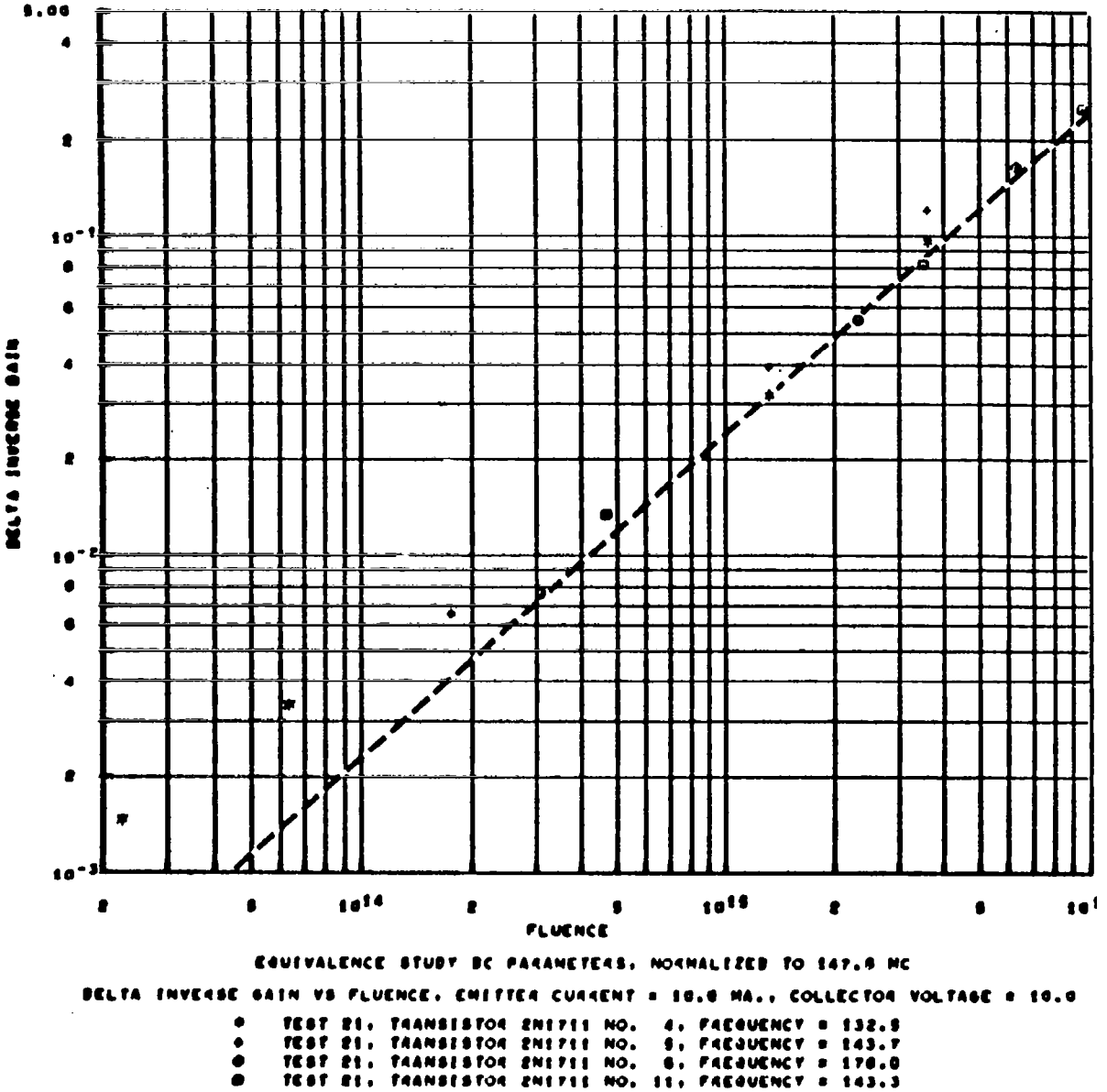

Figure 64. 2N1711 Equivalence Plot, Electron Test 21

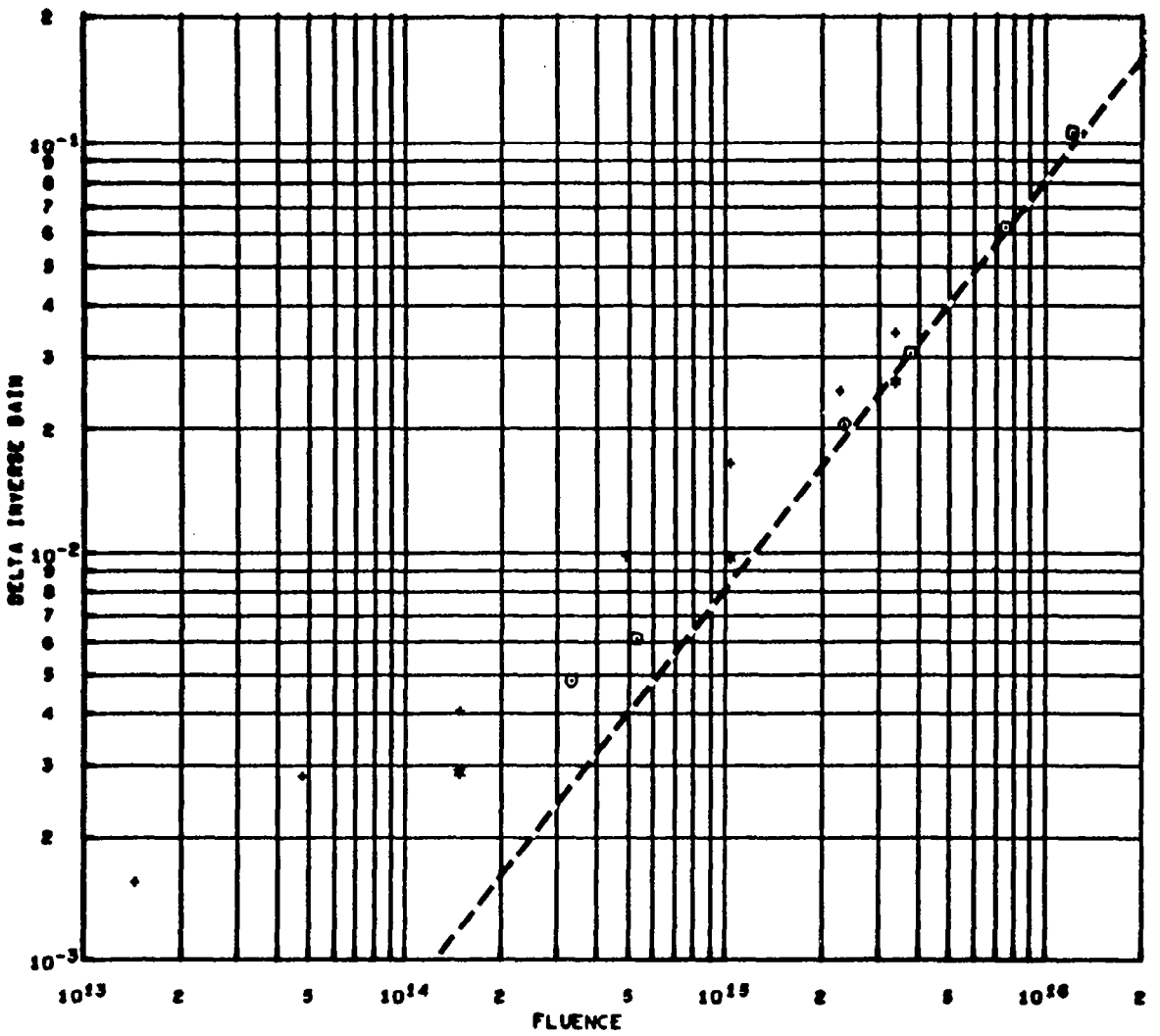

Figure 65. 2N1711 Equivalence Plot, Electron Test 22

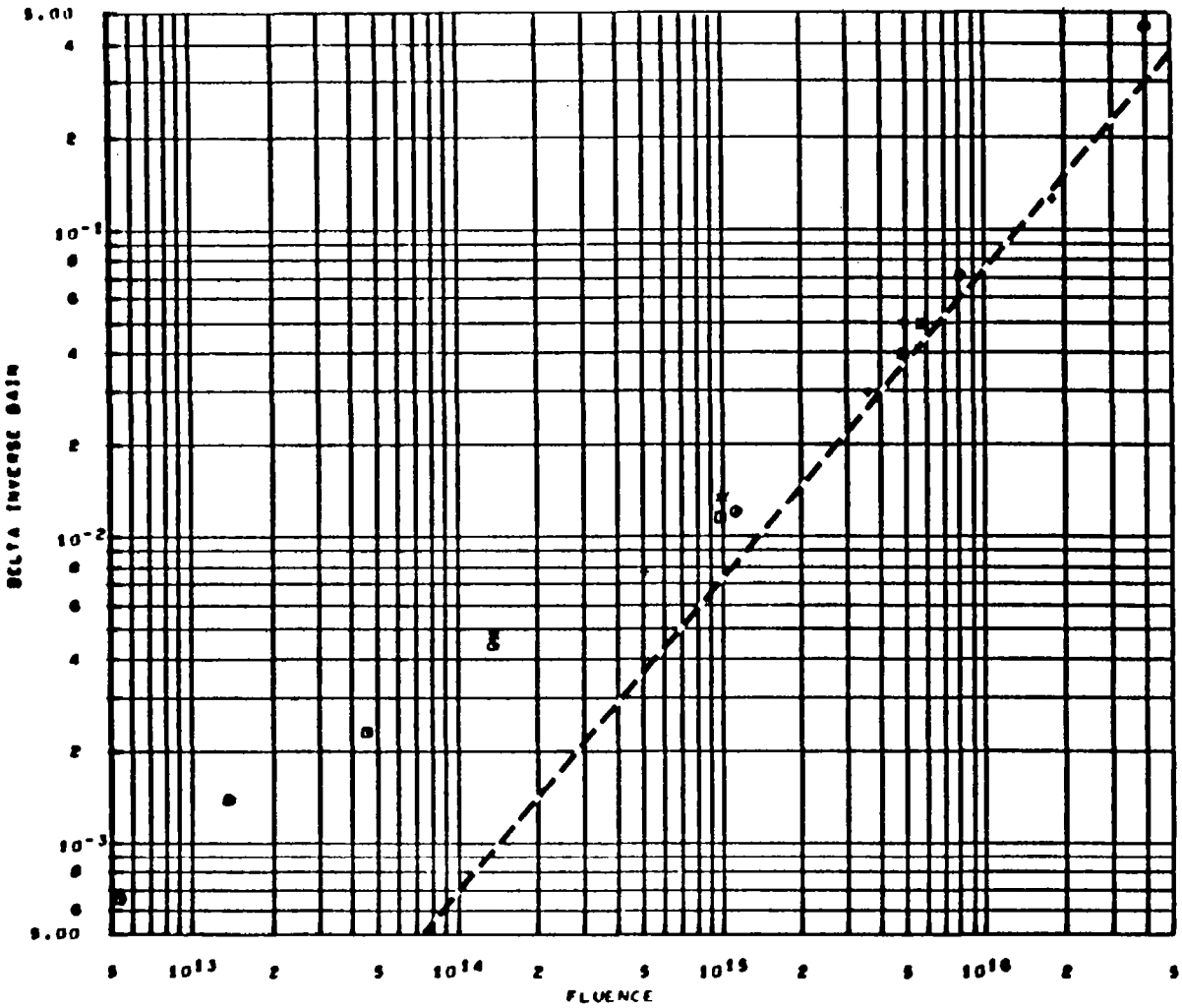

Figure 66. 2N1711 Equivalence Plot, Electron Test 23

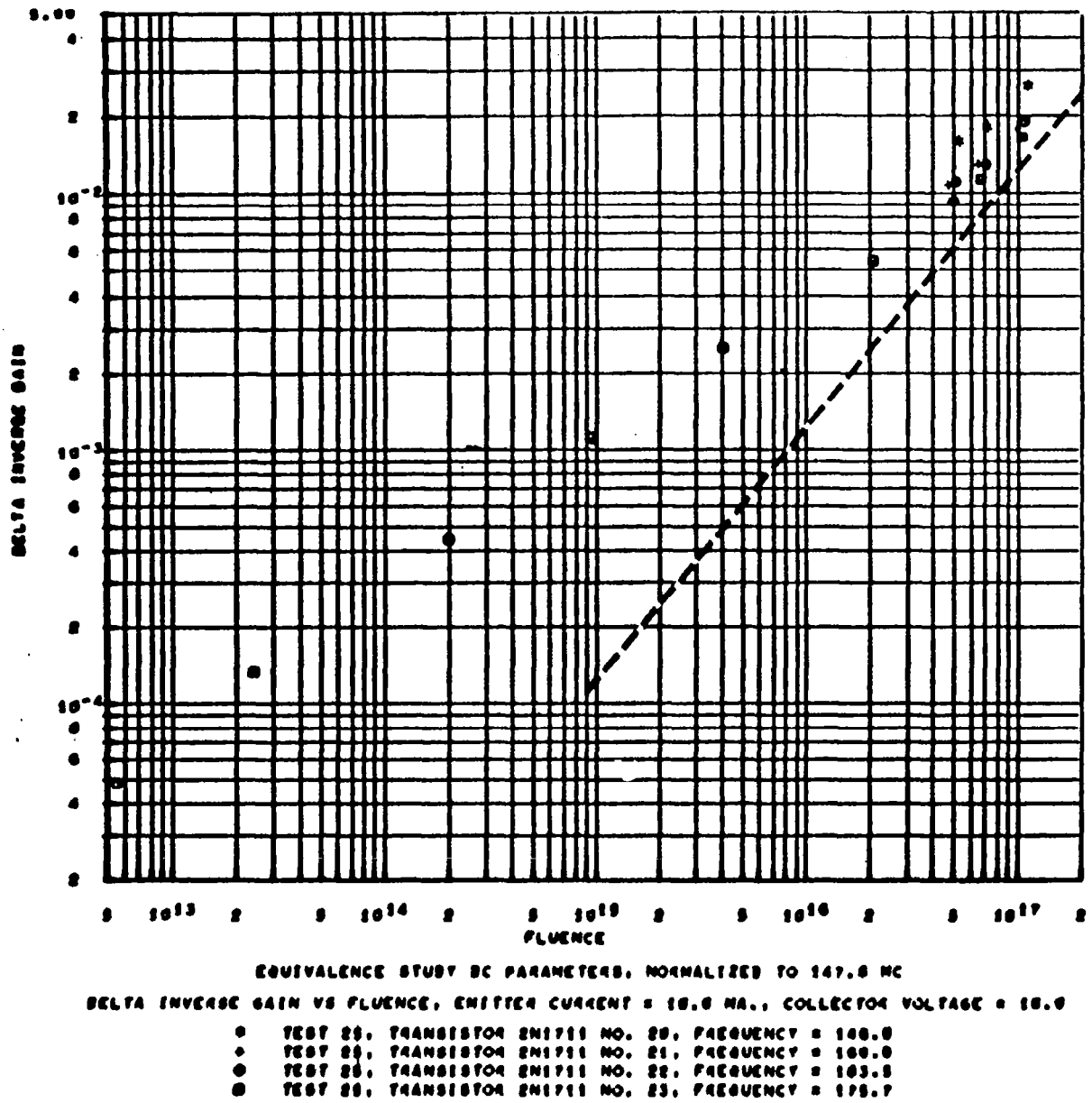

Figure 67. 2N1711 Equivalence Plot, Co^{60} Test

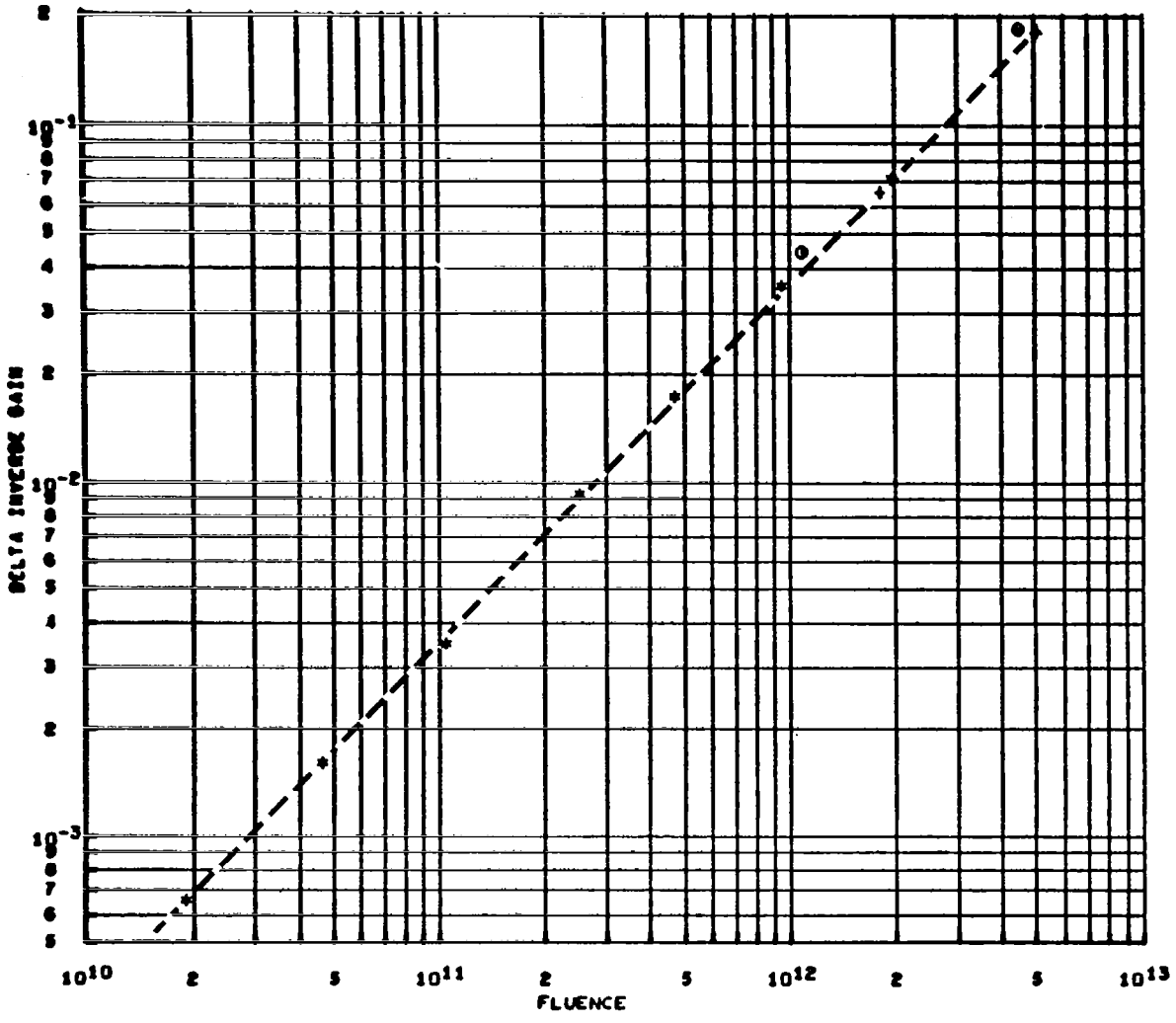

Figure 68. 2N1711 Equivalence Plot, Proton Test 24

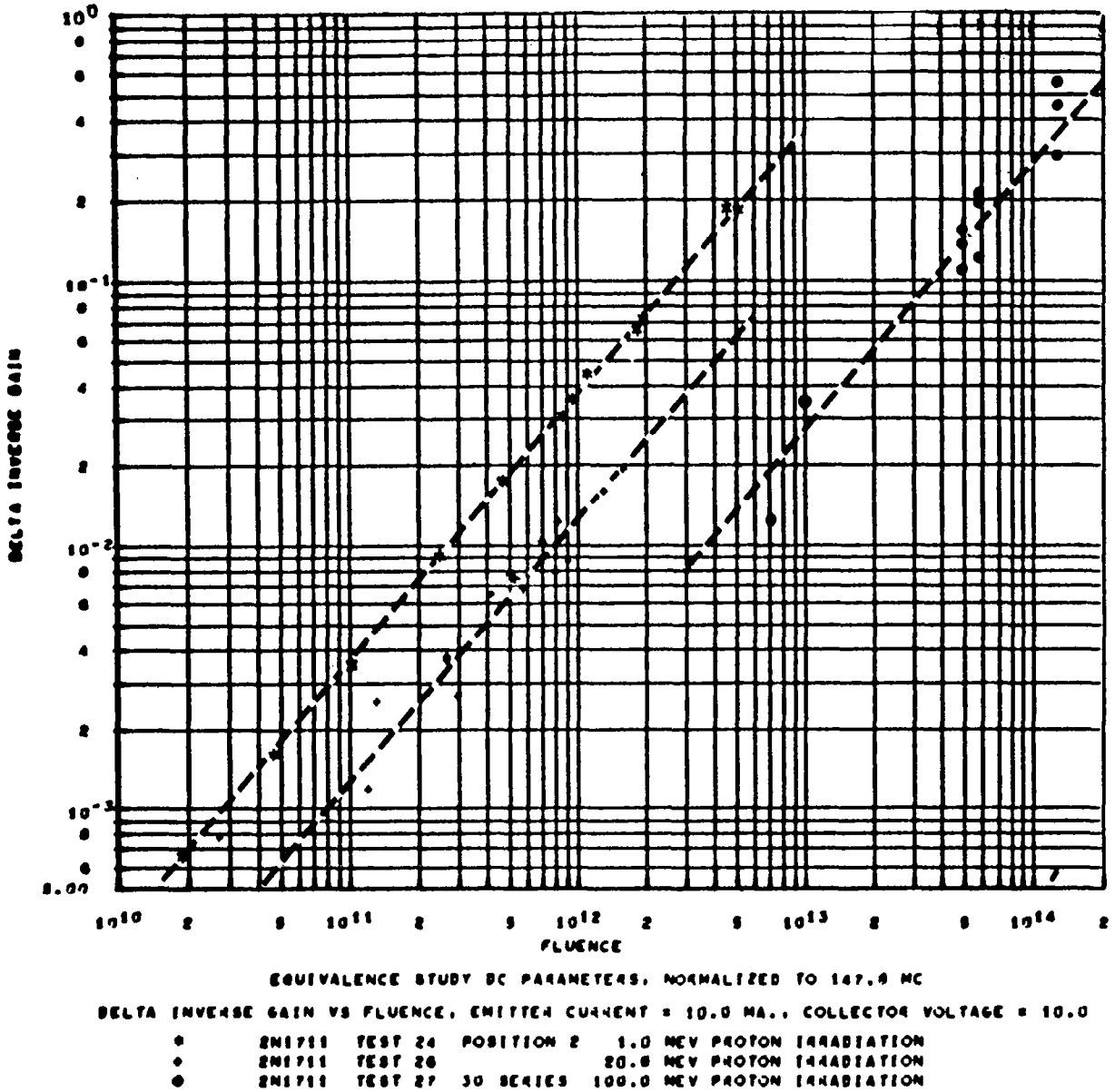

Figure 69. 2N1711 Equivalence Plot, Proton Tests

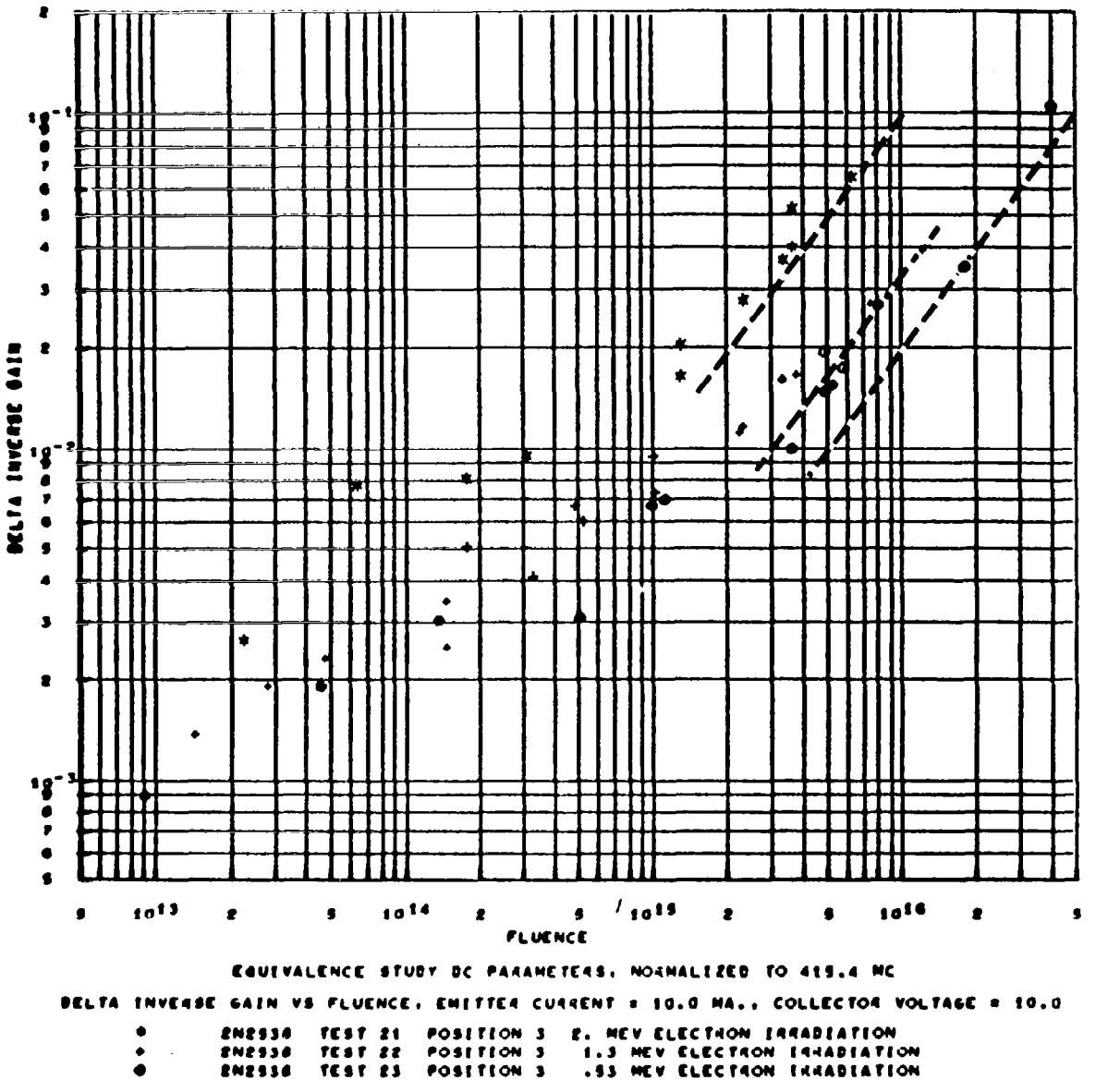

Figure 70. 2N2538 Equivalence Plot, Electron Tests

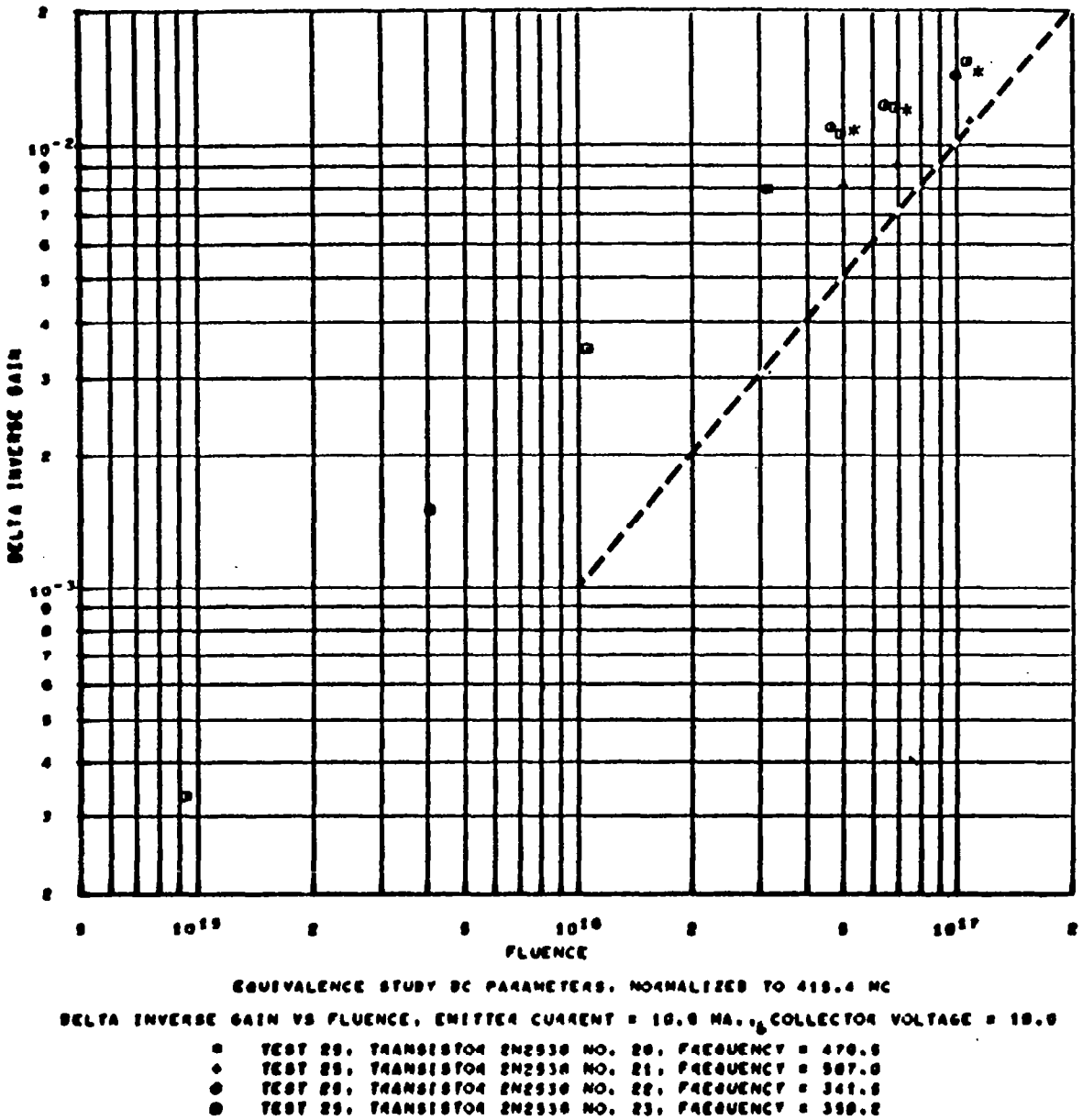

Figure 71. Equivalence Plot, Co^{60} Test

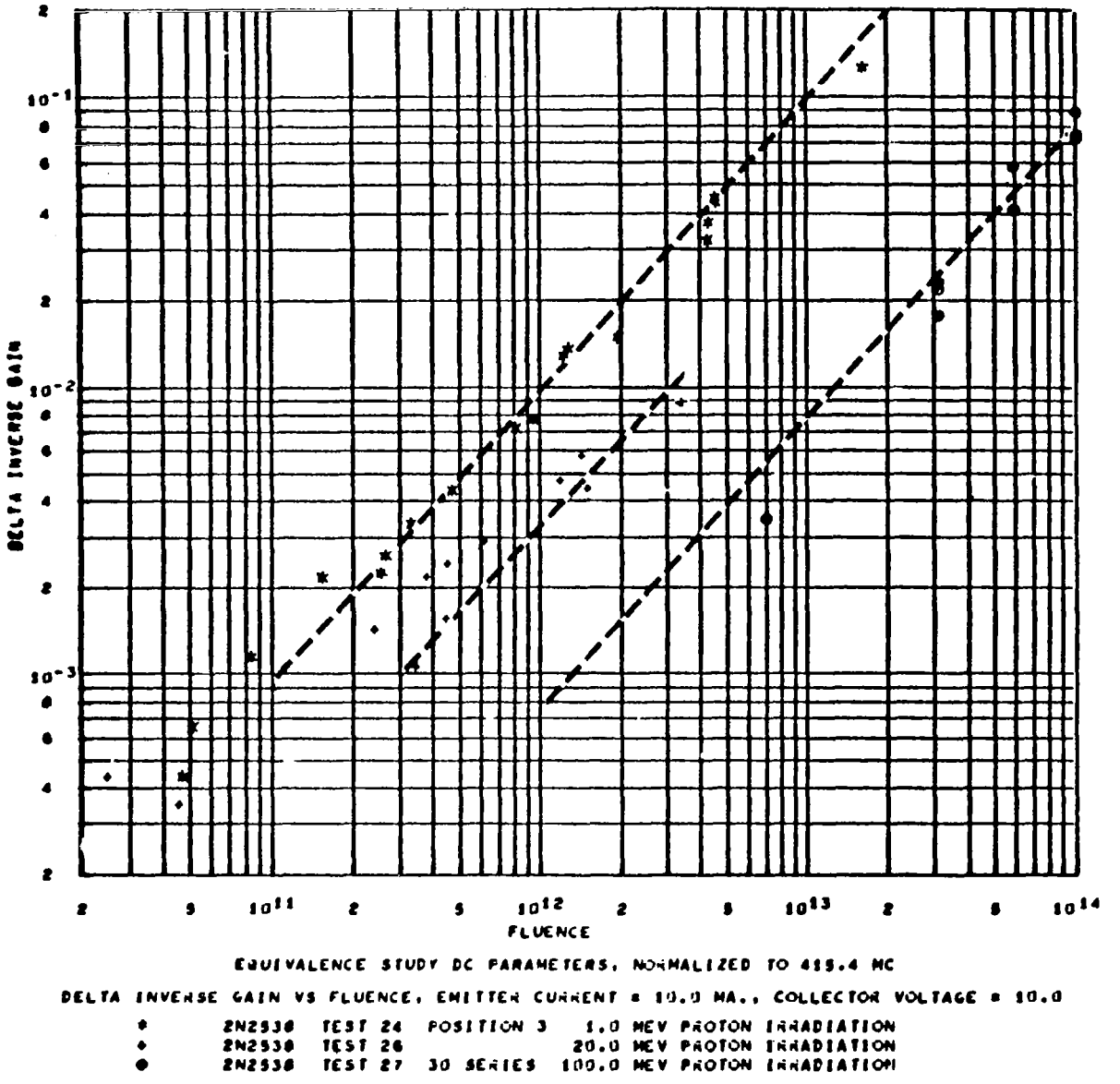

Figure 72. 2N2538 Equivalence Plot, Proton Tests

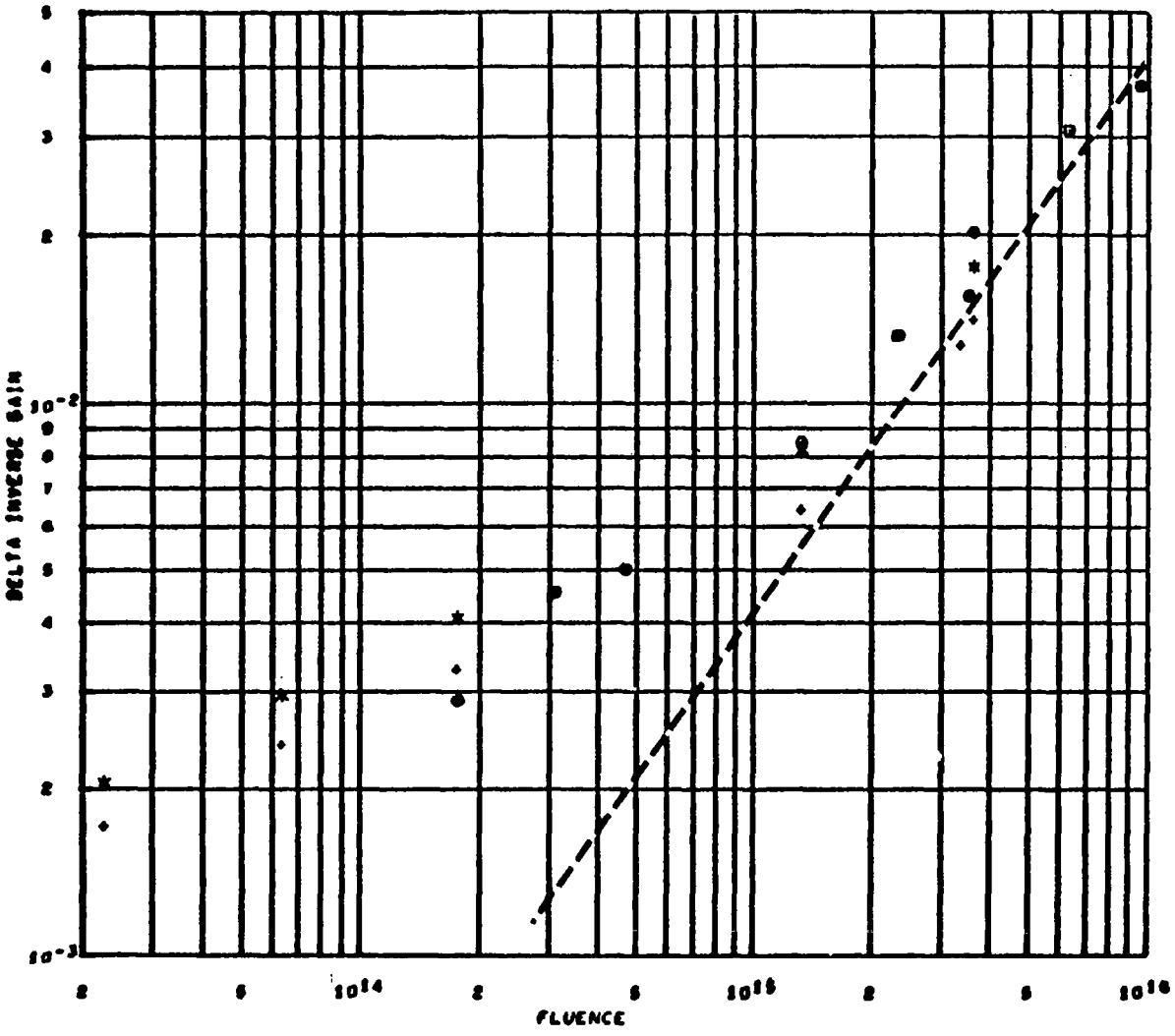

Figure 73. 2N2219 Equivalence Plot, Electron Test 21

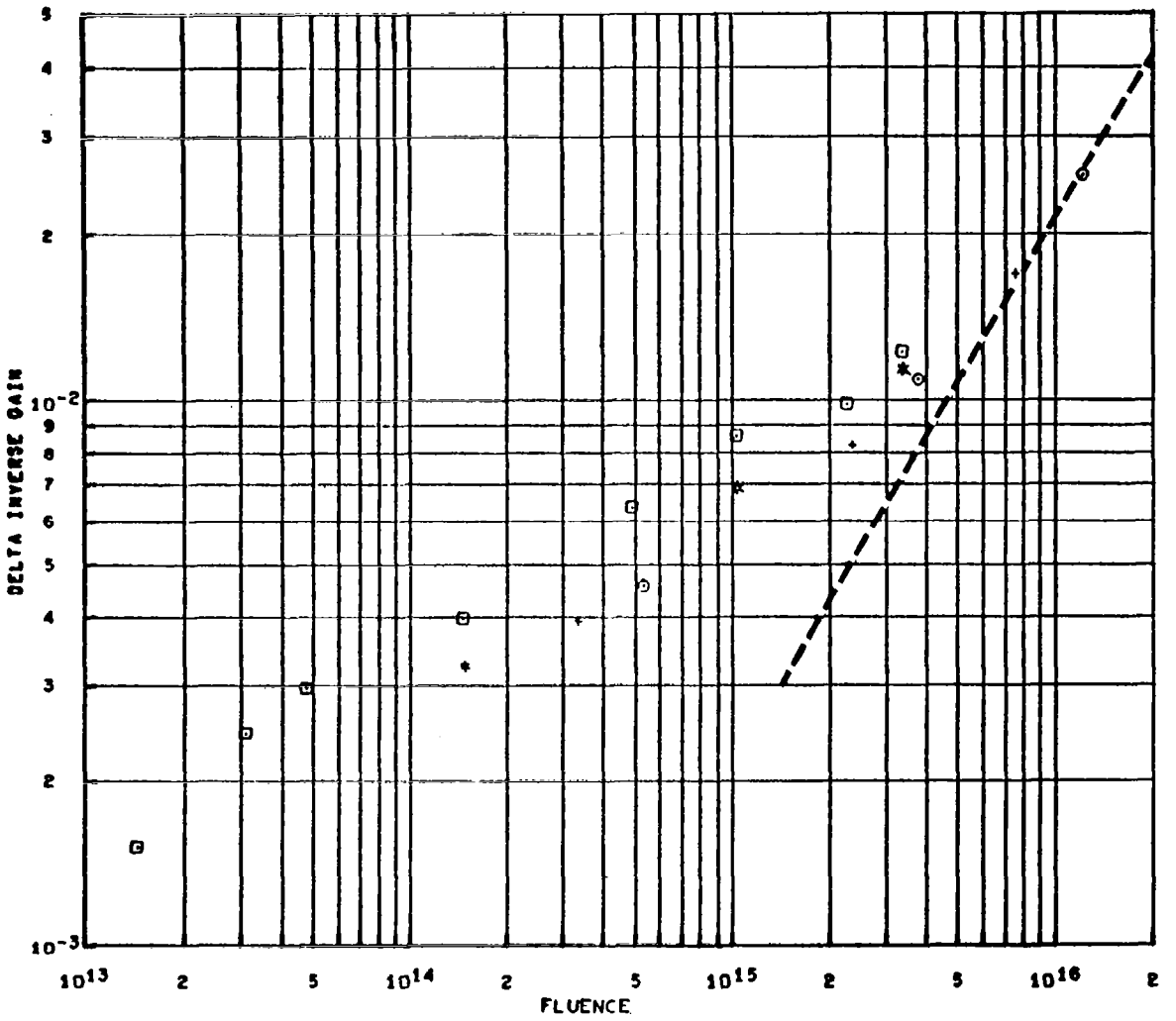

Figure 74. 2N2219 Equivalence Plot, Electron Test 22

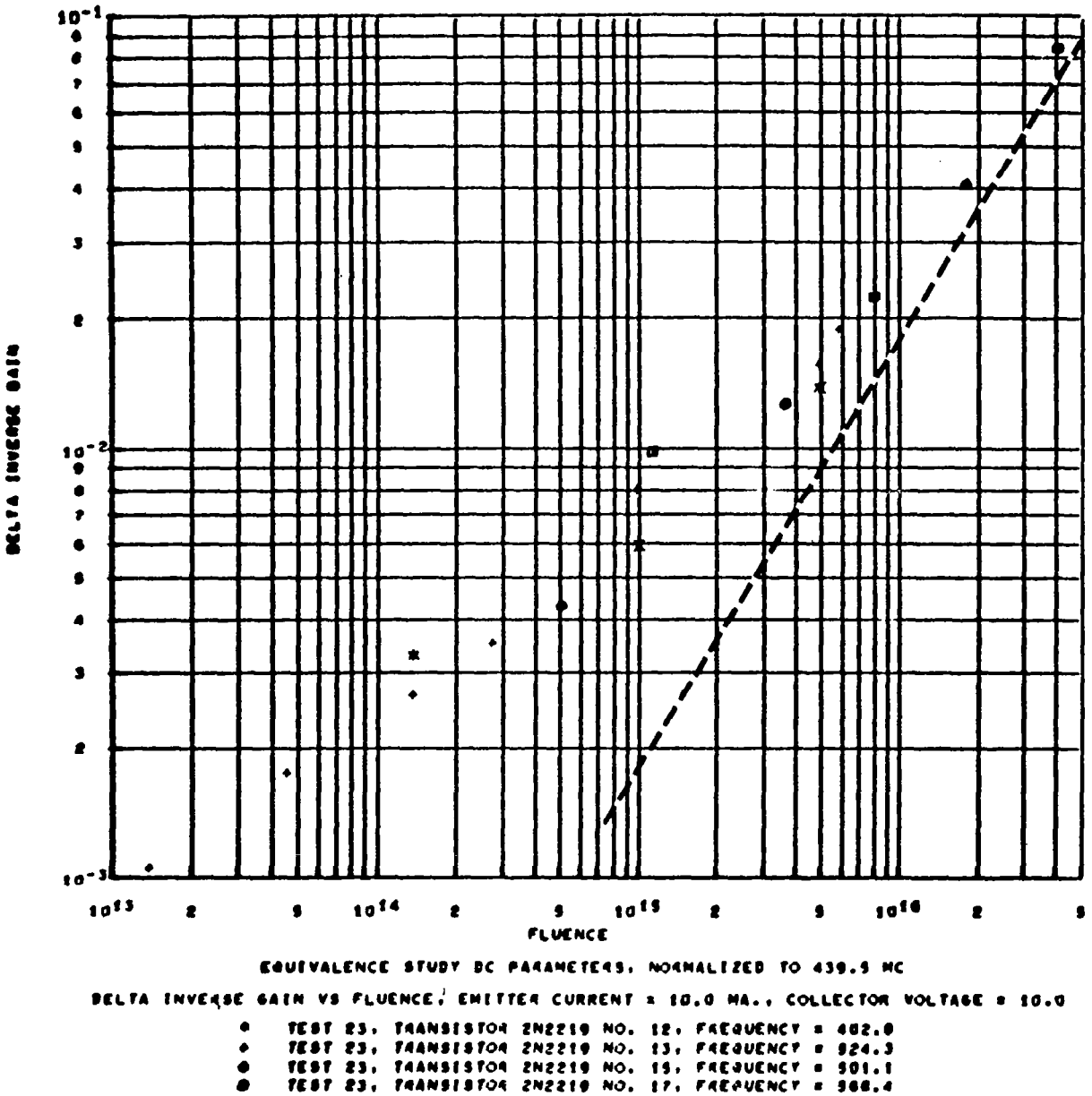

Figure 75. 2N2219 Equivalence Plot, Electron Test 23

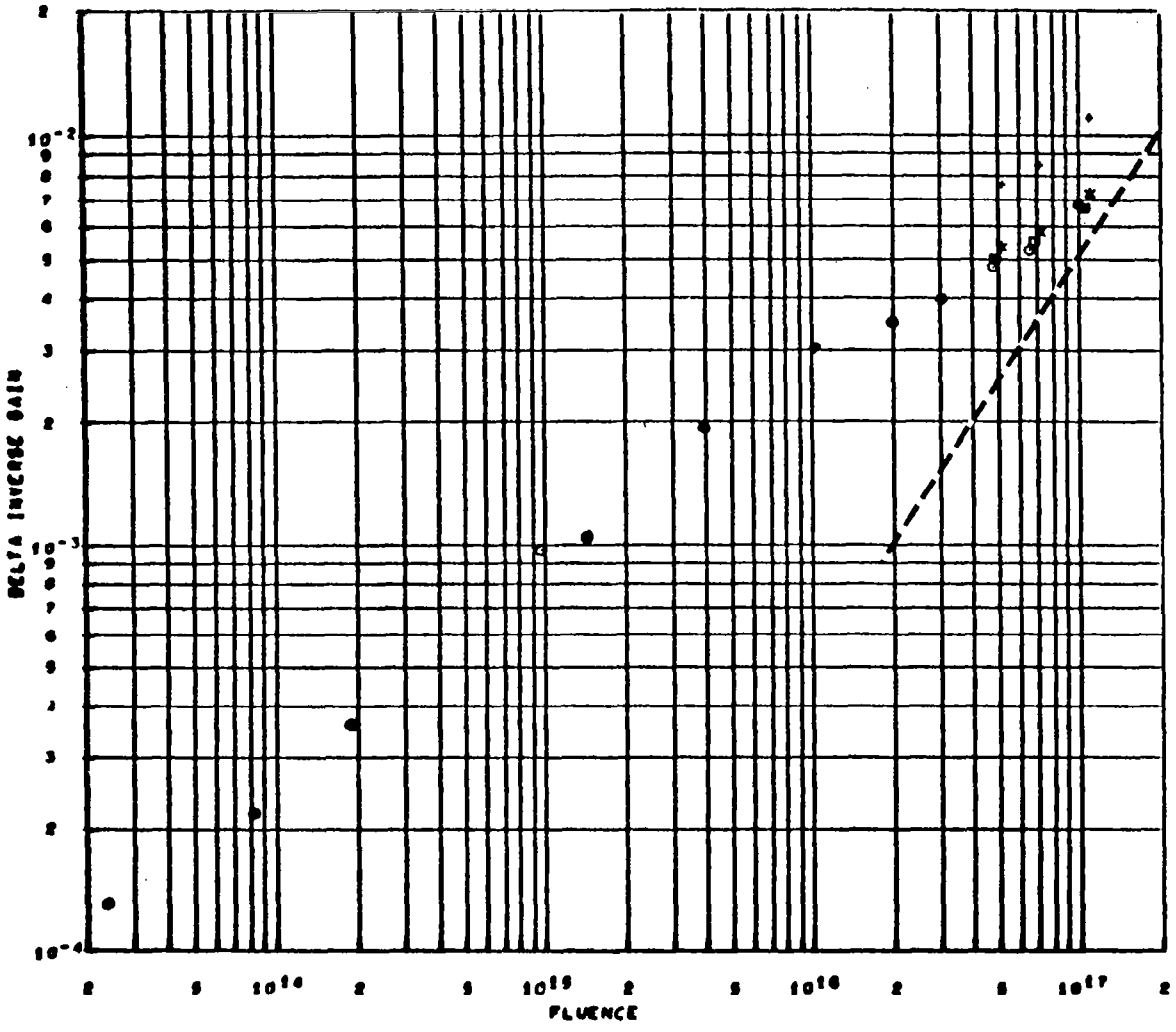

Figure 76. 2N2219 Equivalence Plot, Co^{60} Test

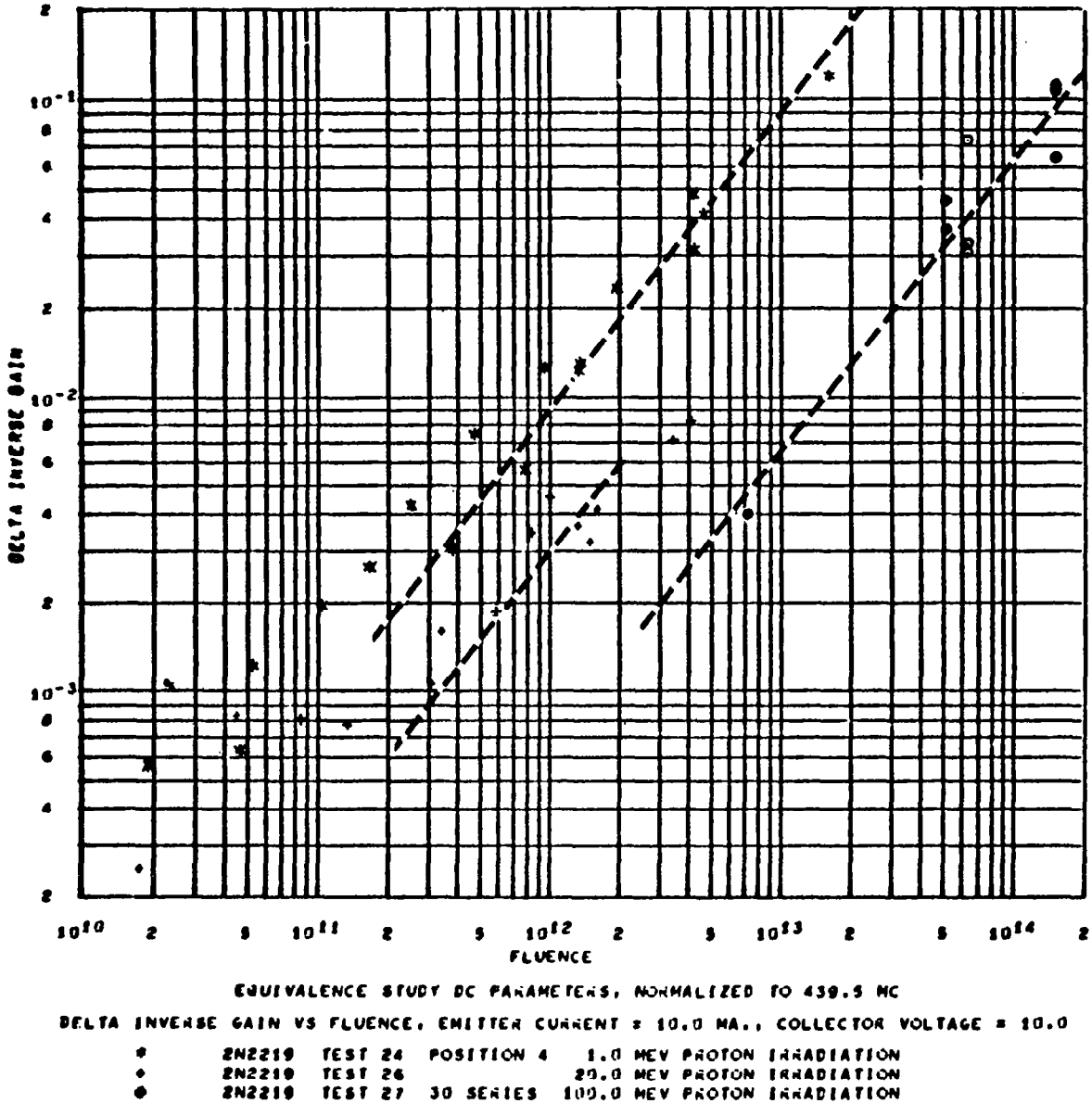

Figure 77. 2N2219 Equivalence Plot, Proton Tests

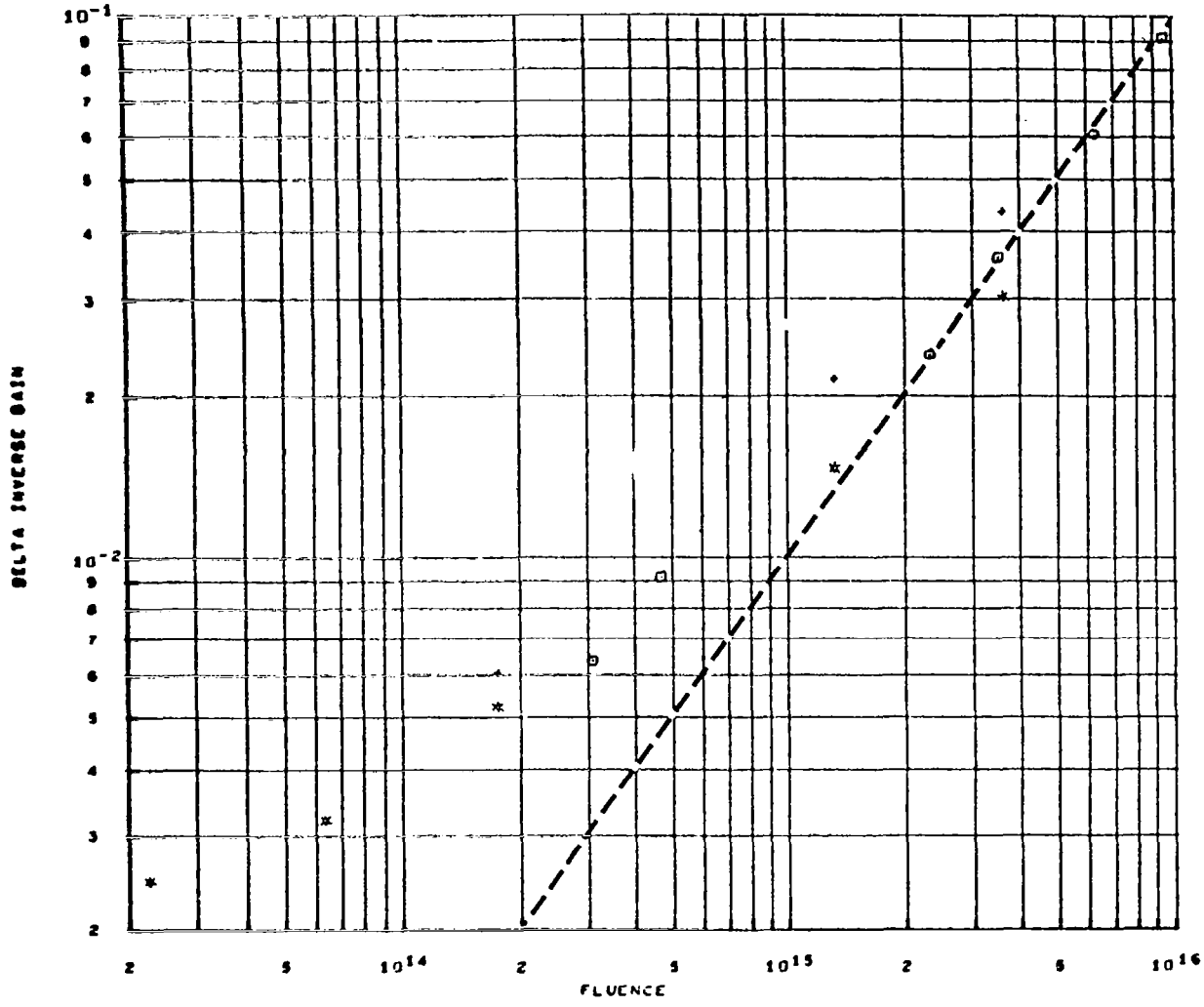

Figure 78. 2N743 Equivalence Plot, Electron Test 21

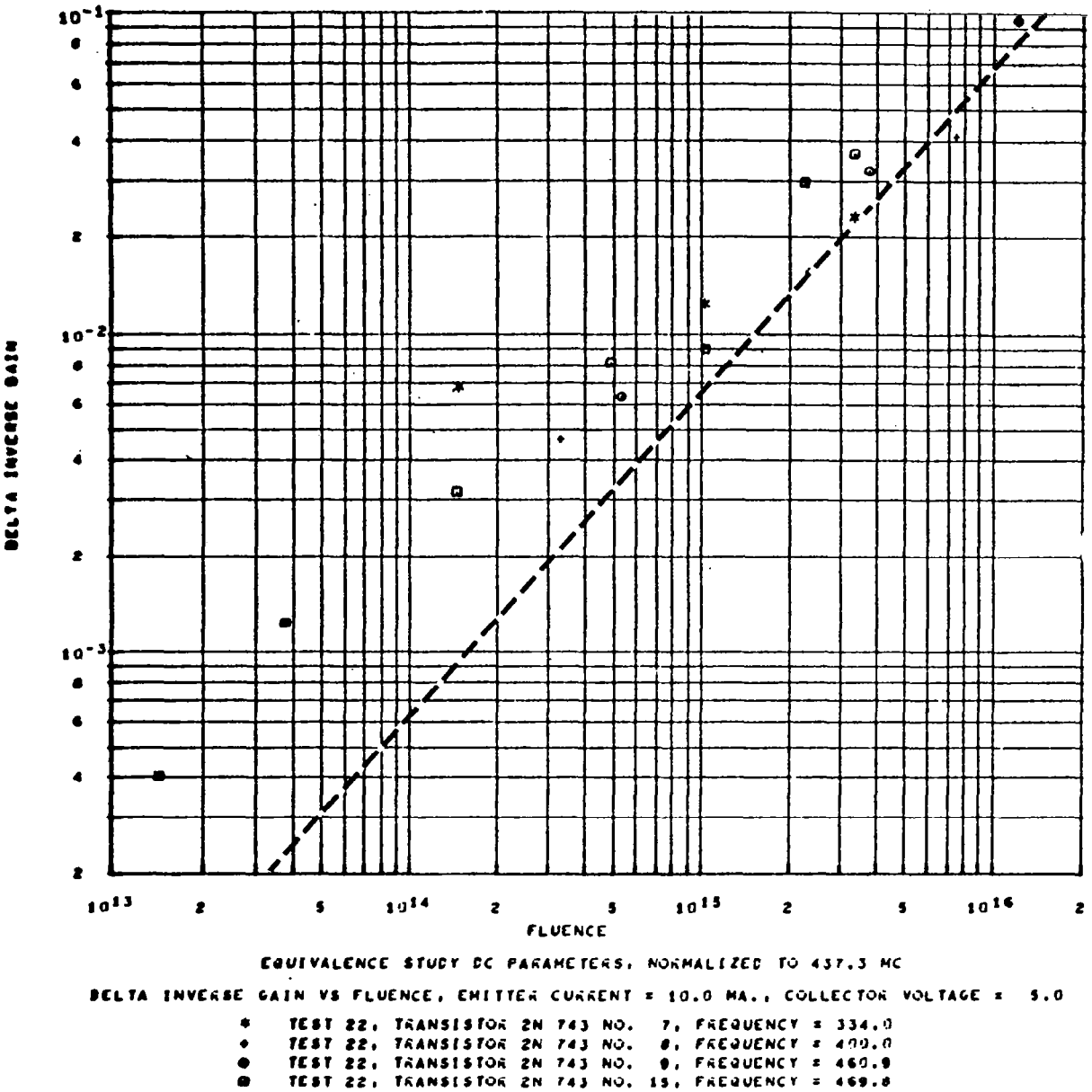

Figure 79. 2N743 Equivalence Plot, Electron Test 22

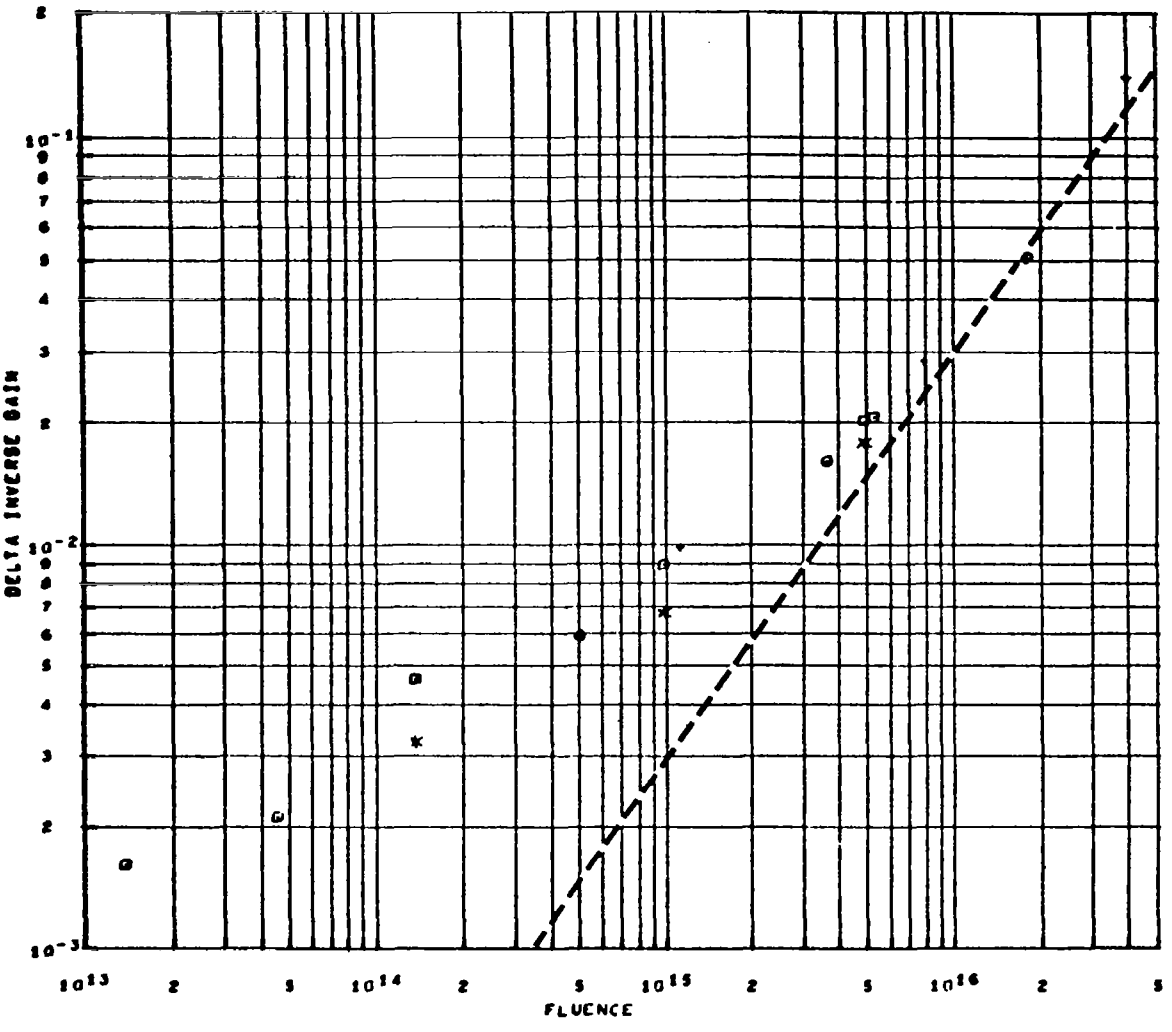

Figure 80. 2N743 Equivalence Plot, Electron Test 23

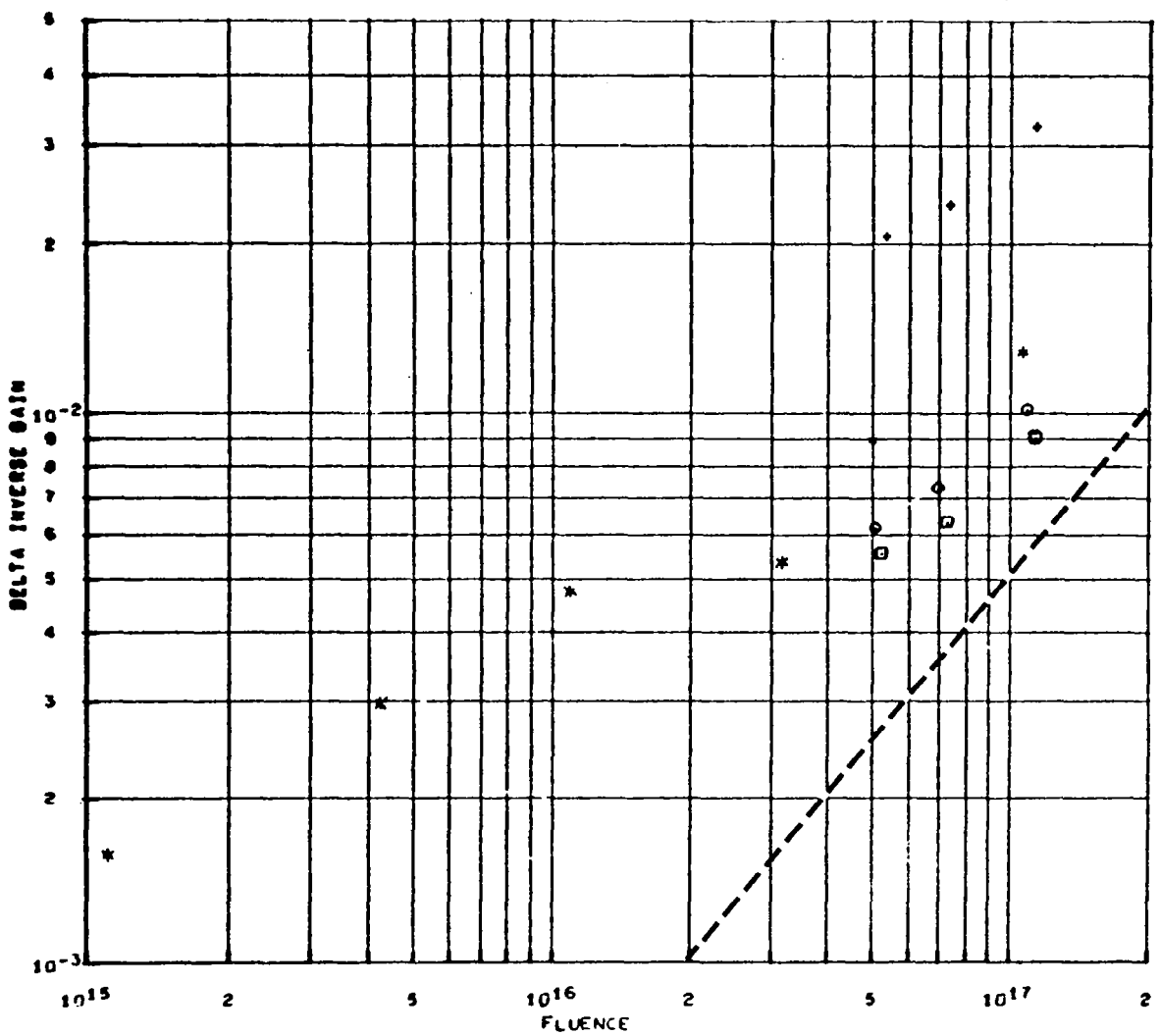

EQUIVALENCE STUDY DC PARAMETERS, NORMALIZED TO 437.3 MC

DELTA INVERSE GAIN VS FLUENCE, EMITTER CURRENT = 10.0 MA., COLLECTOR VOLTAGE = 5.0

* TEST 25, TRANSISTOR 2N 743 NO. 20, FREQUENCY = 611.3
♦ TEST 25, TRANSISTOR 2N 743 NO. 21, FREQUENCY = 702.6
G TEST 25, TRANSISTOR 2N 743 NO. 22, FREQUENCY = 249.2
D TEST 25, TRANSISTOR 2N 743 NO. 23, FREQUENCY = 615.2

Figure 81. 2N743 Equivalence Plot, Co^{60} Test

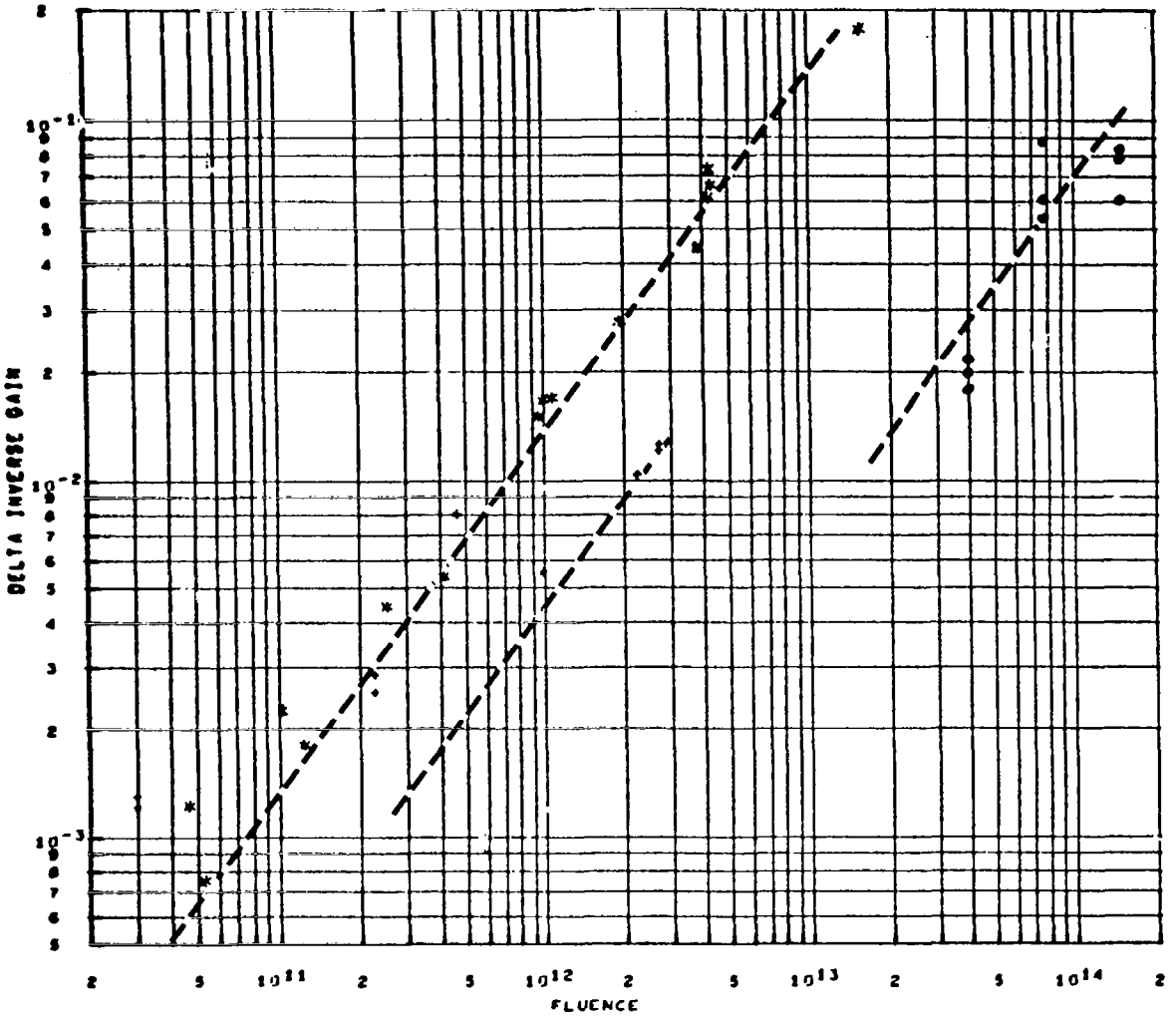

Figure 82. 2N743 Equivalence Plot, Proton Tests

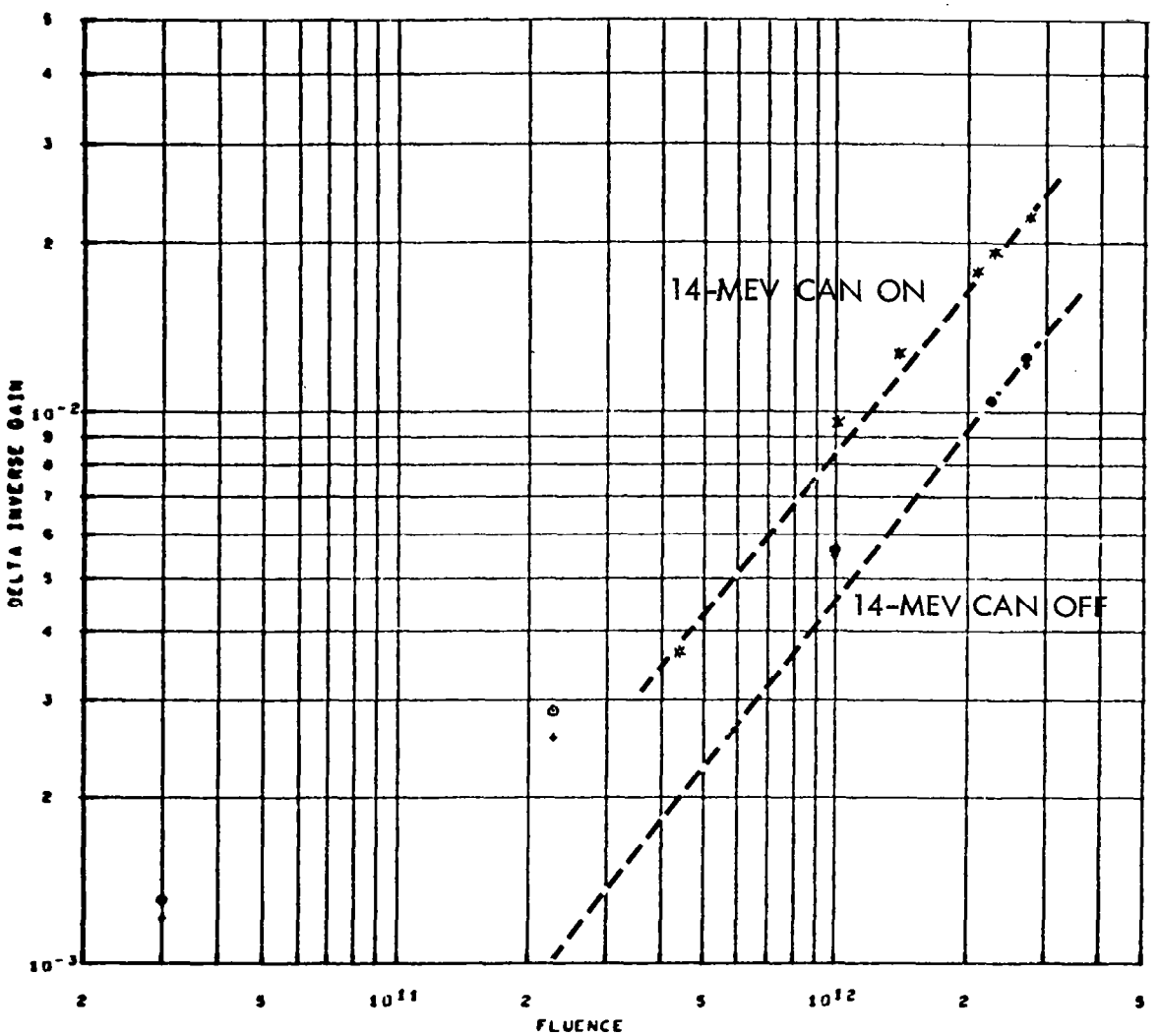

Figure 83. 2N743 Equivalence Plot, Proton Test 26

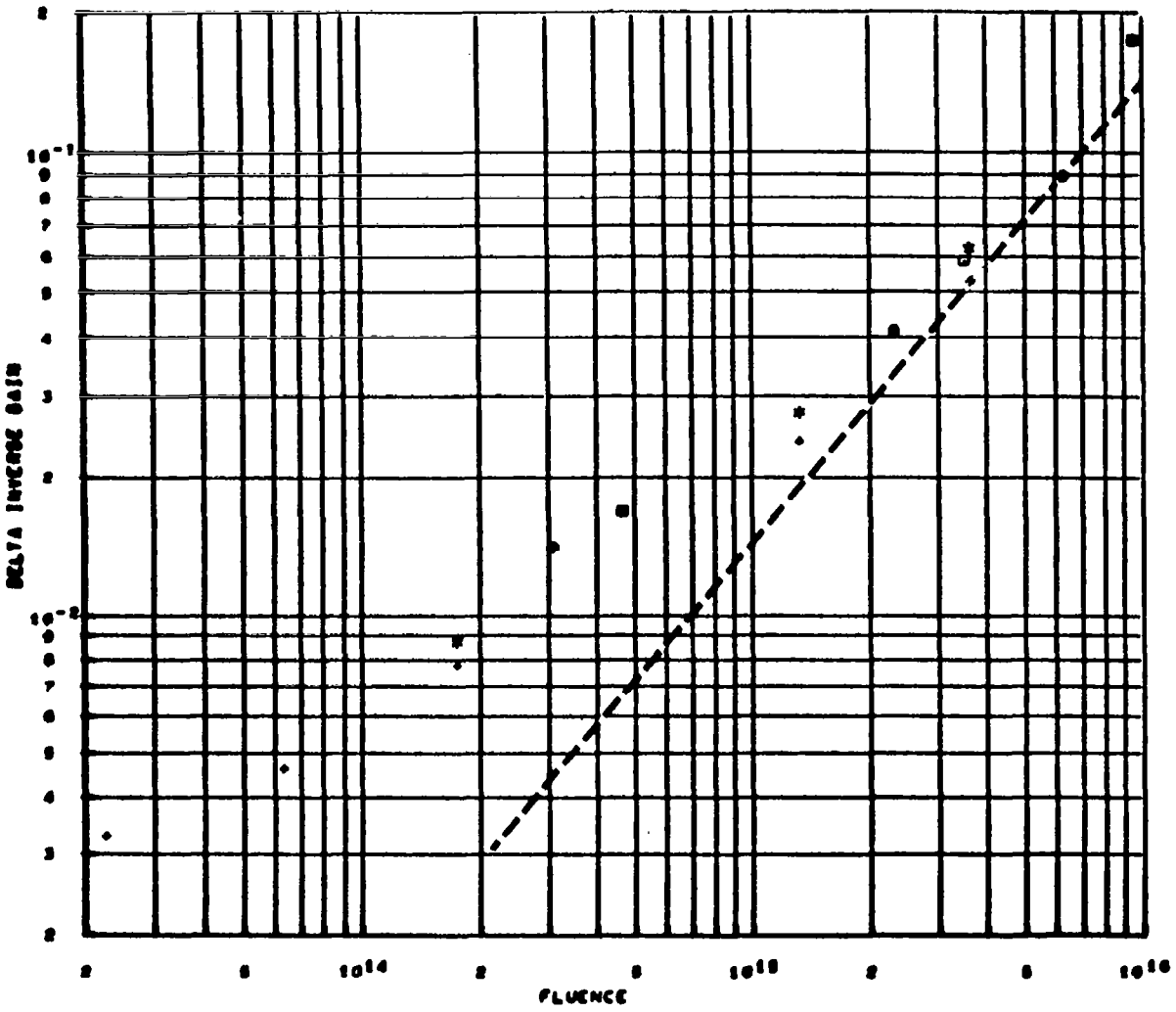

Figure 84. 2N834 Equivalence Plot, Electron Test 21

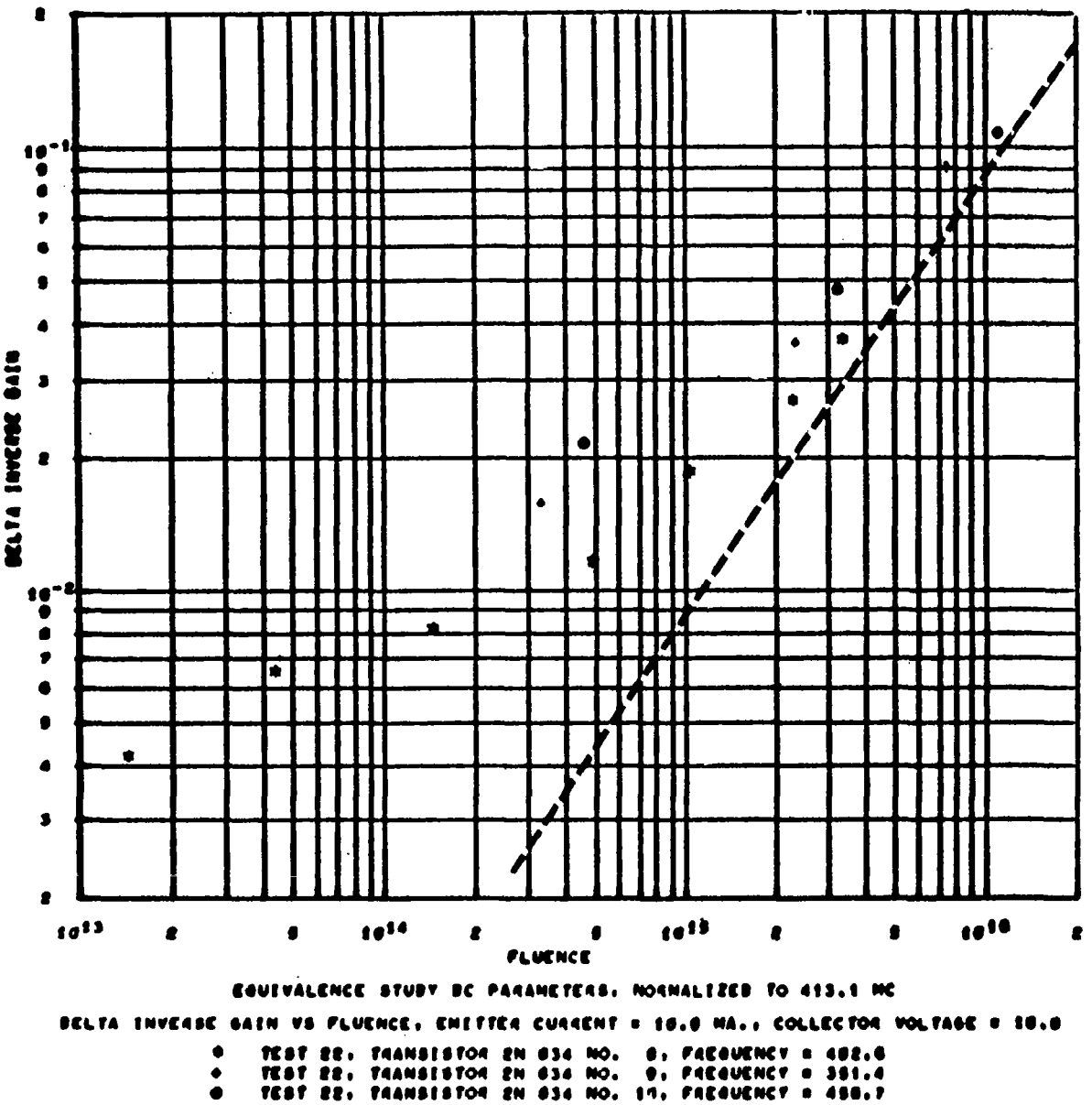

Figure 85. 2N834 Equivalence Plot, Electron Test 22

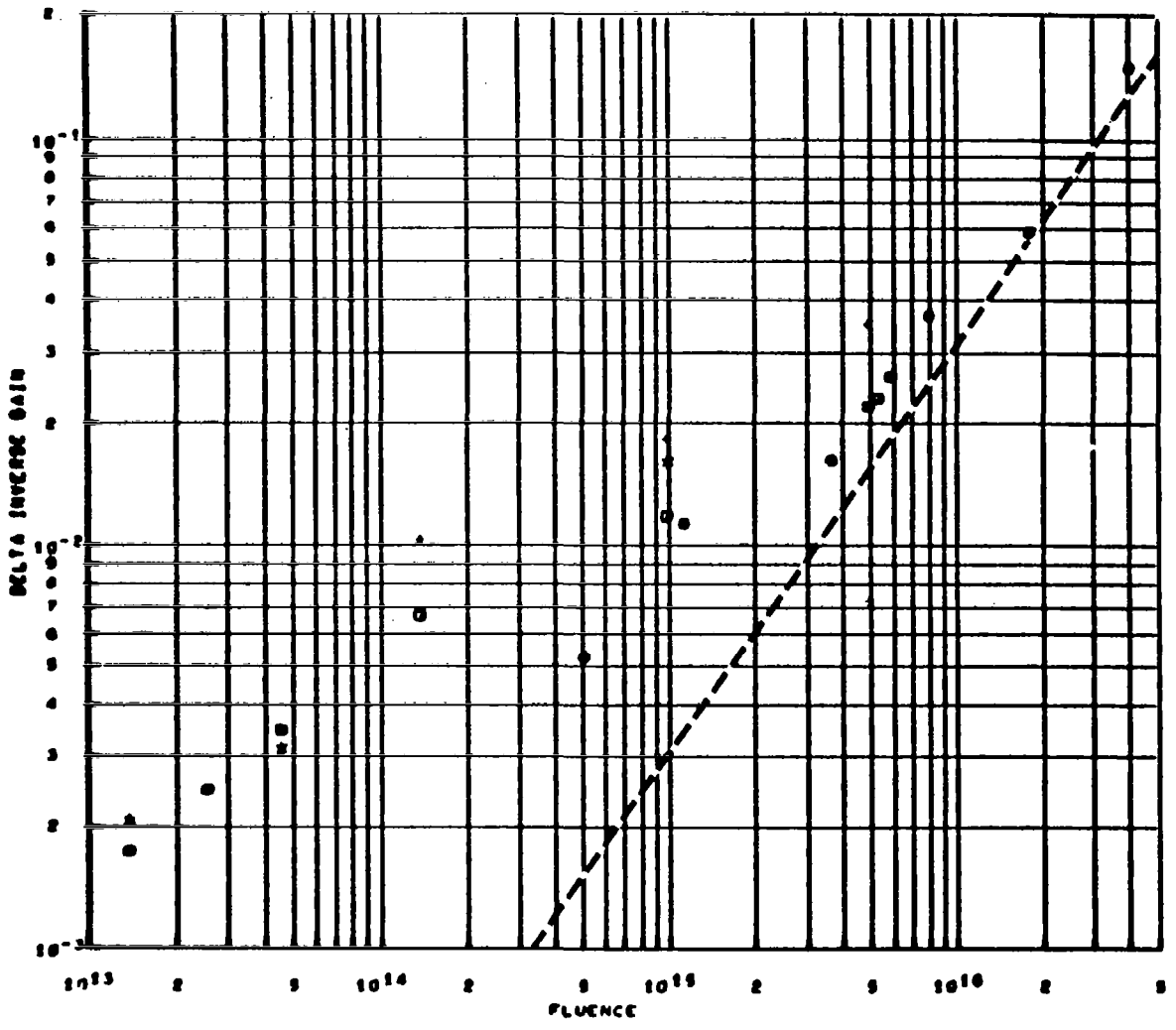

Figure 86. 2N834 Equivalence Plot, Electron Test 23

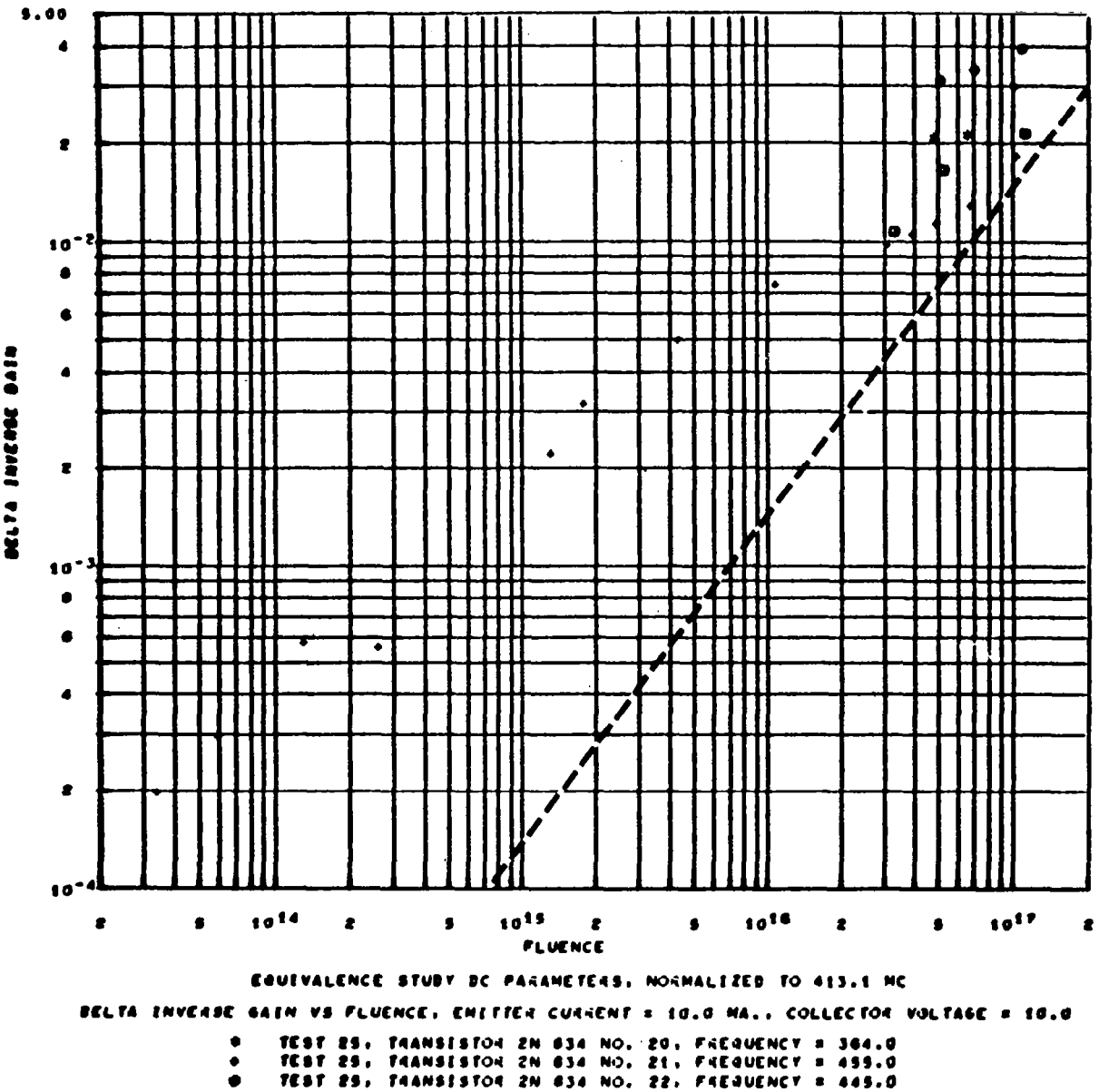

Figure 87. 2N834 Equivalence Plot, Co^{60} Test

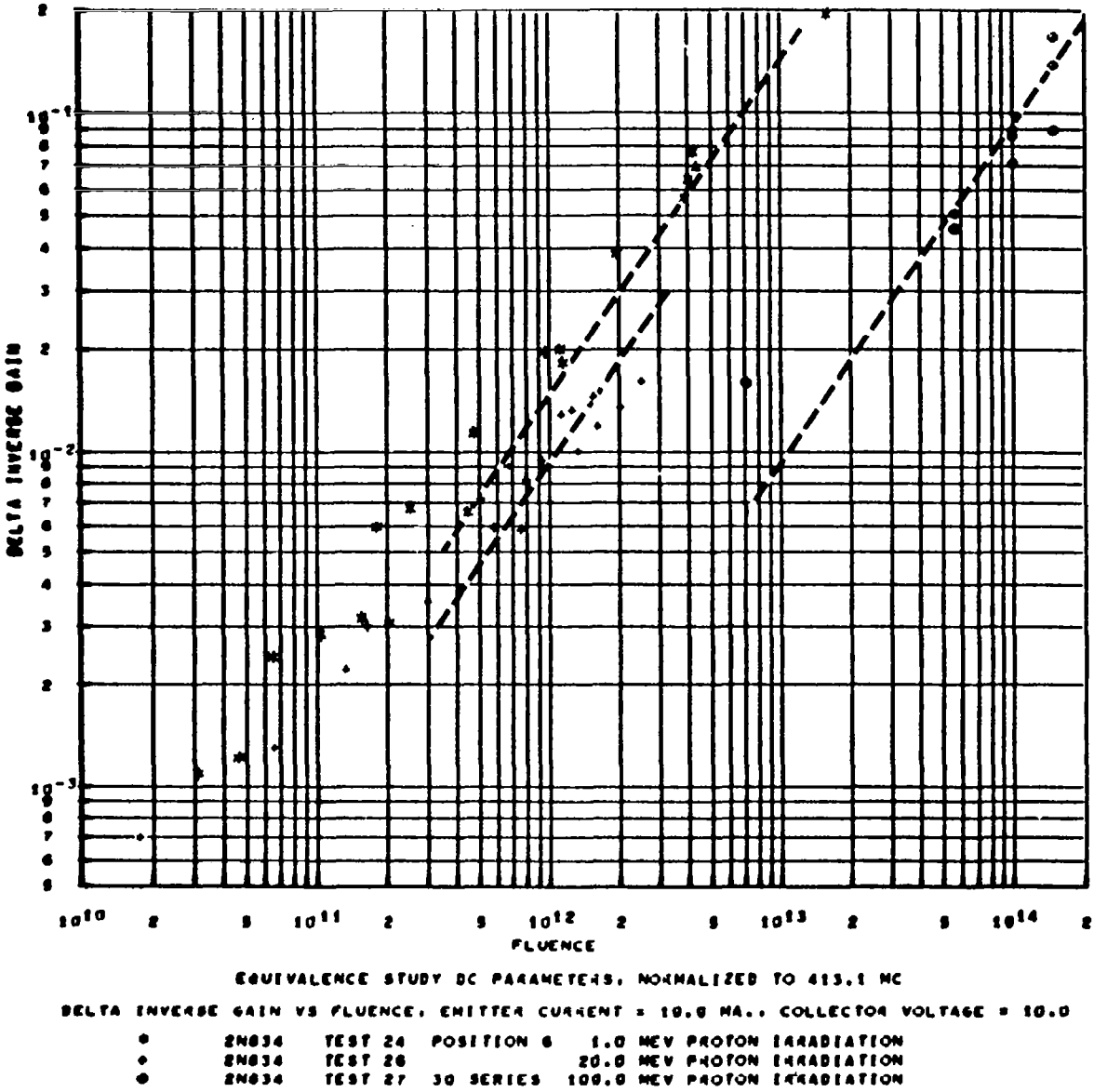

Figure 88. 2N834 Equivalence Plot, Proton Tests

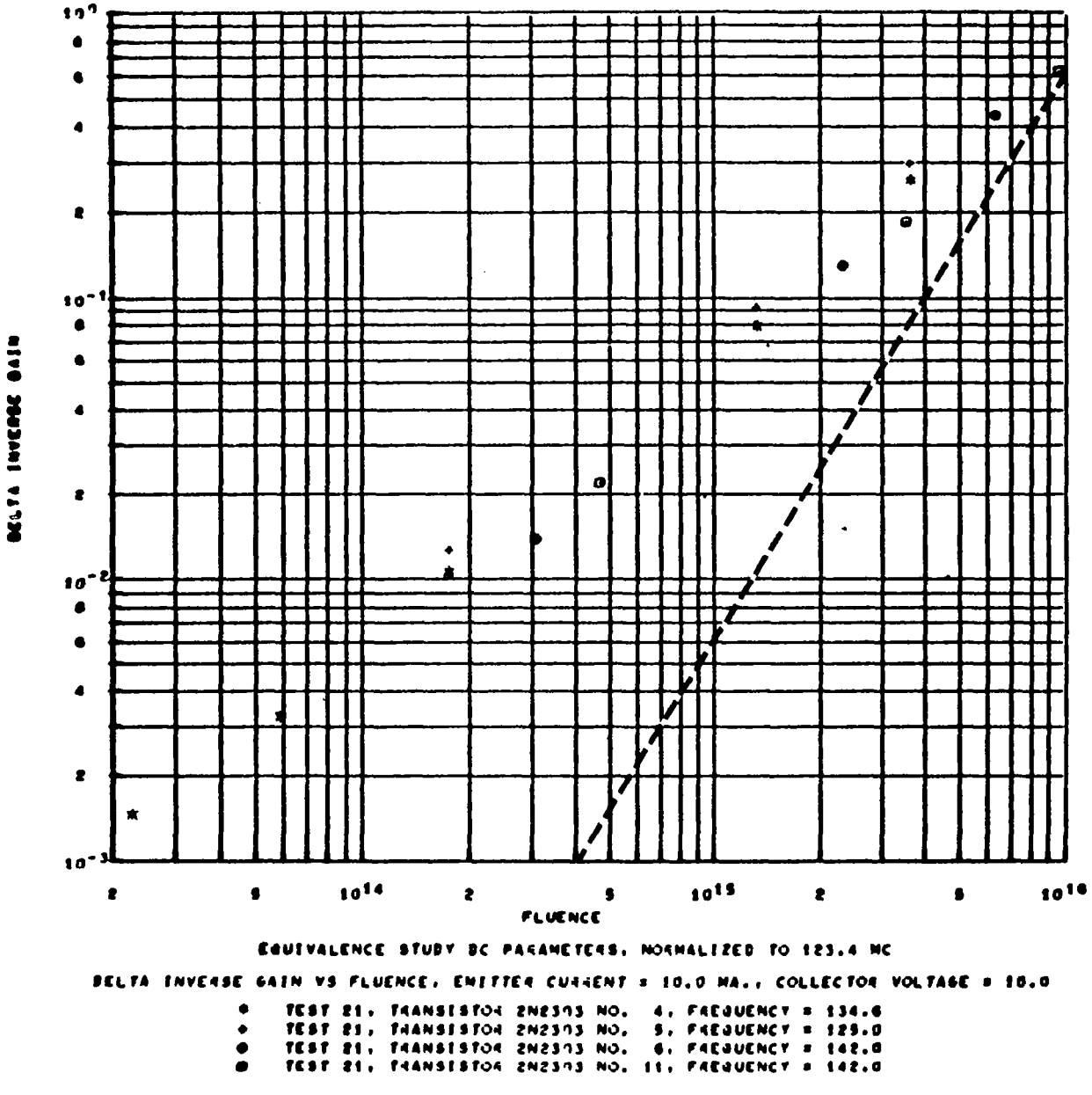

Figure 89. 2N2303 Equivalence Plot, Electron Test 21

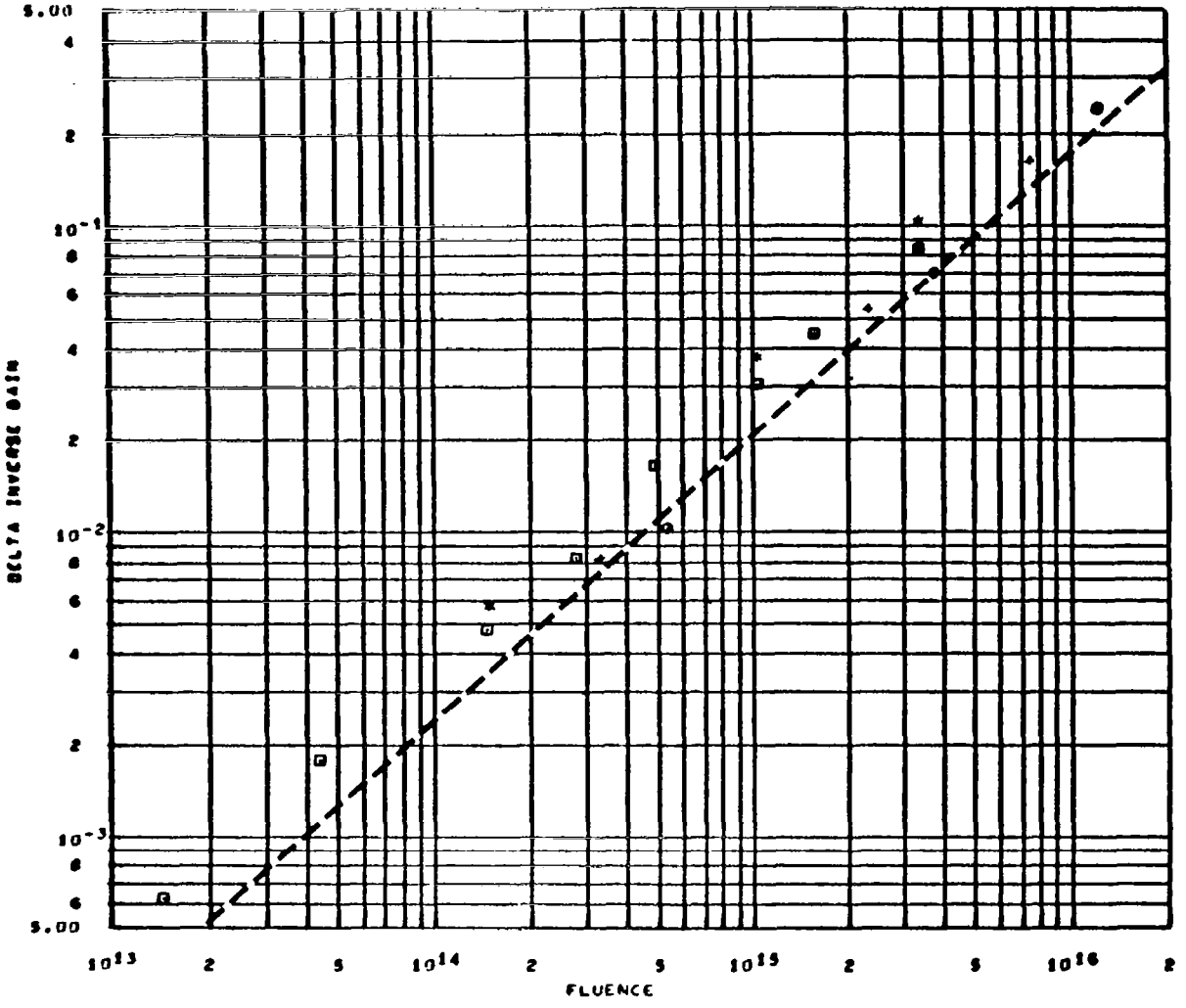

Figure 90. 2N2303 Equivalence Plot, Electron Test 22

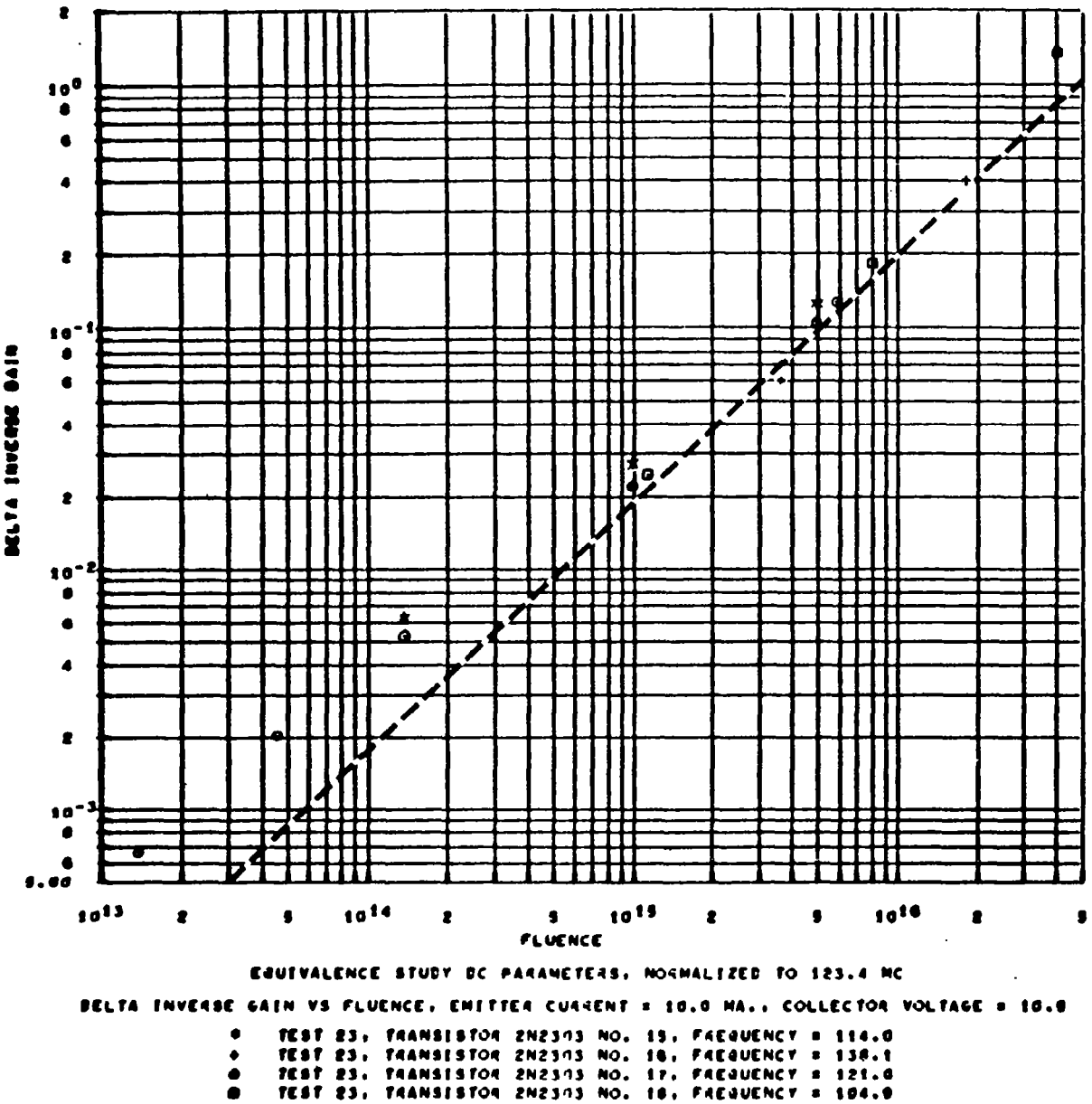

Figure 91. 2N2303 Equivalence Plot, Electron Test 23

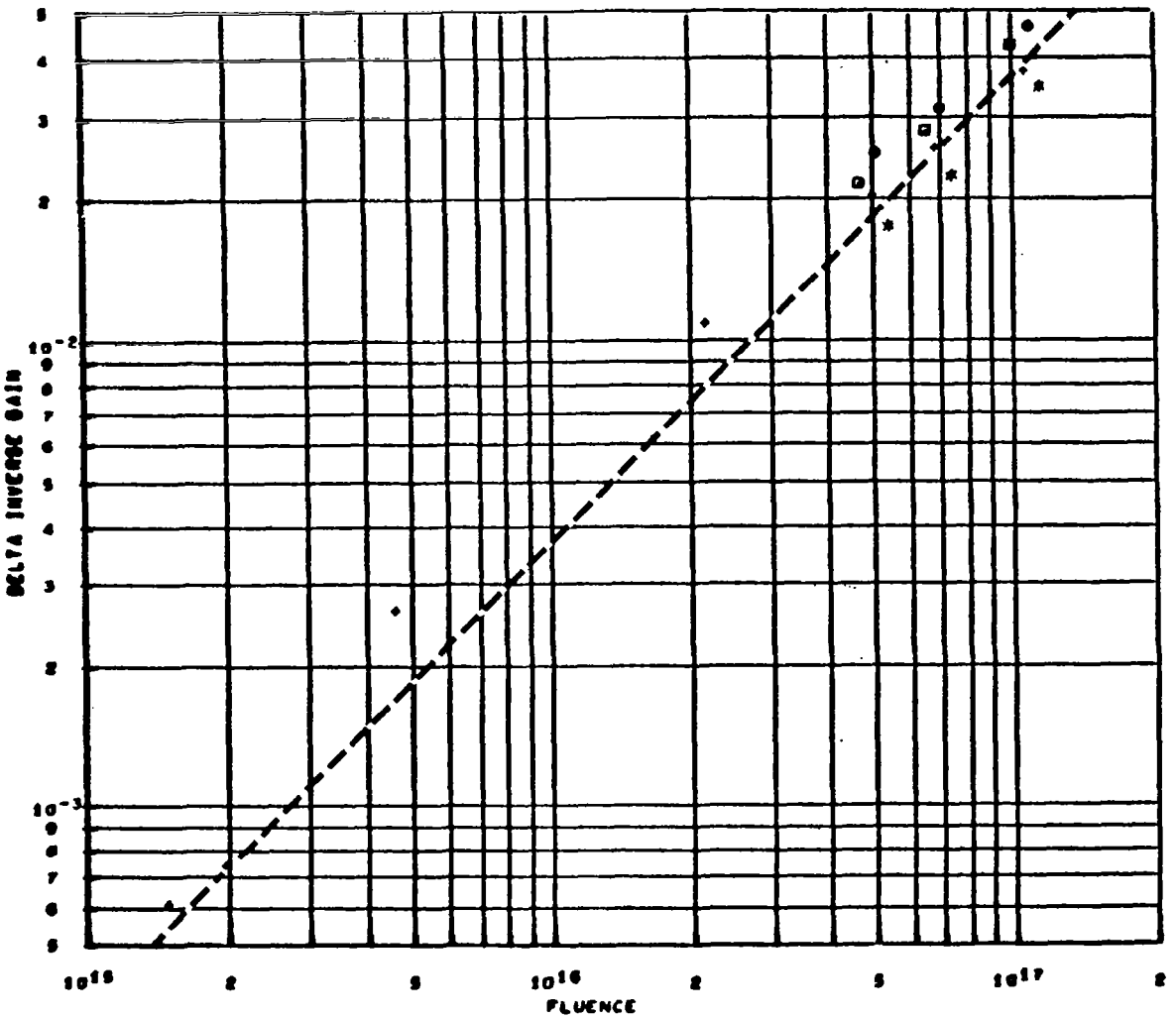

Figure 92. 2N2303 Equivalence Plot, Co^{60} Test

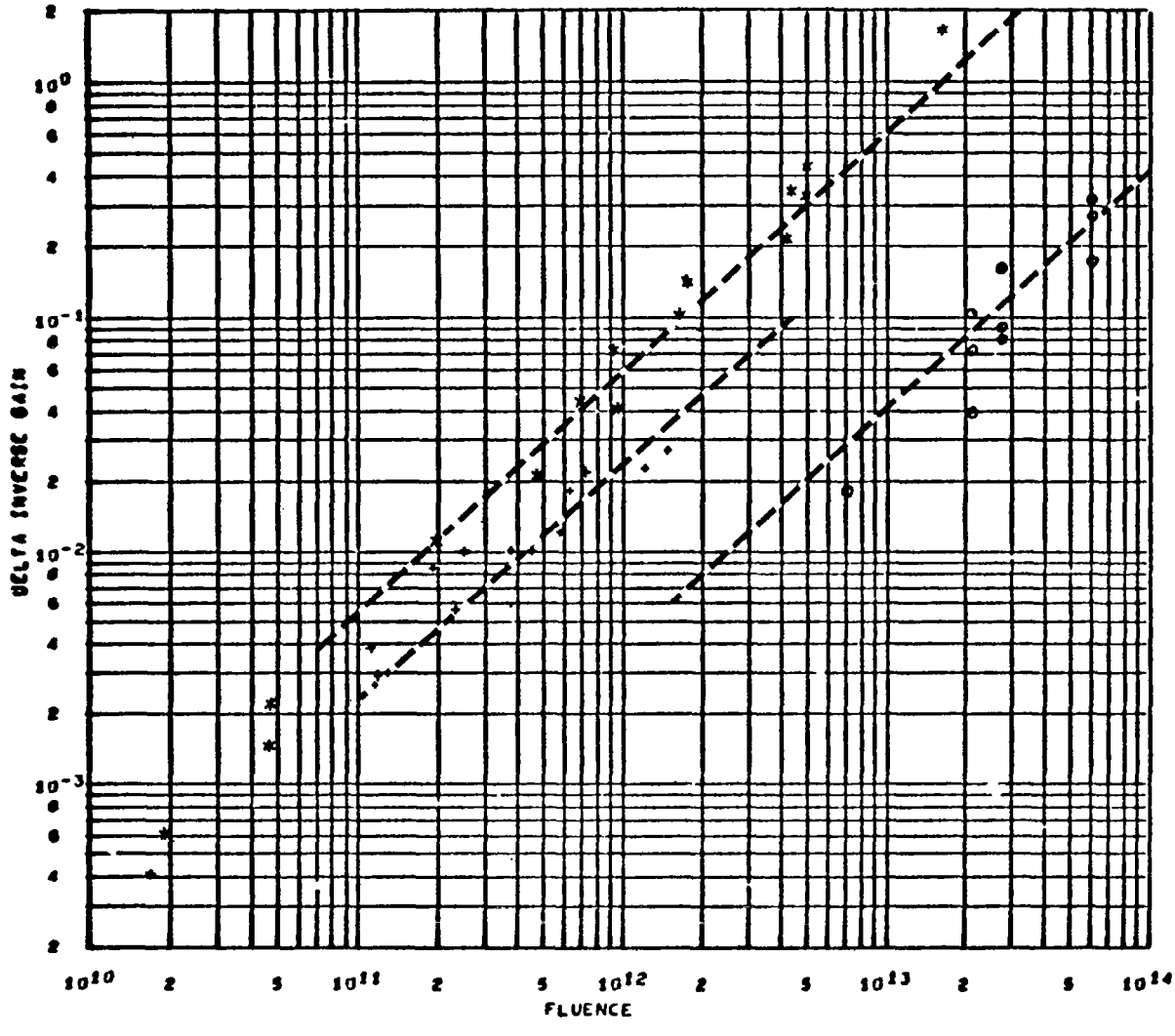

Figure 93. 2N2303 Equivalence Plot, Proton Tests

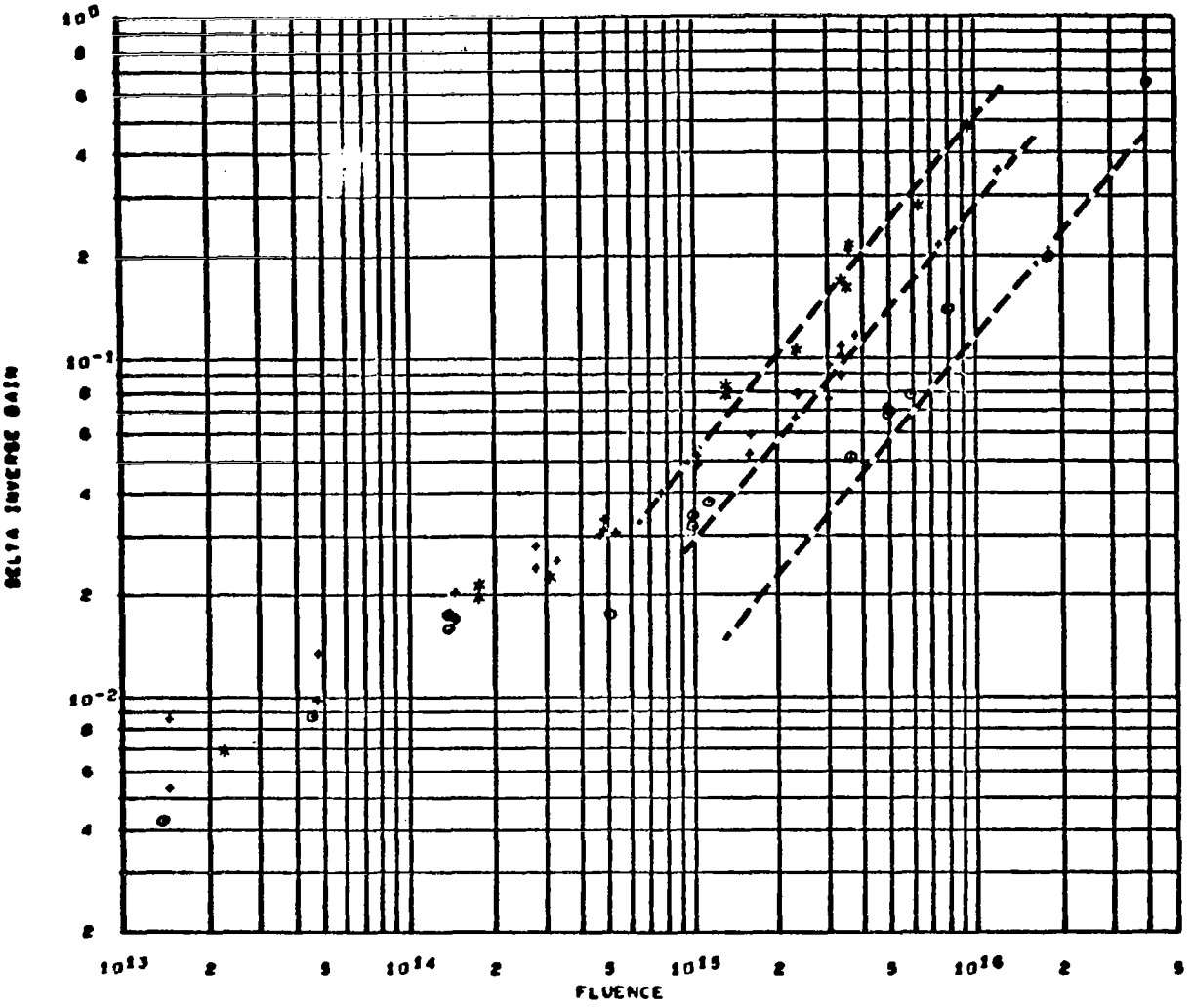

Figure 94. 2N1132 Equivalence Plot, Electron Tests

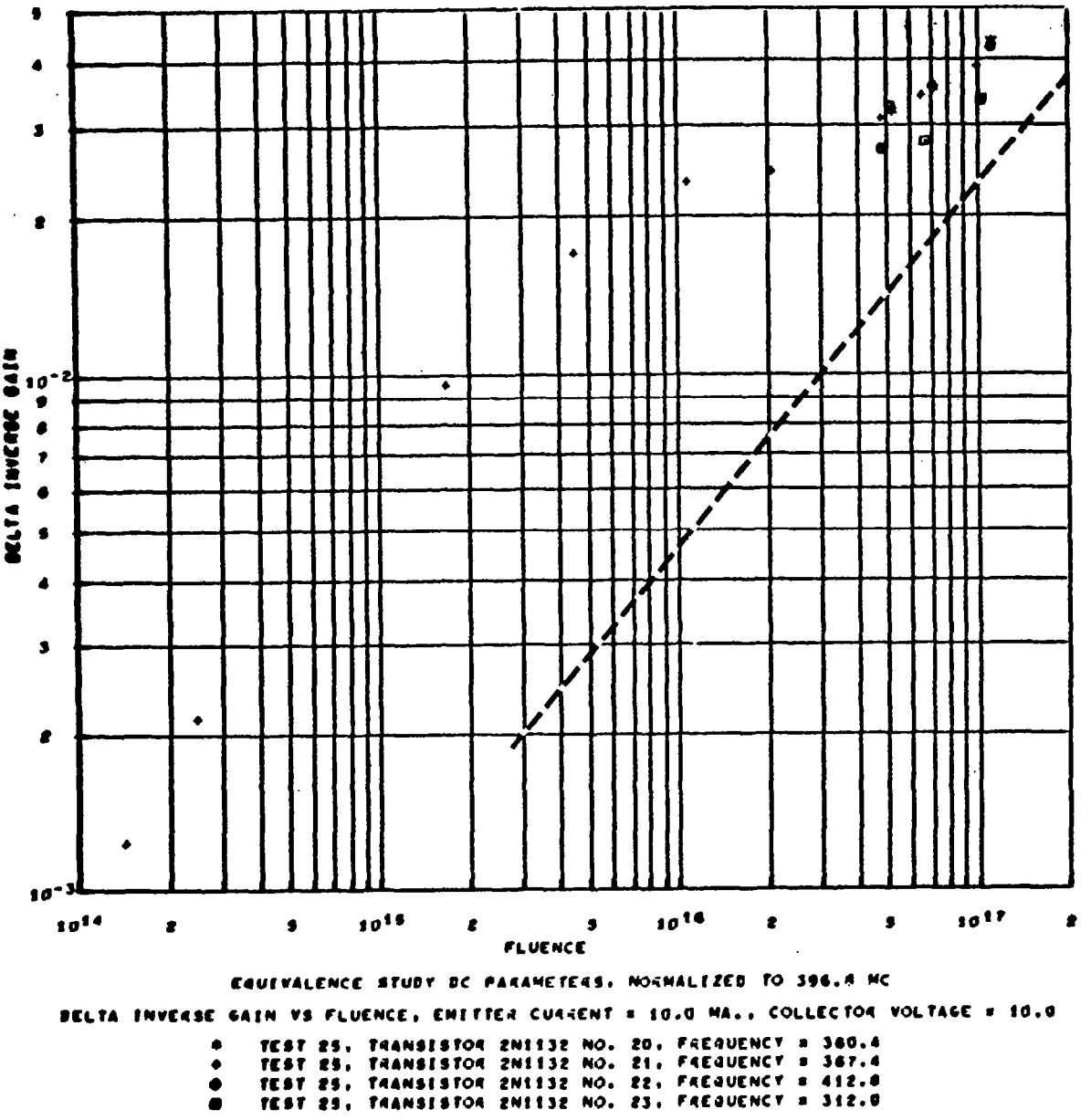

Figure 95. 2N1132 Equivalence Plot, Co^{60} Test

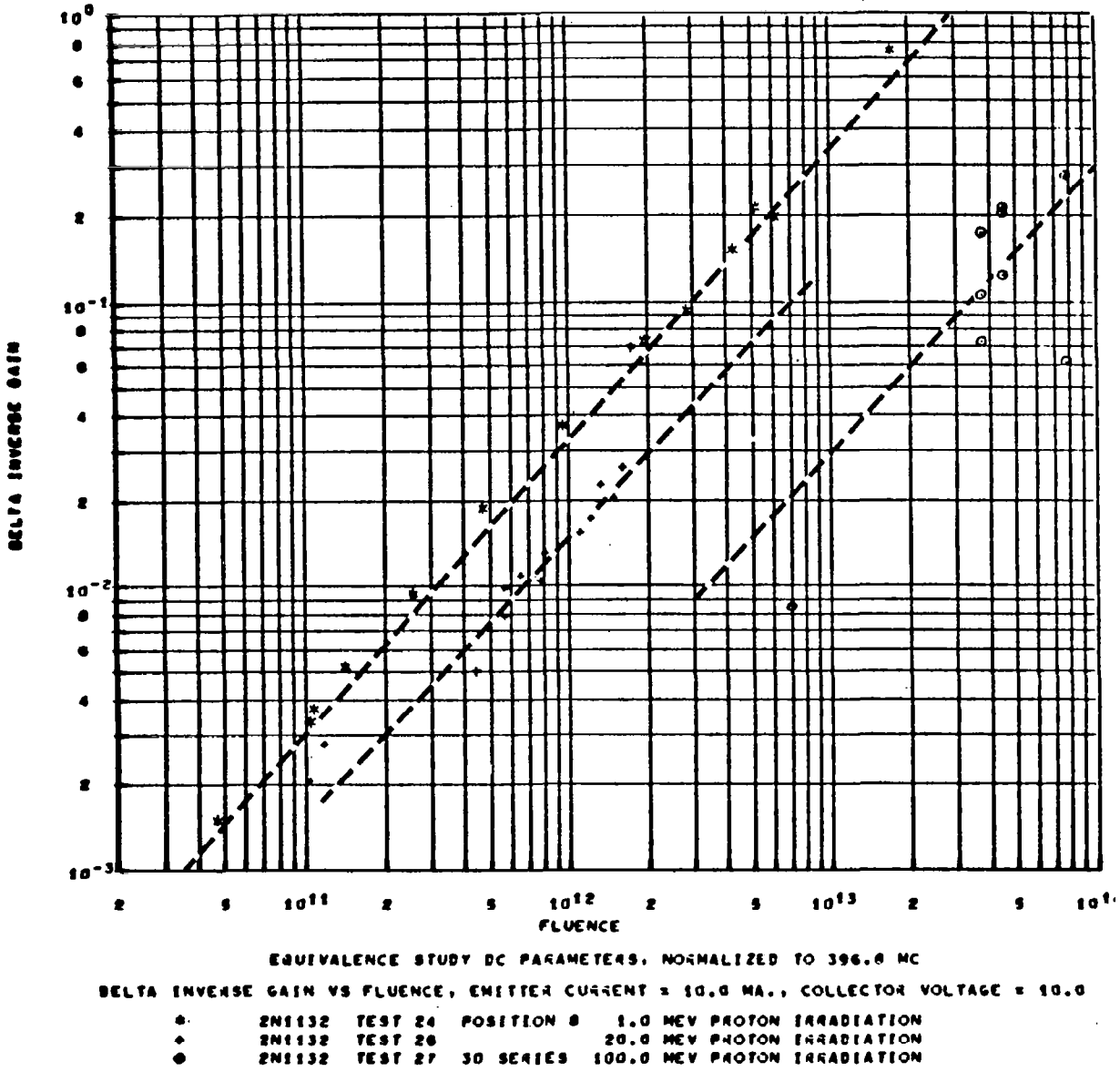

Figure 96. 2N1132 Equivalence Plot, Proton Tests

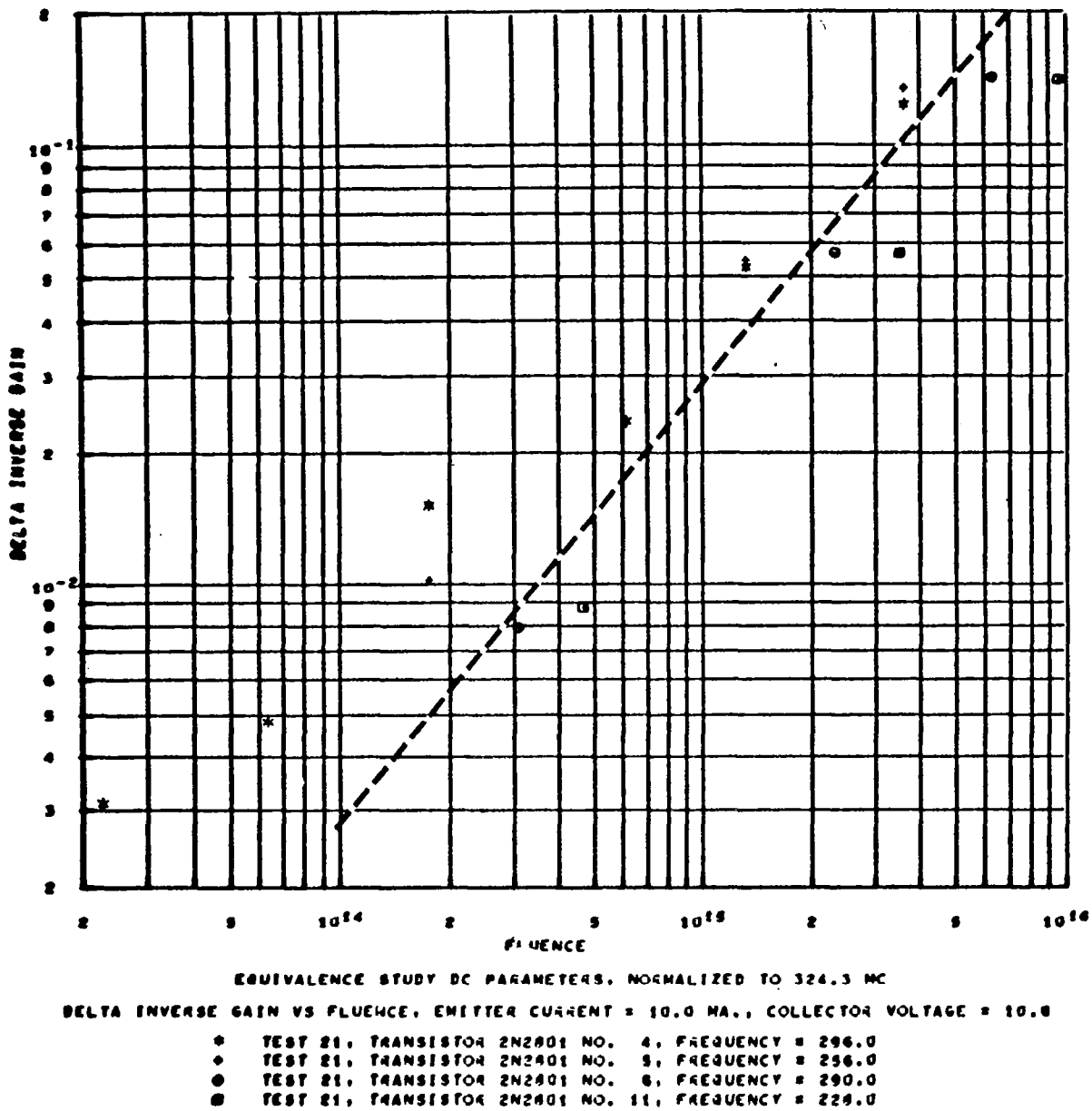

Figure 97. 2N2801 Equivalence Plot, Electron Test 21

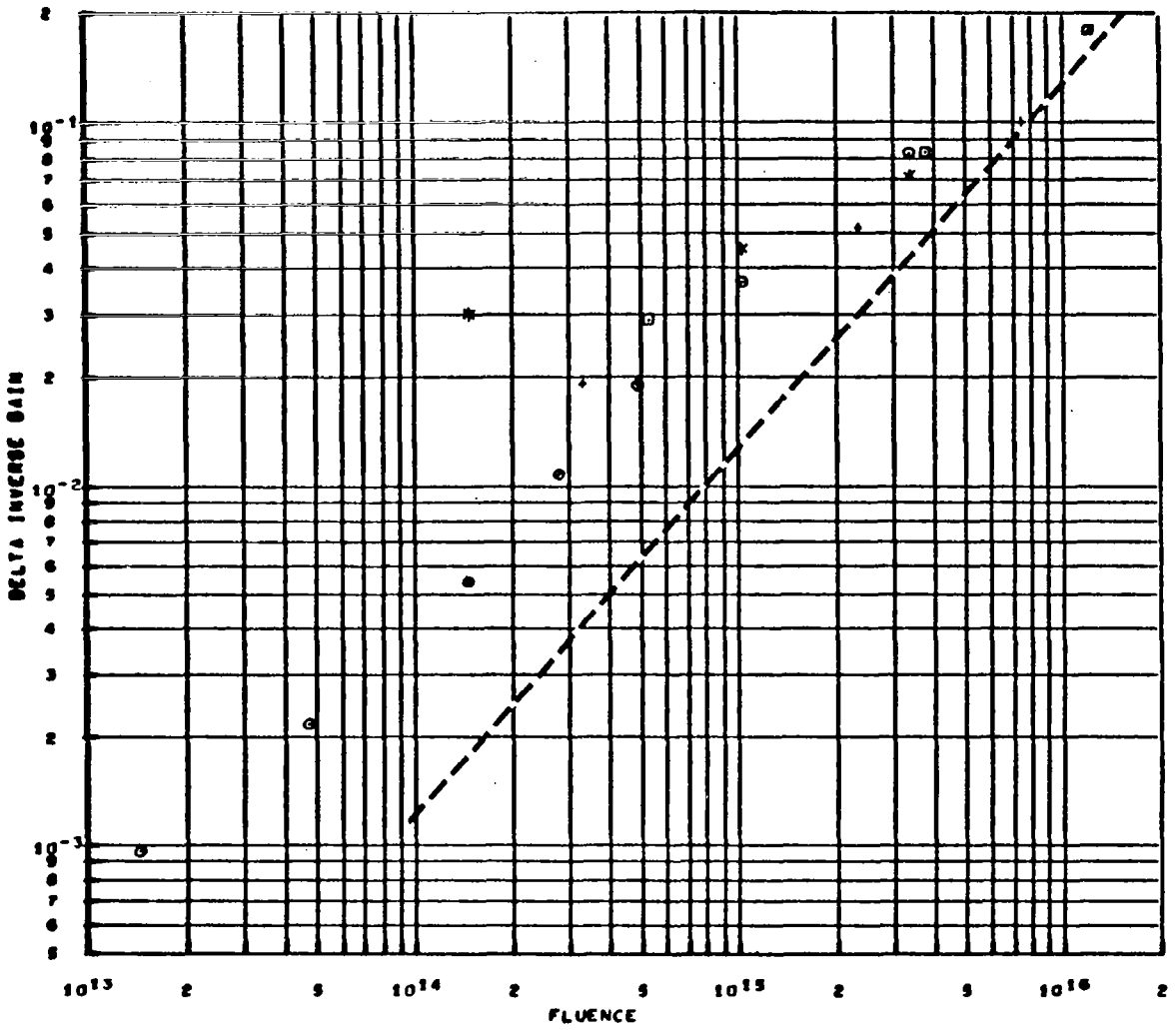

Figure 98. 2N2801 Equivalence Plot, Electron Test 22

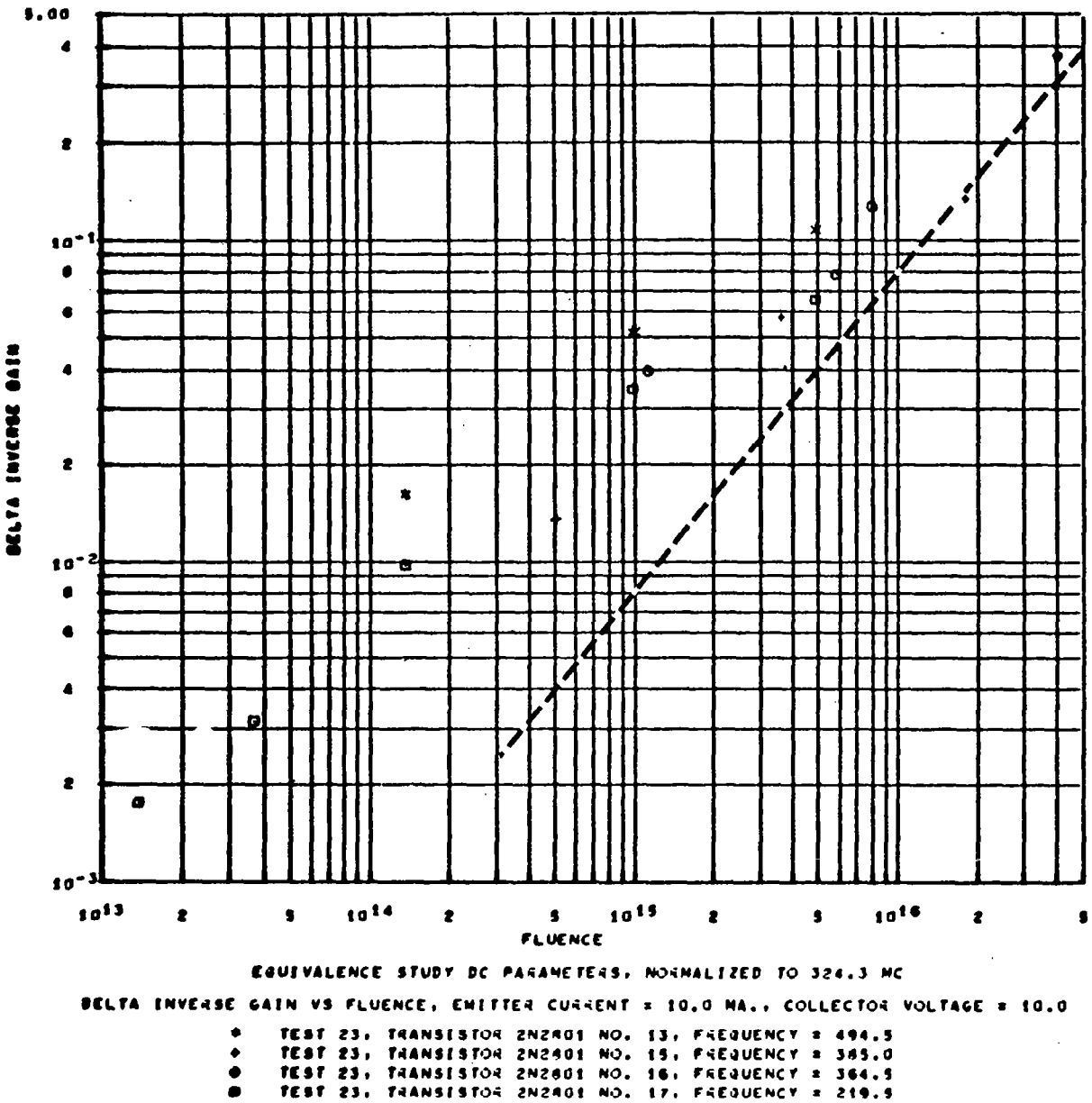

Figure 99. 2N2801 Equivalence Plot, Electron Test 23

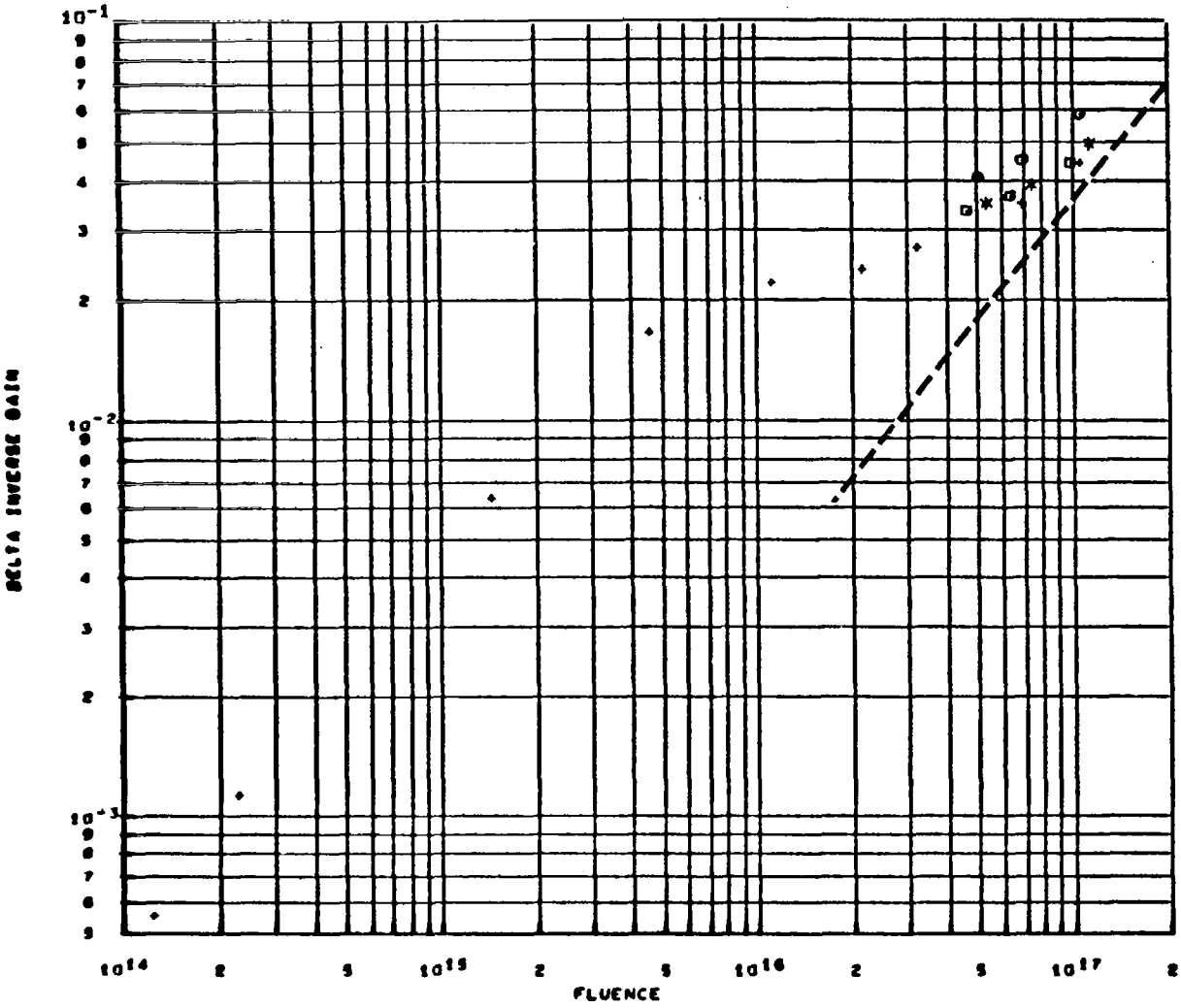

Figure 100. 2N2801 Equivalence Plot, Co^{60} Test

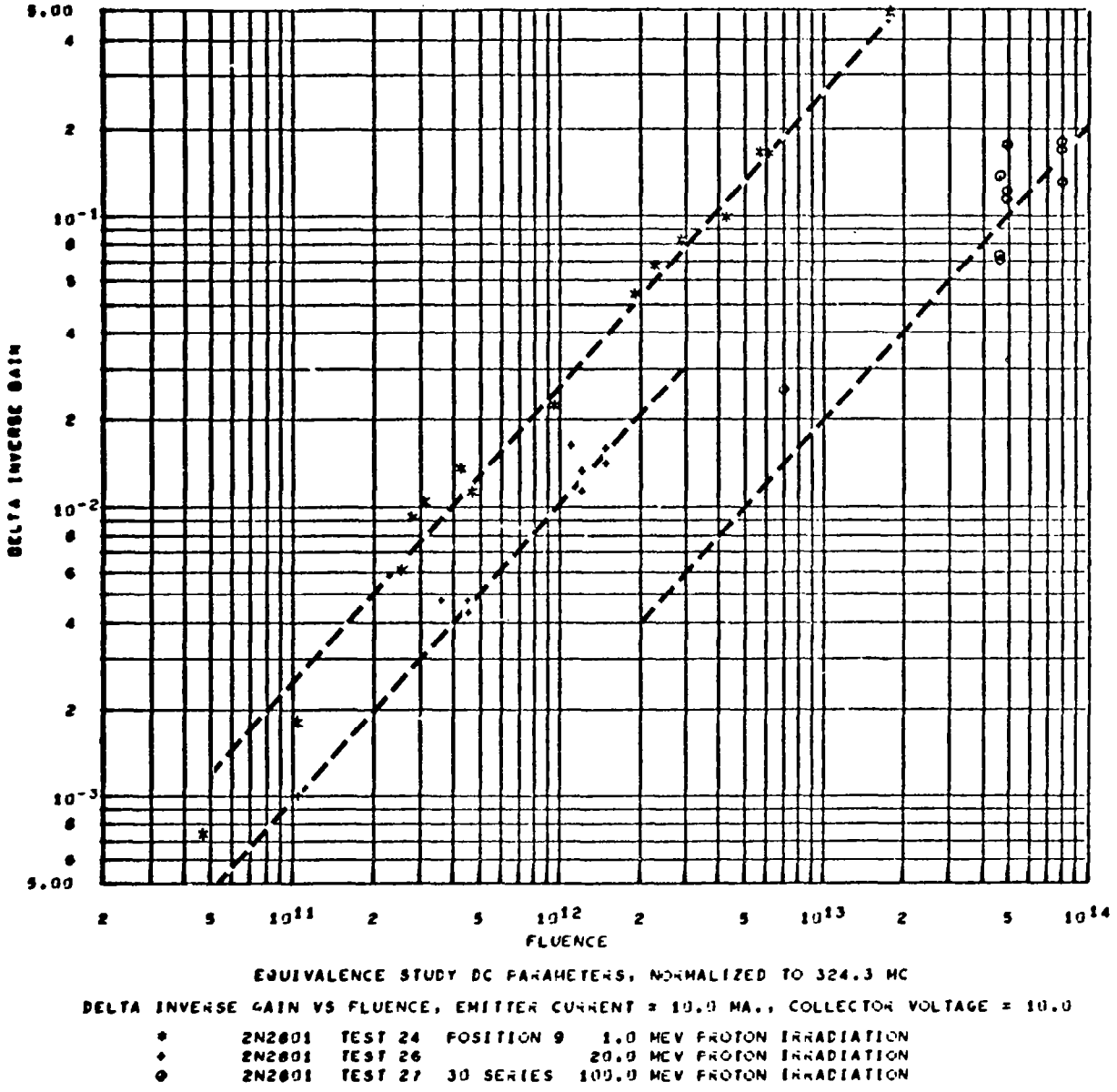

Figure 101. 2N2801 Equivalence Plot, Proton Tests

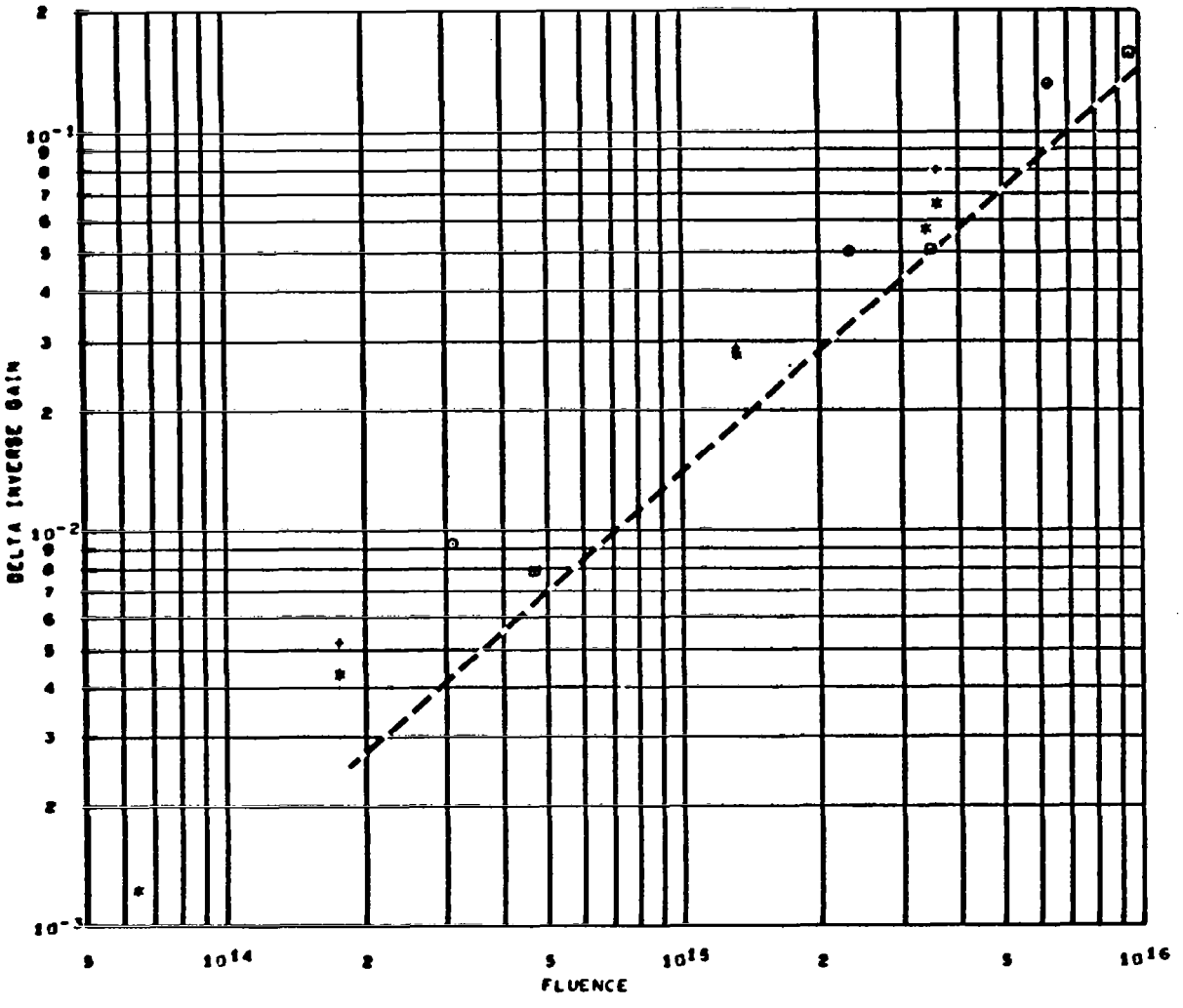

Figure 102. 2N2411 Equivalence Plot, Electron Test 21

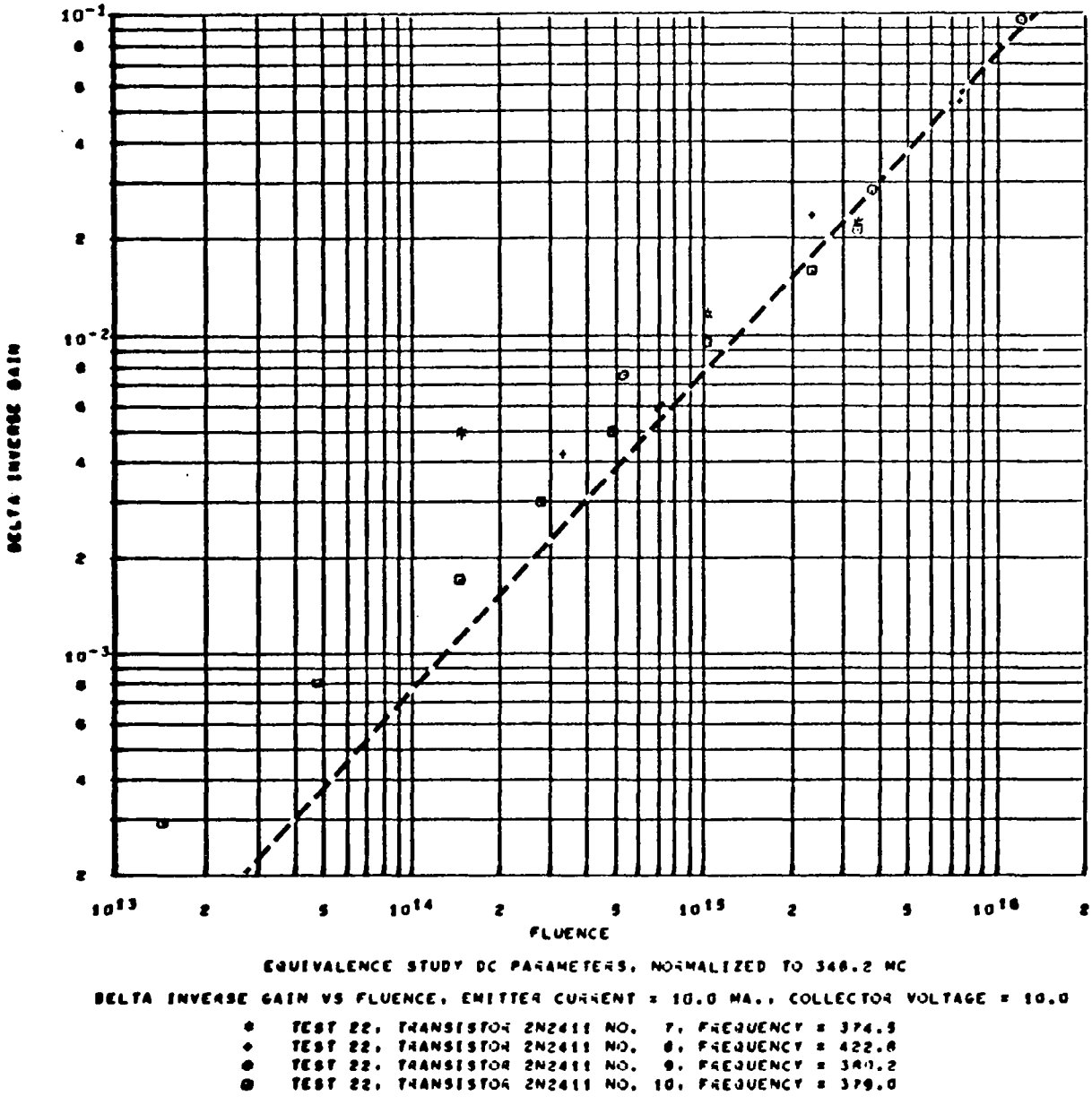

Figure 103. 2N2411 Equivalence Plot, Electron Test 22

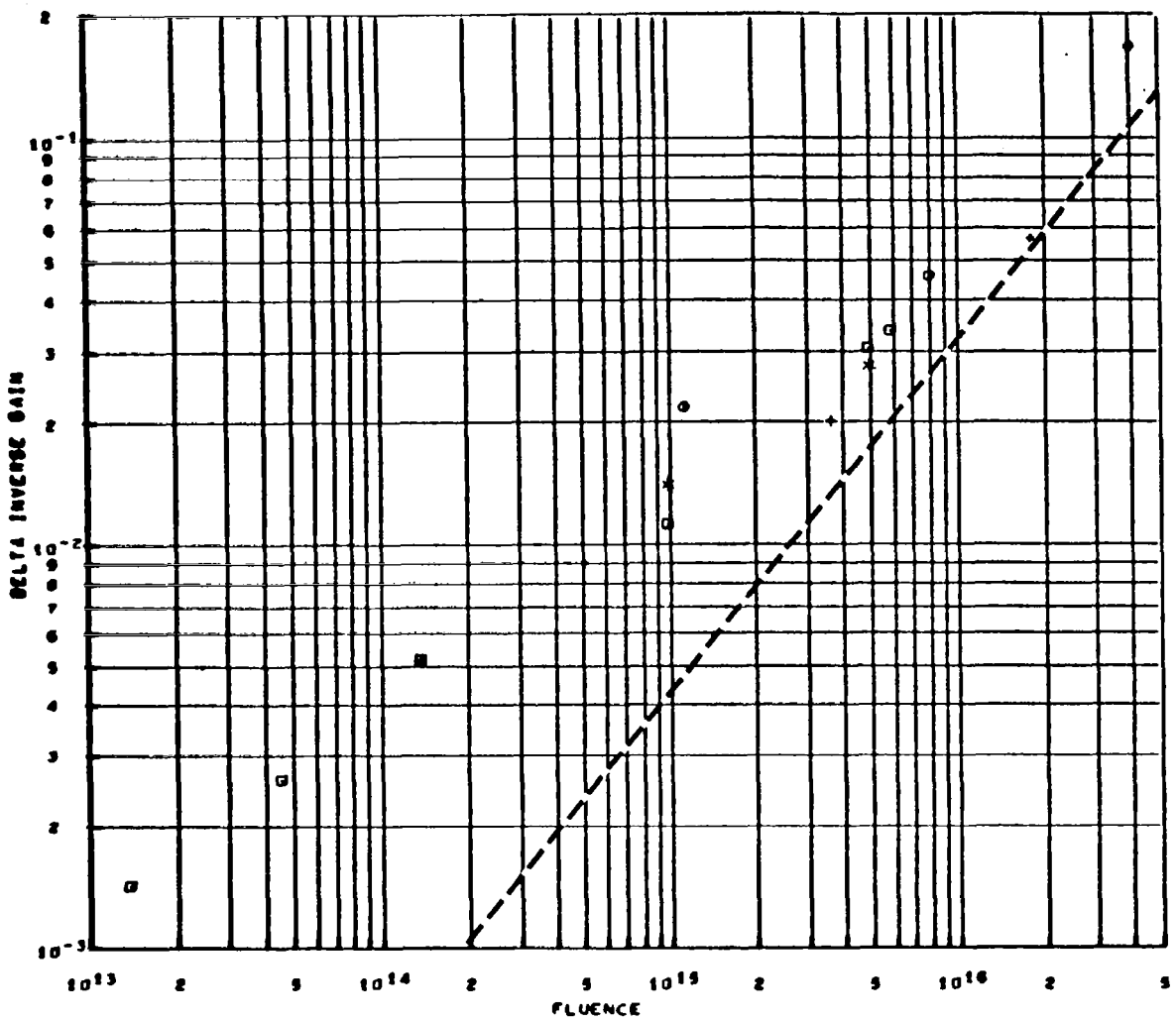

Figure 104. 2N2411 Equivalence Plot, Electron Test 23

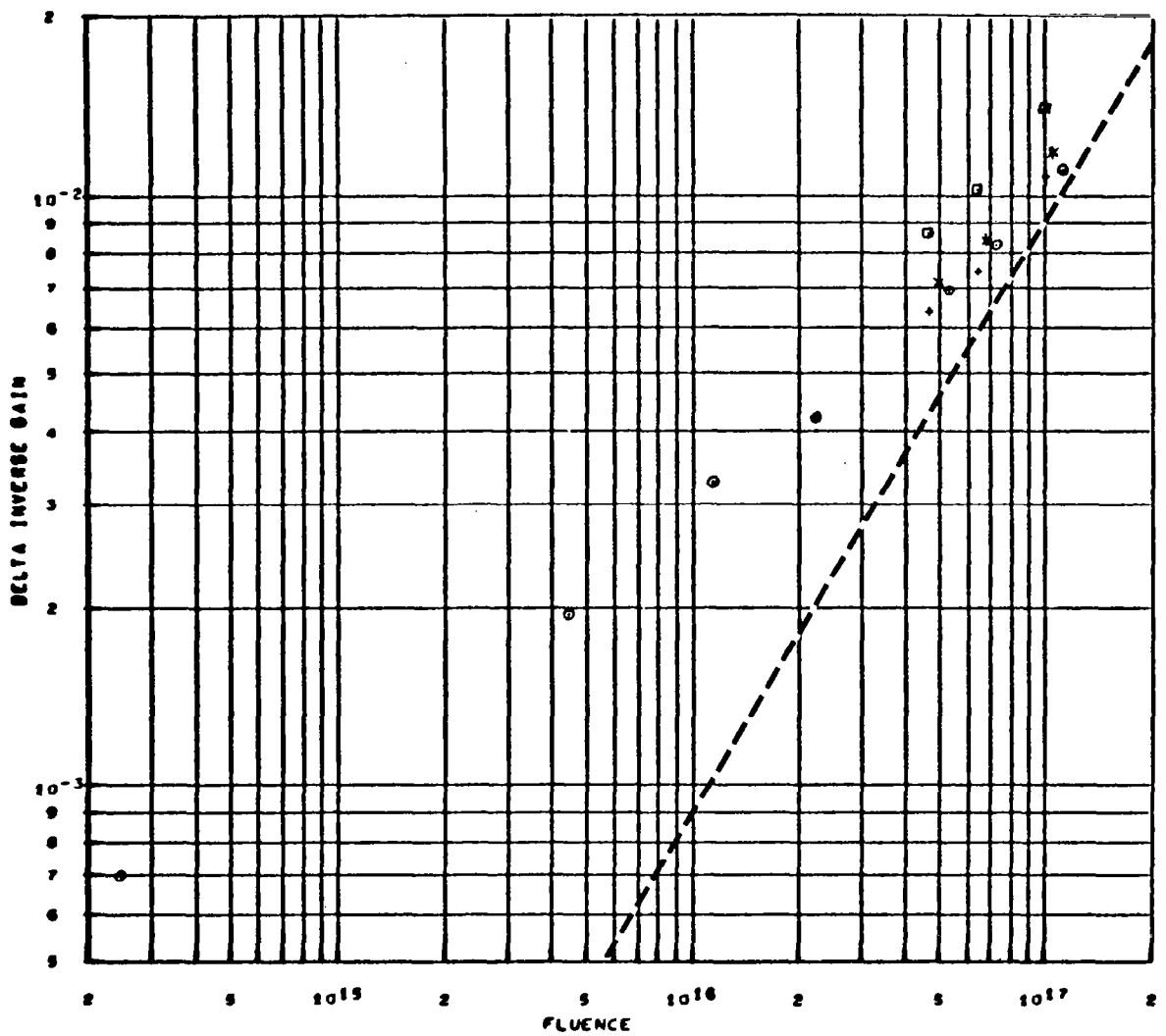

Figure 105. 2N2411 Equivalence Plot, Co^{60} Test

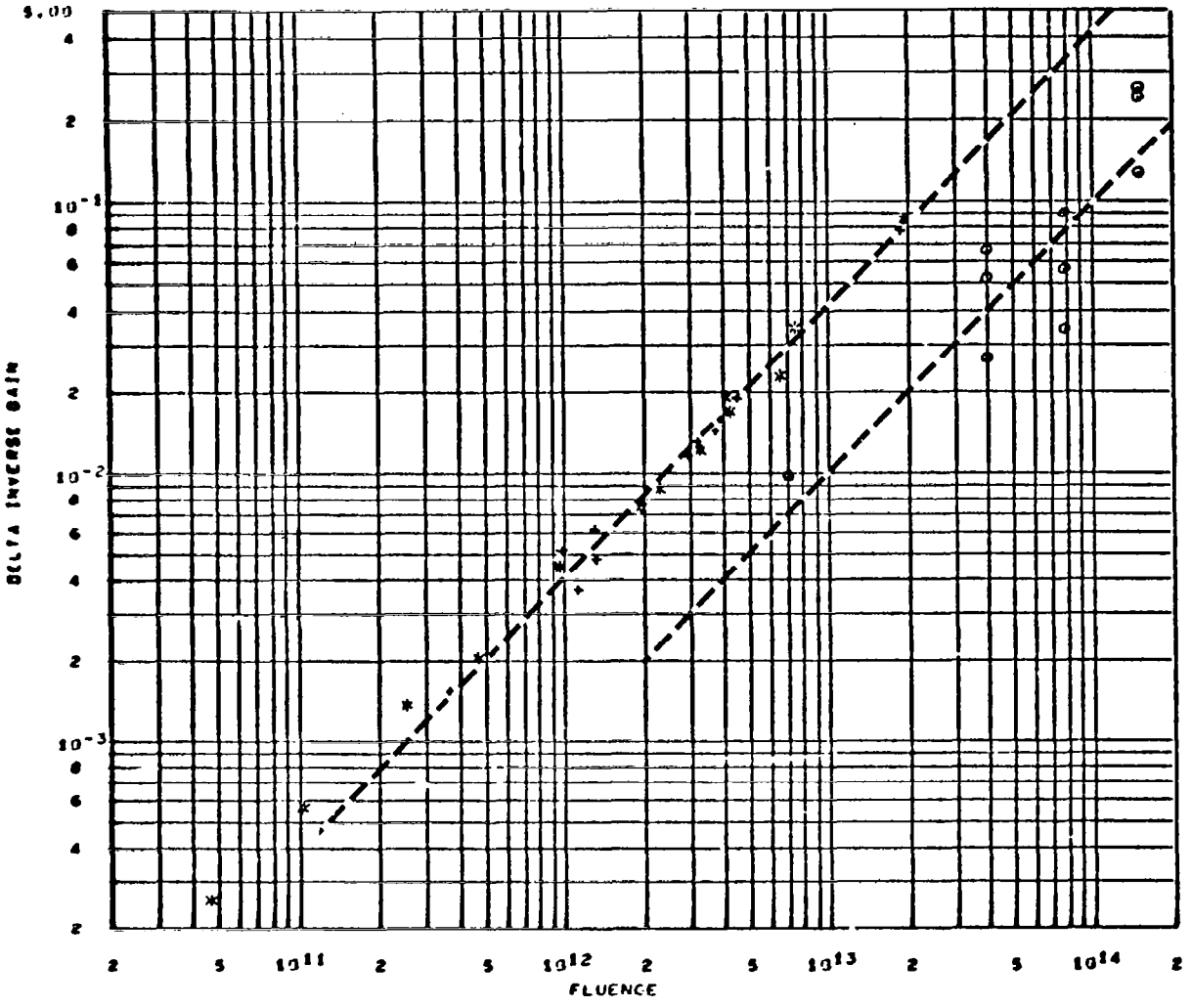

Figure 106. 2N2411 Equivalence Plot, Proton Tests

exposures. A notable exception was the low-frequency pnp device type, 2N2303, which generally showed linear damage. The significance of that result is discussed in Section 2.9.

The three proton tests were condensed onto one computer plot (Figure 62) not only to reduce the number of figures for this document but also to show more clearly the relative effectiveness of proton energy. Figure 68 shows how well the 2N1711 transistors in the 1-Mev proton test normalized when corrected for differences in effective base width. A few plots of Test 26 (20-Mev proton test) are shown separately from the composite plots (e.g., Figures 63 to 83) to indicate differences in the results of transistors which had inherent shielding from those with shielding removed.

Although some composite plots of the three electron tests are shown (e.g., Figure 70), computer plots of Tests 21, 22, and 23 are generally shown separately since nonlinear damage regions on these tests would tend to overlap. All of these plots except one provided consistent results usable for obtaining radiation equivalences. The only exception was the 2N2411 transistors in the 1-Mev proton test (Figure 104) which showed the same damage as the 20-Mev proton test. The computer equivalence plots for the Co^{60} test show extreme nonlinearity, which is discussed in greater detail in Sections 2.8 and 2.9. Proton and electron displacement equivalences, averaged over all of the transistors tested, are shown in Table 12. As an example, this table indicates that one 1-Mev proton is as effective in causing displacement damage as are thirteen 100-Mev protons or 4,400 electrons of 0.53 Mev. These equivalences relate only to displacement effects since values obtained are associated with the linear damage portions of the equivalence plots. Separation of linear and nonlinear damage is discussed in Section 2.9. Asterisks on the values in Table 12 indicate those equivalence values obtained for transistors in the two electron tests where energy and transmission losses due to inherent shielding were significant. The values of equivalences shown for the 1.3- and 2-Mev electron tests were for thin can devices (transistors with ~0.17 gm cm^{-2} of inherent shielding).

Table 12. Energy-Dependent Displacement Equivalences, $\Delta(h_{FE}^{-1})$

Tests	Proton Tests (Mev)			Electron Tests (Mev)		
	.1	16	100	2	1.3	0.53
1-Mev Proton Can Off	1	2.8	1.3×10^{1}	$*1.0\times10^{3}$	$*2.0\times10^{3}$	4.4×10^{3}
16-Mev Proton Can Off	3.6×10^{-1}	1	4.7	$*3.6\times10^{2}$	$*7.3\times10^{2}$	1.5×10^{3}
100-Mev Proton	7.7×10^{-2}	2.1×10^{-1}	1	$*7.7\times10^{1}$	$*1.6\times10^{2}$	3.4×10^{2}
2-Mev Electron	$*1.0\times10^{-3}$	$*2.8\times10^{-3}$	$*1.3\times10^{-2}$	1	*2.0	*4.4
1.3-Mev Electron	$*5.0\times10^{-4}$	$*1.4\times10^{-3}$	$*6.3\times10^{-3}$	$*5\times10^{-1}$	1	*2.2
0.53-Mev Electron Can Off	2.3×10^{-4}	6.7×10^{-4}	2.9×10^{-3}	$*2.3\times10^{-1}$	$*4.5\times10^{-1}$	1

* Transistor cans of ~0.17 gm cm^{-2}.

2.7.3 Proton and Electron Energy Dependence

The influence of inherent shielding of the transistors (encapsulement) for the electron tests was discussed in Reference 1. Table 13 summarizes energy and transmission losses for transistors with typically thin and thick cans. Energy degradation of 14-Mev protons passing into a transistor were determined by integrating the energy loss over 1-Mev increments to account for changes in dE/dX during penetration (Reference 17). Energy losses were calculated for the 1- and 2-Mev electron tests for inherent shielding of the transistor cans (References 18 and 19). In addition, the loss of electron intensity was determined for those two electron tests using a nomograph for electron number transmission (Reference 19).

A summary of the energy dependence of electron displacement damage (Figure 107) and proton displacement damage (Figures 108 and 109) is given for selected npn transistors. The data is plotted relative to a unity value arbitrarily selected for the 0.53-Mev electron test. Data points from energies in addition to those obtained from this study were obtained from preliminary tests performed earlier, as well as concurrent with this study. In each figure, the experimentally determined energy dependence of displacement damage (linear) is shown both for the silicon only and for the thick can inherent shielding.

The effect of shielding on electron displacement damage in silicon transistors acts in accordance with Table 13. Low-energy electrons are either absorbed or reduced in number (scattered out) with subsequent energy loss. The net effect is a significant reduction of the effectiveness of electron displacement damage at low energies. This result would be expected since a rapid falloff with energy is predicted both from displacement theory and from various experiments (see Section 2.7.4). The threshold in silicon for electron atomic displacement is approximately 150 kev (References 20 and 21).

The effect of shielding is particularly significant for space applications since the electron intensity spectra of the Van Allen belts decrease rapidly with increased energy. However, as was evident from $\Delta(h_{FE}^{-1})$ plots, linear displacement damage is not the dominant electron effect on transistors for exposures

Table 13. Energy and Transmission Loss in Transistor Cans

Particle Type	Test No.	Energy Incident (Mev)	dE/dX (Mev cm^2 gm^{-1})		Thick Can Transistor (e.g. 2N2303)			Thin Can Transistor (e.g. 2N2538)		
			Thick Fe Can	Thin Ni Can	Energy Loss (Mev)	Final Energy (Mev)	Transmission Loss (percent)	Energy Loss (Mev)	Final Energy (Mev)	Transmission Loss (percent)
Electron	21	1.95	1.38 (mean)	1.38 (mean)	0.40	1.55	15	0.27	1.68	5
	22	1.28	1.36 (mean)	1.36 (mean)	0.38	0.88	38	0.29	0.99	18
	23	0.53	Can off	Can off	0	0.53	0	0	0.53	0
Proton	24	1.0	Can off	Can off	0	1.0	0	0	1.0	0
	26	14	21.8 to 31.0 (integrate)	21.8 to 26.9 (integrate)	6.1	7.9	---	4.0	10.0	---
			Can off	Can off	0	14.0	0	0	14.0	0
		17	18.5 to 23.5 (integrate)	18.5 to 21.8 (integrate)	5.8	11.2	---	3.3	13.7	---
			Can off	Can off	0	17.0	0	0	17.0	0
	27	100	---	---	---	100.0	---	---	100.0	---

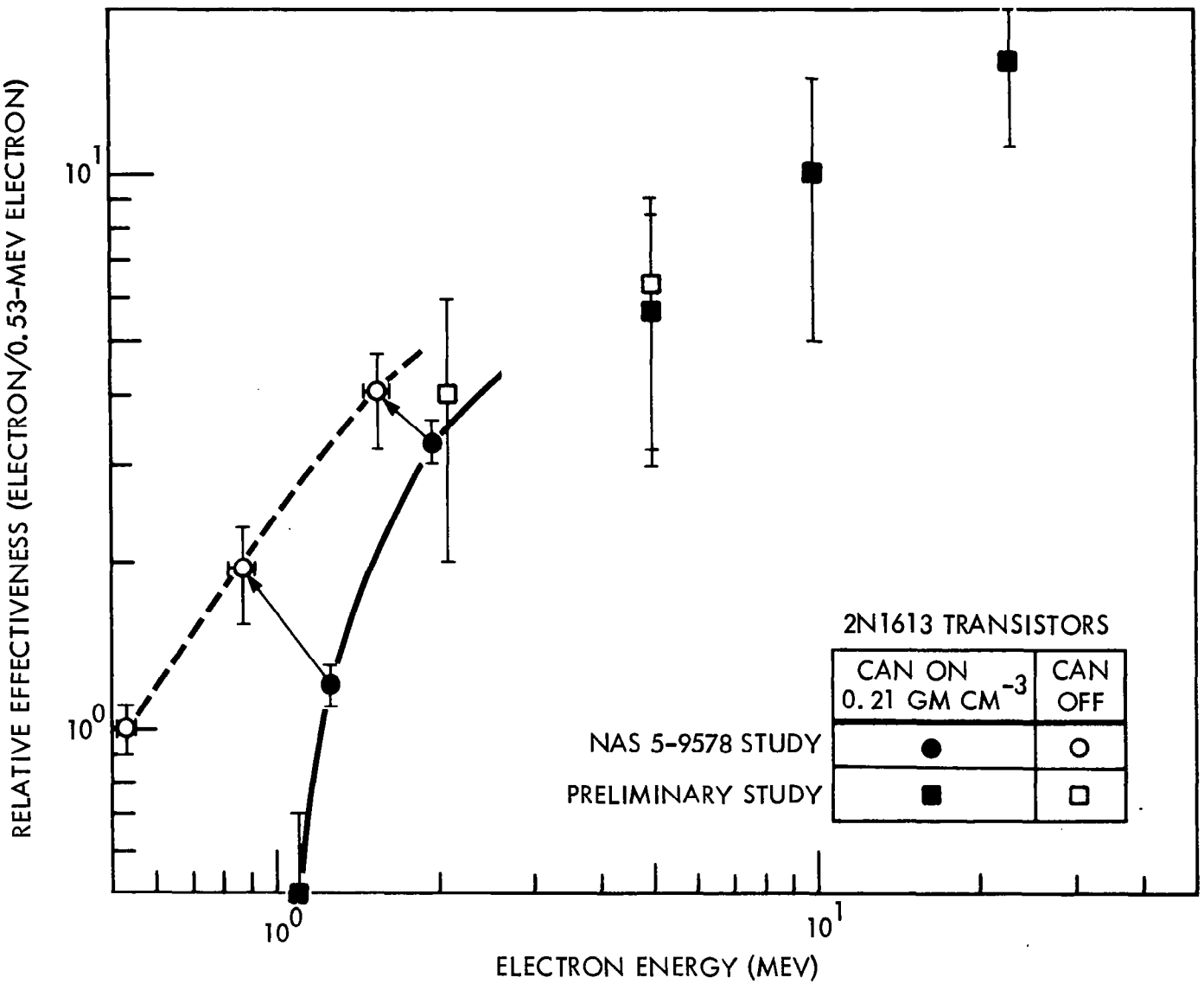

Figure 107. Energy Dependence of Electron-Induced Displacement Damage (2N1613)

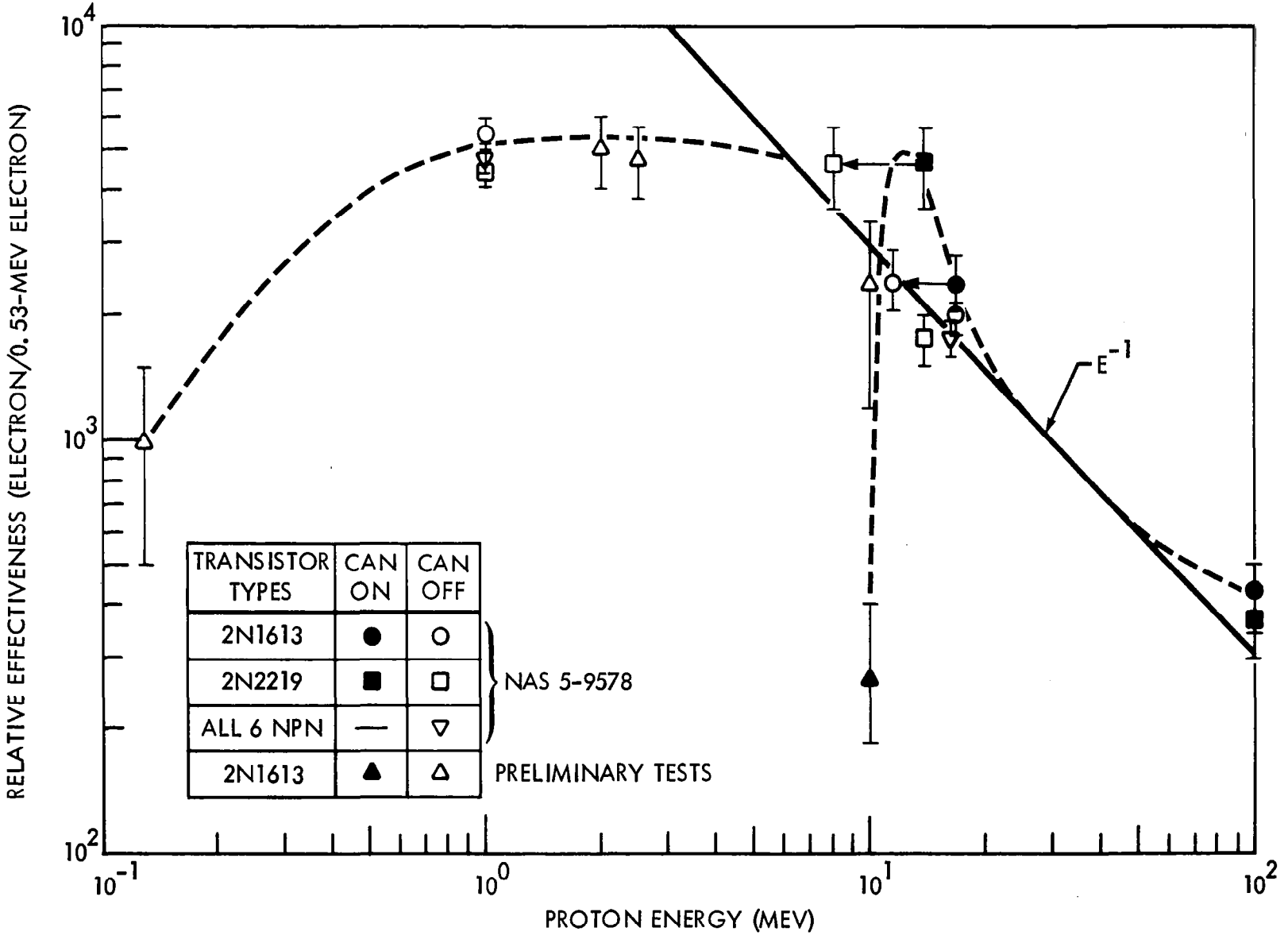

Figure 108. Proton Energy Dependence of Displacement Damage (npn Transistors)

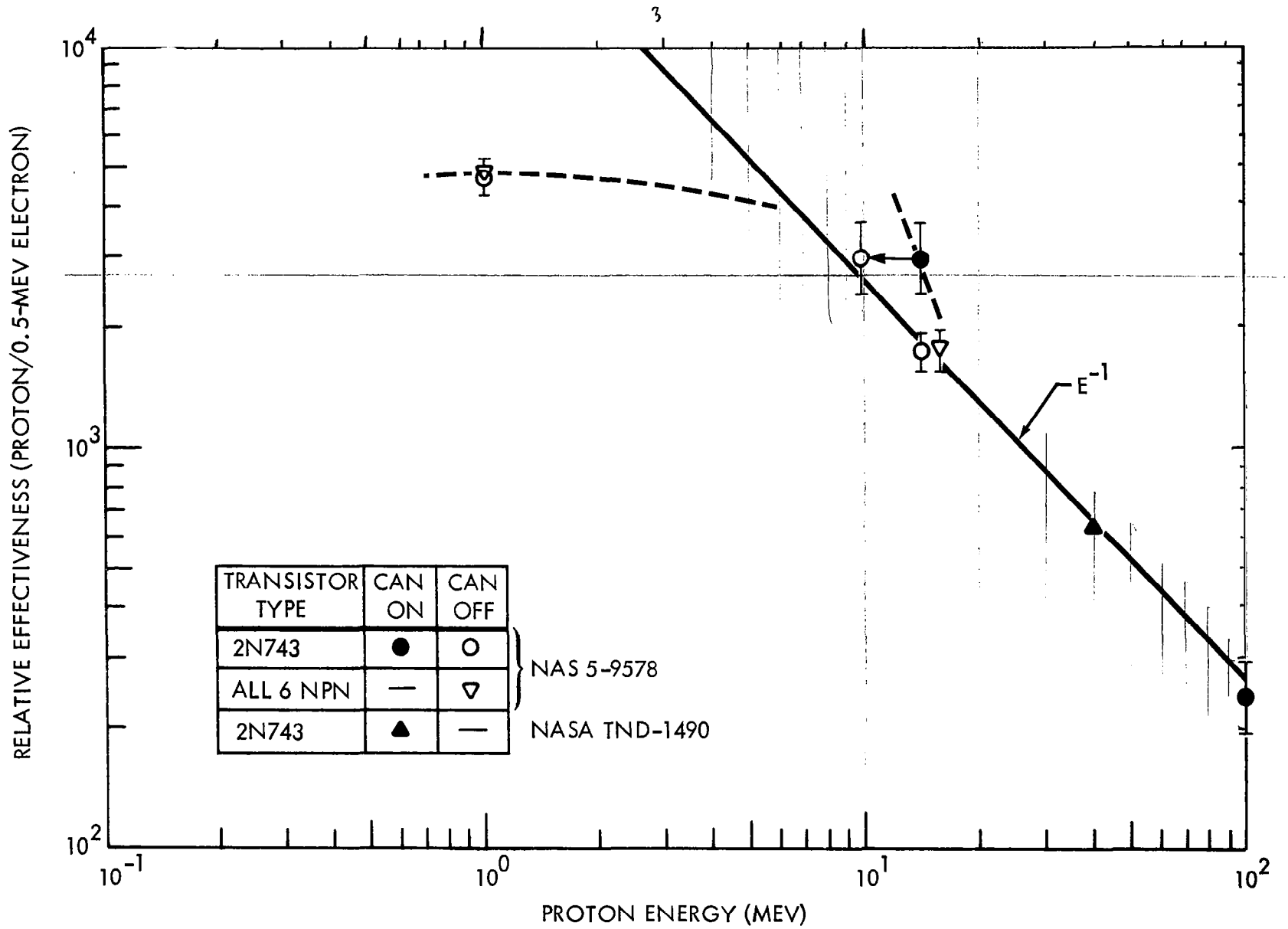

Figure 109. Proton Energy Dependence of Displacement Damage (2N743)

anticipated for space missions. As discussed in Section 2.9, the dominant nonlinear damage appears to be dependent not on displacements but on ionization (absorbed dose). Therefore, nonlinear damage due to secondary radiation would need to be considered in a final assessment of the influence of shielding on electron damage.

The proton energy dependence for displacement damage is also influenced by shielding, in a predictable manner. The lowest energy protons are absorbed by shielding, while other low-energy protons with enough energy to penetrate the shields are further reduced in energy without a significant loss in transmission (except those close to the end of their range where straggling is important). This reduction in energy, rather than making them less effective for displacements (as in the case of electrons), instead causes them to be more effective. This increase in effectiveness accounts for the peaking of the damage curve for transistors with inherent shielding (dotted curve of Figure 108) in the 20-Mev proton test. The solid lines in Figures 108 and 109 illustrate the anticipated theoretical E^{-1} dependence of displacement cross section for proton damage. The data point for 2N743 devices irradiated at 40 Mev was determined from data obtained by Honaker and Bryant (Reference 22). Since the proton intensity spectra of space increase with decreasing energy, the tendency of the damage curve of a shielded device to peak at low energies is particularly significant. To properly assess proton damage for space missions, it appears to be particularly important to integrate the shield-modified environment spectra with the energy dependence for displacement damage.

2.7.4 Other Particle Equivalences and Correlations With Other Studies

Displacement equivalences for five types of "particles" (alpha particle, proton, neutron, electron, and gamma ray) are given in Table 14, with 5-Mev alpha particles being used as the unity reference point since they are the most effective of the particles listed. Values for neutron and alpha particles were obtained from analysis of preliminary Boeing studies of permanent damage (Reference 14). Transistor inherent shielding was removed for the alpha particle test. Neutron exposures were made using the water-moderated spectrum of a TRIGA reactor (Reference 12). Gamma-ray results, shown in Table 14, were obtained from the

Table 14. Particle-Type Displacement Equivalences, $\Delta(h_{FE}^{-1})$

Particle Type and Energy	Alpha Particle (5 Mev)	Proton (1 Mev)	Neutron (Reactor Spectrum)	Electron (1 Mev)	Gamma Ray (Co^{60})
Alpha Particle (5 Mev) Can off	1	3.5	1.4×10^{2}	$*7 \times 10^{3}$	1.5×10^{5}
Proton (1 Mev) Can off	2.9×10^{-1}	1	4×10^{1}	$*2 \times 10^{3}$	4.3×10^{4}
Neutron (Reactor)	7.1×10^{-3}	2.5×10^{-2}	1	$*5 \times 10^{1}$	1.1×10^{3}
Electron (1 Mev) Can off	$*1.4 \times 10^{-4}$	$*5 \times 10^{-4}$	$*2.0 \times 10^{-2}$	1	$*2.2 \times 10^{1}$
Gamma Ray (Co^{60})	6.7×10^{-6}	2.3×10^{-5}	9.1×10^{-4}	$*4.5 \times 10^{-2}$	1

* Transistor cans of 0.17 gm cm^{-2}.

average value of displacement equivalences for the 10 transistor types studied in this contract. Discussion of the significance of gamma rays for studying linear damage is presented in Sections 2.8 and 2.9.

Comparisons can be made between particle type displacement equivalences and data reported for other types of semiconductor devices and other investigators. Figures 110 and 111 show Boeing data for some earlier studies of displacement effects in silicon diodes and solar cells (Reference 14).

The minority-carrier lifetime of diodes was measured using a Tektronix Type S plug-in unit. Two types of silicon alloy diodes were tested, the 1N459 (General Instrument Company) and the 1N462 (Raytheon). Measurements of lifetime were made before and immediately after irradiation. Both devices showed approximately the same sensitivity to radiation and showed no damage annealing over periods of several months.

Although the limits of error are quite large, the changes in lifetime appear to be consistent with Equation (10). Damage constants, K_1, for diode types 1N459 and 1N462 were found to be: $(3\pm2) \times 10^{-7}$ seconds^{-1} for reactor neutrons; $(2\pm1) \times 10^{-8}$ seconds^{-1} for 2-Mev electrons; and $(5\pm3) \times 10^{-11}$ seconds^{-1} for Co^{60} gamma rays. Equivalences obtainable from Figure 110 are in rough agreement with those found for transistor displacement damage.

The diffusion length, L, of minority carriers in silicon semiconductor material can be related to the minority-carrier lifetime.

$$L = (D\tau)^{1/2} \tag{22}$$

Changes in diffusion length, caused by radiation-induced recombination centers, can also be related to particle fluences through Equation 10.

$$\Delta(L^{-2}) = L^{-2} - L_o^{-2} = K_L \Phi \tag{23}$$

$$K_L = K_1 D \tag{24}$$

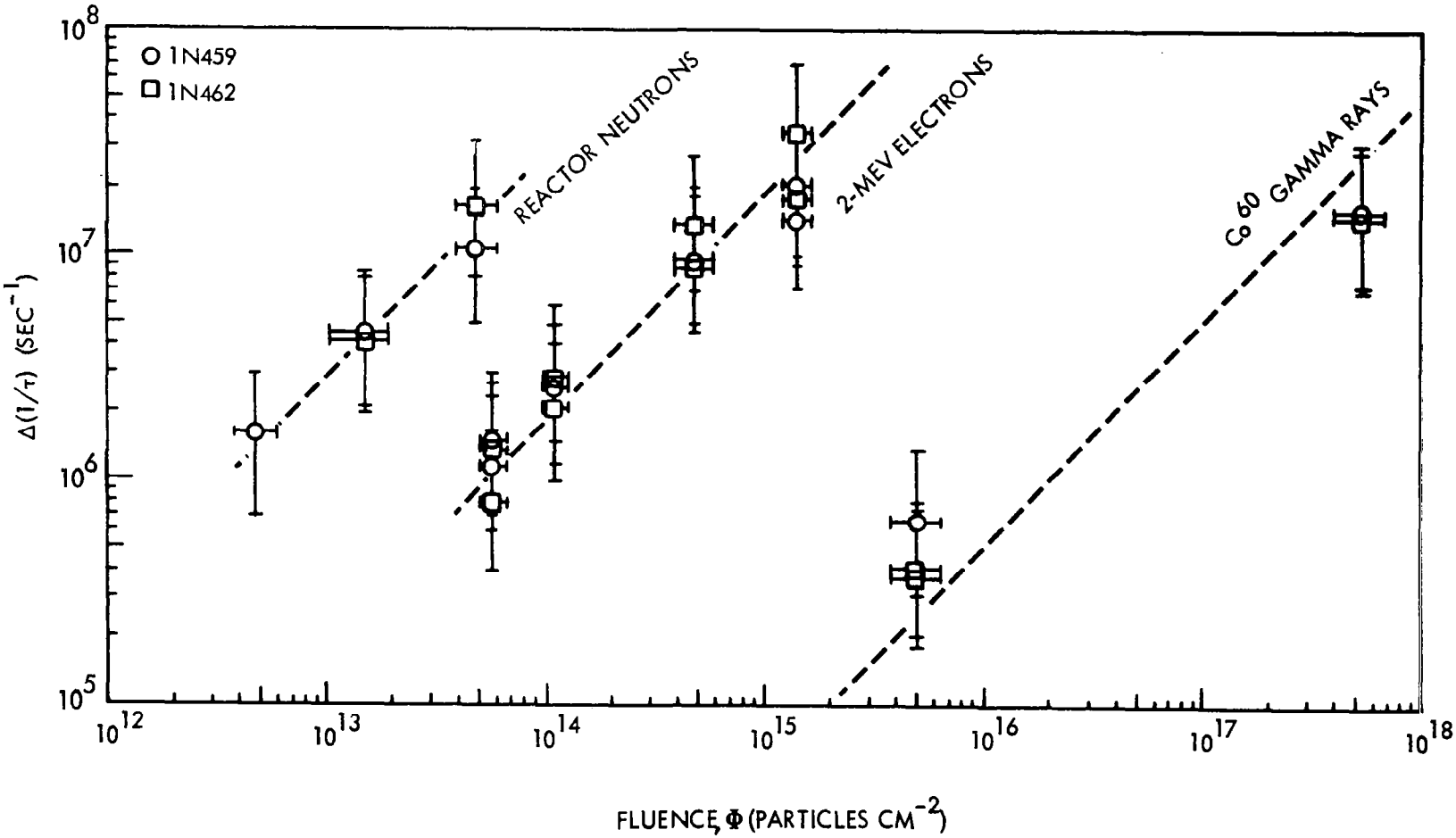

Figure 110. Permanent Damage to Diodes

where L_o is the initial diffusion length.

Short-circuit current, I_{sc}, of p-on-n or p-on-n-silicon solar cells can be related to the diffusion length, L_n, of the n region; the diffusion length, L_p, in the p region; and the junction depth, W. For uniform generation of carriers, short-circuit current is given in Equation 25 (Reference 23):

$$I_{sc} = egA\,(c_1 L_n + c_2 L_p + c_3 W) \tag{25}$$

where:

e = electronic charge

g = generation rate of carriers

A = sensitive area of the cell

Generally, the junction depth is much smaller than either of the diffusion lengths, and the diffusion length of the base region (e.g., n region of a p-on-n solar cell) controls I_{sc}.

An experimentally observed dependence of I_{sc} on L when carriers are generated by solar or artificial light is given in Equation (26), where

$$I_{sc} = b \log_{10} (L/L') \tag{26}$$

b and L' are constants (Reference 24). When L' is eliminated by considering the difference in short-circuit current before and after exposure, Equation (27) is obtained (Reference 14).

$$\Delta(1/L^2) \cong L_o^{-2} \left\{ \exp \left[4.6 \left(I_{sc_o} - I_{sc} \right) / b \right] - 1 \right\} \tag{27}$$

Equation (27) is not valid for radiation exposures that are so extensive that diffusion length of the base region is reduced to a value comparable to the lengths of Equation (25). Solar cell initial diffusion length for data shown in Figure 111 was measured experimentally using the method of Gremmelmaier (Reference 25). The damage obtainable from Figure 111 is in rough agreement with that obtained for displacement damage of transistors.

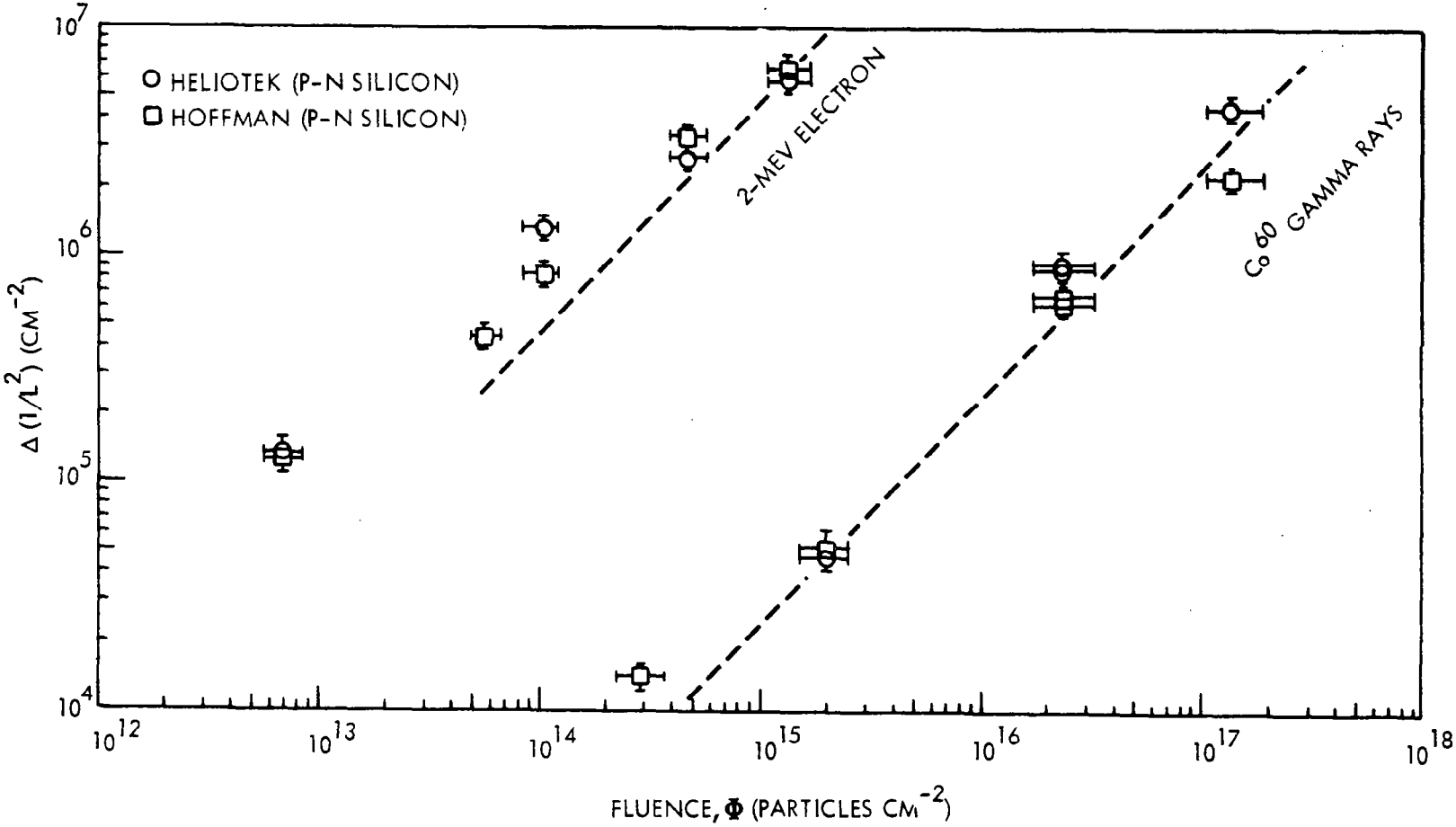

Figure 111. Permanent Damage to Solar Cells

Figure 112 compares the relative effectiveness of electrons for displacement damage to npn and pnp transistors of this study with both experimental and theoretical data from other studies. The curve shown for theoretical cross section for silicon displacements was calculated by Cahn (Reference 21) using basically the simple model of Seitz and Koehler for atomic displacements in silicon (Reference 26) but with relativistic corrections where necessary and assuming a displacement threshold of 0.13 ev. Although the observed transistor energy dependence does not follow this curve, it is in rough agreement with detailed solar cell results found by Carter and Downing (Reference 27). Their n-on-p solar cell data better fit the square of the theoretical cross section which they suggest may mean a defect association with a divacancy. They have attributed electron damage to the $E_v + 0.3$ ev defect level Solar cell points shown in Figure 112 are for Hoffman n-on-p devices of 3.3 ohm cm resistivity.

The proton energy dependence of damage shown in Figures 108 and 109 is in rough agreement with the energy dependence of the displacement cross sections for coulomb elastic scattering ($\sim E^{-1}$) in the region of approximately 7 to almost 100 Mev (References 26 and 28). At 100 Mev, for all devices tested except the epitaxial mesa transistors (2N743 and 2N834), the damage was higher than that predicted by elastic scattering alone. Values of damage at 100 Mev were compared with theoretical defect density published by Simon, et al. (Reference 29). The ratio of total (due to both elastic and inelastic cross sections) theoretical defect density to that of the elastic only is in agreement with the increase of damage (shown above the E^{-1} line of Figure 108) observed with 100-Mev protons. Below about 6 Mev, Carter and Downing observed that proton effectiveness decreases for damage to silicon solar cells. They found maximum sensitivity at about 2 Mev. The relative effectiveness of 1-Mev protons to reactor neutrons of 40.0 : 1.0 shown in Table 14 compares favorably with data obtained for neutrons by Larin and Niehaus for the five 2N1613 devices (Reference 30). The average damage constant yields a ratio of 41.7 : 1.0.

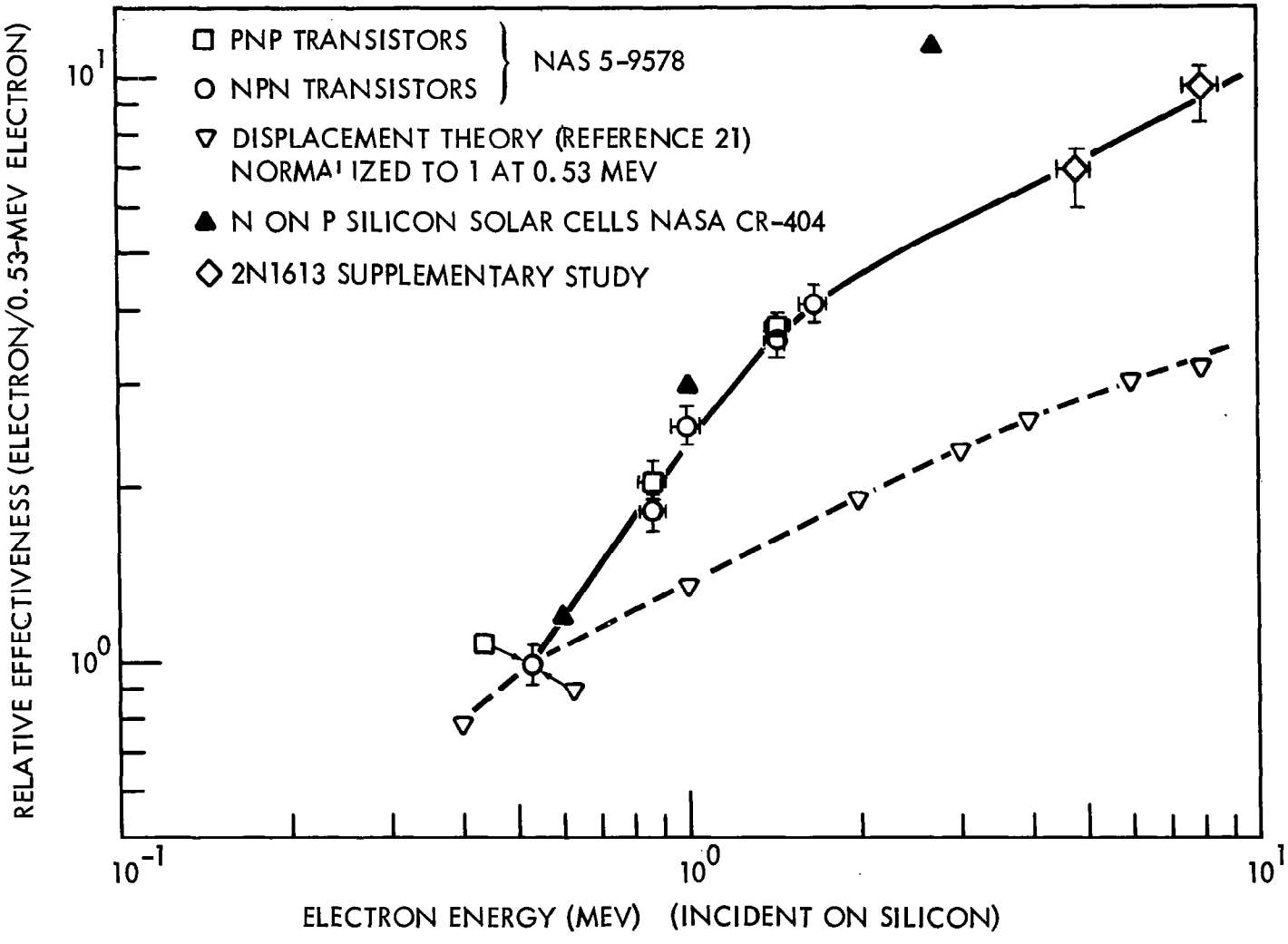

Figure 112. Electron Displacement Damage in Silicon Devices

2.8 FEASIBILITY OF SIMULATION BY Co^{60} GAMMA TESTING

Passive data, as well as curve traces obtained dynamically (during exposure), were analyzed to determine the feasibility of using Co^{60} sources for simulation of electron and proton effects.

Analysis of $\Delta(BV_{CBO})$ generally showed only small changes. Although a strong dependence on fluence was observed for 2N2538 devices irradiated with electrons or protons, no such dependence on exposure was observed for gamma-ray exposure up to 10^{17} photons cm^{-2}. Photon exposure fluence was defined as 1R of Co^{60} gamma radiation equals 1.6×10^{9} photons cm^{-2}. Although one of the 2N2538 transistors shown in Figure 113 suffered a significant decrease in BV_{CBO}, no dependence on fluence was observed, and thus no evidence for a tie-in with displacement theory was demonstrated.

Changes of $V_{CE}(sat)$ did, however, reveal a strong dependence on Φ, as indicated in Figures 114 and 115. The gamma-ray test data could be fitted to the same power law dependence that was observed for the proton and electron tests (Figures 15, 16, and 17); thus, equivalences could be obtained. These equivalences are summarized in Table 15.

Also shown in Table 15 are the displacement equivalences for changes in h_{FE}^{-1}. These values were obtained from an average of the linear damage equivalences of the transistor types. In several cases the linear damage of $\Delta(h_{FE}^{-1})$ plots, such as Figure 57, was heavily obscured by the nonlinear damage. In those cases, equivalence values were extrapolated from an estimate of the saturation level of nonlinear damage. Possible separation of linear and nonlinear damage is discussed in Section 2.9. Approximate values of damage constants for extrapolated linear regions (displacement damage component) are shown in Table 16.

Measurement of I_{CBO} changes made following gamma-ray exposure is shown in Figures 116, 117, and 118. It is apparent from these figures that a dependence on fluence exists, but not the linear dependence observed in Figures 21, 22, and 23 for the proton tests. It also appears (progression from Figure 116

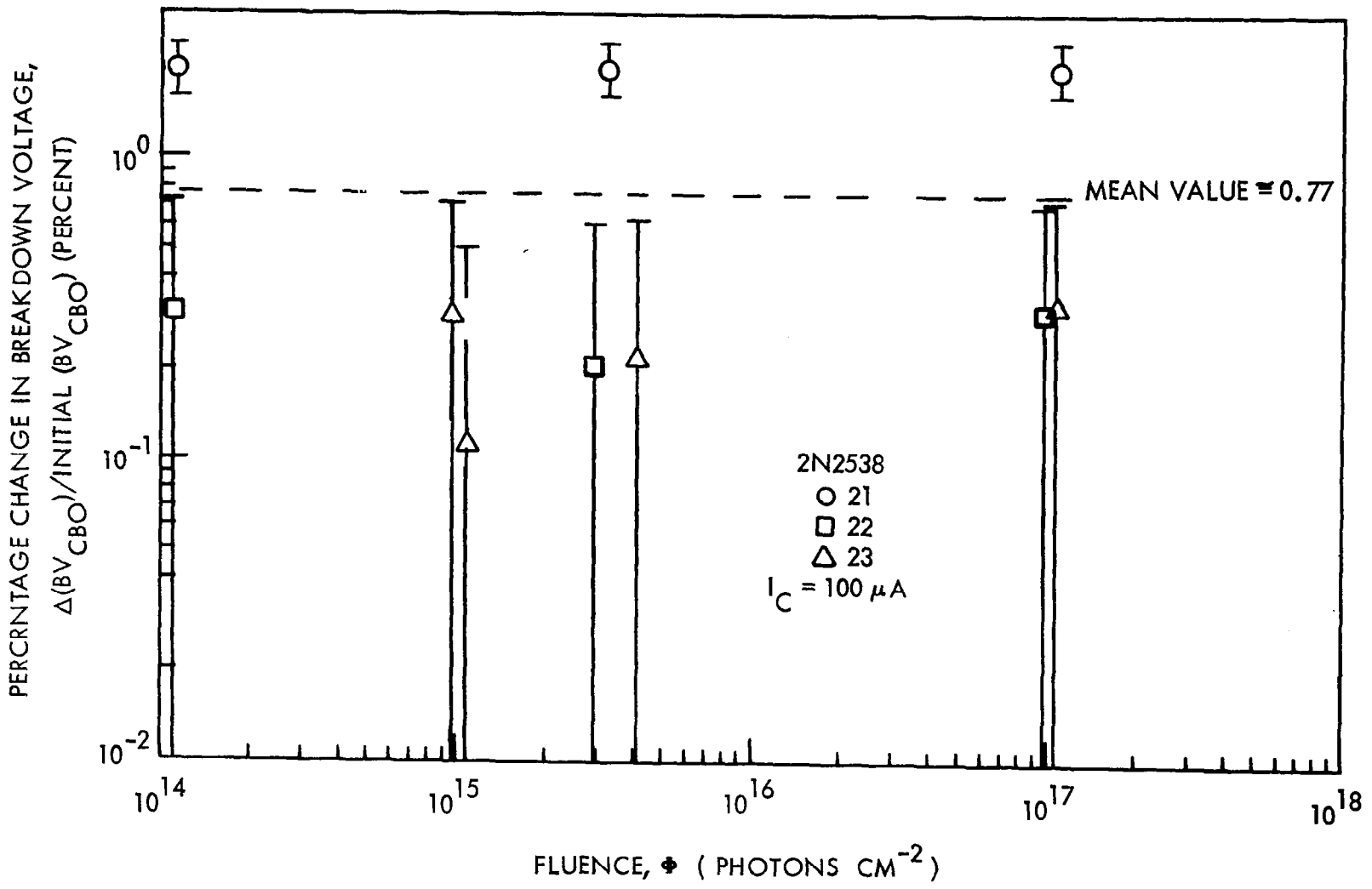

Figure 113. $\Delta(BV_{CBO})$ for Co^{60} Gamma-Ray Exposure (2N2538)

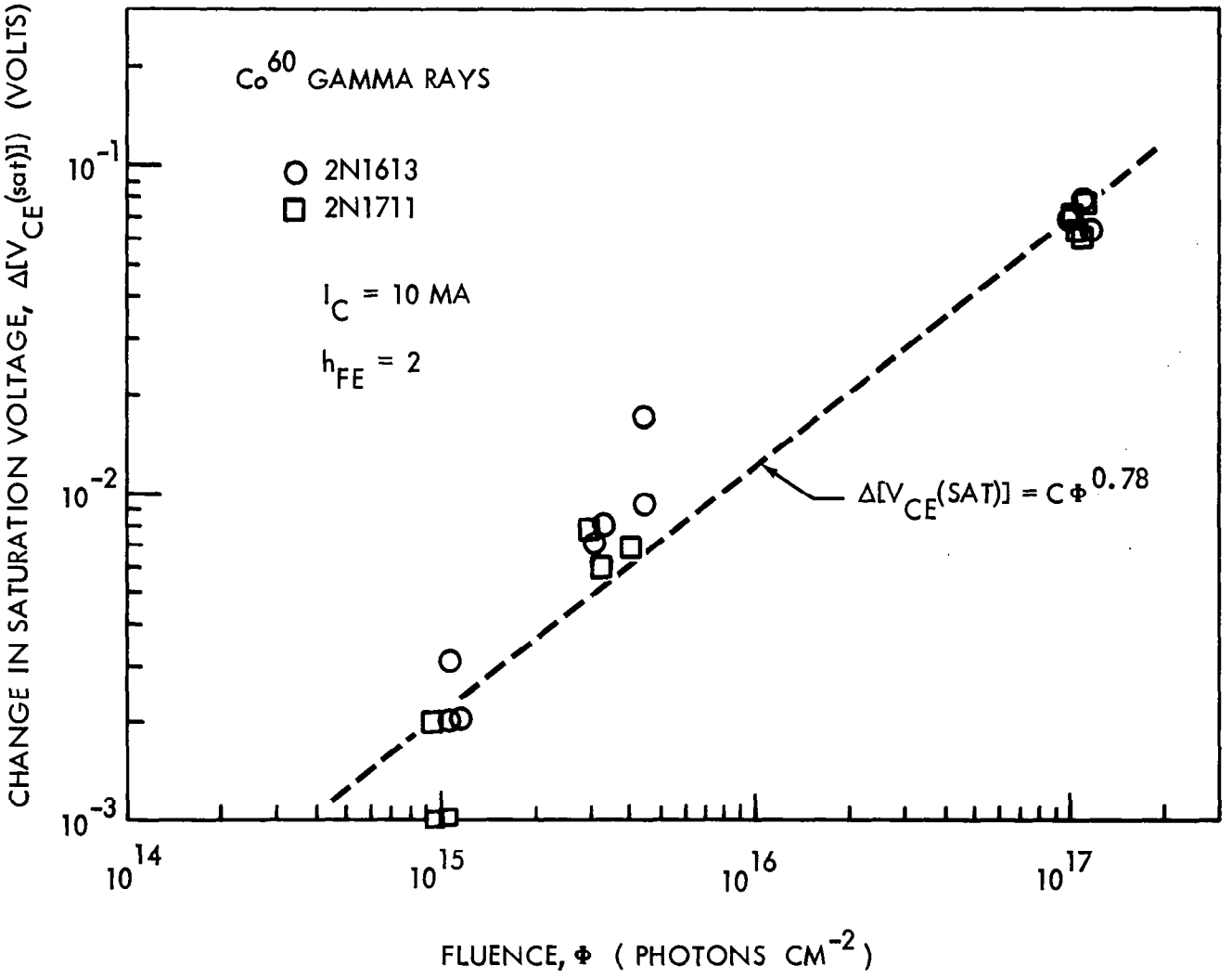

Figure 114. Dependence of $\Delta[V_{CE}(sat)]$ on Co^{60} Gamma-Ray Fluence (2N1613, 2N1711)

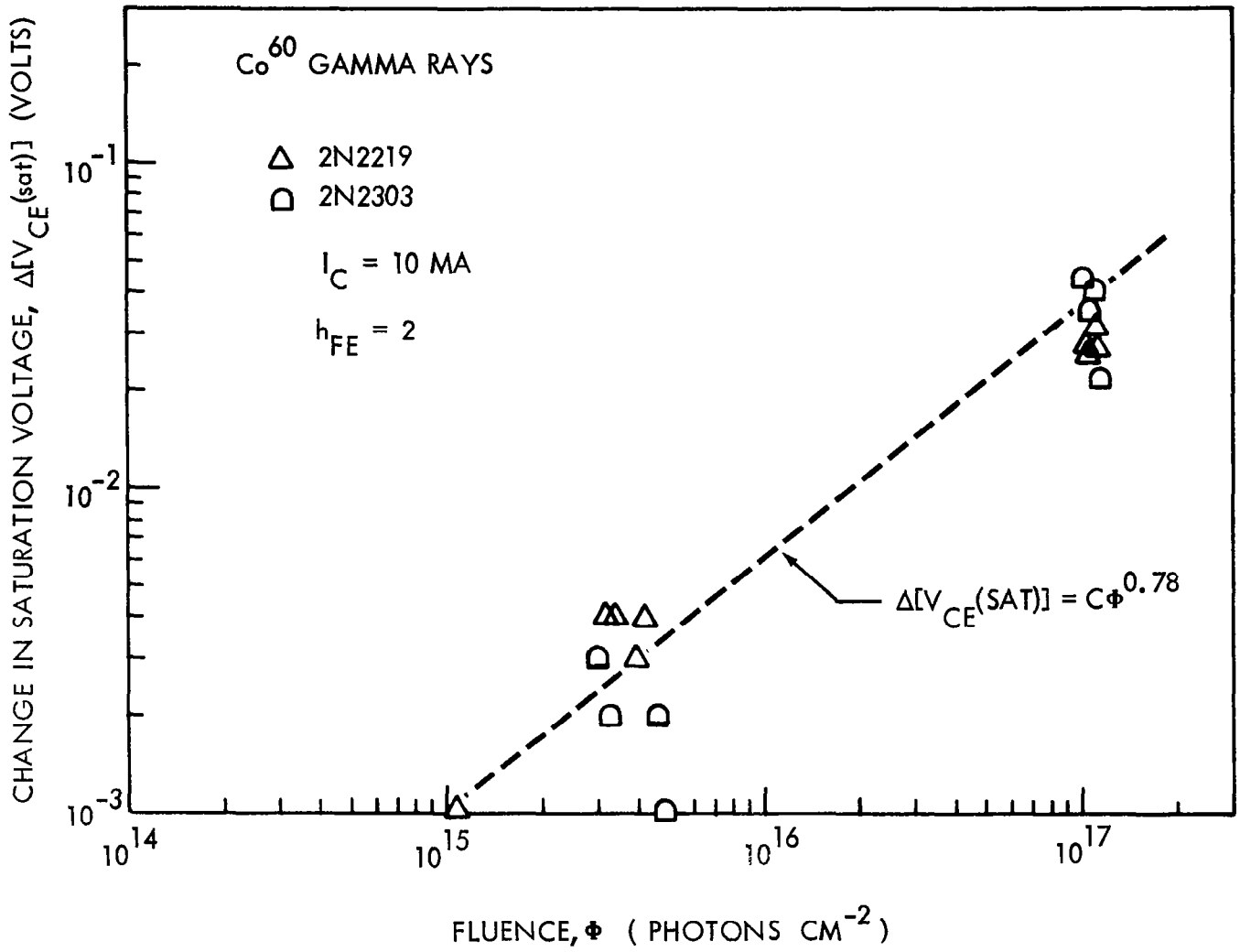

Figure 115. Dependence of $\Delta[V_{CE}(sat)]$ on Co^{60} Gamma-Ray Fluence (2N2219, 2N2303)

Table 15. Gamma-Ray Equivalences (Displacement Damage)

Energy on Silicon	Equivalences	
	for $\Delta[V_{CE}(sat)]$	for $\Delta(h_{FE}^{-1})$ (linear change)
1-Mev Proton	1.6×10^5	1.3×10^5
16-Mev Proton	5.3×10^4	4.7×10^4
100-Mev Proton	1.1×10^4	1.0×10^4
1.7-Mev Electron	1.4×10^2	1.3×10^2
1-Mev Electron	7.0×10^1	6.5×10^1
0.53-Mev Electron	3.5×10^1	2.9×10^1
Co^{60} Gamma	1	1

Table 16. Transistor Damage Constants for Co^{60} Gamma Rays (Displacement Component)

Transistor Type	K'	K_D
2N1613	7.1×10^{-19}	6.7×10^{-17}
2N1711	1.8×10^{-19}	2.7×10^{-17}
2N2538	1.0×10^{-19}	4.2×10^{-17}
2N2219	5.0×10^{-20}	2.2×10^{-17}
2N743	6.7×10^{-20}	2.9×10^{-17}
2N834	1.4×10^{-19}	1.4×10^{-17}
2N2303	3.6×10^{-19}	4.4×10^{-17}
2N1132	3.4×10^{-19}	1.3×10^{-16}
2N2801	3.0×10^{-19}	9.7×10^{-17}
2N2411	7.7×10^{-20}	2.7×10^{-17}

to 117 to 118) that the changes in leakage current seem to be saturating at high exposures much as nonlinear changes in $\Delta(h_{FE}^{-1})$ were observed to saturate for high-level electron exposure. If this nonlinear damage is related to ionization rather than to displacements, it could indicate that the mechanism of nonlinear damage observed in I_{CBO} for the collector-base junction may be similar to the mechanism of nonlinear damage observed for $\Delta(h_{FE}^{-1})$, which will be shown in Section 2.9 to be related to increased recombination current of the emitter-base junction.

To probe whether the permanent changes in I_{CBO} for electron and gamma exposure were related to ionization rather than to displacements (as observed for proton exposure), changes in I_{CBO} were plotted as a function of absorbed dose. The transistors of Figures 116 and 118 have been replotted in Figures 119 and 120. Added to the gamma-ray data points are electron data points for the same transistor types. The results obtained for other device types are similar to those shown in Figures 119 and 120. It thus appears that the electron effects are merely an extension of ionization-produced Co^{60} gamma effects.

The net conclusion is that Co^{60} gamma facilities may be useful in simulating permanent effects caused by ionization such as electron-induced changes in I_{CBO} or possibly nonlinear electron-induced changes in h_{FE}^{-1}. However, except for possible changes in $V_{CE}(sat)$, Co^{60} gamma rays do not appear to be too useful for simulating proton damage. In particular, except at very high exposures ($> 10^8$R), the nonlinear effects mask the linear effects. This is apparently due to the very low ratio of displacement cross section to ionization generation resulting from Compton electrons produced by Co^{60} gamma rays.

2.9 IDENTIFICATION OF NONLINEAR DAMAGE

Nonlinear damage has been identified as a problem for assessment of the "permanent" effects of electron damage to transistors (not to be confused with surface channeling and inversion layers observed for "Telstar" effects described in Reference 31.) This section describes some of the characteristics that have been

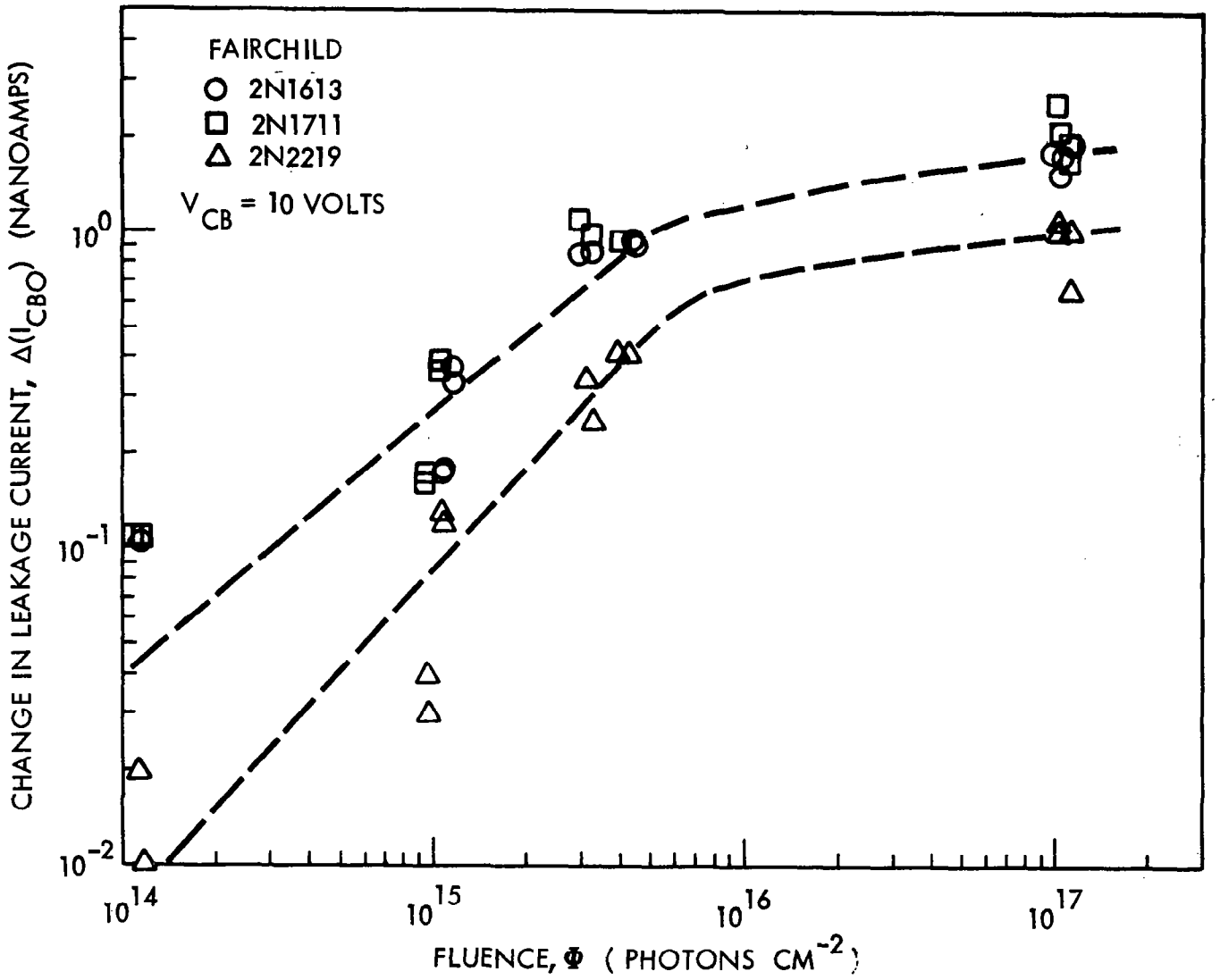

Figure 116. Dependence of $\Delta(I_{CBO})$ on Co^{60} Gamma-Ray Fluence (2N1613, 2N1711, 2N2219)

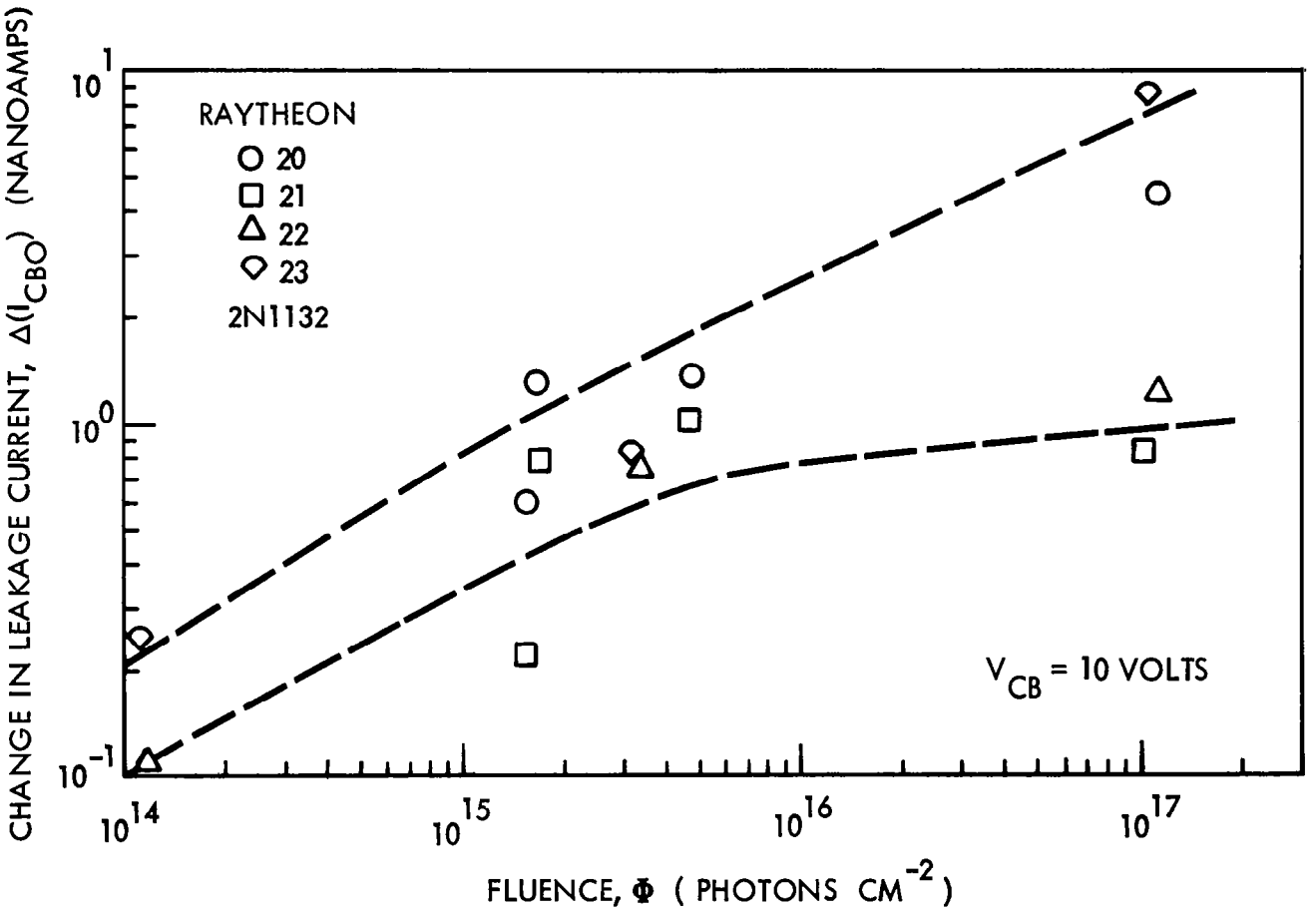

Figure 117. Dependence of $\Delta(I_{CBO})$ on Co^{60} Gamma-Ray Fluence (2N1132)

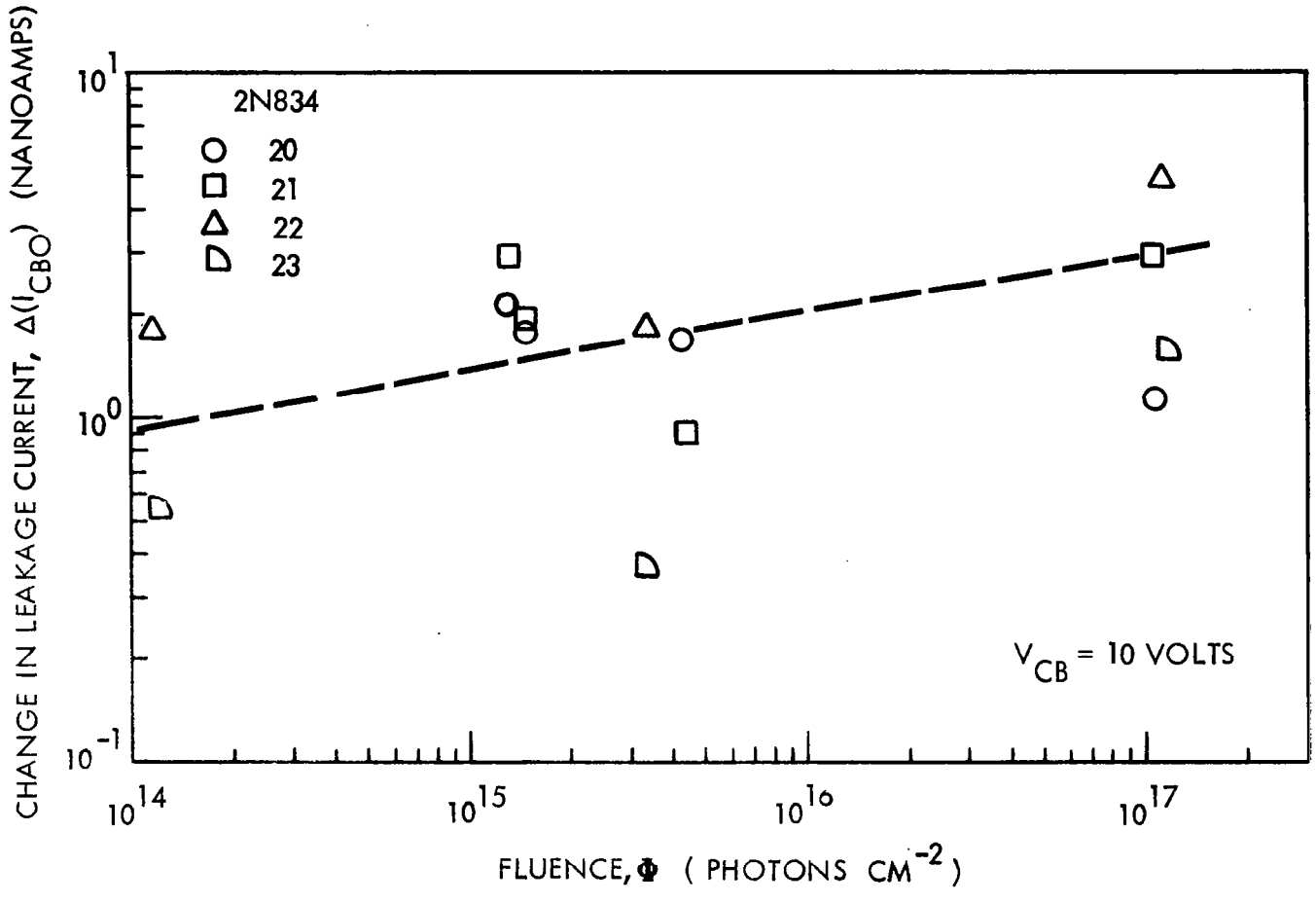

Figure 118. Dependence of $\Delta(I_{CBO})$ on Co^{60} Gamma-Ray Fluence (2N834)

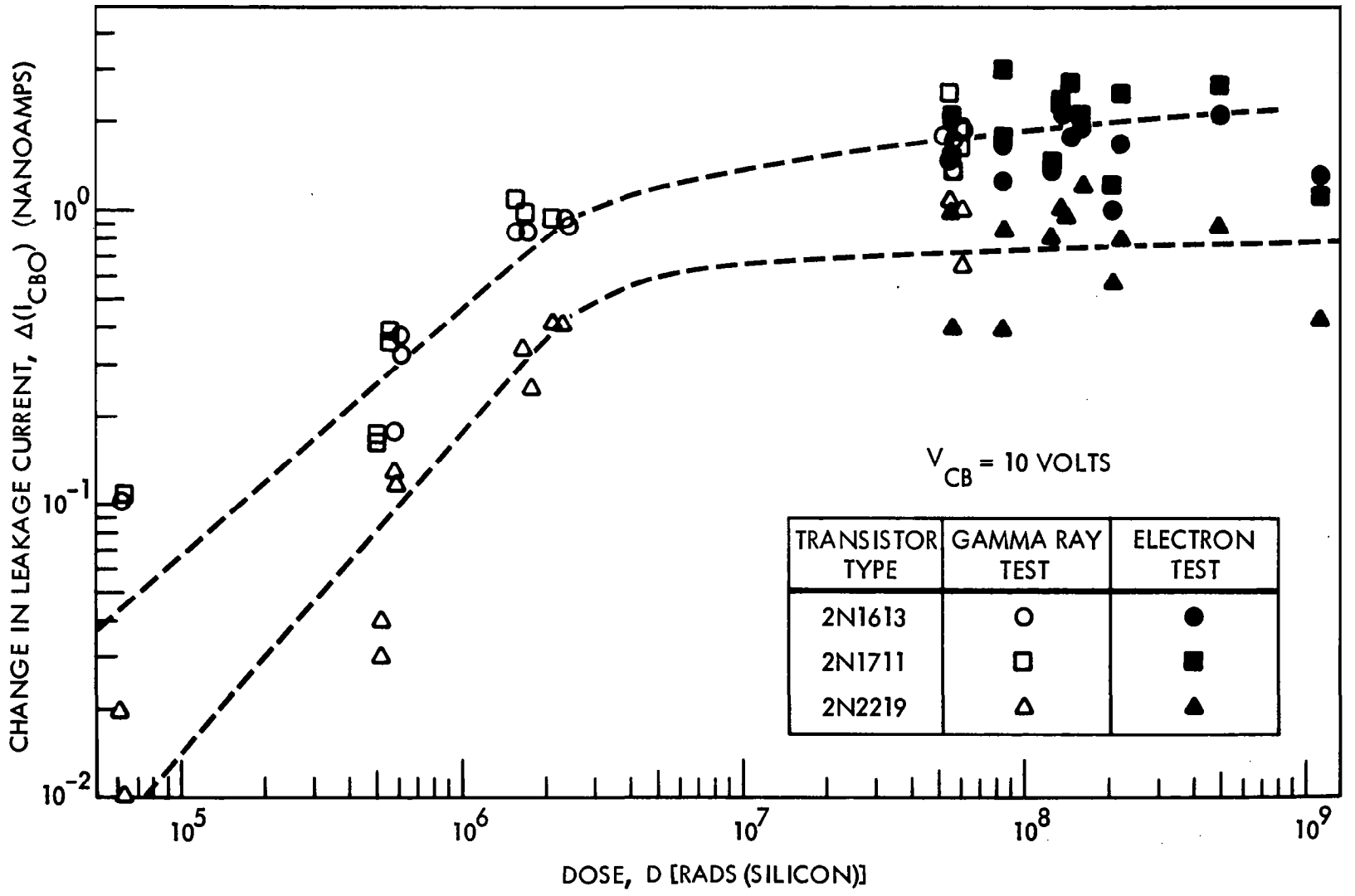

Figure 119. Dependence of $\Delta (I_{CBO})$ on Absorbed Dose (2N1613, 2N1711)

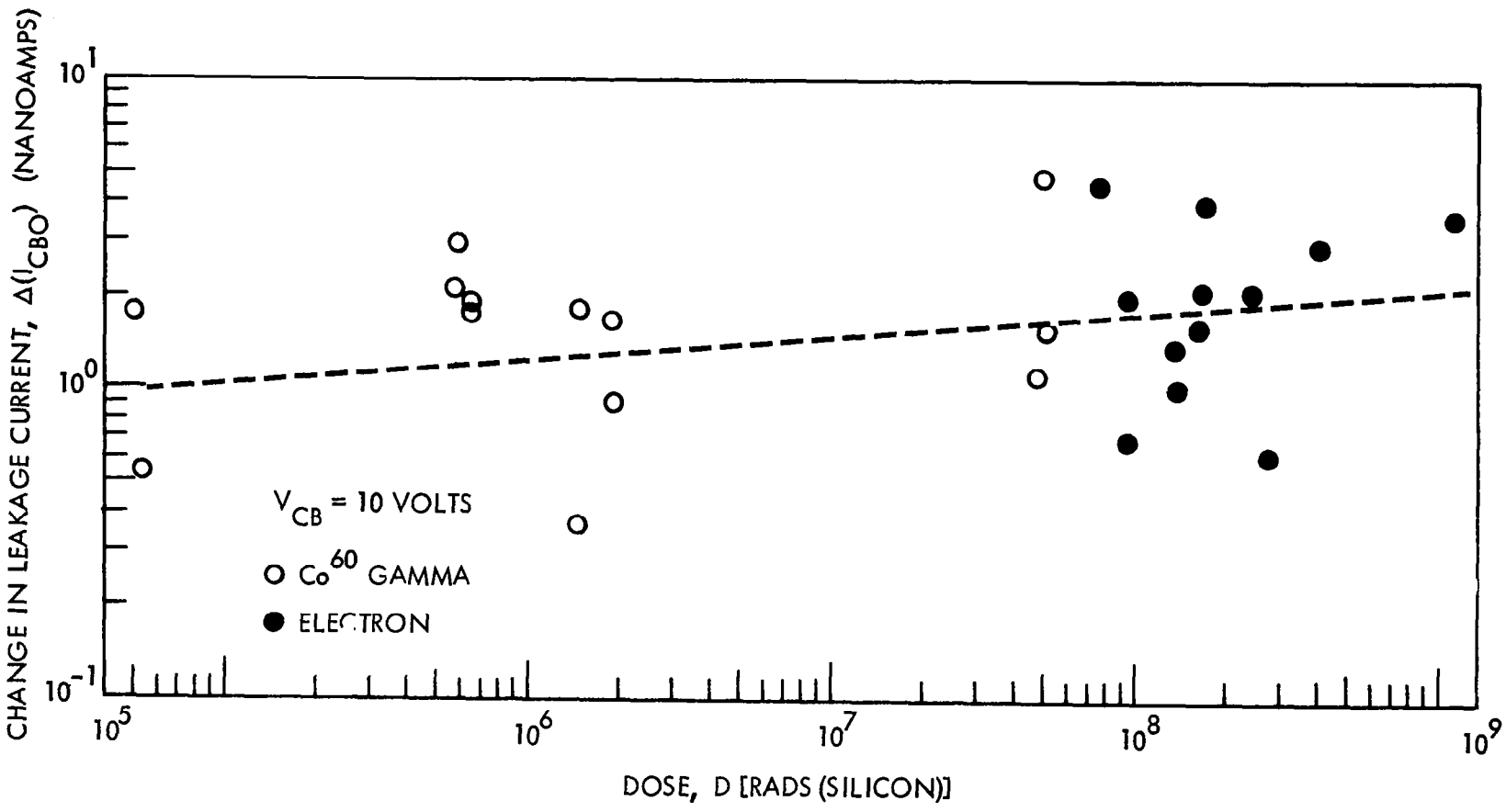

Figure 120. Dependence of $\Delta (I_{CBO})$ on Absorbed Dose (2N834)

identified with this type of damage. These characteristics include:

1. The dependence of nonlinear damage on emitter current;
2. The dependence of the dominance of nonlinear damage over linear damage on the type of semiconductor material and on transistor effective base width;
3. The semipermanency of this type of damage;
4. The apparent saturation of nonlinear damage at high exposures;
5. The possible dependence of nonlinear damage on processing control;
6. The dependence of nonlinear damage on absorbed dose rather than on the density of induced displacements; and
7. The identification of nonlinear damage with base-emitter recombination current.

Computer plots of $\Delta(h_{FE}^{-1})$ versus Φ (e.g., Figure 55) and earlier Boeing studies (Reference 14) indicate that the nonlinear damage is strongly dependent on the level of emitter current at which h_{FE} is measured, but is not strongly dependent on V_{CE}. This nonlinear damage was obtained for irradiation of devices that had no applied bias during irradiation. Figure 121 shows the dependence on emitter current of the change in h_{FE}^{-1} at $V_{CE} \simeq 0.4$ volts for a 2N1132 transistor exposed to 1.3×10^6 R of Co^{60} gamma rays.

The relative dominance of nonlinear damage over linear damage for electron exposure appears to be strongly dependent both on semiconductor-type npn versus pnp and on the value of f_T. This is illustrated in Figure 122 where the threshold for linear displacement damage caused by 0.53-Mev electrons is shown to be lower for the pnp device 2N2303 and to be dependent on f_T for the npn device. The threshold for nonlinear effects, however, does not appear to depend on f_T and, thus, effective base width. Transistors with narrow base widths would appear to be dominated to a greater extent by nonlinear damage than do low-frequency devices. The implication is that although high-frequency devices may be selected for a space mission in order that they be hard to displacement effects, these same devices may not be hard to ionization-induced nonlinear damage. Physical properties

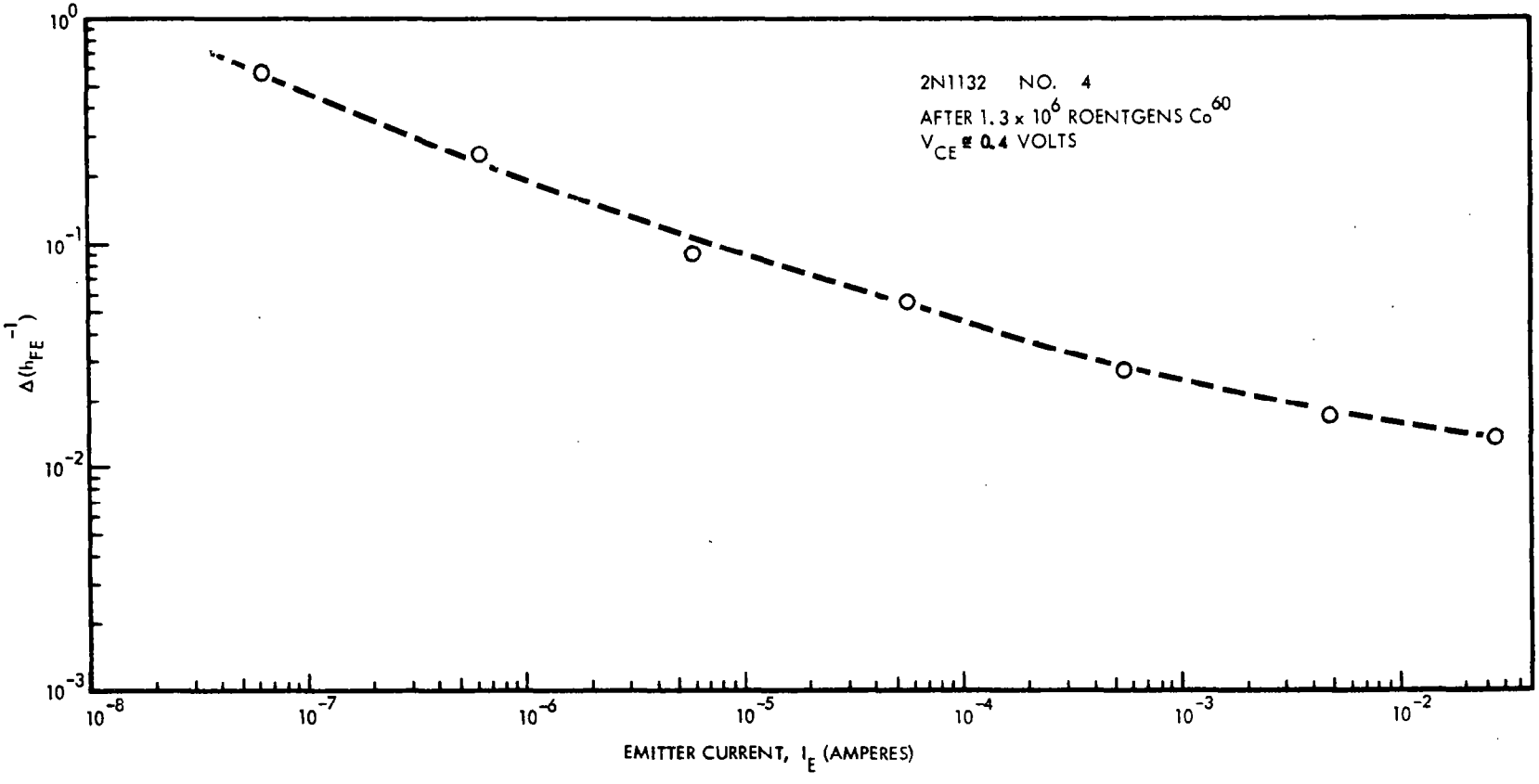

Figure 121. Dependence of Nonlinear Damage on Emitter Current

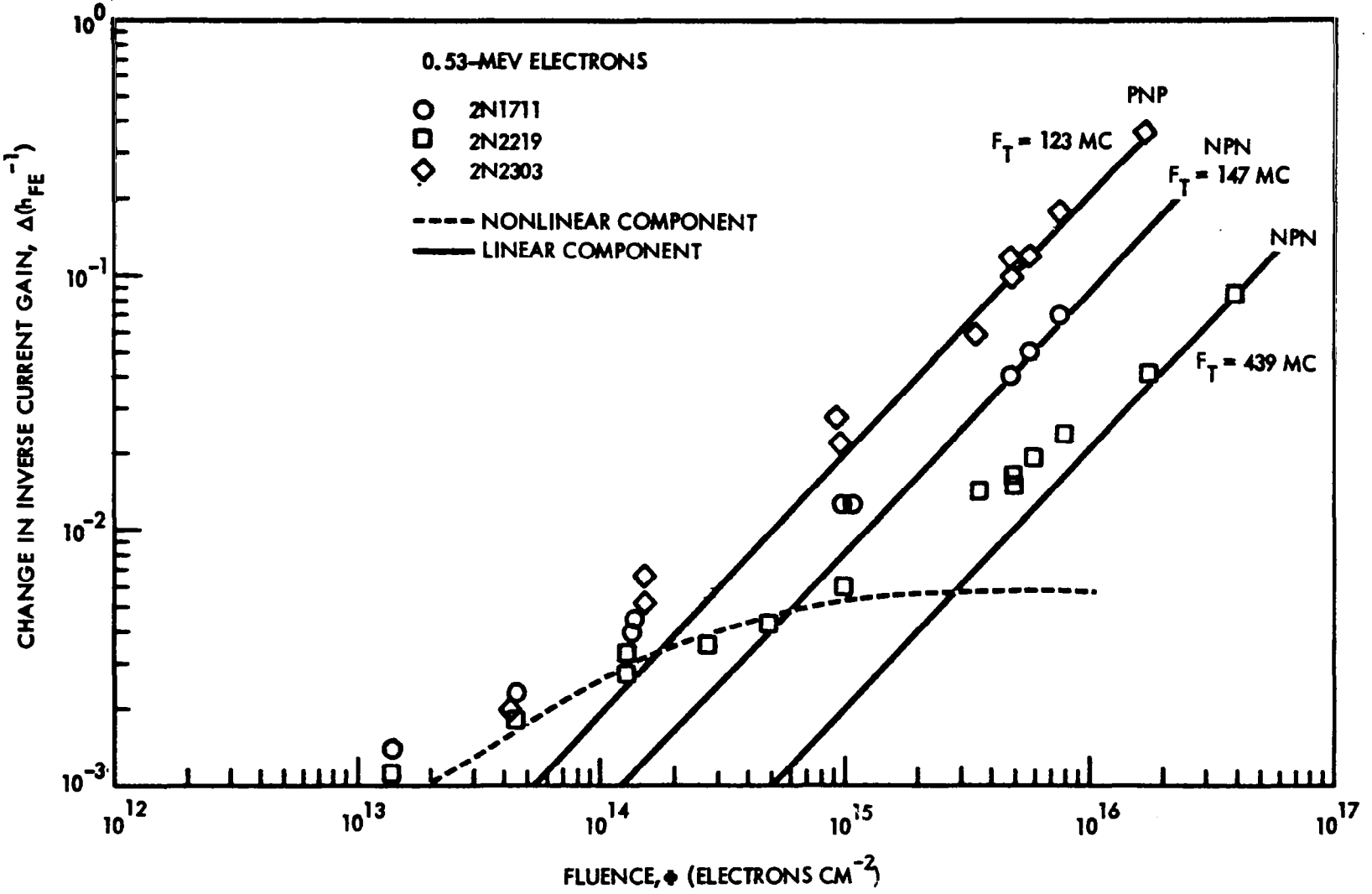

Figure 122. Relative Importance of Linear to Nonlinear Damage

(e.g., effective base width or frequency) that control sensitivity to linear displacement effects do not appear to determine the relative sensitivity of transistors to nonlinear effects which, in general, dominate damage for typical low exposure space missions.

Nonlinear damage appears to be semipermanent in nature, although not as short term as are surface channeling effects (Reference 30). Table 17(a) shows that although some room temperature recovery was noted for 2N2219 transistors that had been heavily exposed to 1-Mev protons, only slight annealing was observed even for a 24-hour bake at 250°C. Preliminary Boeing test data indicates that it is apparently the semipermanent "nonlinear" damage and not the dominant "linear" damage that is annealable. The recovery of nonlinear damage is shown in Table 17(b) both for transistors exposed to electrons and for transistors exposed to X rays of energy below the energy threshold for silicon displacements. From Table 17(b) it can be seen that practically all of the nonlinear damage of the exposed devices recovered after high-temperature treatment.

If ionization of the surface is the cause of the initial electron effects on current gain and if these effects are saturable, then it would seem reasonable to suggest that there may be a limited number of prospective surface sites, N_{s_i}. As these sites are acted upon, their number should decrease, resulting in eventual saturation of the effect. The conversion or rate of change of the prospective sites, N_s, with electron fluence would be expected to be proportional to the number available.

$$dN_s/d\Phi = K_i N_s \tag{28}$$

K_i of Equation (28) would be the energy-dependent ionization-damage constant, since it would include the ionization rate of the incident electron. Then integration of Equation (28) and application of the initial conditions ($\Phi_i = 0$, $N_s = N_{s_i}$) would lead to a relation for the growth of ionization-induced surface recombination sites, N_I, as a function of electron fluence.

Table 17. Annealing of Nonlinear Damage

(a) Annealing of Proton Damage (2N2219) (2.1×10^{14} protons/cm^2 -1 Mev)

NORMALIZED CURRENT GAIN (h_{FE}/h_{FE} initial) FOR ANNEALING TIME AND TEMPERATURE OF					
2219 Device No.	24 Hours at Room Temp	24 Days at Room Temp	42 Days at Room Temp	20 Min. at 100°C	22 Hours at 250°C
1	0.0184	0.0185	0.0196	0.0204	0.0506
2	0.0213	0.0227	0.0234	0.0238	0.0570
3	0.0195	0.0206	0.0210	0.0214	0.0650
4	0.0171	0.0179	0.0183	0.0186	0.0420

(b) Annealing of Nonlinear Electron-Induced Damage

Device Type	Exposure	Source	I_E (ma)	h_{FE}/h_{FE} (initial)	
				Before Annealing	22 Hours at 250°C
2N1711	4.75×10^{14} e/cm^2	1-Mev electrons	10	0.934	0.985
2N1613	4.75×10^{14} e/cm^2	1-Mev electrons	10	0.892	0.927
2N2303	4.75×10^{14} e/cm^2	1-Mev electrons	10	0.730	1.000
2N2801	4.75×10^{14} e/cm^2	1-Mev electrons	10	0.864	0.960
2N1613	1.15×10^5R	X rays (100 kvp)	0.2	0.715	1.000
2N1613	1.15×10^5R	X rays (100 kvp)	0.2	0.665	0.970

$$N_I = N_{s_i} [1 - \exp(-K_I \Phi)] \quad (29)$$

Applying Equation (29) to the observed degradation of current gain would modify the displacement equation for linear damage, as expressed in Equation (30).

$$\Delta(h_{FE}^{-1}) = C_s N_{s_i} [1 - \exp(-K_I \Phi)] + K_D \Phi \quad (30)$$

Figure 123 depicts gain degradation resulting from the 0.53-Mev electron test. The surface term of Equation (30) represents well the observed initial degradation of gain. The linear region of the curve of Figure 123 was extrapolated back and subtracted from the experimental curve in order to separate the postulated displacement and ionization damage. The dashed line, which represents this nonlinear damage, has indeed the shape of a saturation curve. With the constants evaluated, Equation (30), represented by the solid line, fits the experimental data of Figure 123.

Assuming that the so-called ionization-induced damage sites are a result of surface fabrication processes and ambient conditions at the time of fabrication, it seems reasonable that the number of defect sites per-unit-surface area would be similar for devices produced under similar conditions. Processing controls might well regulate the degree of nonlinear damage generated. It might then be expected that devices from different manufacturers would show varying degrees of regulation of nonlinear damage. If nonlinear changes in I_{CBO} of the collector base region are caused by a mechanism similar to that causing nonlinear damage of $\Delta(h_{FE}^{-1})$ in the base-emitter region, then the wide dispersion of $\Delta(I_{CBO})$ for Raytheon 2N1132 transistor (shown in Figure 117) compared to the closer clustering of $\Delta(I_{CBO})$ data points for Fairchild devices (shown in Figure 116) may be an indication of the importance of processing techniques or control.

Earlier tests using X rays of energies below the silicon displacement threshold indicated that permanent nonlinear damage is probably caused by ionization effects (Reference 14). This hypothesis appears to be further substantiated by the results of this research program. Although linear damage is dominant for protons which have a large value for the ratio of displacement cross section to ionization generation,

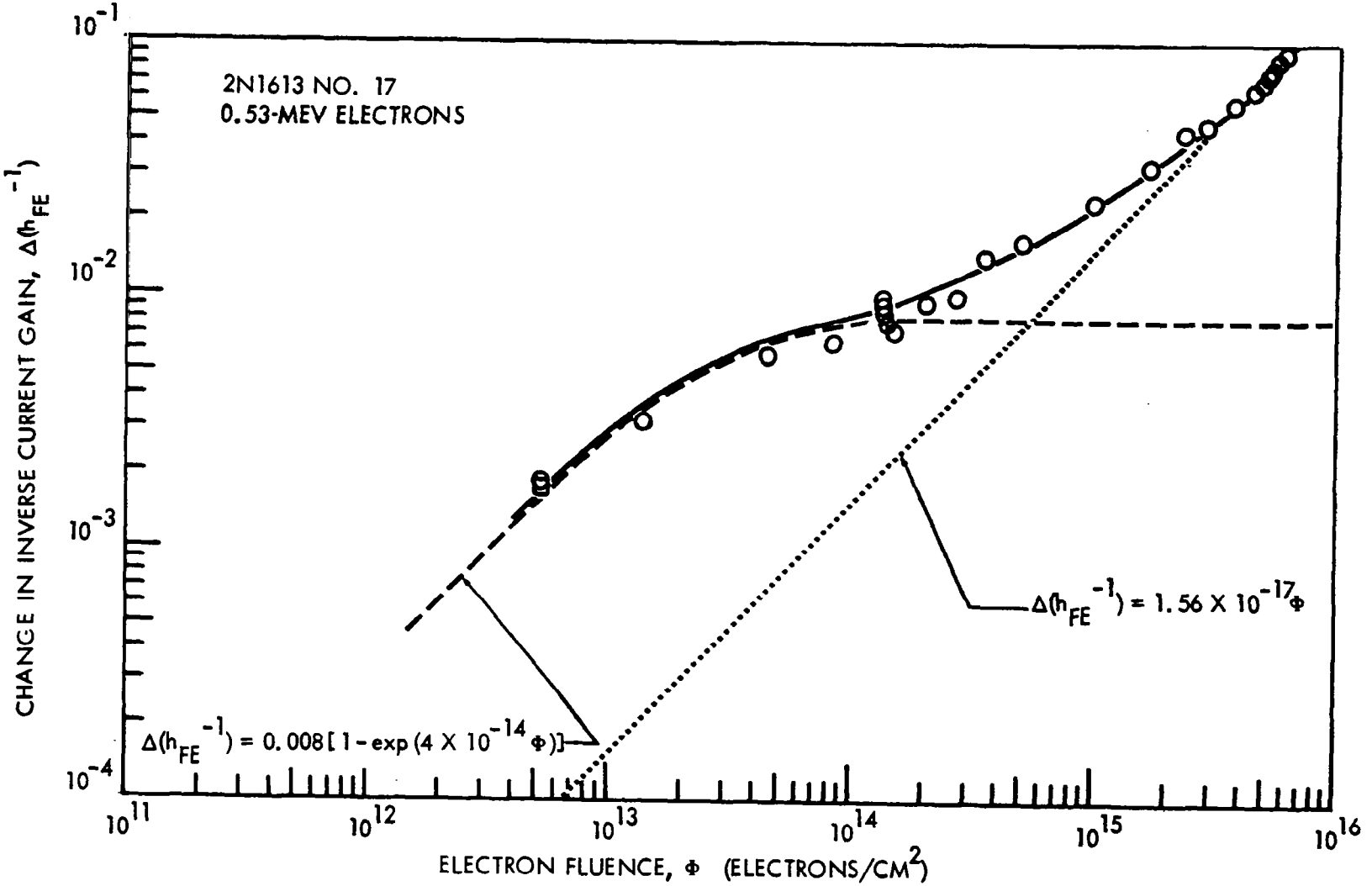

Figure 123. Separation of Nonlinear Damage

nonlinear damage becomes increasingly more pronounced as incident electron energy is reduced. An example was seen in Figure 94, where the displacement linear regions are well separated but the nonlinear regions for the three electron energies blend together. To check the influence of ionization, nonlinear damage, including a slight amount observed at threshold for the 1-Mev proton test, was separated for the 2N1613 devices. This data was first plotted as a function of particle fluence in Figure 124 and then as a function of absorbed dose in Figure 125. The results of Figure 125 (the electron data points pull closer together) appear to be a further strong argument for associating nonlinear damage with ionization.

Preliminary studies of the dependence of I_B on V_{BE} (Reference 9) were used to explore the source of nonlinear damage in transistors exposed to electrons and Co^{60} gamma rays. As described in Section 2.6.1, n components of base recombination current separated graphically from the dependence of I_B on V_{BE} can be used to locate regions of a transistor adversely affecting current gain of irradiated transistors. Figure 126 pictorially associates regions of a transistor with the various n components. A grown device is used for simplicity of display. Figure 127 shows changes in I_B for a 2N2801 transistor that has been exposed to 10^4R of Co^{60} gamma rays. For this low value of radiation exposure, only nonlinear damage was observed. A curve of the separated components of $\Delta(h_{FE}^{-1})$ versus gamma exposure is shown in Figure 128. This curve is for a different 2N2801 transistor, whose threshold for significant nonlinear damage is higher than the 10^4R exposure of the device shown in Figure 127. Significant nonlinear damage is dominated by the $n \tilde{=} 1.6$ component and has a threshold at an exposure less than an order of magnitude from that of the n = 1 component for linear displacement damage. From Figures 127 and 128 and similar data on other devices, it appears that an increase of recombination current associated with the surface of the base-emitter region is responsible for nonlinear damage. The relative sensitivities of the sources of transistor recombination current for those devices tested is summarized in Table 18 in relationship to space mission exposure.

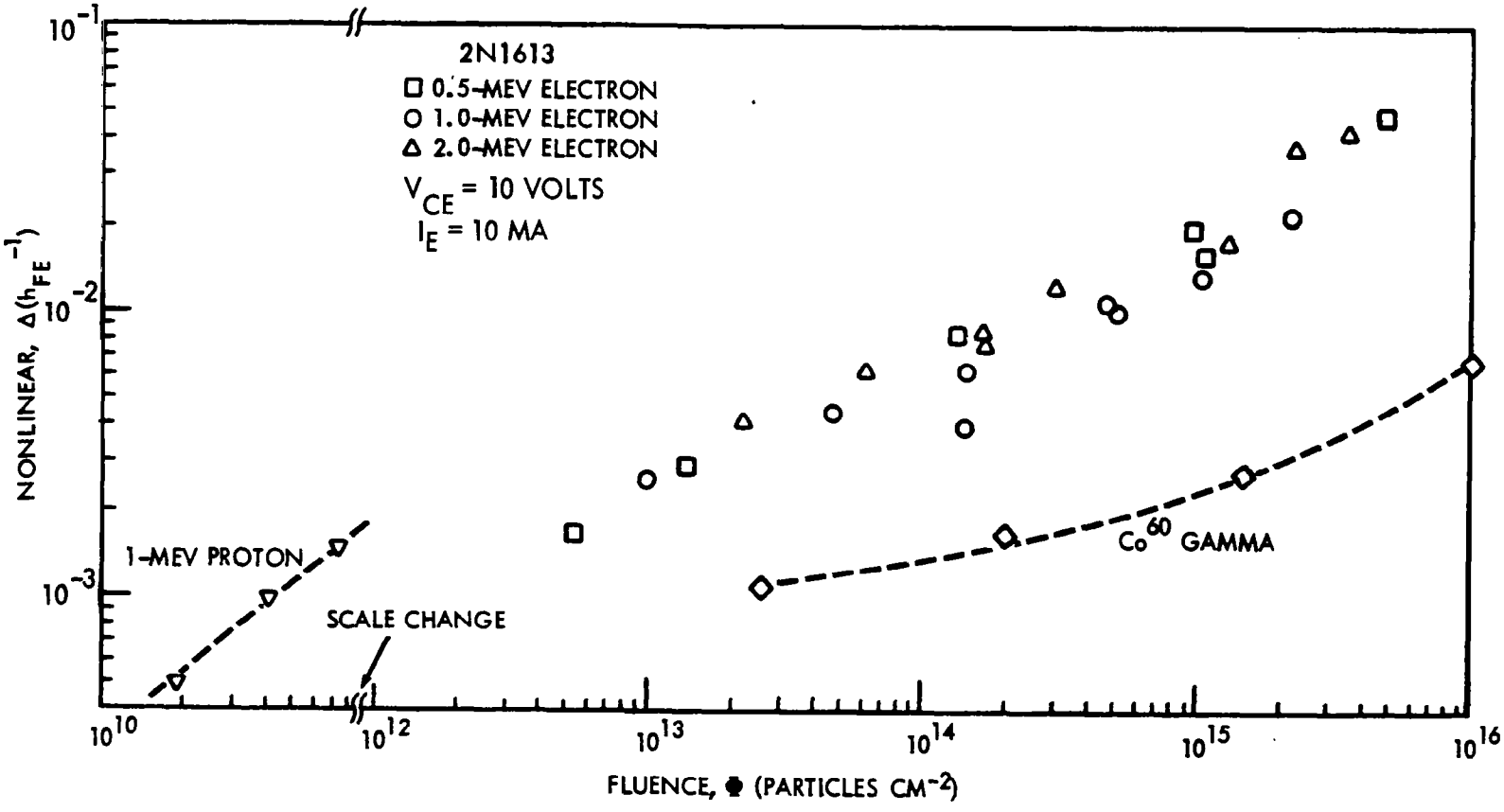

Figure 124. Nonlinear Damage Versus Particle Fluence

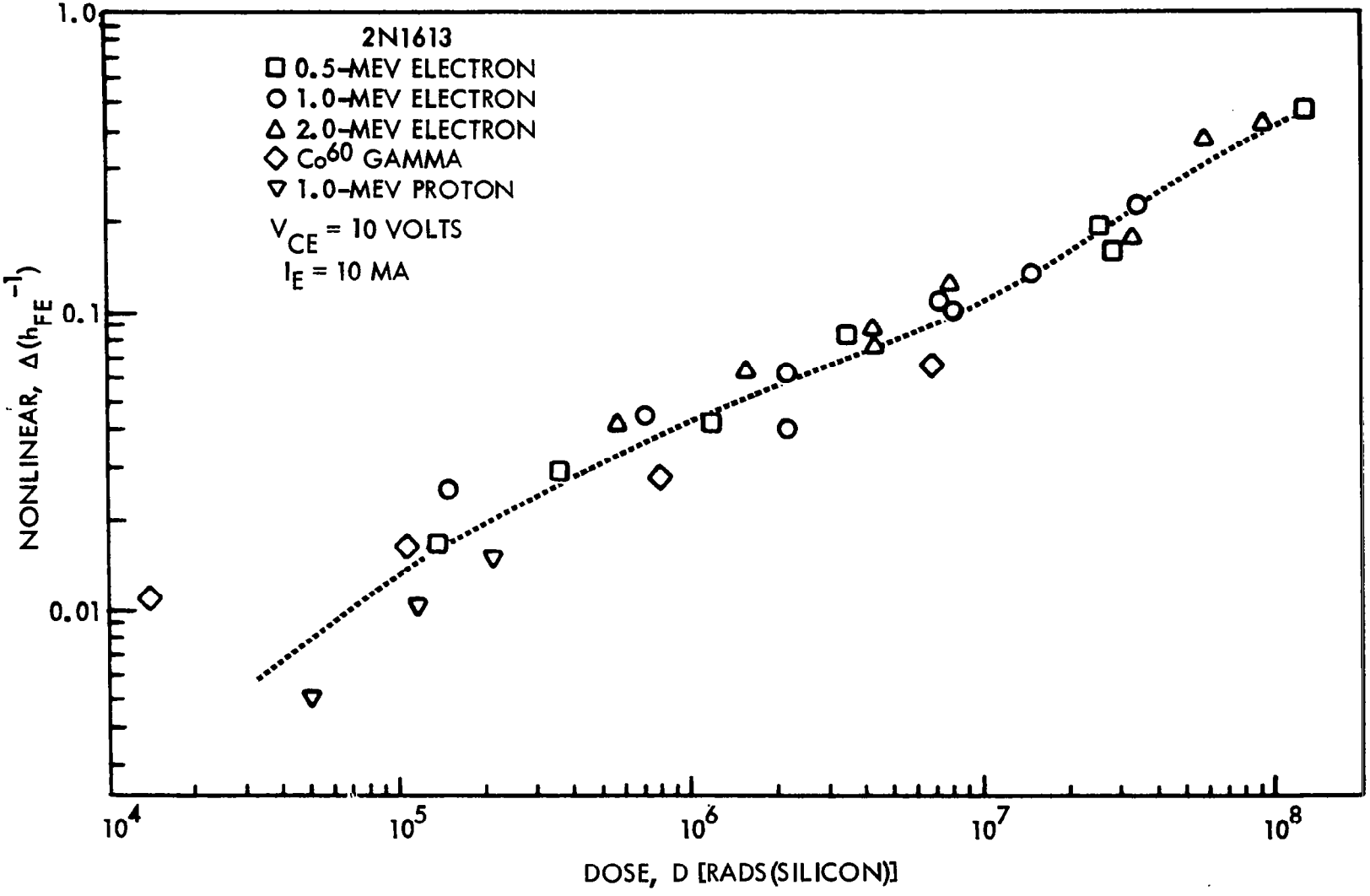

Figure 125. Nonlinear Damage Versus Absorbed Dose

$$I_n = I_{0n}(\phi) \exp(qV_{BE}/n\,KT)$$

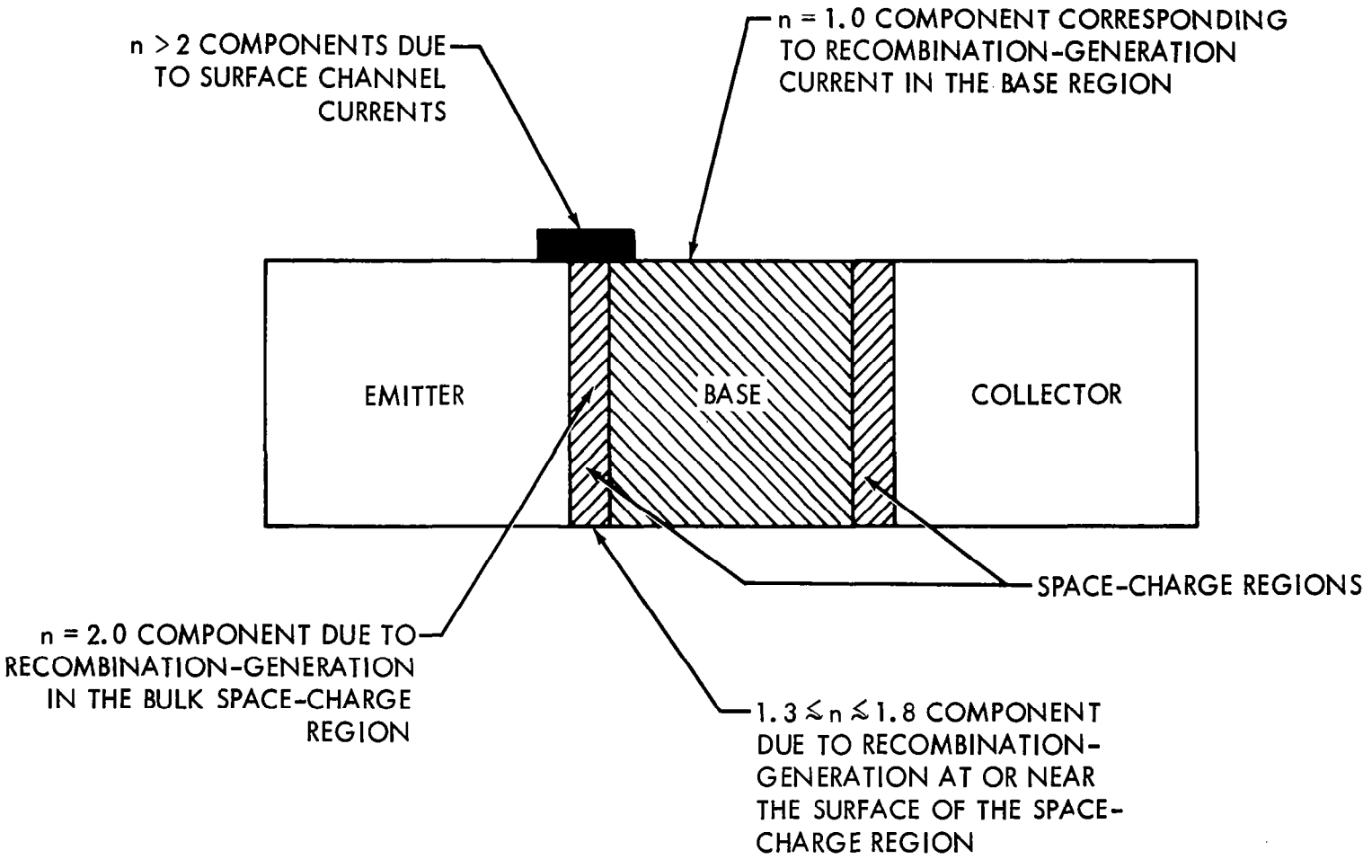

Figure 126. Components of Recombination Current

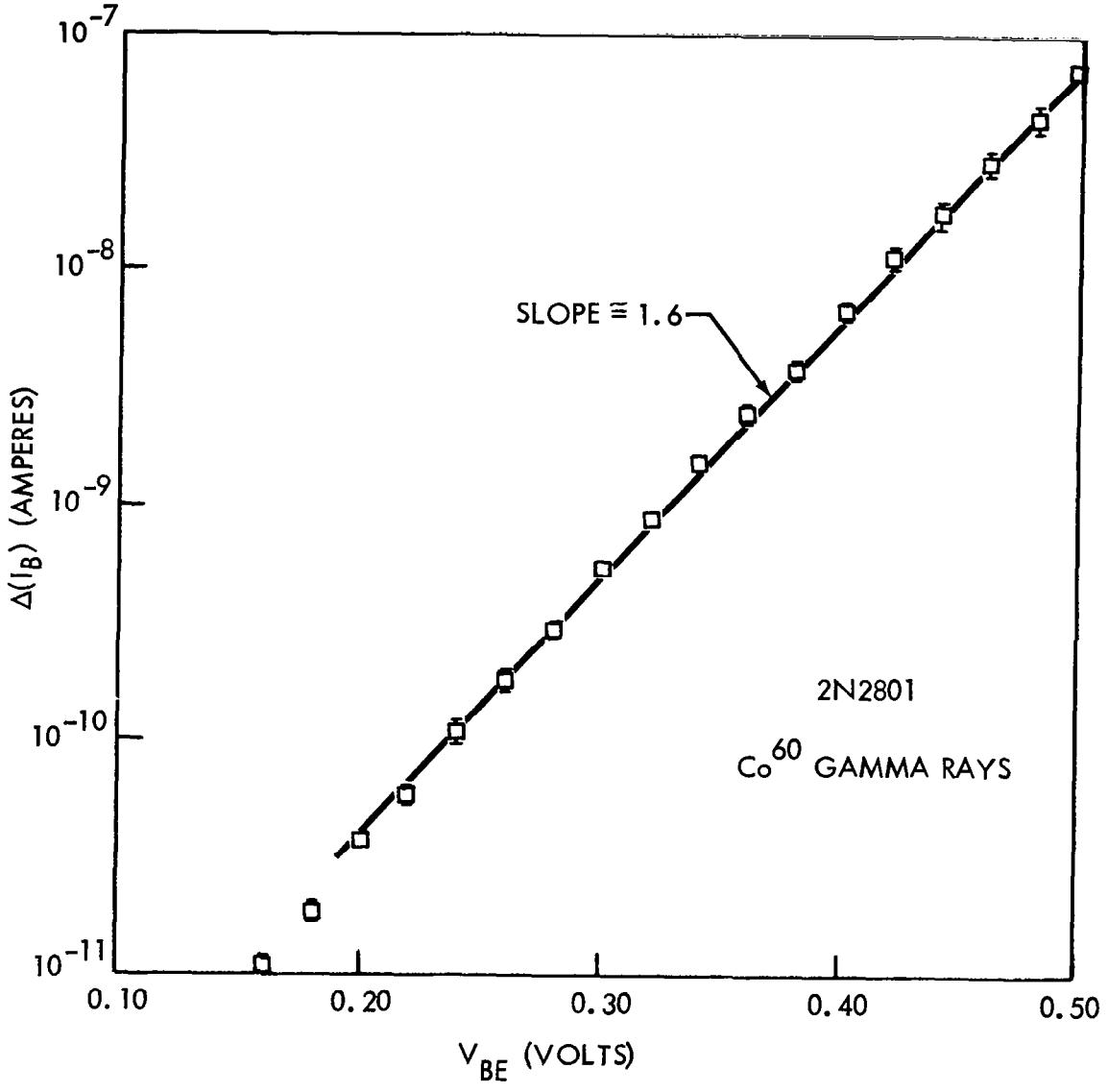

Figure 127. Change in I_B Versus V_{BE} After Exposure to 10^4R (Co^{60} Gamma)

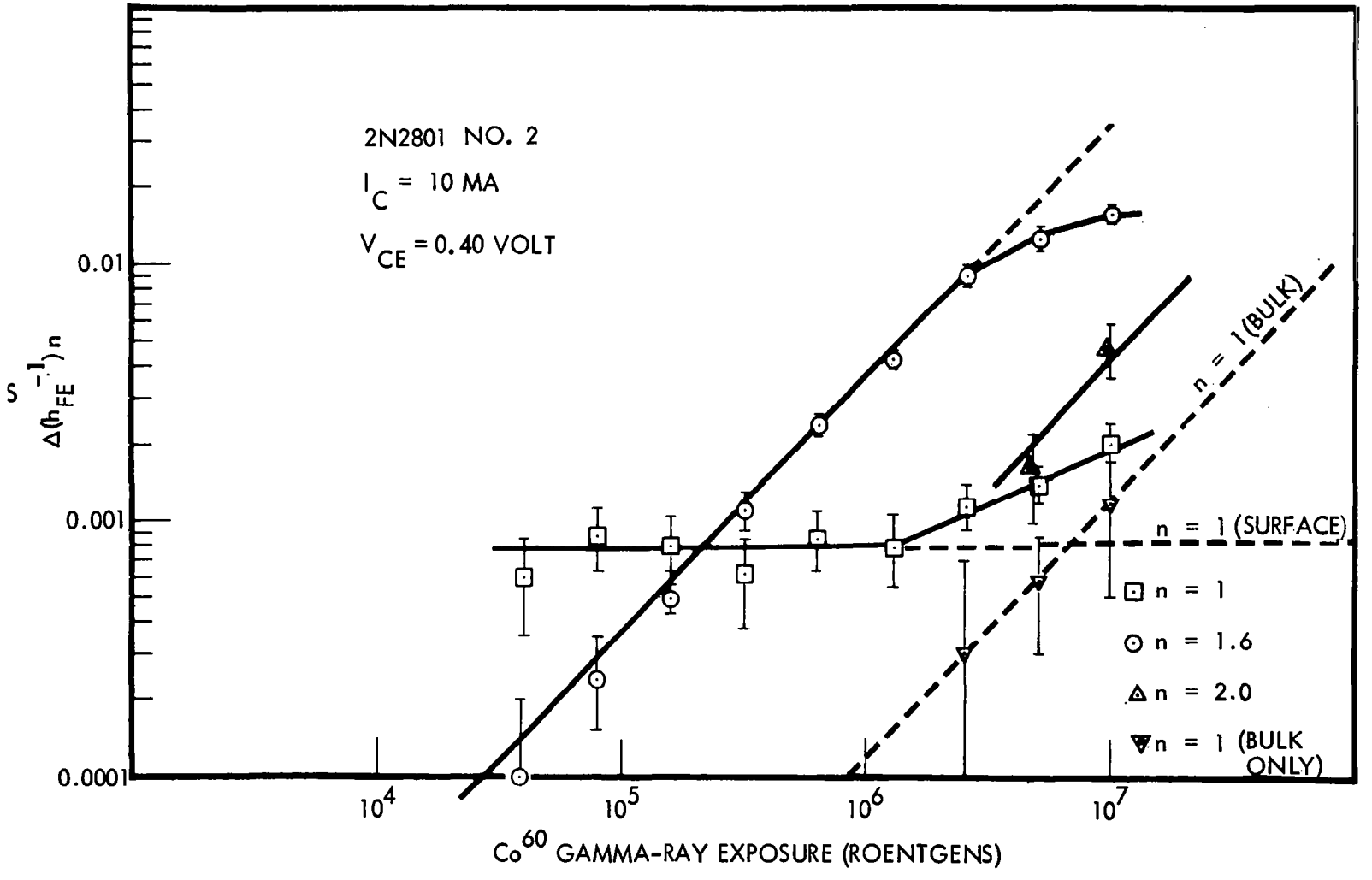

Figure 128. Separated Damage Components

Table 18. Relative Sensitivities of Transistor Regions

Experimentally Observed Recombination Component "n" Numbers	Postulated Recombination Component Regions	Approximate Time in the Maximum Electron Flux Encountered in the Van Allen Belt	
		Threshold Damage	Significant Damage
n = 1.0	Surface of the Base Region	~ 1 Day	Saturates Before Becoming Significant
n = 1.0	Bulk of the Base Region	~ 1 Month	~ 1 Year
$1.3 \lesssim n \lesssim 1.8$	Emitter-Base Space-Charge Region	Few Days	Few Weeks
n = 2.0		< Month	Few Months

3.0 NEW TECHNOLOGY

The research work performed on this contract has been reviewed. To the best of our knowledge there is no new technology to report.

4.0 CONCLUSIONS AND RECOMMENDATIONS

4.1 CONCLUSIONS

The following conclusions were obtained from analysis of test data.

1. Radiation equivalence information was successfully obtained for all of the transistor types tested.

- Displacement equivalences from analysis of $\Delta(h_{FE}^{-1})$ data indicated fairly consistent agreement between the 10 transistor types (both npn and pnp transistors).
- Good correlation was obtained between equivalences for permanent changes in h_{FE}^{-1}, $V_{CE}(sat)$, and I_{CBO}.
- Values of transistor damage constants obtained from transit time normalization of proton test data were consistent between devices of different types and manufacturers, in agreement with neutron studies reported in Reference 32.
- Nonlinear damage was observed to dominate linear damage for electron irradiation of interest for space missions.
- Damage constants obtained for electron irradiation were reasonably consistent between devices of the same type but showed considerable variation between types and manufacturers, possibly reflecting the influence of nonlinear damage.
- Electron and proton displacement equivalences (linear damage) yielded energy dependences for damage that are correlatable in part with displacement theory and in part with published solar cell data.
- Inherent shielding by transistor cans reduces protons of 14 to 17 Mev energy to lower energies that are significantly more effective for displacement damage.

2. Simulation of space radiation effects by Co^{60} gamma rays has limitations.

- Co^{60} gamma radiation can be useful in simulating the nonlinear I_{CBO} and h_{FE} degradation characteristics of electron exposure.
- Only at exposures in excess of approximately 10^8 R can the displacement effects of proton damage be partially simulated by Co^{60} gamma exposures, except possibly changes of $V_{CE}(sat)$.

3. The following characteristics of nonlinear damage appear to be evident.

- Nonlinear damage increases at a rapid rate for emitter currents below 10 ma.
- Nonlinear damage tends to saturate with increased radiation exposure, allowing for a separation of linear from nonlinear damage.
- The relative dominance of nonlinear damage over linear damage is a function of the threshold for displacement damage and the ionization-to-displacement ratio of the incident radiation.
- The dominant portion of nonlinear damage is induced by ionization rather than atomic displacement.
- Nonlinear damage is correlatable with increases in base-emitter recombination current, while linear damage is related to recombination current in the bulk of the base region.

4.2 RECOMMENDATIONS

The following recommendations are made for continued study of radiation equivalences:

1. Nonlinear damage should be more fully characterized, including

- Establishment of the functional dependence of nonlinear damage on emitter current.

- Determination of the statistical variation of nonlinear damage and its association with processing control.
- Firm establishment of the dependence of nonlinear damage on ionization to provide complete radiation equivalences for electron damage.
- Further exploration of the source and control of nonlinear damage.

2. The synergistics of combined effects should be checked by simultaneous exposures to protons and electrons to validate integration of linear and nonlinear effects over particle energy.

3. The influence of electrical bias (bias applied during radiation) on nonlinear damage, in particular, should be studied.

A flow chart illustrating the recommended tasks for a continuation of this research study is shown in Figure 129.

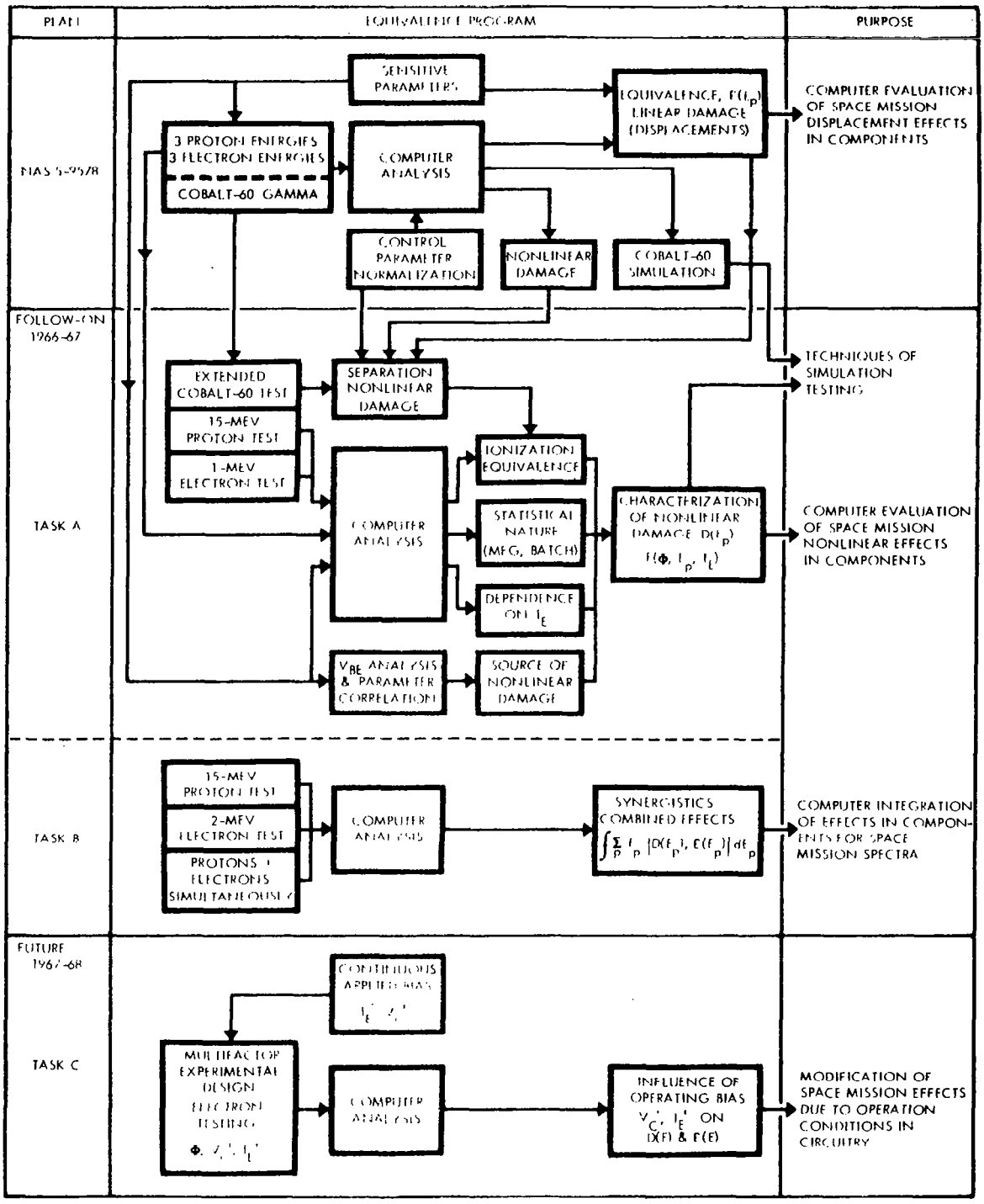

Figure 129. Recommended Follow-on Study

5.0 BIBLIOGRAPHY

1. Brown, R. R., and Horne, W. E., "The Effects of Electron Radiation on Transistors," Six-Month Progress Report for NAS 5-9578, Boeing Document D2-84088-1, December 1965. (See Appendix I)

2. Brown, R. R., "Identification of Radiation Preferred Electronics," Record of the 1965 International Space Electronics Symposium, Institute of Electrical and Electronic Engineers, Inc., New York, N. Y., 1965.

3. Easley, J. W., and Dooley, J. A., "On the Neutron Bombardment Reduction of Transistor Current Gain," J. Appl. Phys., Vol. 3, No. 6, 1960.

4. Goben, C. A., and Smits, F. M., "Anomalous Base Current Component in Neutron-Irradiated Transistors," Sandia Corporation Reprint SC-R-64-195, July 1964.

5. Goben, C. A., "A Study of the Neutron-Induced Base Current Component in Silicon Transistors," IEEE Trans. on Nuc. Sci., Vol. NS-12, No. 5, pp. 134-146, 1965.

6. Sah, C. T., "Effect of Recombinations and Channel on P-N Junction and Transistor Characteristics," IRE Trans. on Elec. Dev., Vol. ED-9, No. 1, 1962.

7. Sah, C. T., Noyce, R. N., and Shockley, W., "Carrier Generation and Recombination in P-N Junctions and P-N Junction Characteristics," Proc. IRE, Vol. 45, September 1957.

8. Iwerson, J. W. et al., "Low Current Alpha in Silicon Transistors," IRE Trans. on Elec. Dev., Vol. ED-9, No. 6, November 1962.

9. Horne, W. E., and Brown, R. R., "Correlation of Electron-Induced Changes in Transistor Gain With Components of Recombination Current," presented at the Annual IEEE Conference on Nuclear and Space Radiation Effects, Stanford University, July 1966 (to be published soon in IEEE Trans.)

10. Rooney, J. A., "Transistor Damage Plotting Program," Boeing Document AS1706, March 1964.

11. Webster, W. M., "On the Variation of Junction Transistor Current Amplification Factor With Emitter Current," Proc. IRE, Vol. 42, No. 6, pp. 914-920, June 1954.

12. Easley, J. W., "Comparison of Neutron Damage in Germanium and Silicon Transistors," Proceedings Third Semiannual Radiation Effects Symposium, Vol. 4, October 28-30, 1958.

13. Brown, R. R., "Equivalence of Radiation Particles for Permanent Damage in Semiconductor Devices," IEEE Trans. on Nuc. Sci., Vol. NS-10, No. 5, pp. 54-59, 1963.

14. Brown, R. R., "Proton and Electron Permanent Damage in Silicon Semiconductor Devices," in Radiation Effects in Electronics, STP-384, American Society for Testing and Materials, July 1965.

15. Phillips, A. B., Transistor Engineering and Introduction to Integrated Semiconductor Circuits, McGraw-Hill Book Co., New York, N. Y., 1962.

16. Thomas, D. E., and Moll, J. L., "Junction Transistor Short-Circuit Current Gain and Phase Determination," Proc. IRE, Vol. 46, pp. 1177-1184, June 1958.

17. Rich, M., and Madey, R., "Range-Energy Tables," UCRL-2301, March 1954.

18. Nelms, A. T., "Energy Loss and Range of Electrons and Positrons," N. B. S. Circular 577, July 26, 1956.

19. Mar, B. W., "An Electron Shielding Analysis for Space Vehicles," Nuc. Sci. and Eng., Vol. 24, pp. 193-199, 1966.

20. Loferski, J. J., and Rappaport, P., "Displacement Theory in Semiconductors," J. Appl. Phys., Vol. 30, No. 8, pp. 1296-1299, 1959.

21. Cahn, J. H., "Irradiation Damage in Germanium and Silicon Due to Electrons and Gamma Rays," J. Appl. Phys., Vol. 30, No. 8, p. 1310, 1959.

22. Honaker, W. C., and Bryant, F. R., "Irradiation of 40-Mev and 440-Mev Protons on Transistors," NASA TND-1490, Langley Research Center, January 1963.

23. Cummerow, R. L., "Photovoltaic Effect in P/N Junctions," Phys. Rev., Vol. 95, pp. 16-24, July 1, 1954.

24. Denney, J. M. et al., "Charged Particle Radiation Damage in Semiconductors, V: Effect of 1-Mev Electron Bombardment on Solar Cells," Space Technology Laboratories Report, MR-28, 8653-6018-KV-000, 1963.

25. Gremmelmaier, R., "Irradiation of P/N Junctions With Gamma Rays: A Method of Measuring Diffusion Lengths," Proc. IRE, Vol. 46, pp. 1045-1049, June 1958.

26. Seitz, F., and Koehler, J. S., "Displacement of Atoms During Irradiation", in Solid State Physics, Vol. 2, Academic Press, pp. 305-448, 1956.

27. Carter, J. R., and Downing, R. G., "Effects of Low Energy Protons and High Energy Electrons on Silicon," NASA CR-404, March 1966.

28. Dienes, G. J., and Vineyard, G. H., "Radiation Effects in Solids," Monographs in Physics and Astronomy, Vol. II, Interscience Publishers, Inc., 1957.

29. Simon, G. W., Denney, J. M., and Downing, R. G., "Energy Dependence of Proton Damage in Silicon," Phys. Rev., Vol. 129, No. 6, pp. 2454-2459, 1963.

30. Larin, F., and Niehaus, D. J., "A Generalized Approach to Transistor Damage by Radiation," Nucleonics, Vol. 22, No. 9, September 1964.

31. Peck, N. W., Blair, R. R., Brown, W. L., and Smits, F. M., "Surface Effects of Radiation on Transistors," Bell System Tech. Jour. XIII, No. 1, pp. 95-129, 1963.

32. Frank, M., and Larin, F., "Effect of Operating Conditions and Transistor Parameters on Gain Degradation," IEEE Trans. on Nuc. Sci., Vol. NS-12, No. 5, pp. 126-133, 1965.

6.0 GLOSSARY

A	Sensitive area of solar cell
A_c	Area of conduction path
A_s	Effective area for surface recombination
BV_{CBO}	Collector-base breakdown voltage
C_{Tc}	Collector transition capacitance
C_{Te}	Emitter transition capacitance
c	Constant used in various equations
D	Diffusion length
D_b	Minority-carrier diffusion constant in the base
D_{pb}	Hole diffusion constant in the base
E_f	Electron energy loss in foil
e	Electronic charge
f	Transit frequency
f_N	Normalization frequency
f_T	Gain-bandwidth frequency
f_α	Alpha cutoff frequency
G	Geometric constant
g	Generation rate of carriers
h	Height of the transmitted beam (100-Mev test)
h_{FE}	d.c. common-emitter current gain
h_{fe}	a.c. common-emitter current gain
I	Faraday cup current in amps

I_B	d.c. base current
I_C	d.c. collector current
I_{CBO}	Collector-base reverse current
I_E	d.c. emitter current
I_o	Leakage current of ideal diode
I_{o_n}	A constant used in the diode equation (I_B versus V_{BE})
I_{sc}	Short-circuit current of a solar cell
K, K_1	Damage constants
K'	Normalized damage constant (transistors)
K_D	Displacement-induced transistor damage constant
K_i	Energy-dependent ionization damage constant
K_θ	The excess phase constant
k	Boltzmann's constant
L	Diffusion length
L_e	Emitter diffusion length
L_n	Diffusion length of n region
L_o	Initial diffusion length
L_p	Diffusion length of p region
$M(\theta)$	Angular anisotropy correction factor
$N_{B'}$	Base impurity concentration at emitter junction
N_{BC}	Background impurity concentration
N_I	Ionization-induced surface damage recombination sites
N_i	Initial density of carrier-recombination centers

N_r	Radiation-induced defect sites
N_s	Prospective surface-damage sites
N_{s_i}	Initial density of prospective surface-damage sites
q	Electronic charge
R	Roentgen
R_L	Load resistance
r	Distance (target to sample)
S	Surface recombination velocity
T	Absolute temperature
t_b	Base-transit time
$V_{BE}(sat)$	Base-to-emitter saturation voltage (grounded emitter)
V_C	Collector voltage
V_{CB}	Collector-base voltage
$V_{CE}(sat)$	Collector-to-emitter saturation voltage (grounded emitter)
W	Effective base width
W_c	Width of collimating slit
Y	Count rate (scintillation counter)
α_o	The grounded emitter current gain (low frequency)
$\frac{dE}{dX}$	The rate of energy loss
θ	Scattering angle
τ_b	Minority-carrier lifetime in the base region
τ_{b_i}	Initial minority-carrier lifetime in the base region
ϕ	Particle flux

Φ	Particle fluence
σ_b	Conductivity of base region
σ_e	Conductivity of emitter region

APPENDIX I

SIX-MONTH PROGRESS REPORT FOR SPACE RADIATION EQUIVALENCE FOR EFFECTS ON TRANSISTORS D2-84088-1

ABSTRACT

This document constitutes the semi-annual progress report for NASA Goddard Contract NAS 5-9578. Included is a detailed description of research conducted during the period of May 15 through November 15, 1965. Experimental testing has been directed toward accomplishing the main objective which is the establishment of valid space radiation equivalences for transistor permanent damage. Research is progressing essentially in accordance with the program plan as outlined in the Boeing technical proposal document D2-90619, "Space Radiation Equivalence for Effects on Transistors," January 1965.

Transistors, representing selected semiconductor designs and construction types, were procured from among those devices currently preferred for space application. A description is given of equipment and the methods used for characterization of those transistor parameters which are sensitive to radiation or which control radiation damage.

Electron irradiation tests have been conducted at energies of 0.5, 1, and 2 Mev. Preparations for these tests including mapping of electron scattering, removal of inherent shielding, and development of test circuitry are described as well as the techniques used for reliable dosimetry and for dynamic data acquisition. The results of preliminary data analysis on selected transistors are presented as an indication of typical analyzed data that will be obtained from the computer damage-plotting program. These results indicate that values of base transit time can be used effectively to normalize the degradation of transistor current gain when bulk displacement damage is dominant. The data also indicates that the energy dependence of electron damage should be readily separable and should provide useful equivalence information. All of the transistor types, however, also displayed an initial degradation of current gain, over a significant electron exposure, which appears to be attributable to the effect of ionization on the surface recombination velocity. Post-irradiation data obtained using the Fairchild Series 500 Semiconductor Tester showed changes in the dependence of collector current on base turn-on voltage, $V_{BE}(on)$, as well as pronounced increases in leakage current, I_{CBO}, and in saturation voltage, $V_{CE}(sat)$.

During the remaining tests attempts will be made to obtain more detailed statistical data on the effectiveness of base transit time, t_b, as a normalizing parameter of permanent displacement damage. The relative merit of the three methods of measuring t_b will be further explored. Attempts will also be made to investigate: (1) the influence of emitter collection efficiency on gain degradation by careful measurement and analysis of $V_{BE}(on)$, and (2) methods of finding equivalences for radiation-induced changes in surface recombination velocity.

KEY WORDS

Base transit time
Damage normalization
Dynamic testing
Electrons
Permanent damage
Radiation equivalence
Surface effects
Transistors

ACKNOWLEDGMENTS

Particular thanks is to be extended to Chalmers R. Brittain II for tedious hours spent in reducing data and to Edward D. Sullivan for his part in assembling test equipment and patient acquisition of test data.

TABLE OF CONTENTS

LIST OF ILLUSTRATIONS

LIST OF ILLUSTRATIONS (Continued)

LIST OF TABLES

1.0 INTRODUCTION

1.1 PROGRAM DESCRIPTION

The objective of the program is the establishment of valid space radiation equivalences for permanent damage to silicon transistors. The phrase, radiation equivalence for permanent damage, is used to express the relative effectiveness of different types and energies of radiation for producing an equivalent amount of permanent damage.

Reliable silicon transistors of specified constructions and designs are to be selected for radiation effects testing. All of these transistors will be electrically characterized before and after radiation exposure. Selected devices will also be characterized during irradiation. In addition to obtaining oscillograms of common emitter characteristic curves, the following electrical parameters will be measured: d. c. and small-signal a. c. common-emitter current gain, base turn-on voltage, saturation voltages, breakdown voltage, leakage current, base transit time, alpha cut-off frequency, gain-bandwidth frequency, and transition capacitances.

Charged particle irradiation of transistors will be performed using electrons of energies of 0.5, 1, and 2 Mev and protons of energies of 1, 20, and 100 Mev. These tests should establish the radiation equivalences for permanent damage for significant radiation components of the Van Allen space environment. Gamma-ray equivalence for permanent damage will also be experimentally determined in order to assess the practicality of using cobalt-60 facilities for simulation testing of space radiation effects.

Data from oscillograms of transistor curve traces will be computer analyzed not only to show the dependence of radiation damage on particle fluence but also on radiation type and particle energy. Radiation equivalences for permanent damage, normalized to transistor base transit time, will be determined for all the types of radiation used in the test program. The results of this study will also be compared with data obtained in earlier Boeing studies using different particle

energies and different transistor types. Data will be presented whenever practical in a form that is most suited to the needs of design engineers.

1.2 PROGRESS SUMMARY

Silicon transistors of 10 registered types were selected for radiation effects testing and 40 of each type were procured. The 10 types represent two of each of five construction designs: npn and pnp diffused planar, npn and pnp epitaxial planar, and npn epitaxial mesa.

These transistors were electrically characterized using a Fairchild Series 500 Semiconductor Tester to measure selected values of current gain, base turn-on voltage, saturation voltages, breakdown voltage, and leakage current. Oscillograms were also obtained of transistor common-emitter characteristics displayed on a Tektronix 575 Curve Tracer. In addition, a correlation study was conducted in order to determine the relative merit of various means of data acquisition for normalization of the degradation of transistor current gain. Transistor parameters used for this study included: (1) gain bandwidth frequency as determined from measurements made with a General Radio Type 1607A Transfer Function and Immittance Bridge, (2) gain bandwidth frequency as determined from rise-time measurements using the Tektronix 567 Sampling Oscilloscope and associated equipment, (3) transition capacities obtained using the Boonton Capacity Bridge 74C-S8, and (4) base transit time obtained from a circuit specially designed for this purpose. Data analysis from this correlation study also provided information concerning the usefulness of the above methods for measuring these transistors over different ranges of effective base widths and ranges of collector currents.

Electron irradiation testing of transistors was conducted at energies of 0.5, 1, and 2 Mev. Prior to these tests scattering foils were procured and the flux of scattered electrons was mapped as a function of scattering angle. This mapping was also correlated with theoretical values which were obtained from a Monte Carlo computer program. In preparation for the 0.5-Mev electron test, the transistors were de-encapsulated to eliminate inherent shielding and selected measurements

were repeated to verify the continued stability of the device. In addition a test fixture was wired for remote selection of transistors and subsequent dynamic recording of transistor curve traces during the irradiation tests. For the 0.5- and 1-Mev electron tests, transistor ambient temperatures were monitored within the test chamber. Careful dosimetry was also performed to assure both a symmetric exposure of the transistor arrays and a valid determination of exposure fluences. A preliminary analysis of test data, from selected transistors, has been performed. Further detailed analysis of the information contained in oscillograms of transistor curve traces, obtained both during and after electron exposure, will be performed by use of the computer damage-plotting program.

2.0 DETAILED DISCUSSION OF PROGRESS

After all transistors needed for this study were procured and characterized electrically, a schedule for experimental testing was established. The accelerator facility was modified for the first tests (electrons) and both the transistors and the necessary test fixtures were prepared. Three electron irradiation tests were performed with both radiation dosimetry and transistor degradation being monitored dynamically. Following the tests the transistors were recharacterized electrically and a preliminary analysis of data ensued.

2.1 SELECTION OF TRANSISTORS

Ten registered types of silicon transistors were selected for radiation effects testing. Information which identifies those specific devices is listed in Table 1. Transistor selection was made on the basis of reliability and present utilization for missile and space vehicle electronic circuitry. These transistor types also represent three classes of design—epitaxial mesa, diffused planar, and epitaxial planar—which appear to be promising for future space system applications as well. Both npn and pnp semiconductor constructions were considered in order to permit a comparison to be made between radiation equivalences obtained from transistors with p- and n-type base regions. Two different registered transistors of each of the same class of construction designs (e.g., npn diffused planar) were selected in order to investigate the validity of extending radiation equivalence information to other transistor types of the same construction design.

Forty transistors of each type (400 total) were procured with the specification that transistors of the same type be of the same batch number (manufacture date). By so doing there is more assurance that the semiconductor batch, the construction details, and the surface conditions are the same. Thus, comparisons can be made between transistors irradiated with different types of radiation with a greater assurance of no marked differences in the devices themselves. These batch numbers are also listed in Table 1. All 40 devices of each of the transistor types listed were procured with a consistent set of batch numbers except for the 2N2303.

Table 1. Identification of Selected Transistor Types

Design	Construction	Registration Number	Manufacturer	Batch Number	Typical Use
Epitaxial mesa	npn	2N743	Texas Instruments	520A	Very high speed switching
	npn	2N834	Motorola	444	Very high speed switching
Diffused planar	npn	2N1613	Fairchild	436	Universal amplifier and switching
	npn	2N1711	Fairchild	513	Universal amplifier and switching
	pnp	2N1132	Raytheon	6511	VHf amplifier and switching
	pnp	2N2303	Fairchild	410 (435)	Medium frequency amplifier
Epitaxial planar	npn	2N2219	Fairchild	507	High speed switching
	npn	2N2538	Raytheon	6525	High speed switching
	pnp	2N2411	Texas Instruments	450A	VHf amplifier and very high speed switching
	pnp	2N2801	Motorola	324.	Medium speed switching and complementary circuitry

For this particular transistor type, six devices have a different batch number (No. 435). These six transistors will be included in the test as extra devices. Each one will be irradiated in conjunction with a mate 2N2303 of batch number 410 and the test results of each pair will be carefully compared. Batch numbers will also be useful for obtaining further information from the manufacturers concerning details of the manufacturing process if test results indicate the need.

2.2 ELECTRICAL CHARACTERIZATION OF TRANSISTORS

Transistor parameters which are radiation sensitive were measured with specialized equipment prior to radiation exposure. Transistor parameters which control radiation sensitivity were also measured in order to provide data for analytically normalizing the degradation of current gain for different transistors. Careful procedures were employed both during instrument calibration and during data acquisition. A study was also made to determine the validity of various methods of obtaining damage normalization parameters.

2.2.1 Measurement of Radiation Sensitive Parameters

Values of radiation sensitive parameters were measured by the use of a Fairchild Series 500 Semiconductor Tester, a Tektronix Model 575 Transistor Curve Tracer, and a measurement circuit for base turn-on voltage.

The Fairchild Series 500 Semiconductor Tester was programmed to automatically perform 16 transistor measurements in sequence with direct digital readout. This tester is of a modular construction and its capability is described in detail in its instruction manual and its electronic specification sheets (Reference 1). The test modules that were available for use in this research study include: (1) Test Module Model 500A which provides for both low power d.c. and pulsed d.c. (high current) measurements of current gain and of saturation voltage with readout accuracy of ±2 percent, and (2) Test Module Model 500B which provides for measurement of breakdown voltage and leakage current with ±1 percent readout accuracy. Also used for this program was Special Option H which provided the means for measuring base turn-on voltage with ±2 percent readout accuracy. In

addition, special low beta program cards were available for measuring h_{FE} in the range of 0.2 to 9. One additional accessory is the Wyle Environmental Chamber Model CN1060640 (-185°C to 325°C) which provides a means for controlling the ambient temperature of a transistor, during measurement, within a range of approximately -100°C to +200°C.

The Fairchild Series 500 is under constant surveillance by a factory-trained maintenance technician. Timing checks are made at three-week intervals and calibration checks are made at shorter periods by the use of a precision resistor plug-in unit. The tester underwent a complete checkout by factory representatives during the week prior to the start of measurements for this program.

The Fairchild Series 500 was programmed to measure the following transistor parameters: d.c. common emitter current gain, h_{FE}, at a collector voltage of 10 volts and at collector currents of 2 and 10 ma; base turn-on voltage at collector currents of 10, 50, 100, and 500 μa, 1, 2, 5, and 10 ma; $V_{CE}(sat)$ at 2 and 10 ma collector currents (with a gain of 2); $V_{BE}(sat)$ at 2 and 10 ma collector current (with a gain of 2); BV_{CBO} at 100 μa; and I_{CBO} at V_{CB} = 10 volts. A 30-minute warm-up time was allowed for the tester before the measurements were taken. The measured values were then read out sequentially in the order, top to bottom and left to right, as shown in Table 2 (a typical Fairchild 500 data sheet).

During these measurements the ambient temperature was maintained at 27°C ±1°. The actual temperature (±0.05°C) was recorded on the data sheets at the time of measurement readout. The transistors were handled with insulated pincers rather than fingers in order to assure temperature stability. Date and time were recorded on each data sheet with an automatic time stamp. To verify instrument repeatability, control transistors were measured periodically and the values were compared with standard values obtained earlier.

The Tektronix Model 575 Curve Tracer is described in detail in its instruction manual (Reference 2). The curve tracer is used in this study to display a family of transistor common-emitter characteristic curves. Regulated steps of base current are applied to the input of a transistor while a rectified sine wave is used to sweep

Table 2. A Typical Fairchild Series 500 Data Sheet

DEVICE TYPE: 2N1613 DEVICE NUMBER: 1

DATE: 10 August 1965 TIME: 1305 PARTICLE FLUENCE: 0

I_C (MA)	V_{BE}(on) (VOLTS)	BV_{CBO} (VOLTS)	h_{FE} (V_C = 10 VOLTS)	V_{CE}(sat) (VOLTS)	V_{BE}(sat) (VOLTS)	I_{CBO}(na) (V_{CB}=10 VOLTS)
0.01	0.518					
0.05	0.545					
0.10	0.562	118				
0.50	0.602					
1.0	0.620					
2.0	0.638		44.8	0.078	0.652	
5.0	0.663		---	---	---	
10.0	0.689		52.7	0.103	0.727	0.33

collector voltage. Five to ten current steps are selected with repetitive displays at 120 to 240 steps per second.

Three accessories were used with the curve tracer: (1) a Sorenson a. c. Voltage Regulator Model Number 1000S was used to provide ±1 percent control of the input voltage; (2) a Tektronix Model C27 Camera Assembly with an object to image ratio of 1:0.85 was recently procured to ensure complete presentation, including the full graticule scale, of characteristic curves on the oscillograms; (3) a ground glass viewer was used during calibration to eliminate possible error due to parallax. An additional accessory that has recently been made available is the Type 175 High Current Adapter which provides the capability for 100a peak continuous supply current and 1 kw continuous collector power.

Factory circuit specifications cite a maximum error of ±2 percent for: (1) collector voltage and volt-per-step selector, (2) collector current and ma-per-step selector, and (3) base current. Actual accuracy, however, is strongly dependent on precision calibration and zero adjusting. The curve tracer instruction manual suggests recalibration after 500 hours of use. A high degree of consistency in transistor oscillograms was obtained, however, by daily application of the following recalibration procedure:

1. A 20- to 30-minute warm-up time is allowed. (The manufacturer recommends 10 minutes.)

2. The -150 volt supply is set to ±0.1 percent of its nominal value by use of a Fluke Differential Voltmeter Model 801. The +100 volt and +300 volt power supplies, internal to curve tracer, are checked for a tolerance of ±3 percent of the nominal value.

3. The d. c. balance control is precisely set for both the vertical and the horizontal amplifiers.

4. Vertical gain and horizontal gain are set for both 0.5 and 0.01 base voltage.

5. The zero adjustment, the ± adjustment, and the volt/step adjustment are made as described in the curve tracer manual.

6. The step-selector switch is checked using 1 percent precision resistors.

7. An oscillogram is taken of the 2N1613 control transistor and it is compared with the standard oscillograms obtained earlier. A current gain variation of no greater than 2 percent is allowed between oscillograms.

Zero adjustment of the display is set each time an oscillogram is taken. The step zero adjustment is used to displace the oscilloscope display toward the graticule line of zero-collector current. As the display is shifted, a position is reached at which the zero-current trace no longer moves. When this position is determined, further adjustment is made with the vertical-position and horizontal-position controls. These controls are used (for npn transistors) to place the lower left hand portion of the display in coincidence with the lower left hand corner of the graticule scale. (For pnp transistors the coincidence is established at the upper right hand corner.) All oscillograms for this program have been taken by the same technician in order to maintain the maximum degree of consistency. These oscillograms were taken before, during, and after irradiation tests.

A typical oscillogram of a set of transistor common-emitter characteristic curves taken before irradiation is shown in Figure 1a. The ordinate represents collector current, I_C. The abscissa represents collector voltage, V_C. A family of base-current curves is shown. Writing on the face of the oscillogram identifies the transistor as device number 4 of transistor type 2N1711 used in test number 21 (2 Mev electrons). There are eight I_B current steps, counting the zero step, and collector voltage for each of these steps is over a range of 7 centimeters. This serial identification numbering is used to key punch the picture heading card and data cards at the oscillogram reader facility. Figure 1b shows the back of the oscillogram. Listed is pertinent data recorded at the time the picture was taken. This includes the I_B current per step, particle fluence, temperature, etc. This data will be used as input information for a transistor damage-plotting program to be analyzed using an SRU 1107 Computer.

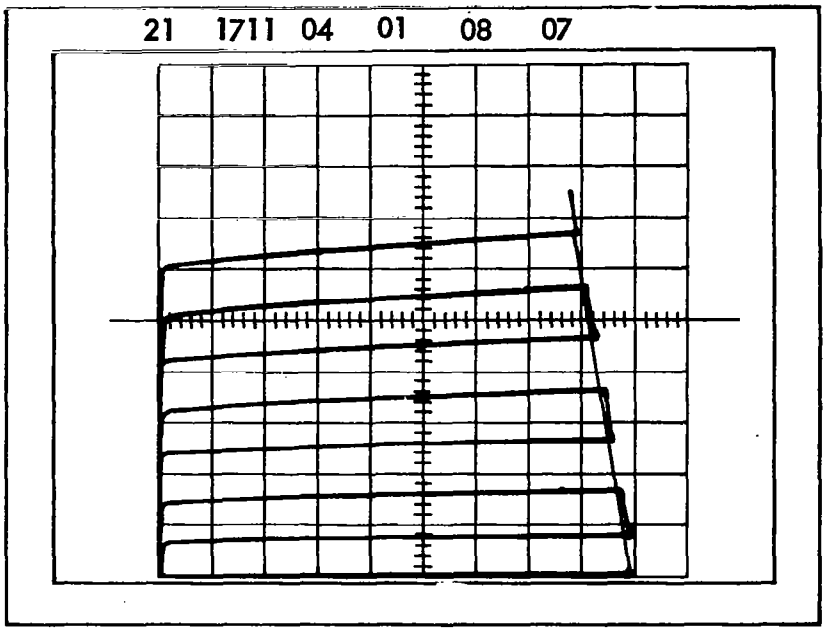

A. Front View

PIC	IB	VC	DATE	TIME
A1	07	08	072865	0927

V/D	IC/D	IBSTEP	RL
2.0V	2.0 ma	0.01 ma	0.0001 megohms

FLU.	TEMP.
0	26.5°C

B. Back View

Figure 1. Oscillogram of a Set of Characteristic Curves

Values of some of the more sensitive parameters measured on the control transistors (numbered 1) of the 10 transistor types are shown in Table 3. The a. c. current gain is also determined for most of the devices by use of the base transit time circuit described in Section 2. 2. 2.

A measurement circuit for base turn-on voltage was used to obtain I_B and I_C as a function of V_{BE}(on). This circuit, shown in Figure 2, was designed and built at Boeing.

A plot of typical data obtained from this circuit is shown in Figure 3. The divergence of the collector and base currents from the straight lines is caused by the transverse voltage drop in the base region (Reference 3). If the straight line portion of the collector current is extrapolated upward, then the voltage deviation can be determined as the voltage difference between the measured points and the extrapolated line. The voltage increment determined from the collector current can then be subtracted from the base current voltages to correct for the deviation. This yields lines with three distinct slopes. By extrapolating the intermediate portion of the curve to both higher and lower currents and subtracting it from the lower and upper regions one obtains three components of base current with reciprocal slopes of approximately $2\ kTq^{-1}$, $1.5\ kTq^{-1}$, and kTq^{-1} as shown in Figure 4. The three components have been identified as originating in the transition (space charge) region, at the perimeter of the emitter (that is, where the emitter base junction intersects the surface), and in the bulk region of the base, respectively (Reference 3).

2. 2. 2 Measurement of Radiation Control Parameters

The common-emitter current gain of a minority carrier injection-type transistor can be related to various regions and physical parameters of the transistor. For charged particle degradation of transistor current gain, which can be attributed to atomic displacements generated in the base region, the following dependence of d. c, current gain has been observed (Reference 4).

Table 3. Selected Values of Sensitive Parameters
(at 10 volts and/or 2 ma)

CONTROL TRANSISTORS (NUMBERED 1)	h_{FE}	h_{fe}	V_{BE}(on) (VOLTS)	V_{CE}(sat) (VOLTS)	V_{BE}(sat) (VOLTS)	I_{CBO} (NA)
2N743	25.3	39	0.684	0.104	0.700	2.42
2N834	93.7	114	0.675	0.137	0.688	13.3
2N1613	44.8	50.5	0.638	0.078	0.652	0.33
2N1711	185	196.5	0.600	0.051	0.639	0.11
2N1132	60.0	62.5	0.674	0.030	0.691	0.10
2N2303	139	127	0.619	0.049	0.652	0.20
2N2219	97.9	112.5	0.636	0.013	0.687	0.06
2N2538	77.5	95.3	0.629	0.100	0.643	9.93
2N2411	92.0	88.0	0.705	0.085	0.719	0.90
2N2801	94.0	91.5	0.636	0.022	0.650	0.35

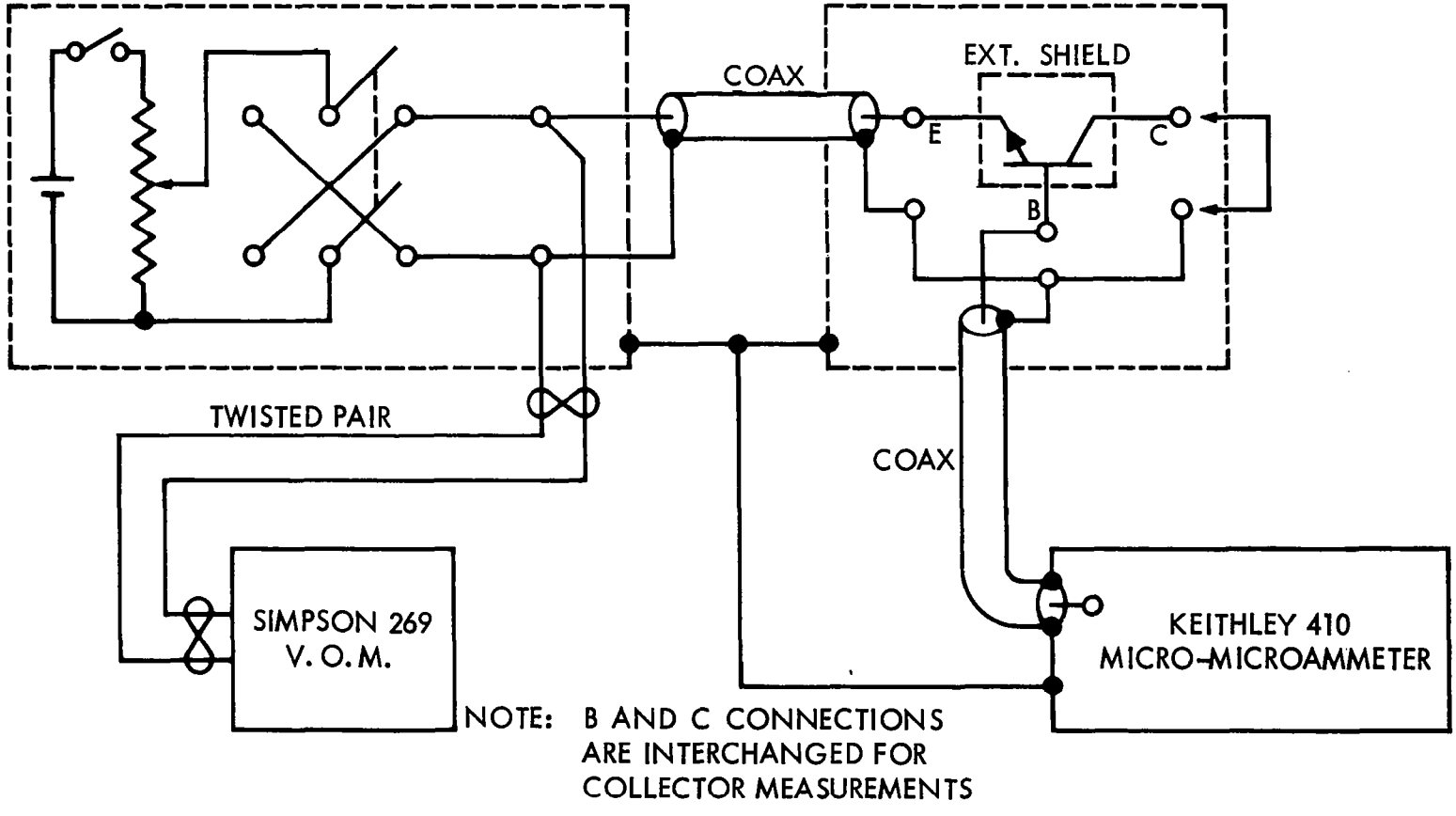

Figure 2. Circuit for V_{BE}(on) Measurement

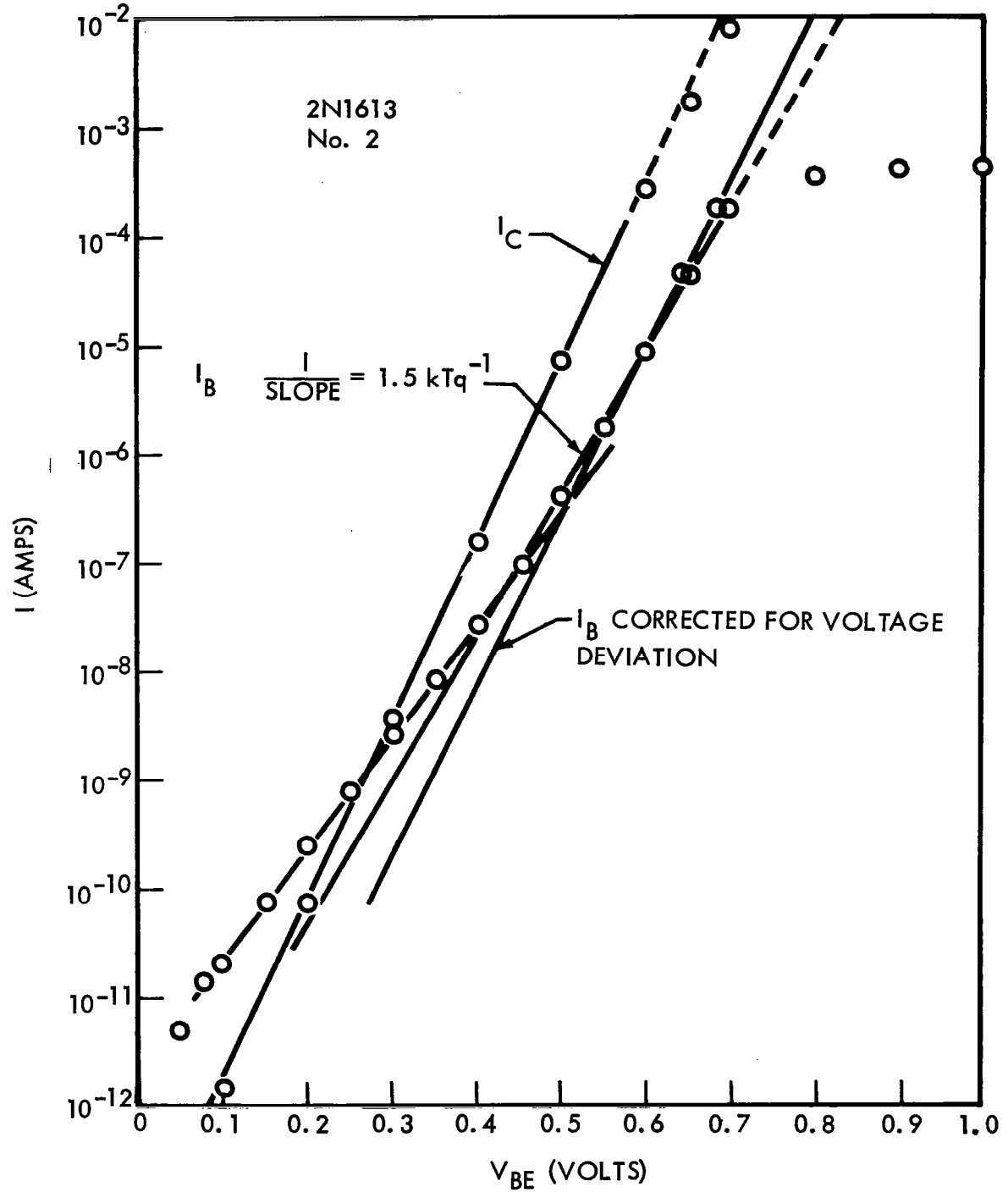

Figure 3. I_B and I_C Versus V_{BE}

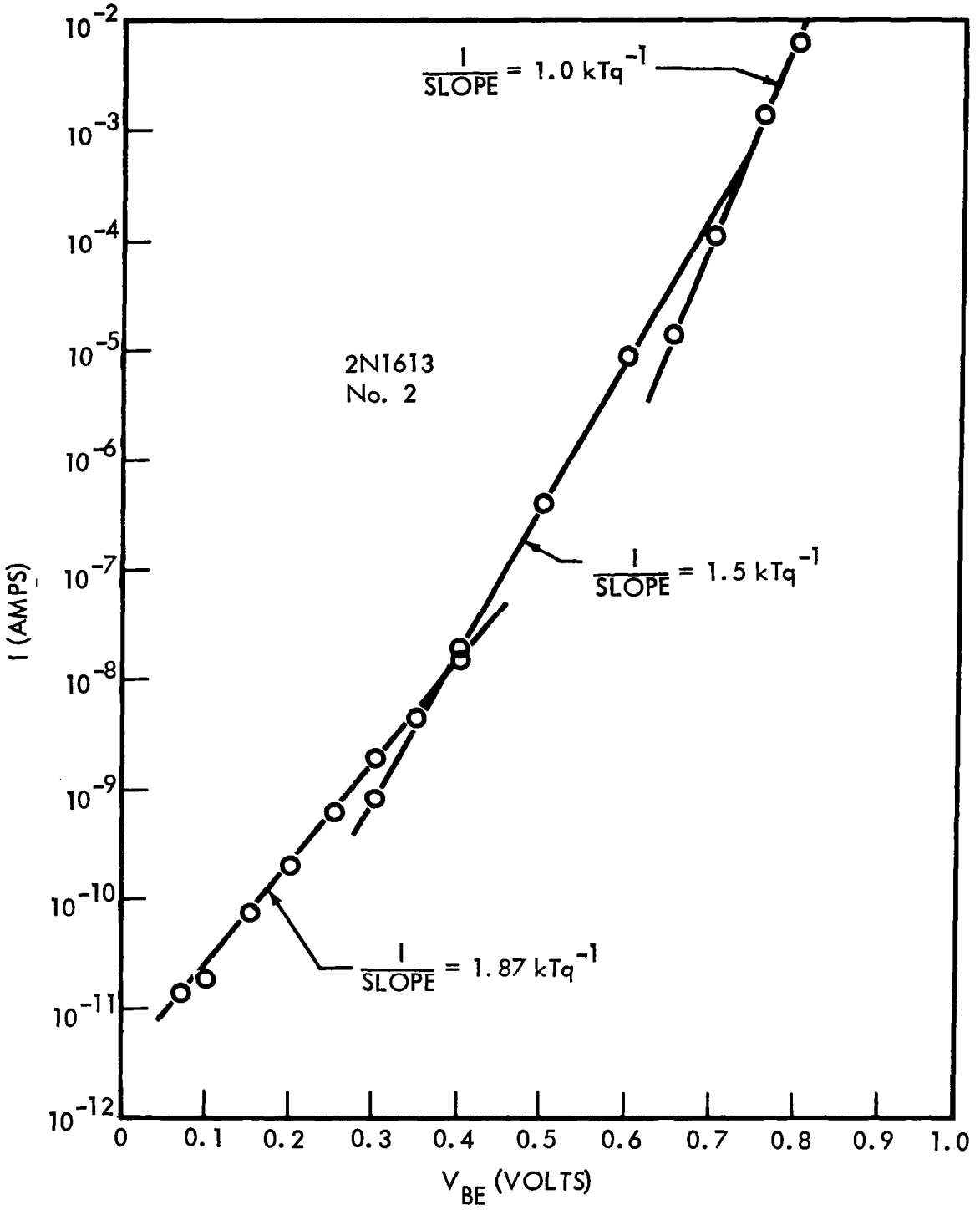

Figure 4. Resolved Components of I_B Versus V_{BE}(on)

$$\Delta(1/h_{FE}) = 0.5\ W^2 D_b^{-1}\ \Delta(1/\tau_b) = K\Phi \qquad (1)$$

where W = effective base width

D_b = minority carrier diffusion constant in the base

τ_b = minority carrier lifetime in the base region

K = damage constant

Φ = charged particle fluence

According to Equation 1 current gain degradation can be normalized provided the radiation control parameters can be evaluated. It is desirable to determine transistor base transit time since it also is a function of $W^2 D_b^{-1}$. Such a determination, however, requires the measurement of either the alpha cut-off frequency or gain-bandwidth frequency as well as an evaluation of emitter and collector transition capacities.

Values of these transistor parameters that are needed in order to determine radiation control parameters were measured by the use of the following equipment: A General Radio Type 1607A Transfer Function and Immittance Bridge, a Tektronix 567 Sampling Oscilloscope, a Boonton Capacity Bridge, and a specially designed base transit time circuit.

A block diagram of the General Radio Type 1607A Transfer Function and Immittance Bridge and the accessories used to determine gain bandwidth frequency (f_T) is shown in Figure 5. The system is essentially a balancing bridge used to determine a.c. current gain at high frequencies. Detailed capabilities of the type 1607A bridge are described in the operator's manual (Reference 5). The amplitude (real part) and the phase (imaginary part) of the collector current of a transistor are balanced against the base current (through variable current loops) by the use of the null detector. The variable current loops, A and B, are calibrated against a resistance standard and a susceptance standard respectively (50 ohm impedance). The magnitude of the base-drive current is set by ar indicator (multiplier), M. The a.c. current gain at the fixed frequency is then determined from Equation 2.

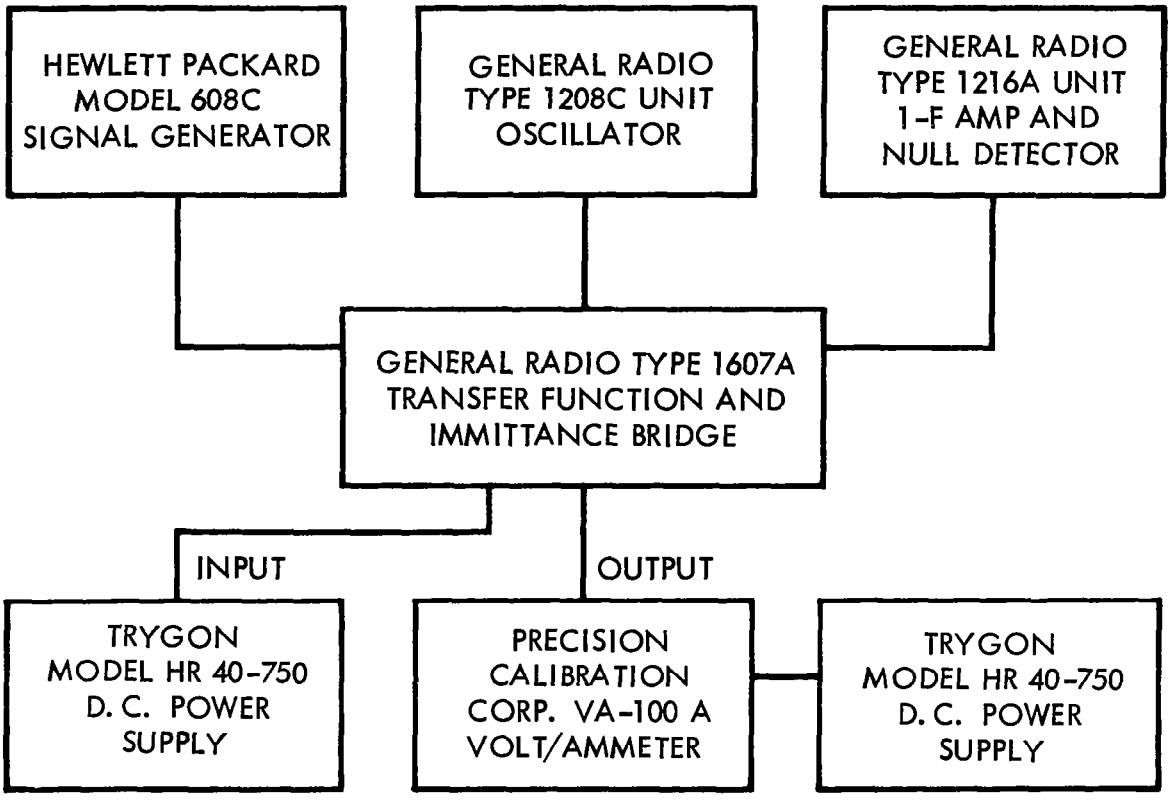

Figure 5. Bridge Measurement of f_T

$$h_{fe} = M\sqrt{A^2 + B^2} \qquad (2)$$

The proper quarter wave phase relationship between base and collector currents were established earlier by proper tuning. The bridge can be tuned within a frequency range of approximately 70 to 1,500 mc, with a reduction in accuracy for frequencies above 1,000 mc. Precision measurements made with the bridge are a function of operating region as described in the manual. However, overall validity of the measurement depends on proper tuning.

A detailed description of the tuning procedure for the bridge is given in the operating manual. The following is an outline of tuning procedure that was followed for this program:

1. A calibrated signal generator is set at the desired input frequency, f.

2. The local oscillator is set at f + 30 mc.

3. The susceptance standard is set at f.

4. The output line is adjusted to the conditions required of the input line, i.e., quarter wave length $\frac{n\lambda}{4}$ (n_{odd}) with the A arm at full scale, B arm at zero, and multiplier arm at ∞ with the WO5 open circuit termination in the output terminal.

5. The input line is tuned to the conditions $\frac{n\lambda}{4}(n_{odd})$ by inserting a WU 4 shorting block across the input output terminals.

6. The output is tuned to a half wave length $\frac{n\lambda}{2}$ (n_{even}) with a WN5 short circuit termination in the output terminals.

7. The setting of the susceptance standard is then verified by inserting a WU 4 shorting block into the input and output terminals, setting the A arm to zero and the multiplier arm to +1.0. In this condition the B arm should give a null at +1.0 and -1.0 with the multiplier on +1 or -1. When these conditions are met the susceptance standard is properly set.

8. The local oscillator is then trapped out by interchanging the connections of the signal generator and local oscillator, setting the A and B arms to full scale and the multiplier to ∞ and adjusting the trap until a null is obtained for the signal. For good repeatability, the trap should be adjusted very carefully. The two signal inputs are then returned to their respective positions.

9. The common emitter connector is inserted into the input and output terminals and the d.c. bias conditions are established for the transistor.

Measurement repeatability was checked each time data was taken by checking the control device of each transistor type at each frequency.

The a.c. current gain was determined for several frequencies and emitter currents using the 1607A bridge. Table 4 lists bridge data obtained and gain calculated using Equation 2. In order to determine f_T, the values of h_{fe}(db) are plotted as a function of frequency as shown in Figure 6. The intercept of the gain-frequency curves with the zero db abscissa is, by definition, the gain-bandwidth frequency, f_T. This step is necessary to check the conventional assumption of a 6-db-per-octave curve. This procedure must be repeated for different values of emitter current, I_E, in order to determine f_T as a function of emitter current. The base transit time, t_b, can be determined from a plot of ω_T versus I_E^{-1}. The dependence of the angular gain-bandwidth frequency, ω_T, on various time constants is given by Equation 3 (Reference 6).

$$\omega_T^{-1} = 1/2\pi f_T = K_\theta^{-1} \alpha_o^{-1} (t_b + t_e + t_c) \qquad (3)$$

where K_θ = the excess phase constant

α_o = the grounded emitter current gain (low frequency)

t_e = emitter delay time

t_c = collector delay time

Table 4. 1607A Bridge Measurements on Transistor 2N743 No. 1

I_C (ma)	f (mc)	A	B	M	h_{fe}	h_{fe} (db)
0.5	400	0.35	0.44	1	0.56	-5.50
	200	0.37	0.32	2	0.98	-0.20
	70	0.80	0.21	3	2.48	+7.90
0.75	400	0.45	0.48	1	0.65	-3.78
	200	0.63	0.48	1.5	1.18	+1.41
	70	1.03	0.16	3	3.12	+9.88
1.00	400	0.51	0.51	1	0.72	-2.84
	200	0.73	0.52	1.5	1.35	+2.59
	70	0.74	0.14	5	3.67	+11.30
2.0	400	0.70	0.61	1	0.93	-0.64
	200	1.03	0.58	1.5	1.76	+4.90
	70	1.05	0.13	5.0	5.07	+14.45

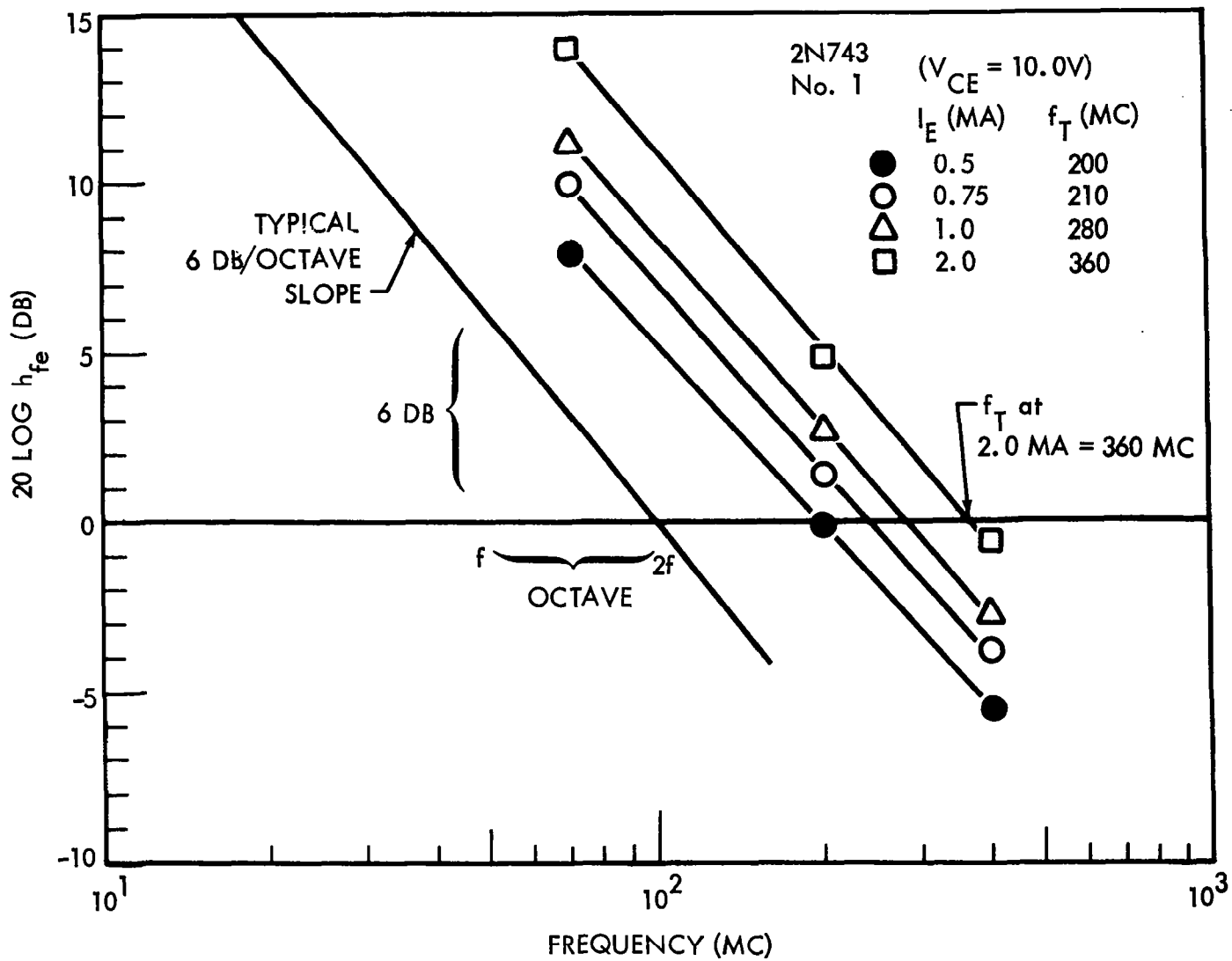

Figure 6. Graphical Determination of f_T

The influence of t_e and t_c can be subtracted graphically from f_T, as shown in Figure 7, in order to yield a term which is proportional to the base transit time. The low current value of t_b, a constant, is equal to the intercept of the straight line portion of the curve with the ω_T^{-1} ordinate. The values of $K_\theta^{-1}\, a_o^{-1}\, t_b$ at high current are obtained by a subtraction between ω_T and t_e, since t_e is assumed to be the major term responsible for the current dependent portion of the curve in Figure 4. A more complete discussion of the composition of Equation 3 is given in Section 3. 2. 3.

The Tektronix Type RM567 Sampling Oscilloscope and accessory equipment are used for obtaining values of f_T by the measurement of rise time. The rise-time measurement circuit and accessories are shown in Figure 8. Circuit elements are mounted on a low capacitance test fixture. The sampling oscilloscope has a low level sensitivity of approximately 1-millivolt-per-cm and a rise time of 0. 4 nanoseconds. A detailed description of the capabilities of this oscilloscope is given in the operating manual (Reference 7).

The Data Pulse 106A Pulse Generator has the following desirable characteristics: 10-nanosecond rise time, ±10-volt output amplitude, 10-megacycle repetition rate, variable pulse width and pulse delay, and low output impedance.

The determination of f_T by the measurement of rise time is based on Equation 4 (Reference 6).

$$T_r \simeq h_{FE}(\omega_T^{-1} + 1.7\, R_L\, C_{Tc})\, \ln \left[h_{FE}\, I_{B1} / (h_{FE}\, I_{B1} - 0.9\, I_C) \right] \qquad (4)$$

where T_r = rise time

h_{FE} = common emitter d. c. current gain

ω_T = angular current-gain-bandwidth frequency

R_L = load resistance

C_{Tc} = collector transition capacitance

I_{B1} = turn-on base current

I_C = collector current

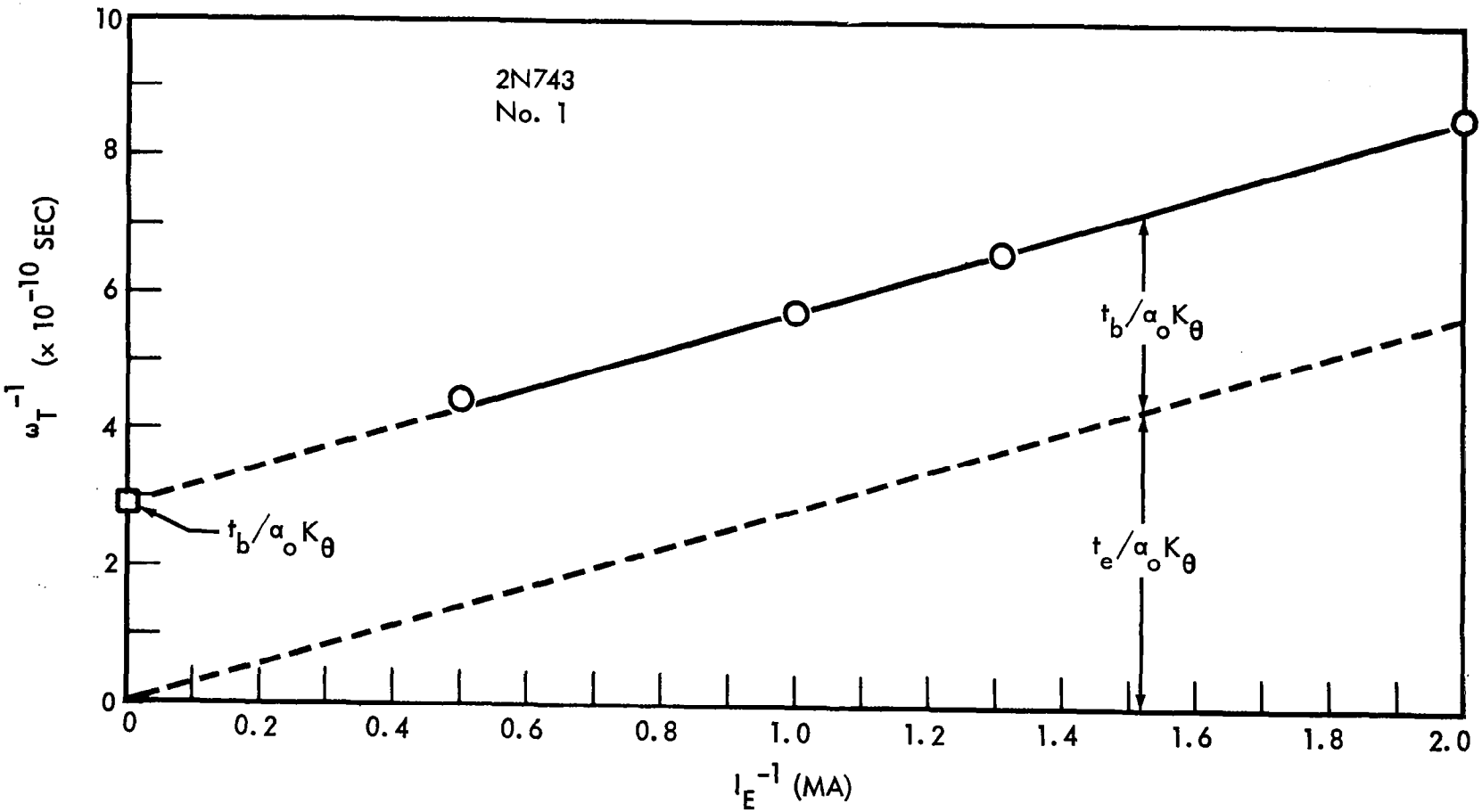

Figure 7. Graphical Determination of $\alpha_o^{-1} K_\theta^{-1} t_b$

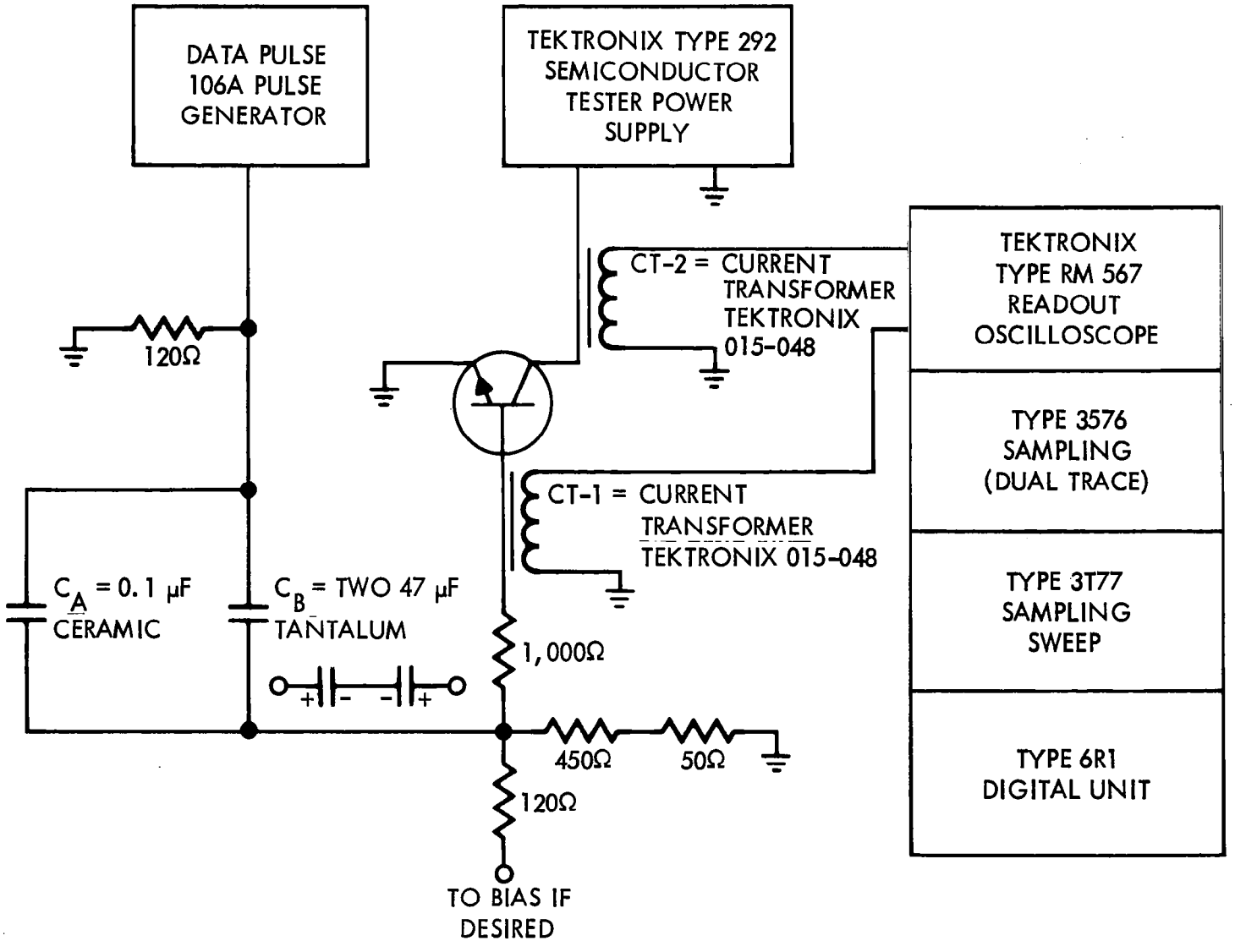

Figure 8. Rise Time Measurement Circuit

If one assumes that $R_L \simeq 0$, $h_{FE} I_{B1} = I_C$ then Equation 4 reduces to

$$T_r = 2.3\, h_{FE} \omega^{-1} \tag{5}$$

or

$$f_T \simeq 2.3\, h_{FE} / 2\pi T_r \tag{6}$$

The current gain h_{FE} is measured on the Fairchild Series 500 Semiconductor Tester. In determining T_r the desired bias voltages were established on the Tektronix 292 Power Supply and a pulse was supplied of sufficient amplitude to give an output pulse with the peak current desired. The duration of the pulse was adjusted by observing the output pulse and ascertaining when it reached full amplitude (became flat on top). The rise time was then read out on a Tektronix 6R1 Digital Unit. The rise time so obtained includes the rise time of the pulse generator and oscilloscope as well as that of the transistor being tested. The rise time of the device is separated by use of Equation 7.

$$T_r(\text{measured}) = \left[T_r^2(\text{transistor}) + T_r^2(\text{generator}) + T_r^2(\text{scope}) \right]^{1/2} \tag{7}$$

The sampling oscilloscope has a rise time of 0.4 nanoseconds. The specified value of rise time of the generator was 10 nanoseconds and was verified by measurement on the oscilloscope. As a typical example, a rise time of 52 nanoseconds was measured at a collector current of 10 ma for transistor No. 2 of type 2N2411. Thus the actual rise time when separated, by Equation 7, from the rise time of the oscilloscope and generator was found to be 51 nanoseconds. The d.c. current gain at 10 ma collector current, as measured using the Fairchild Series 500 Semiconductor Tester was 56.2; thus f_T, as calculated from Equation 6, was 404 mc.

The Boonton Capacity Bridge Model 74C-S8 is used to determine both emitter and collector transition capacitances. These measurements are desired in order to separate out the influence of RC-time constants on the measurements of both gain-bandwidth frequency and alpha cut-off frequency (e.g., t_e or t_c of Equation 3; discussed in more detail in Section 3.2.3). Desirable features of

the Boonton bridge include: (1) accurate capacity determinations to within 0.05 picofarads, (2) an a. c. signal level which can be reduced to less than 1 mv (although useful nulls occur between 2 and 3 mv), and (3) an internal direct current bias supply. Equations for determining accuracy of this instrument, as a function of the magnitude of capacity being measured, are described in its instruction book (Reference 8). The equipment used for measuring transition capacity is shown in Figure 9. Before measurements are made the bridge is zeroed to insure that a null is obtained at 0.0 picofarads and 0.0 conductance with the test jig in place.

The determination of transition capacitance is based on Equation 8 for graded junctions (Reference 6).

$$C_T = (K_\epsilon^2 q/12)^{1/3} (a/V)^{1/3} \tag{8}$$

where K_ϵ = dielectric constant for the material
q = electronic charge
a = the grade constant in atoms/cm^2
$V = V_o + V_T$
V_o = external applied bias
V_T = contact potential
C_T = transition capacitance

Taking the logarithm of both sides Equation 9 is obtained from Equation 8.

$$\ln C_T = (1/3) \left[\ln (K_\epsilon^2 qa/12) - \ln V \right] \tag{9}$$

Experimentally, C_T is measured for bias voltages, V_o, ranging from values near reverse breakdown voltage to about 0.2 volts forward bias using the circuit shown in Figure 9. Log C_T is then plotted as a function of log V_o. A value for the contact potential is obtained by adding trial values to V_o until a reasonably straight line results. C_T can be found for forward bias conditions by extrapolation of the linear plot.

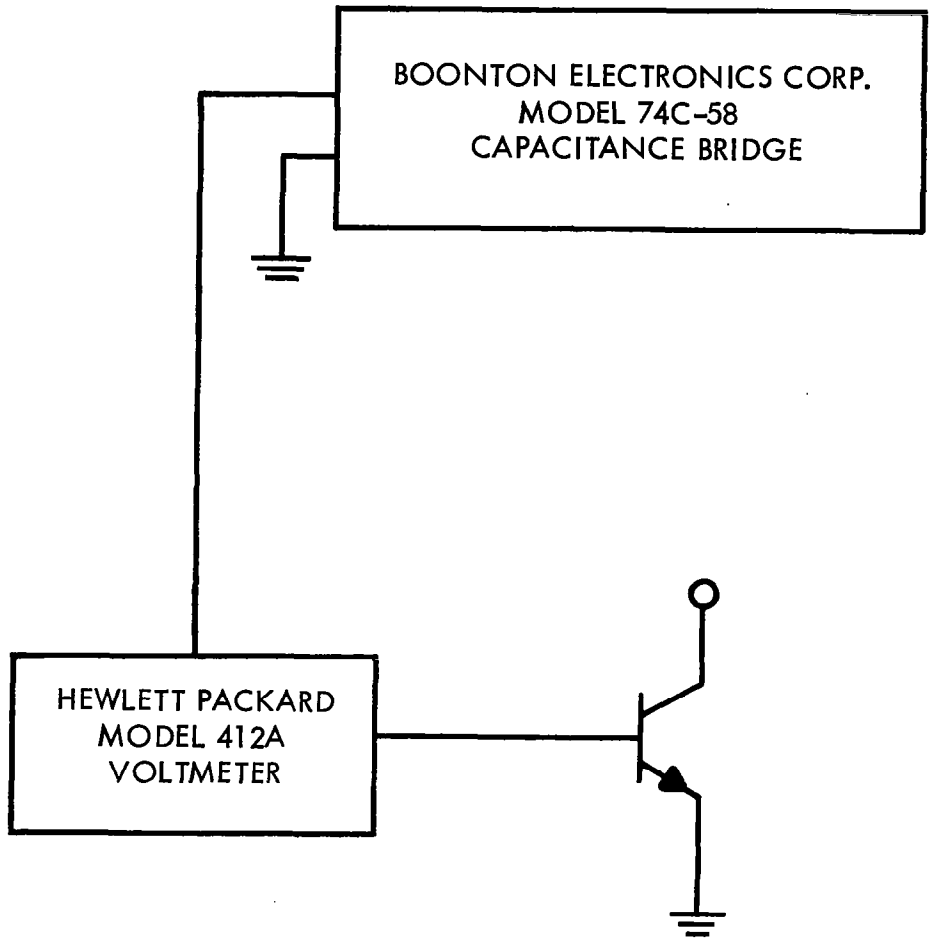

Figure 9. Measurement of Emitter Transition Capacitance

It should be noted that Equation 9 does not hold for all types of junctions. The relation for step junctions, for example, has a square root rather than cube root dependence. Also some junctions obey the above equation for low bias voltages yet tend to behave as step junctions as the voltage is increased; however, this effect was not observed in any of the transistors tested for this program.

For measurements made of C_{Te} to be compared with the average C_{Te} obtained from the slope of ω_T^{-1} versus I_E^{-1} curves, the forward bias voltage from base to emitter was measured for several currents and the average taken as the average forward bias in the current range spanned.

A typical example of the capacitance data is given in Table 5. V_o or V_{BE} was plotted against C_{Te}, as shown in Figure 10. It was found that if one assumed $V_T = 0.9$ volts, then a reasonably straight line resulted when V_T was added to V_o. The average value of C_{Te} over the current range of interest was then obtained by extrapolating the line up to $0.73 + V_T$ volts bias.

Table 5. Measured Values for C_{Te} Transistor Type 2N1132 No. 1.

	(Boonton bridge data)		(Transit time bridge forward bias data)	
	$V_o = V_{BE}$ (VOLTS)	C_{Te} (PF)	I_E	V_{BE}
Forward	0.3	40.9	1 ma	0.64 volts
	0.2	38.0	2 ma	0.68 volts
	0.1	35.7	6 ma	0.78 volts
	0	---	8 ma	0.82 volts
Reverse	0.2	31.2	V_{BE}(average) = 0.73 volts	
	0.4	29.2		
	0.6	27.6		
	0.8	26.2		
	1.0	25.2		
	2.0	21.4		
	4.0	17.6		
	6.0	15.4		
	7.0	14.5		

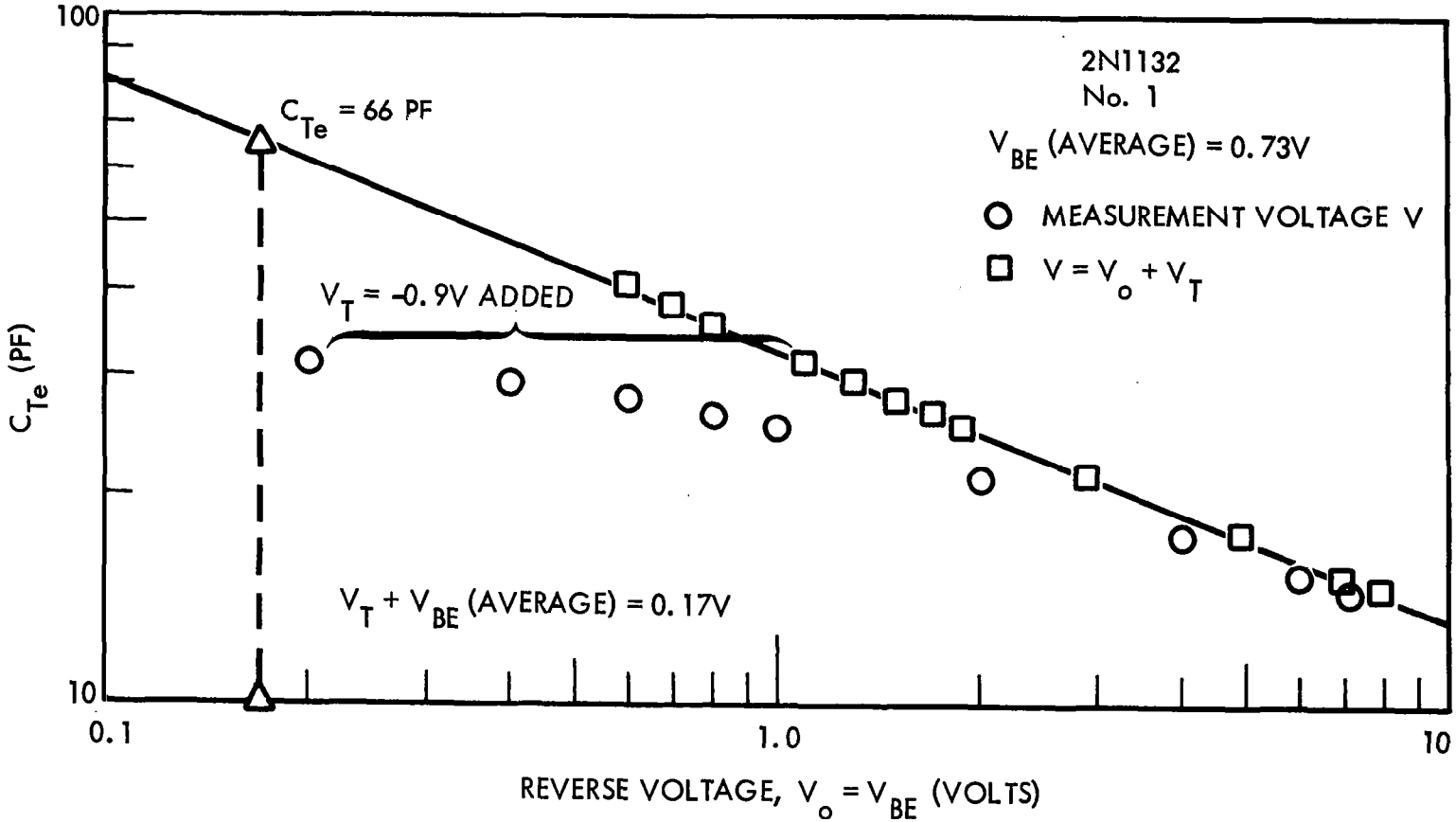

Figure 10. Graphical Determination of C_{Te}

The Base Transit Time Bridge circuit used for the measurement of base transit time was designed and assembled at Boeing. A detailed schematic of this bridge is shown in Figure 11 and a photograph of the accessory equipment is shown in Figure 12. The test circuit is operated as follows:

1. The desired bias voltage and emitter current is obtained by adjusting the d. c. emitter and collector power supplies.

2. A small a. c. signal is impressed on the emitter circuit.

3. The variable resistance, R_x, and capacitance, C_x, in the base circuit is adjusted to obtain a null on the detector. At the null condition Ashar (Reference 9) has shown that the measured time constant is given by Equation 10.

$$t_x = \omega_a^{-1} = R_x C_x R_c/(R_x + R_c) \tag{10}$$

Table 6 lists typical calculated values obtained for t_x at selected emitter currents for the 2N1613 control transistor (R_c = 20.7 ohms).

With the assumption that in general $R_c \ll R_x$, Equation 10 reduces to Equation 11 and an estimate can be made of the frequency limitations of the bridge.

$$f \simeq 1/2\pi C_x R_c \tag{11}$$

Substituting into Equation 11 the stray capacitance in the base circuit, approximately 20 picofarads, limits the measurements to a frequency of approximately 400 mc.

The base transit time circuit measures the quantity t_x which is related to the base transit time as shown in Equation 12,

$$t_x = t_b + t_e \tag{12}$$

where t_e is the emitter delay time.

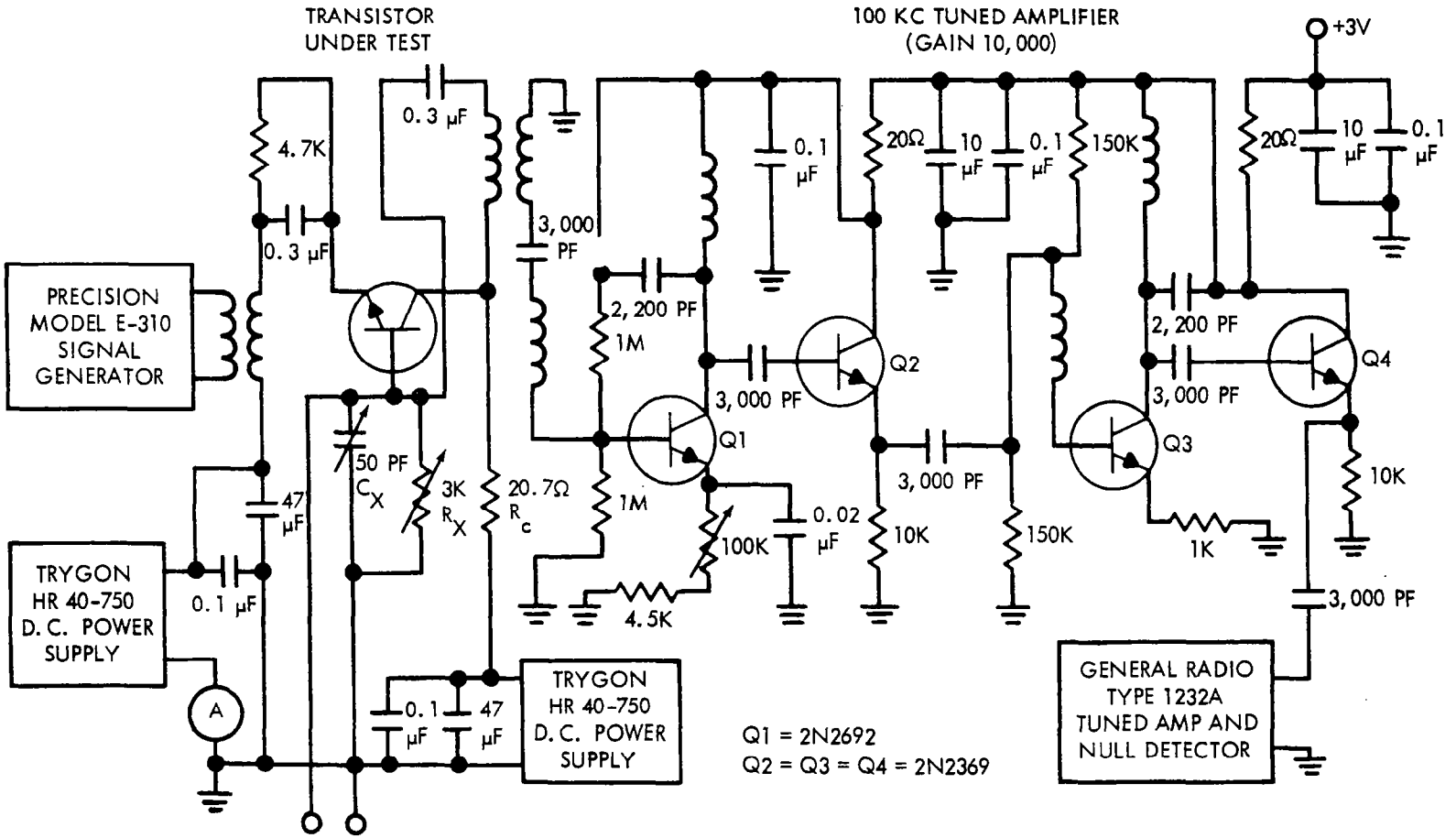

Figure 11. Base-Transit Time Circuit

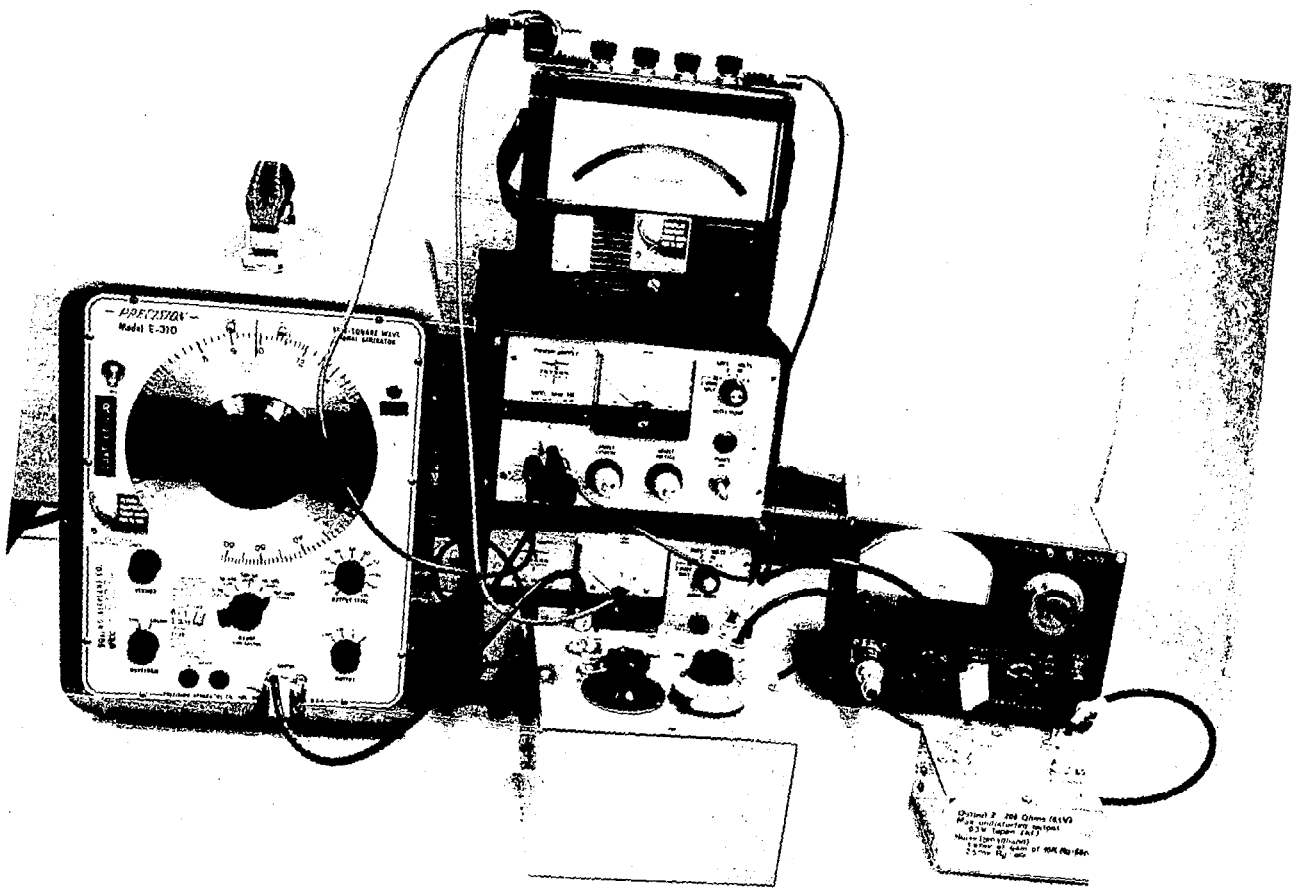

Figure 12. Base-Transit Time Measurement

Table 6. Calculated Values of t_x Transistor 2N1613 No. 1

I_E (ma)	C_x (pf)	R_x (Ω)	R_c (Ω)	t_x (sec)
1.00	309	960	20.7	6.26×10^{-9}
1.25	264	995	20.7	5.35×10^{-9}
2.00	200	1,050	20.7	4.06×10^{-9}
10.00	105	1,295	20.7	2.14×10^{-9}

The reciprocal of the emitter current can be plotted versus t_x as shown in Figure 13 and the emitter delay time subtracted graphically to yield a value of the base transit time. In general at low currents the plot is linear. The intercept of the linear portion on the t_x axis is t_b for low currents. At high currents values of t_x may vary from the linear line. If this occurs, then the transit time for that current would be equal to the difference between the emitter delay time, t_e, at that current and t_x at that current. Thus care is needed in selecting a value of t_b for normalization of radiation damage which is consistent with the current at which the gain is measured.

Small-signal a. c. common-emitter current gains can also be determined during these bridge measurements. Values of h_{fe} are found by use of Equation 13 (Reference 13).

$$h_{fe} \cong R_x/R_c \tag{13}$$

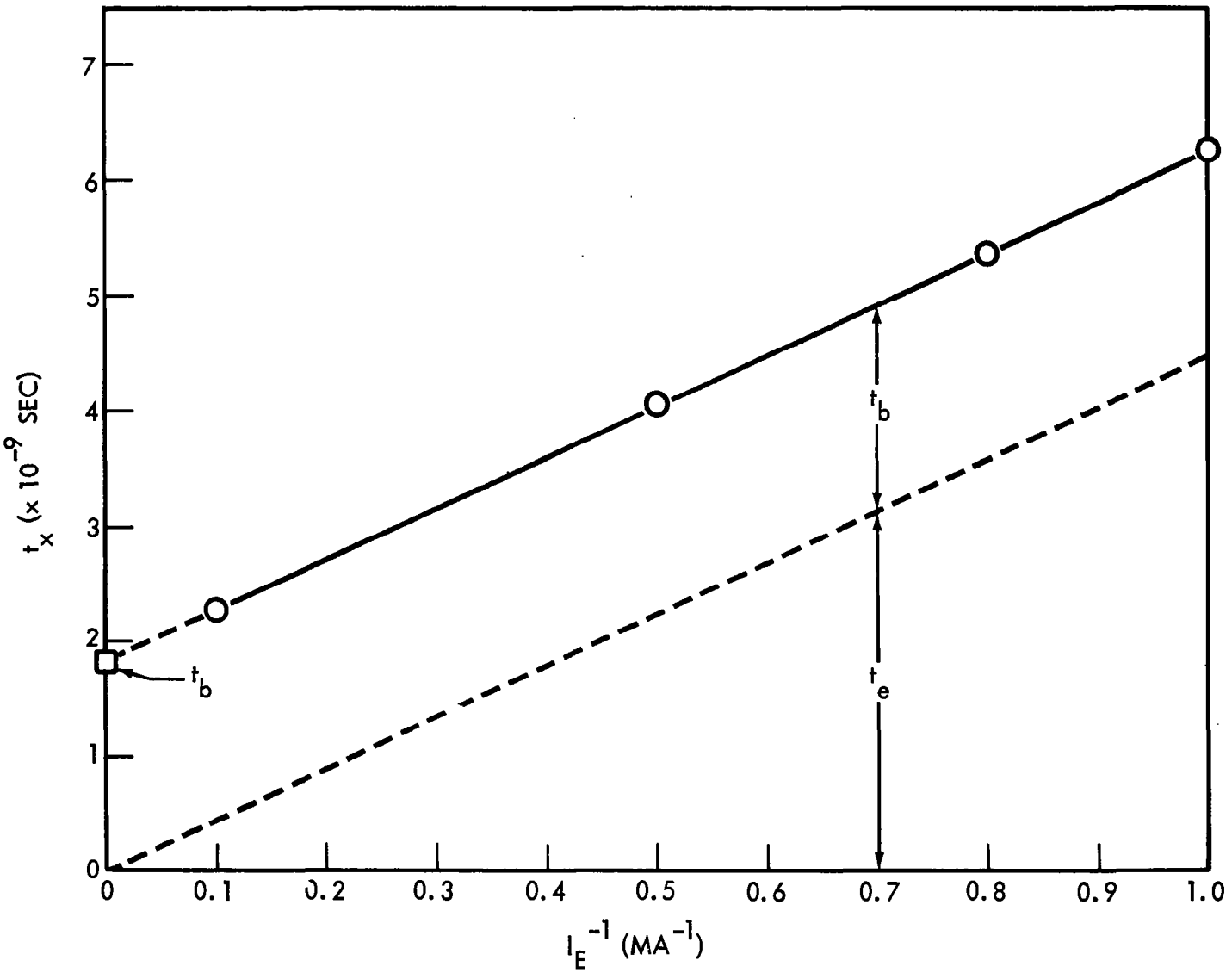

Figure 13. Graphical Determination of t_b

2.2.3 Correlation of Damage Normalization Parameters

The three methods for obtaining relative values of damage-normalization parameters, in terms of the base transit time, can be compared. Both the rise time and the General Radio (G. R.) bridge method require determination of current gain-bandwidth frequency f_T while the base transit time circuit is used to determine the alpha cutoff frequency f_α. The two frequencies can be related to npn transistor parameters as in Equations 15 and 16 respectively (Reference 6).

$$f_T^{-1} = \alpha_o^{-1} K_\theta^{-1} f_\alpha^{-1} \tag{14}$$

$$f_\alpha^{-1} = 2\pi \left[R_e (C_{Te} + C_{Tc}) + W^2/2.43 D_{pb} \ell n (N_{B'}/N_{BC}) + R_{sc} C_{Tc} + X_m/2V_{sc} \right] \tag{15}$$

where R_e = emitter resistance (a. c.)

C_{Te} = emitter transition capacitance

C_{Tc} = collector transition capacitance

R_{sc} = collector series resistance

W = effective base width

$N_{B'}$ = base impurity concentration at emitter junction

N_{BC} = background impurity concentration

D_{pb} = hole diffusion constant in base

X_m = collector depletion layer thickness

V_{sc} = scattering limited velocity

α_o = grounded base current gain (low frequency)

K_θ = excess phase constant

To obtain the base transit time it is assumed that $R_s C_{Tc}$ and $X_m/2V_{sc}$ are small compared to $W^2/2.43 D_{pb} \ell n (N_{B'}/N_{BC})$. This approximation is not good for very high frequency devices. In such cases the $R_s C_{Tc}$ term may become important.

These assumptions, and Equation 16, result in a reduction of Equation 15.

$$R_e = \frac{kT}{q} \tag{16}$$

$$f_\alpha^{-1} \simeq 2\pi \left[kTq^{-1} I_E^{-1} (C_{Te} + C_{Tc}) + t_b \right] \tag{17}$$

$$t_b = W^2/2.43 D_{pb} \ln(N_{B'}/N_{BC}) \tag{18}$$

Thus if ω_{ab}^{-1} is plotted versus I_E^{-1} the transition capacities can be subtracted out graphically.

The linear portion of the curve is proportional to t_e, the emitter delay time which contains the transition capacities.

$$t_e = R_e (C_{Te} + C_{Tc}) \tag{19}$$

where $\omega_\alpha^{-1} - t_e$ then equals the base transit time. The curve becomes nonlinear at high currents due to high level injection effects. It is important in radiation damage normalization that the transit time used be measured at the same emitter current that the transistor gain is to be measured. The alpha cutoff frequency provides a means of obtaining the actual base transit time.

The gain-bandwidth frequency (f_T) can be analyzed in the same manner as f_α; however, after the graphical separation, the term obtained is not t_b but $t_{b'}$.

$$t_{b'} = \alpha_o^{-1} K_\theta^{-1} t_b \tag{20}$$

α_o is usually close to unity so that

$$t_{b'} \cong K_\theta^{-1} t_b \tag{21}$$

At present, no attempt has been made to measure K_θ. It has been assumed that the variation of K_θ between transistors of the same type is small. The variation of K_θ could become quite large between different types of transistors since K_θ is a result of built-in electric fields peculiar to the construction of the device and may vary

between 0.5 and 1.0 with different constructions (Reference 10). Thus it would seem that f_α, which leads directly to t_b, would yield better agreement for damage constants between different type devices.

By the gain-bandwidth concept, one should be able to measure the gain at some frequency above the beta cutoff frequency and, by the product of the measurement frequency and gain, obtain f_T; however, actual measurements on the G. R. bridge show that the curves can deviate substantially from the anticipated 6 db/octave slope. This effect was noted particularly near unity gain. Small deviations from the predicted slope were expected since internal electric fields may influence the slope (Reference 10) but the amount of deviation occurring below unity gain as illustrated in Figure 14 is not consistent with the above theory. Work is continuing to determine why this large deviation occurs.

The conclusions from these findings are that one should be very careful in applying the gain-bandwidth concept. Measurements for this report were made by plotting h_{fe} (db) for several frequencies and taking the intercept of the line with 0 db as f_T. Frequencies obtained in this manner on the G. R. bridge yield f_T^{-1} versus I_E^{-1} curves which agree well with f_α^{-1} versus I_E^{-1} curves obtained on the transit time bridge, as shown in Figures 15a and b.

The flattening effect near unity gain also places a limitation on the method. The G. R. bridge used in this study has a lower tuning frequency of approximately 70 mc and thus transistors with f_T below 70 mc cannot be measured by this bridge.

The transistor rise time is also being employed to obtain f_T. However, low current measurements (below 5 ma) are masked by noise and graphical separation of the emitter delay time, as discussed earlier, is not very successful; therefore, the rise time technique yields a high current value of f_T which still includes the effects of junction capacities as well as the term $1/\alpha_o K_\theta$.

Preliminary data indicates that in general the rise time technique yields considerably higher values of gain-bandwidth frequency than the transfer function and immittance bridge. The difference is attributed to the fact that the rise time

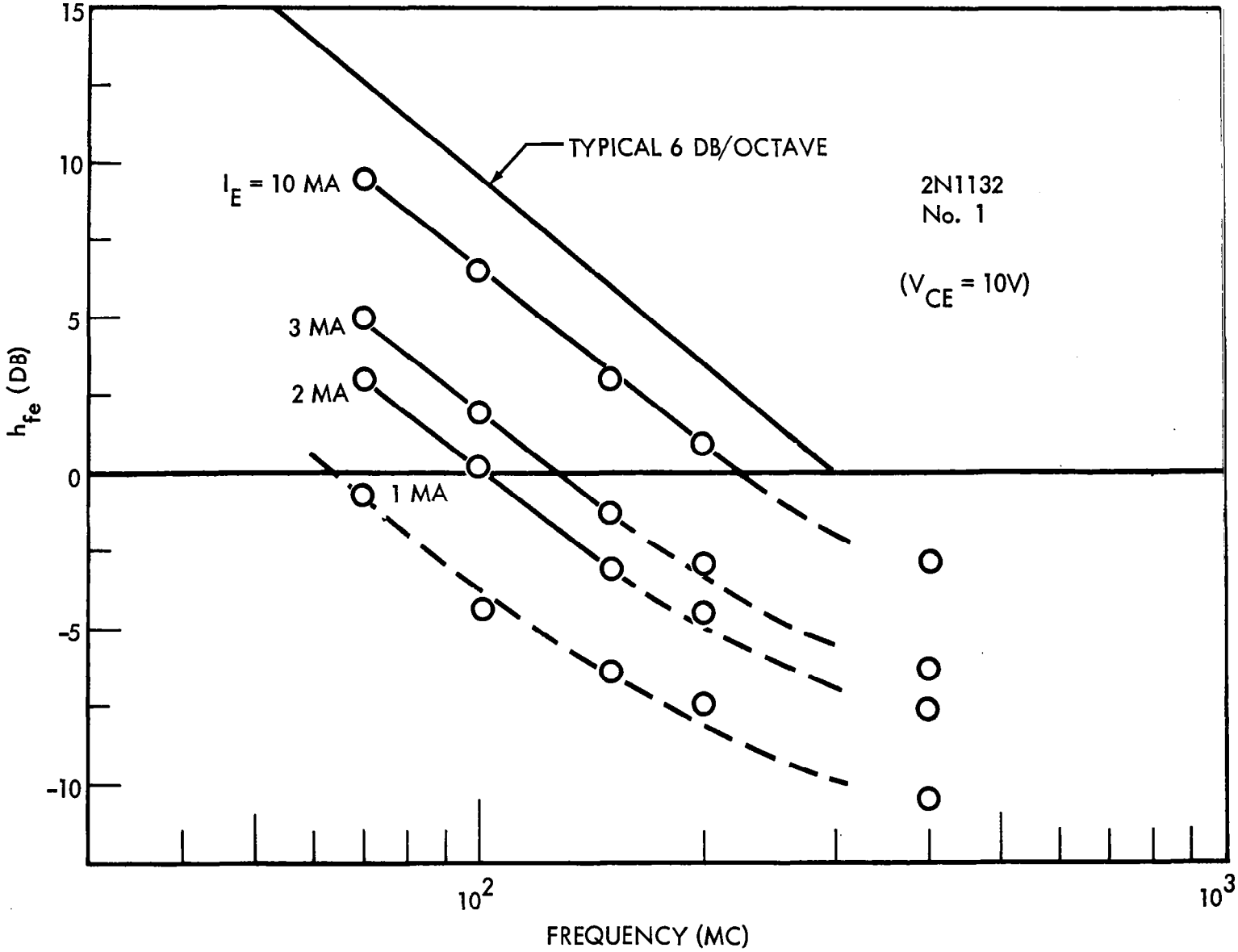

Figure 14. Deviations From a 6 db per Octave Slope

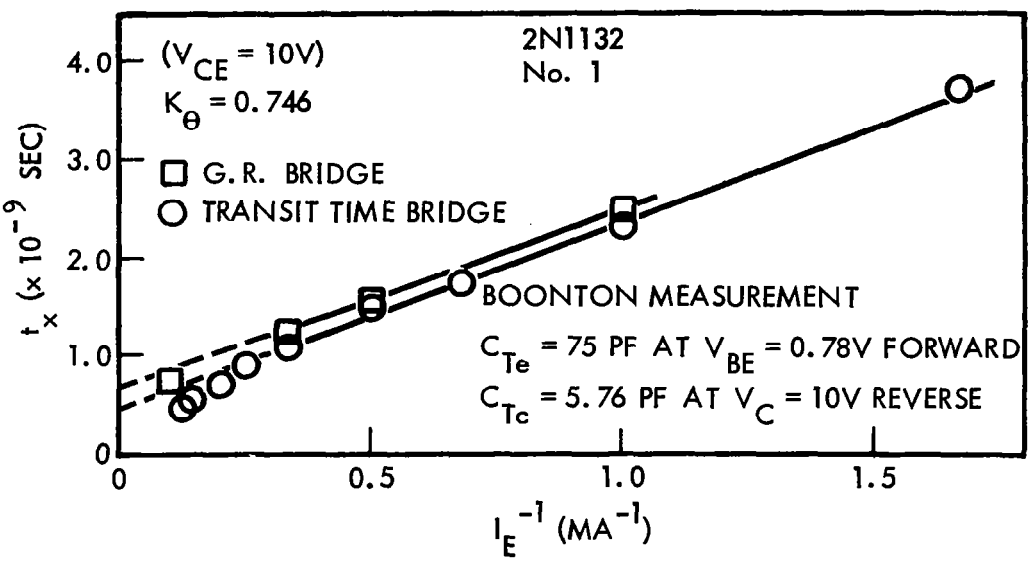

A

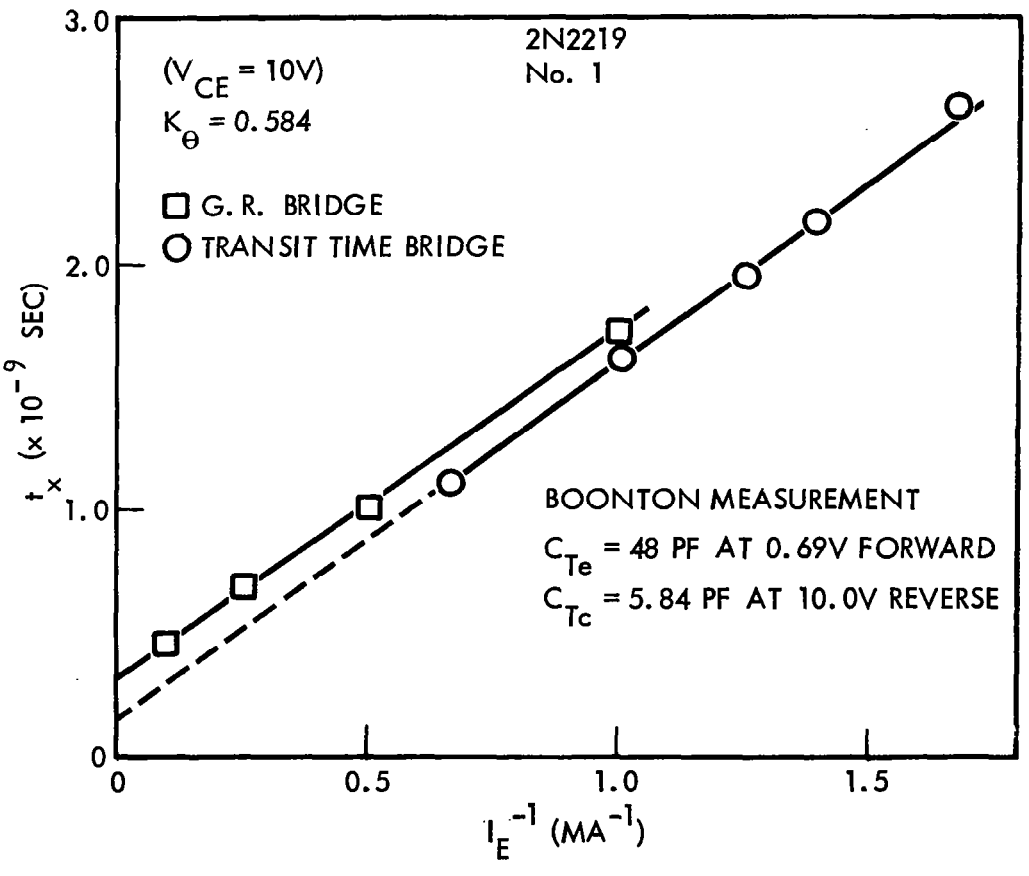

B

Figure 15. Comparison of Bridge Determinations of t_B

method is a large-signal measurement while the G. R. bridge method is a small-signal measurement. Preliminary data also shows, however, that the rise-time technique yields rather large variations in f_T within a given type of transistors. It is hoped that further analysis will indicate which measurement technique yields the best normalization results. Table 7 lists data for comparison using the three methods. It can be seen that graphically determined values of transition capacitance also agree reasonably well with those measured. The f_α measurement on the base transit time bridge agrees well with the transfer function bridge data. The slopes of the f_α^{-1} versus I_E^{-1} lines have been found to agree well with separate measurements of the junction capacities on the Boonton Capacitance Bridge. The method is limited to low frequency devices, however, by the amount of stray capacity in the bridge circuitry.

In continuing work, a detailed comparison will be made of normalization constants obtained by all three measurements on the same devices. The transit time will also be checked as a function of radiation exposure to insure that it remains constant under radiation.

2.3 TEST SCHEDULE

In order to simulate transistor damage for earth orbital missions, electrons of three energies and protons of three energies were selected for transistor irradiation. A gamma-ray test is also planned to assess the validity of space radiation simulation using a cobalt-60 facility. To date electron irradiation tests at energies of 0.5, 1, and 2 Mev have been performed. Electrons of 0.5-Mev energy are representative of those present with high intensity in a shield-modified spectrum. Transistor inherent shielding was removed for the 0.5-Mev test. Electrons of 1-Mev energy can readily pass through the thickness of a transistor can. Although the 1-Mev intensity in space is less than that for lower-energy electrons the displacement cross section is greater. Electrons of 2-Mev energy are representative of those high-energy electrons still having sufficient Van Allen intensity to be significant for transistor damage.

Table 7. Comparison of Values of Parameters for Normalization
(I_C = 10 ma, V_C = 10 volts)

	Frequency (mc)			Transition Capacity (pf)			
	f_T Rise Time	f_T G. R. Bridge	f_{ab} T. T. Bridge	C_{Te} Boonton	C_{Tc} Boonton	$C_{Te} + C_{Tc}$ G. R. Slope	$C_{Te} + C_{Tc}$ T. T. Slope
2N743*	515	500	---	9.0	3.19	7.4	---
2N834	645	470	456**	10.8	2.82	11.6	11.6
2N1613	68.5	84	93.7	165	17.5	168	168
2N1711	241	---	133	93.0	17.5	---	112
2N1132	236	280	234**	75	5.76	72	65.5
2N2303	165	103	122	135	30.5	156	156
2N2219	467	442	500**	48.0	5.8	55.2	51.0
2N2538	492	397	397**	46.0	4.9	48	40
2N2411	566	398	408**	10.8	3.37	16.0	11.2
2N2801	191	398	398	134	14.4	144	164

* V_C = 5 volts
** Low current level

The current schedule showing both past and future tests is shown in Table 8.

Table 8. Test Schedule

Radiation Type	Energy (Mev)	Source	Approximate Date	Test Number
Electrons	0.5	Boeing Dynamitron	October 1965	23
	1	Boeing Dynamitron	September 1965	22
	2	Boeing Dynamitron	September 1965	21
Protons	1	Boeing Dynamitron	November 1965	24
	20	He^3 (d, p) He^4 reaction	February 1966	26
	100	Cyclotron	March 1966	27
Gamma Rays	1.17 and 1.33	Boeing Cobalt-60 Facility	December 1965	25

A total of 400 transistors were procured for this research program. The planned disposition of these devices is shown in Table 9. Two each of the 10 transistor types will serve as a control for the tests; five each will be held as auxiliary devices. Four of each type of transistor will be exposed for each test, except for the 100-Mev proton test. On each of the other tests, one of each transistor type will be dynamically monitored by means of curve-tracer photographs taken during irradiation. The other three devices of each type will have curve traces taken periodically (passive measurements) following three exposure runs. For the 100-Mev experiment, nine of each type of transistor will be exposed in equal groups for three different integrated fluxes.

Table 9. Transistor Evaluation Test Plan

Tests	Number of Transistors of Each Type	Number of Types of Transistors	Radiation Tests	Total Transistors
Dynamic (all tests except 100 Mev)	1	10	6	60
Passive (all tests except 100 Mev)	3	10	6	180
100-Mev test	9	10	1	90
Controls	2	10	---	20
Auxiliary Devices	3	10	---	50

2.4 PREPARATION FOR ELECTRON TESTS

The Dynamitron facility at the Boeing Radiation Effects Laboratory was modified in order to irradiate transistors with a scattered beam of electrons. The angular dependence of the flux of scattered electrons was determined both experimentally and theoretically. Transistors were then prepared for irradiation testing and test circuitry was designed and assembled.

2.4.1 Electron Scattering

Transistors were exposed, in a vacuum chamber, to electrons scattered by a thin foil. This is different from earlier Boeing tests where the transistors were exposed in air to a scanned beam. The advantages of scattering in a vacuum rather than scanning in air include: (1) more meaningful dynamic monitoring of transistors since exposure is continuous rather than periodic, (2) more uniform electron intensity over a large exposure area, (3) more reliable dosimetry (no air ionization in the Faraday cups), and (4) no air ionization present at the surfaces of decapitated transistors. Disadvantages of this method include: (1) the need for more complex test circuitry, (2) time loss for opening of the test chamber, for passive measurements

between exposures, and subsequent evacuation, and (3) long exposure times, at low rates, due to the slower dissipation rate of radiation-induced heat in a vacuum.

Since the Dynamitron accelerator is mounted vertically, it was necessary to bend the electron beam to pass horizontally into the scattering chamber. This chamber and the associated pumping system, mounted on its portable table, are shown in Figure 16. The height of the chamber is adjustable to allow for mating with the horizontal beam port. The chamber can also be gated off from the accelerator and evacuated using its 6-inch silicone oil diffusion pump with a liquid-nitrogen-cooled baffle and a fore pump.

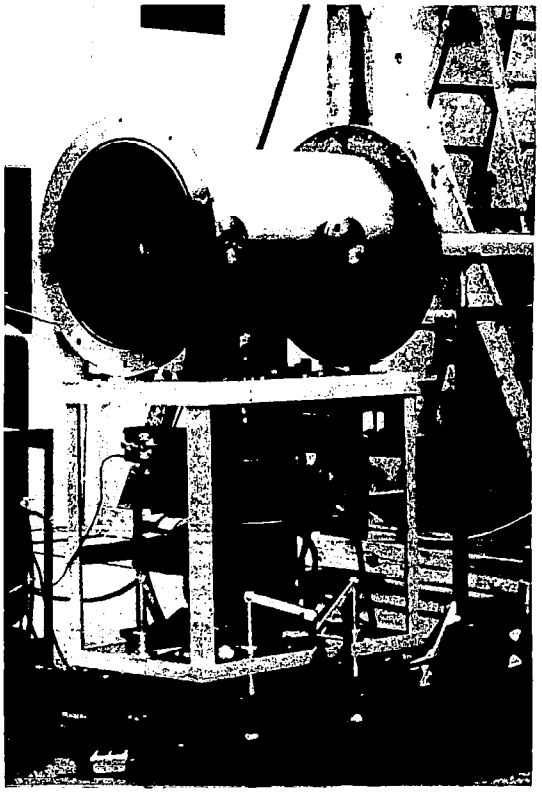

Figure 16. Electron Scattering Chamber

A Magnion 90-degree bending magnet was available for bending the electron beam. This magnet (mass energy product 16) was designed for bending protons. In order to obtain sufficiently low magnetic field strengths, a Kepco regulated low-current supply was procured. Then the horizontal beam was focused using a Magnion (mass product 12) triplet-quadrupole-lensing magnet (4-foot focus). The quadrupole magnet was controlled by a Magnion, current-regulated, duo-channel and duo-range, power supply (0 to 400 millivolts per channel). A polarity reversing switch was added in order to convert from electrons to the future proton tests by selection of the proper channel and range. Once the focused beam was obtained, considerable alignment of the exit beam tubing was still required in order to compensate for the earth's magnetic field.

A multiple-foil holder (6 positions) was designed and built for selection of scattering foils. Thin aluminum foils 0.25 and 1.6 mills thick with a purity of 99.99 percent and a 5.0 mil foil with a purity of 99.0 percent were procured from A. D. Mackay Inc., New York. The electron energy loss, ΔE_f, within these foils for electrons of energies selected for the tests are given in Table 10. Energy loss was calculated from Equation 22.

$$\Delta E_f = \rho t \, (dE/dX) \tag{22}$$

where ρ = density of the foil

t = thickness of the foil

(dE/dX) = the rate of energy loss

The density of aluminum is 2.7 gm/cm^{-3}.

Table 10. Energy Loss in Scattering Foils

Test No.	Nominal Electron Test Energy (Mev)	Energy Incident on Foils (Mev)	Foil Thickness (Mils)	$\frac{(dE/dX)_{Al}}{(Mev\ cm^2\ gm^{-1})}$	ΔE_f (Mev)
21	2	2.0	5.0	1.54	0.053
22	1	1.3	1.6	1.51	0.017
23	0.5	0.53	0.25	1.61	0.0028

The flux of scattered electrons, from the foils selected, was mapped prior to each test in order to determine the exposure rates at the transistor arrays. Experimental data was accumulated by the monitoring of current collected in a shielded Faraday probe which was rotated to selected angles about the center of the scattering foil. Figures 17, 18, and 19 show experimental data from the mapping of electron scattering in terms of the flux at the sample mounting disk (24-inch radius from the foil). A theoretical determination of the gaussian scattering was calculated by an SRU 1107 computer using a Monte Carlo code. The Monte Carlo scheme that is used represents, by straight line segments, the path an electron follows when slowing down in a material. Both the electron energy loss due to ionization or bremsstrahlung is determined for each segment and the resultant scattering of the electron after each segment is computed from the Bethe-modified Moliere scattering relations (Reference 11). The results of Monte Carlo analysis are also shown in histogram form on the flux plots. Both experimental and theoretical data were normalized to 1 μa total beam current. Agreement between experiment and theory is quite good at the forward angles where the transistor arrays were located.

2.4.2 Transistor Preparation

Transistors, for each of the 10 types procured, were numbered serially from 1 to 40 for purposes of identification. Control transistors as well as those selected for tests are designated in this manner.

Transistor cans provided inherent shielding from electrons and consequently their effect was considered in selecting test energies. Information concerning the thickness of the cans was obtained both by contacting the manufacturers (Reference 12) and by decapitating transistors and measuring the thickness of the tops of their cans with a micrometer. The pertinent properties of transistor cans are summarized in Table 11. Kovar, listed in Table 11, is a mild steel of composition 29 percent Ni, 17 percent Co, 0.3 percent Mn, and 53.7 percent Fe (Reference 13). Equation 22 was used to calculate the energy loss of electrons passing through the transistor cans. This energy loss and the resultant energy of electrons incident on the silicon surface of transistors are listed in Table 12 for the "thinnest" and "thickest"

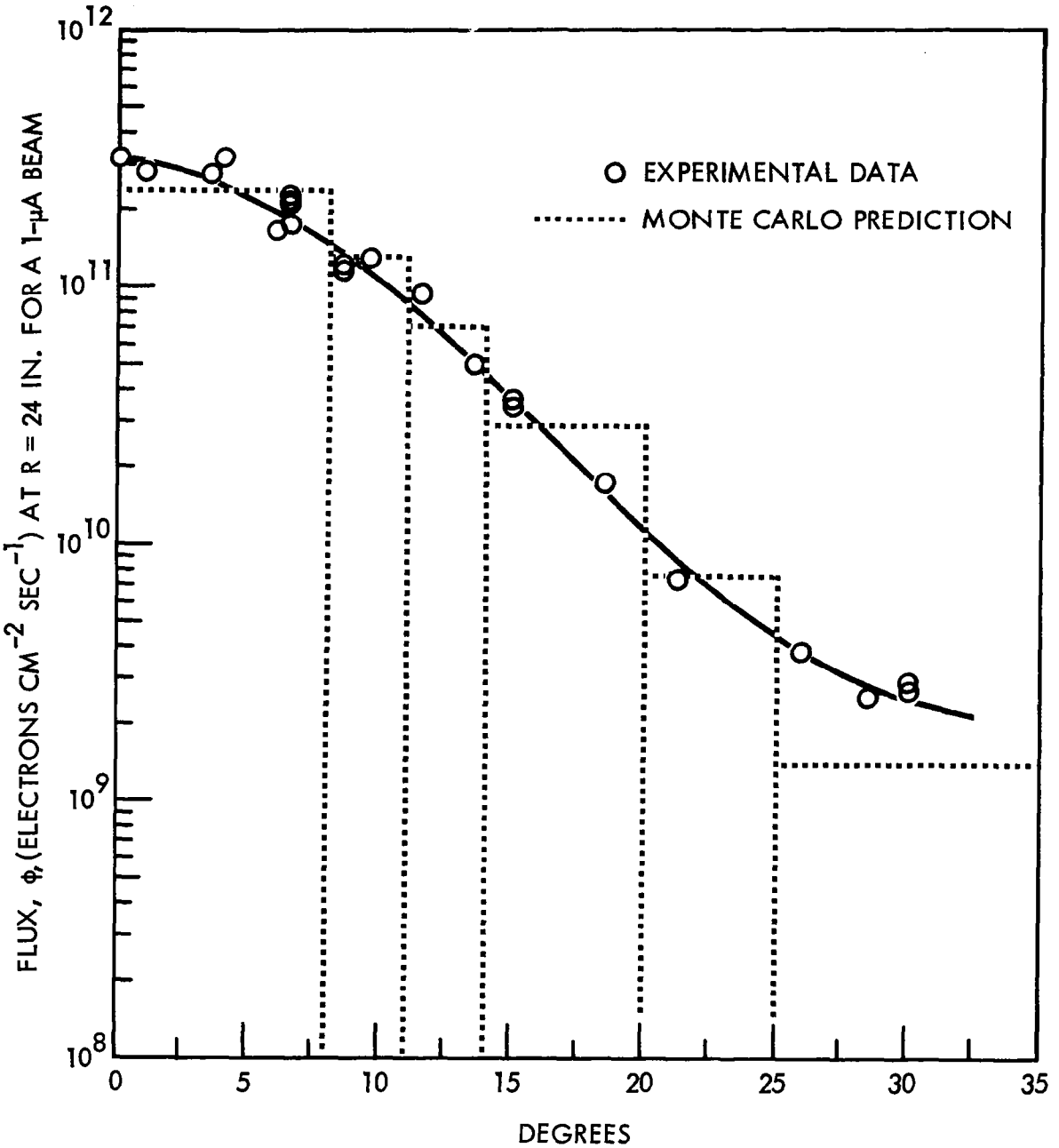

Figure 17. 2.0-Mev Electron Flux From 5.0 mil Al

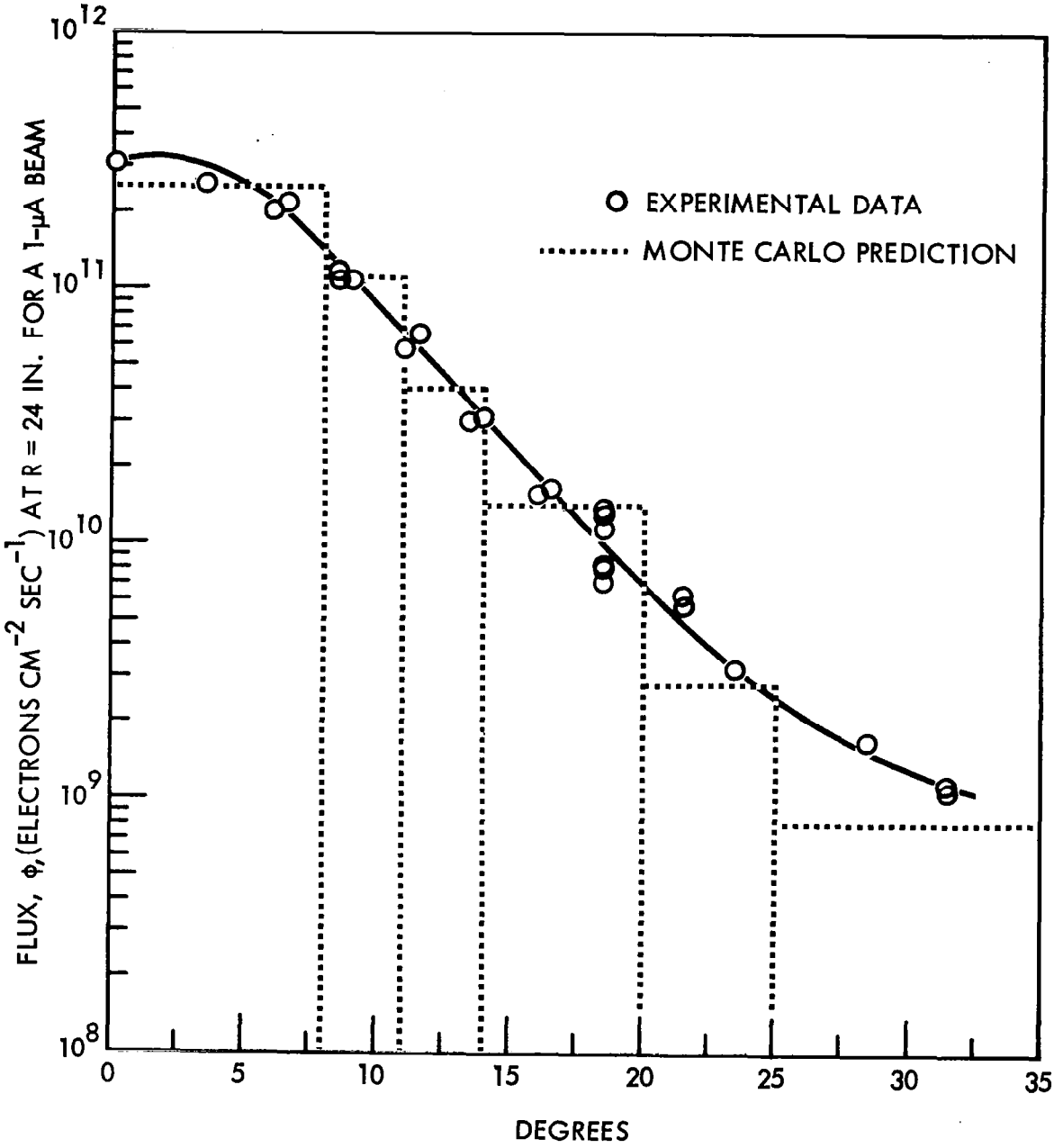

Figure 18. 1.3-Mev Electron Flux From 1.6 mil Al

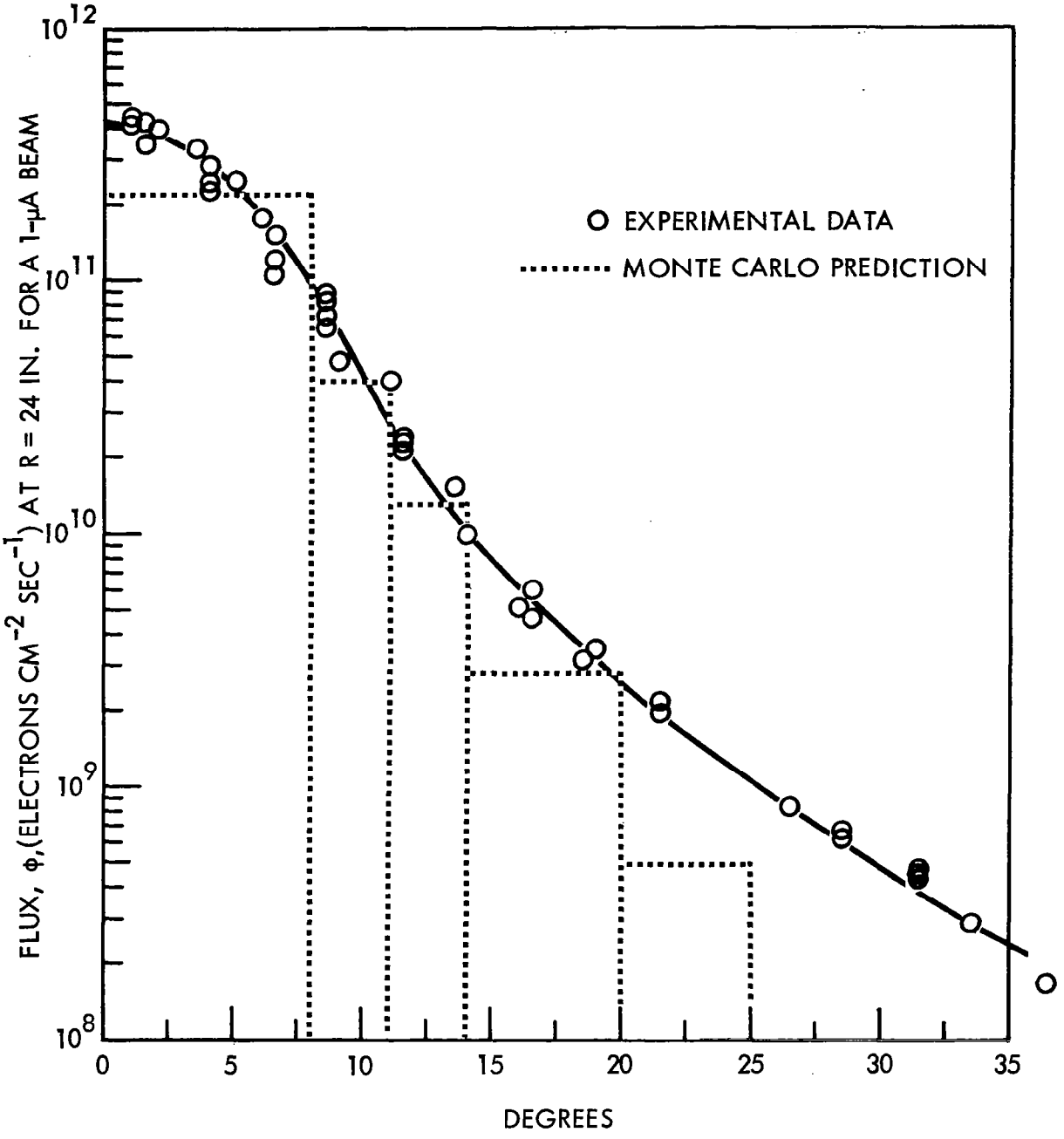

Figure 19. 0.53-Mev Electron Flux From 0.25 mil Al

Table 11. Properties of Transistor Encapsulement

Transistor Type	Manufacturer	Can Thickness, Mfg. Estimate (Mils)	Measured Can Thickness (Mils, ±0.2)	Can Material	T. O. Can Type
2N834	Motorla	$7^{+1.5}_{-0.0}$	8	Nickel	18
2N743	Tex. Inst.	8^{+2}_{-1}	7.5	Nickel (Type 330)	18
2N1613	Fairchild	15	11	Kovar	5
2N1711	Fairchild	15	11	Kovar	5
2N1132	Raytheon	$7^{+0.5}_{-0.5}$	7.5	Nickel	5
2N2303	Fairchild	15	13	Kovar	5
2N2538	Raytheon	$7^{+0.5}_{-0.5}$	8	Nickel	5
2N2219	Fairchild	15	12	Kovar	5
2N2801	Motorola	$9^{+1.0}_{-0.0}$	10	Nickel	5
2N2411	Tex. Inst.	8^{+2}_{+1}	7.5	Nickel (Type 330)	18

Table 12. Energy Loss in Transistor Can

Test No.	Energy Incident on Transistor (Mev)	$(dE/dX)_{Fe}$ (Mev cm^2 gm^{-1})	$(dE/dX)_{Ni}$ (Mev cm^2 gm^{-1})	Thick Can Transistor 2N2303		Thin Can Transistor 2N2538	
				Energy Loss (Mev)	Final Energy (Mev)	Energy Loss (Mev)	Final Energy (Mev)
21	2	1.40	1.35	0.36	1.64	0.22	1.78
22	1.3	1.36	1.32	0.35	0.95	0.21	1.09
23	0.53	Can off	Can off	0	0.53	0	0.53

transistor cans. Incident 2.0-Mev electrons were chosen since the spectra of electrons in the Van Allen belts decrease rapidly above 2 Mev. Incident electrons of energy 1.3 Mev, which result in approximately 1.0 Mev incident on the semiconductor chip, provided a good energy separation between the 2-Mev and 0.53-Mev tests. Cans were removed from the transistors for the 0.53-Mev test; thus exposure was representative of electrons of approximately 0.8 Mev. Electrons of 0.8 Mev were not used for direct exposure of capsulated transistors because of a serious loss of energy resolution and electron intensity in passing through a transistor can.

A jig was made for holding the transistors during the removal of the transistor cans. A jeweler's saw was used for can removal and filings were kept clear of the semiconductor chips. Transistors with their cases removed were color coded and a control transistor of each type was designated.

The stability of transistors which had been decapitated was verified by the repeatability of values obtained on the transit time and G.R. bridges, Fairchild Series 500 Tester, and the transistor curve tracer oscillograms taken before, after in air, and after in a vacuum.

2.4.3 Preparation of Test Equipment

Test fixtures were prepared for the mounting and remote switching of transistors as well as for the dynamic monitoring of transistor characteristic-curve traces. Transistors were mounted in sockets that were attached to the sample-mounting dish. The dish was spun out of aluminum in the form of a section of a sphere of 24-inch radius. Thus, electrons scattered from the foil (24 inches away) impinged at normal incidence to the tops of the transistors. The dish is attached to the inside of the end plate of the scattering chamber. Shielded leads from the transistors passed through a Deutsch high-vacuum feedthrough to a Leadex stepping switch which was mounted to the outside of the chamber end plate. Shields on these leads were grounded to the feedthrough which, in turn, was grounded to the chamber. Remote control was necessary in order to monitor the transistors during irradiation without the hazard of being exposed to the X rays generated in the magnet room. The

transistors are located approximately 100 feet from the data acquisition area. The Leadex switch allowed remote selection of the transistors to be characterized. Leadex switch wafers were modified so that selection of one transistor for characterization automatically grounded the base and collector leads of the remaining transistors to the Leadex switch box which in turn was grounded to the chamber (Figure 20). Also seen in Figure 20 are the leads for a transistor which was left under continuous bias during the tests. A remote position indicator was located in the data acquisition area to allow the operator to identify the transistor under test. The circuit of the positioner, which was designed and assembled for this program, is shown in Figure 21. Both the Leadex stepping unit and the positioning unit are shown in Figure 22.

A bench checkout of the transistor monitoring system revealed severe distortion of the common-emitter characteristic curves. Thus, a variety of grounding systems was investigated. However, no combination of grounding methods gave consistently satisfactory results for all transistors. The problem was brought under control by two additions to the circuitry: (1) 0.001-microfarad bypass condensers were installed from each collector to the aluminum mounting dish and the common-emitter line was connected to the dish through 200Ω resistors at several points which in turn was grounded through the chamber. The placing of these components was determined empirically. Subsequent testing indicates no significant difference between oscillograms of the same transistor taken when mounted on the mounting dish and when taken directly on the Tektronix Model 575 Curve Tracer. Figure 23 shows the final connections on back side of the transistor mounting dish. Shielded base leads and shielded emitter leads were tied into separate bundles and all lead cross overs were made at 90°.

2.5 ELECTRON IRRADIATION TESTS

Electrons of energies 0.53, 1.3, and 2.0 Mev were obtained using the Dynamitron accelerator. The accelerating potential is maintained by a stack of high-voltage rectifiers. The lowest voltage at which stable-beam currents could

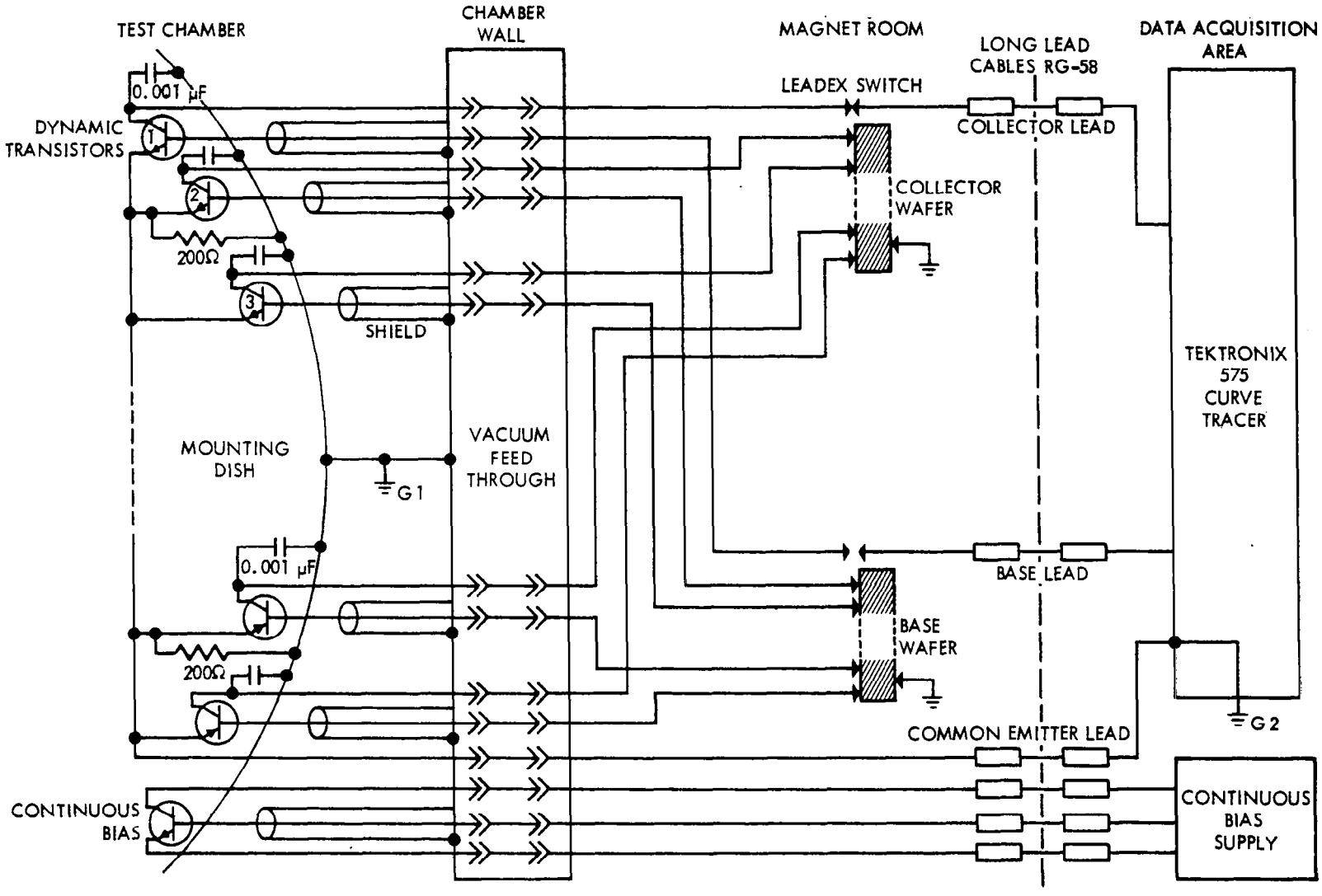

Figure 20. Dynamic Test Switching Circuitry

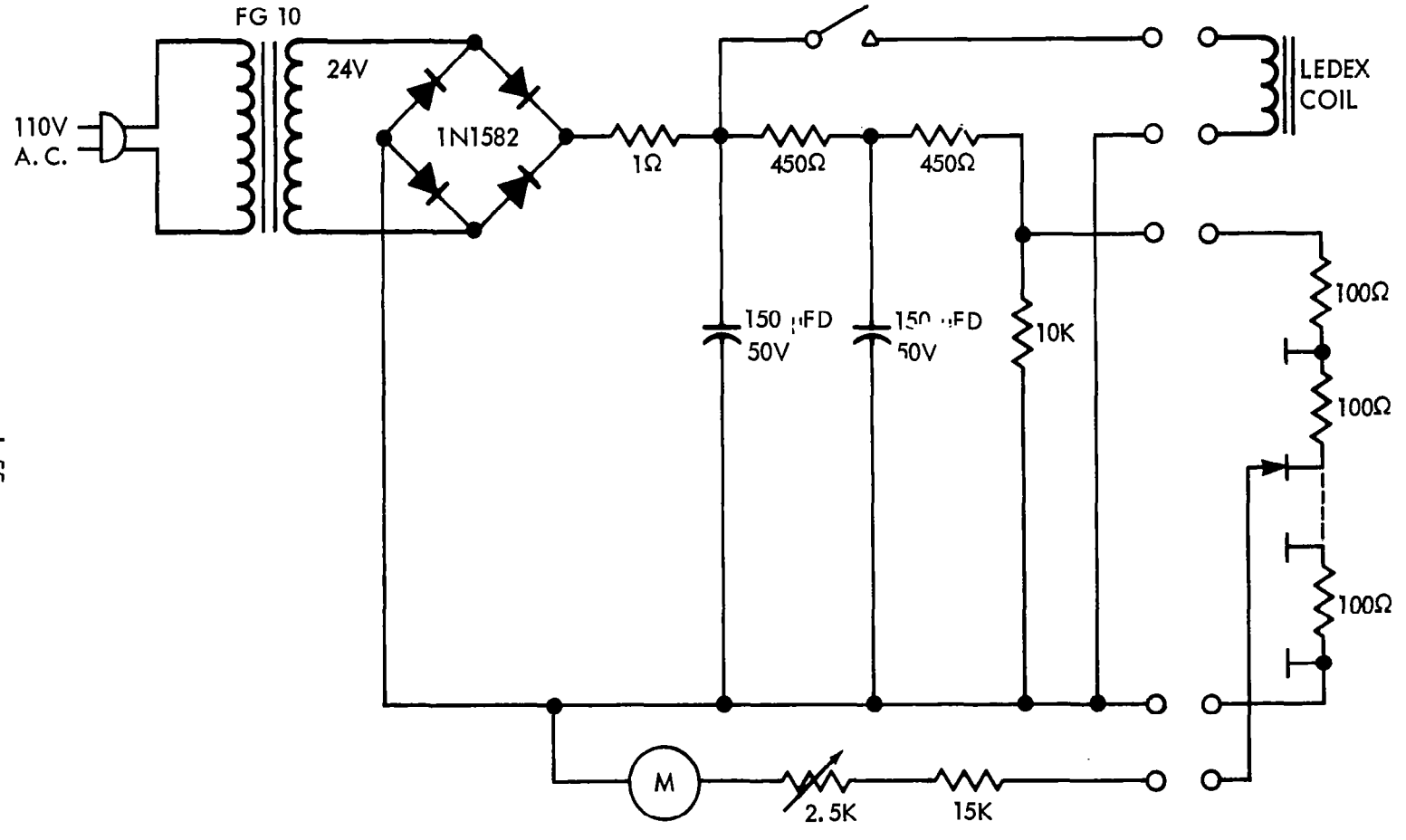

Figure 21. Position Selector and Indicator Circuit

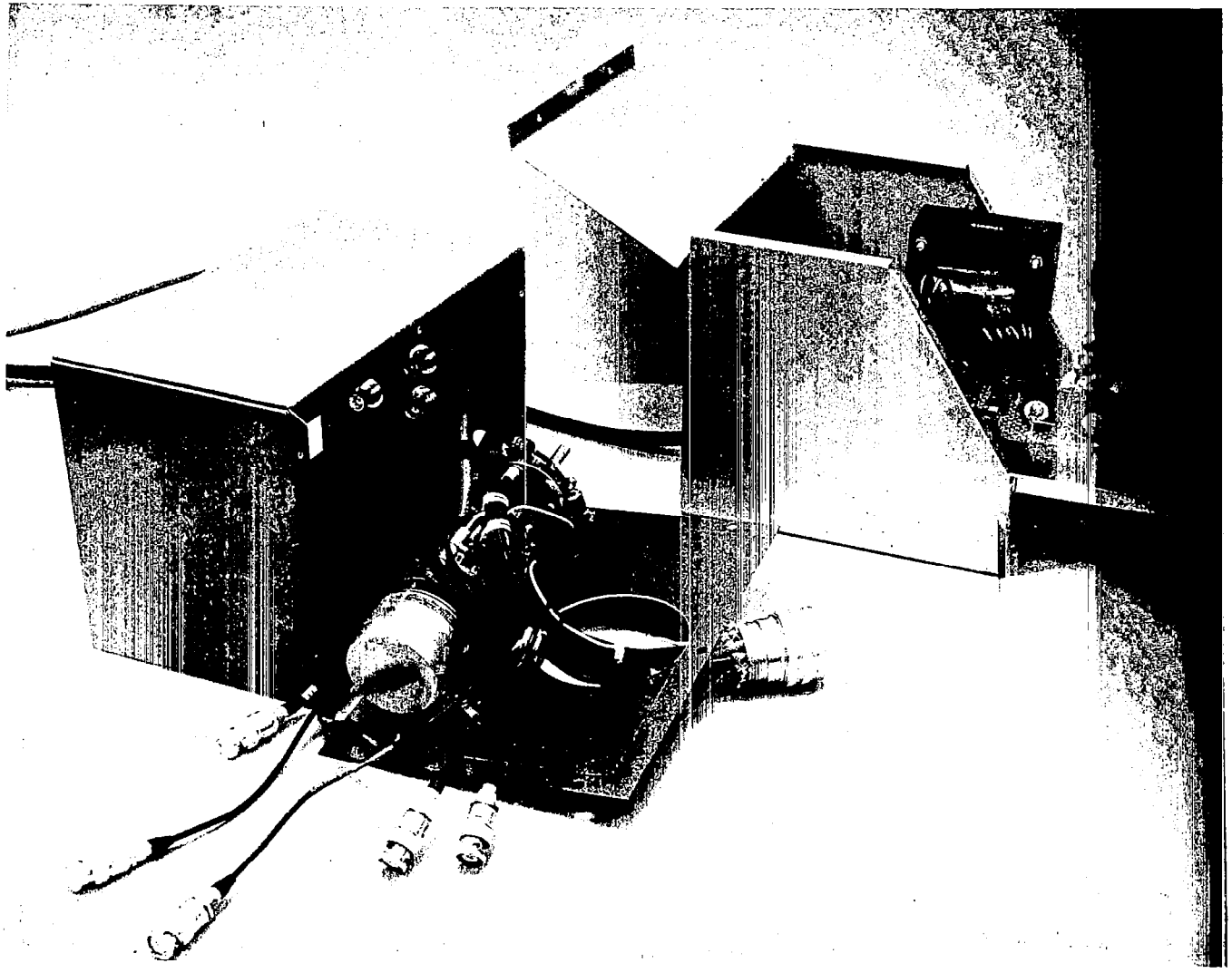

Figure 22. Stepping Selector and Positioner

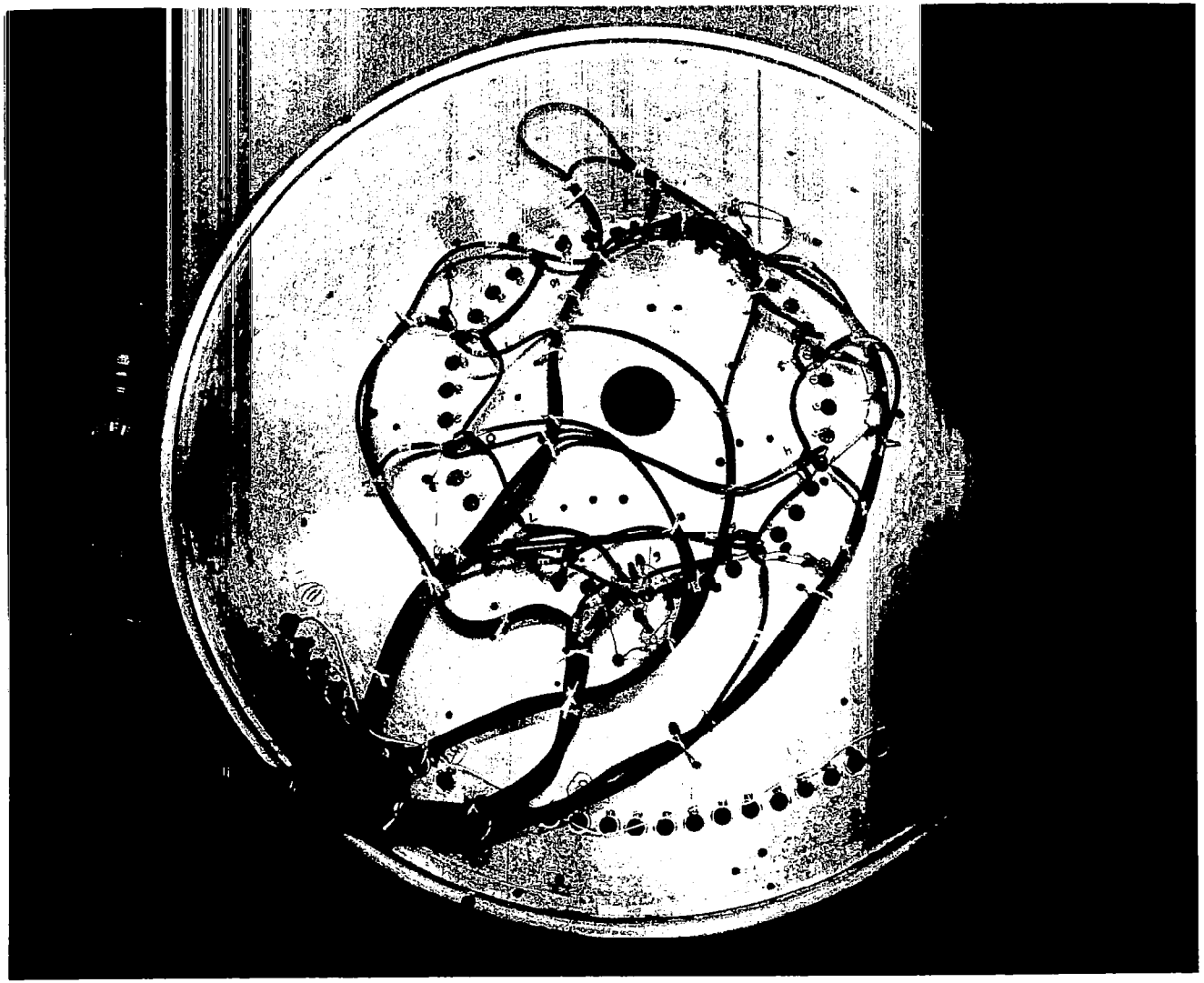

Figure 23. Lead Connections on the Mounting Dish

readily be maintained was 0.53 Mev. The beam spot characteristics and centering were adjusted by the exit-beam handling system. Detailed dosimetry measurements were performed during the test and controlled procedures were followed for obtaining dynamic test data.

2.5.1 The Test Configuration

Figure 24 shows the exit-beam handling system from the 90° bending magnet, which is attached to the Dynamitron vertical beam port, to the scattering chamber. Electrostatic lenses in the accelerator gun were adjusted in order to align the beam for optimum entrance into the bending-magnet chamber. This alignment was determined from the ratio of the current monitored on the water-cooled straight-through aperature, A_1, to the straight-through beam current striking the magnet chamber walls.

The current through the bending magnet is adjusted by a regulated-current supply in order to bend the beam into the quadrupole lensing magnet. The exit side of the magnet is evacuated by a 4-inch oil-diffusion pump with its associated liquid-nitrogen baffles and fore pump. Proper beam alignment is determined by minimizing the current collected on the quadrupole entrance aperture, A_2. The quadrupole magnet is adjusted by a regulated supply in order to focus the beam for its entrance into the chamber aperture and subsequent impingement on the scattering foil. Optimum focusing by the quadrupole magnet is determined by the ratio of current collected on the chamber aperture, A_3, to that passing straight through into a fixed Faraday cup at the back of the chamber. Figure 25 shows a schematic of the scattering chamber. The chamber is evacuated by a 6-inch oil-diffusion pump and can be sealed off from the exit-beam tubing by use of a gate valve. When beam passes through the entrance aperture, it can either pass directly into a fixed Faraday cup or be scattered by a thin foil. The back of the Faraday cup consists of a quartz window for beam viewing and a wire screen for charge collection. A positive 300 volts is applied to the screen to reduce electron back scatter and to reduce electron-charge buildup and its subsequent arcing in the quartz window.

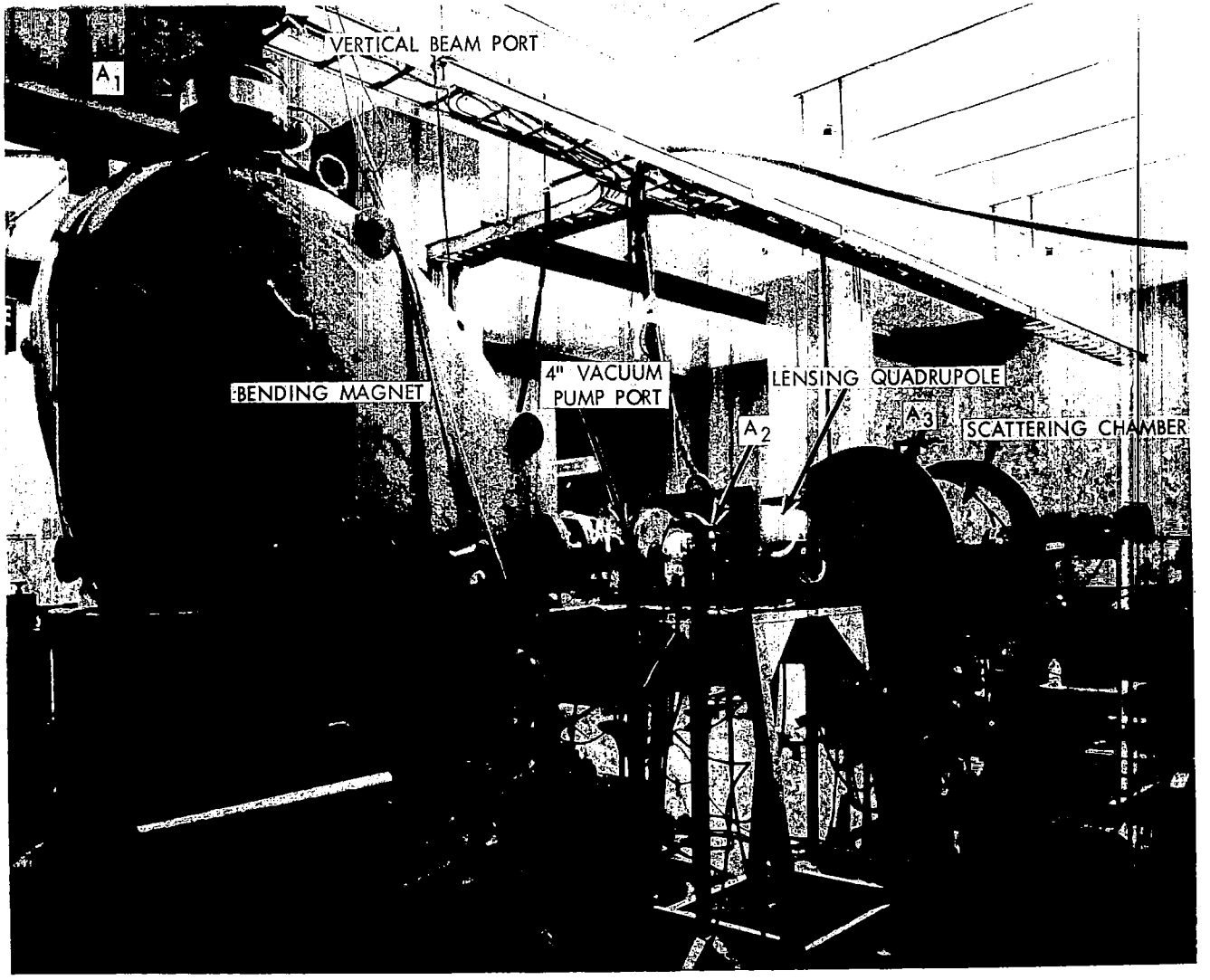

Figure 24. Electron Beam Handling System

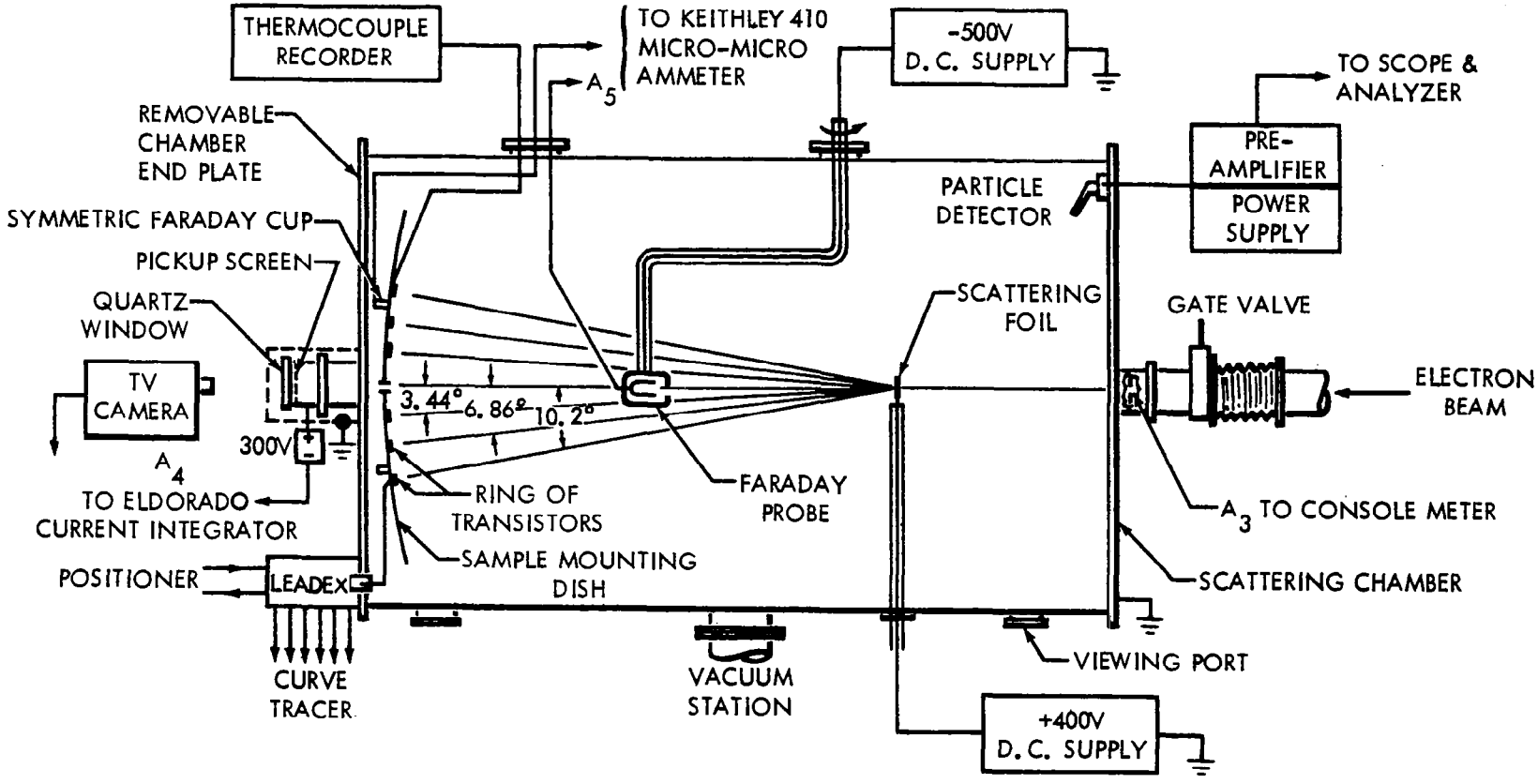

Figure 25. Scattering Chamber Schematic

With a selected foil in place the beam will be scattered as illustrated in Figure 25. The magnitude of the scattered flux decreased as a function of angle, as was shown in Figures 17, 18, and 19, respectively, for the various tests. These angles at which the transistor arrays were located are also shown in Figure 25. A positive voltage of 400 volts was applied to the foil holder to aid in suppressing the forward scattering of secondary electrons generated in the foil.

2.5.2 Dosimetry

The fluorescence of the Faraday-cup quartz window, resulting from the incident straight-through beam, was observed using a closed-circuit television system. The television camera was focused on the quartz window and was used to observe beam-spot shape, size, and centering. The spot shape and size were altered by adjusting the field strength of the quadruople lensing magnet. An empty-foil position on the foil holder was then centered on the beam to determine if the spot size was small enough and whether optical alignment was accurate. Initially, alignment had been determined by sighting with a surveyor's transit through the viewing plate and chamber aperture back down the beam tube to a window at the exit of the 90-degree bending magnet. The scattering chamber was adjusted vertically and horizontally so that the straight-through beam spot was centered on the quartz viewing plate which, in turn, centered on the transistor mounting dish. Straight-through beam current was collected on a wire screen, A_4, on the face of the quartz window at the back of the Faraday cup. A coaxial pickup cable was connected to the screen and the beam current was monitored and integrated using an Eldorado Electronics Model CI-110 current integrator. The fixed Faraday cup was shielded by a grounded-wire screen to reduce noise pickup and allow for accurate low-current readings. The ratio between the current readings in the fixed Faraday cup, A_4, with the foil in and with the foil out was measured at the beginning of a test to provide an accurate means for continuous monitoring of the beam current during a test.

Thin aluminum foils were used for scattering electrons in order to provide large exposure areas with uniform particle fluxes. Electron scattering provided a

constant value of uniform flux on those transistors located in a circular array at the same angle from the beam axis. Different fluxes were obtained by mounting transistors at different angles. A large number of transistors were exposed at each of three different fluxes during a single test. Figure 26 shows the inside of the scattering chamber with both the foil holder and the rotating Faraday probe in place, and with transistors mounted on the dish. Measurement and calculation of scattered flux were described in Section 2.4.1. Those measurements were made using the Faraday probe, which was rotated about the foil to determine mapping as a function of scattering angle. The cup of the Faraday probe, A_5, is contained in and insulated from an outer housing which acts both as a shield and a limiting aperture. Current collected by the probe was measured on a Keithley Model 410A micro-micro ammeter. Care was taken to zero the meter before each reading.

Table 13 shows typical current readings on the various cups and apertures for each of the three tests, respectively. In addition to the probe and large fixed Faraday cup, four smaller cups were placed on the sample-mounting dish in symmetric positions (up and down, left and right). These cups verified symmetry of the scattered beam and were used to detect changes of the beam alignment during an exposure run.

2.5.3 Test Procedure

At the start of each test the curve tracer was allowed to warm up. The curve tracer was then calibrated and the $I_B = 0$ line was zeroed and a picture was taken of the standard 2N1613 control. The dynamic devices (one transistor of each of the 10 types which were to be monitored on long leads during irradiation) and the continuous-bias device were placed on the mounting dish and their long-lead curve traces were compared with their original oscillograms. The passive devices (three transistors of each of the 10 types which would be recharacterized directly on the curve tracer at periods when the chamber was opened) were placed on the mounting dish.

To begin a typical irradiation test, the scattering chamber was evacuated to approximately 1×10^{-6} torr and then opened to the evacuated beam tubing.

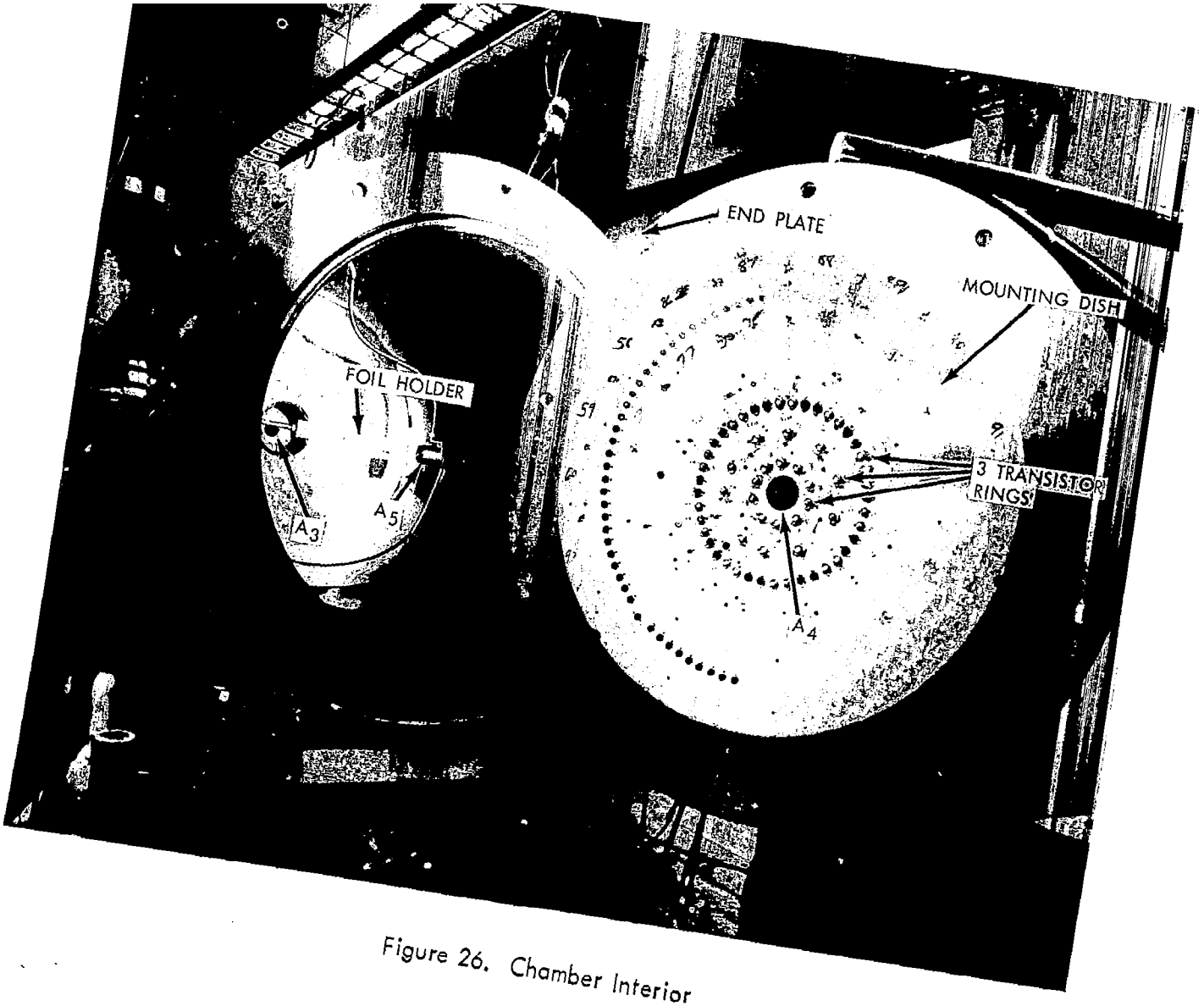

Figure 26. Chamber Interior

Table 13. Typical Data From Current Monitoring

Test Energy (Mev)	Date	Time	Straight-Through Limiter, A_1 (μamp)	Quadrupole Aperture, A_2 (μamp)	Chamber Aperture, A_3 (μamp)	Faraday Cup, A_4 (μamp)	Al Foil (mil)	Probe Angle (degrees)	Probe (R = 8.8"), A_5 (μamp)
2.0	9/16/65	01:45	10.5	1.1	3.7	9.4	0	--	--
		01:48	10.5	0.9	3.5	0.5	5.0	45	4.9×10^{-4}
1.3	9/23/65	10:55	13.0	1.0	1.0	6.4	0	--	--
		11:03	15.4	1.0	1.0	0.4	1.6	10	3.4×10^{-2}
0.53	9/30/65	12:57	22.0	3.2	10.2	34	0	--	--
		13:03	22.0	3.2	10.5	2.9	0.25	20	7.4×10^{-3}

Vacuum was maintained until the end of an exposure run when the passive devices were removed and recharacterized. Each test consisted of three exposure runs. A full set of oscillograms on the dynamic devices were taken before exposure.

Beam current was then turned up and appropriate dosimetry was performed, including a foil-out to foil-in measurement of current ratio. The rotatable Faraday probe was then set at a fixed angle, out of the way of the transistor arrays. With the foil in place the integration of that portion of the current collected into the fixed Faraday cup commenced. Flux rates and exposure times for each run had been predetermined by a preliminary exposure of a selected number of transistors. This preliminary test also aided in determining the transistor arrays and exposure range to cover a significant range of damage.

The continuous-bias transistor and each of the dynamic transistors were monitored periodically during a particular run with oscillograms of curve traces taken as desired. Integrated current was recorded each time an oscillogram was taken. Occasionally during an exposure run, the beam was turned down and a full set of pictures was taken on the dynamic transistors all at the same fluence. At the end of an exposure run the beam was turned down, a full set of dynamic pictures were taken, fluence was calculated, and the temperature of a spare transistor in the test chamber was recorded. Following the 2-Mev electron test the temperature of the transistor mounting plate was monitored with a portable thermocouple probe. A fixed thermocouple was then installed in the chamber prior to the 1-Mev electron test in order to periodically monitor transistor ambient temperature. After the chamber was opened to the air another set of oscillograms of the dynamic transistors was taken. The passive transistors were removed and measured directly on the curve tracer. These transistors were then placed back in the chamber, the Faraday probe was set at a different angle, and the procedure was repeated until three exposure runs were completed. Thus, four oscillograms of all passive transistors were obtained, one before picture and three pictures at different fluences. Table 14 shows typical data recorded on a computer keypunch data form for a passively tested transistor. As many as 20 dynamic pictures, as a function of

Table 14. **KEYPUNCH DATA FORM**

TEST HEADING CARD

Test	Transistor Type	Transistor No.	No. of Pictures	Batch No.	Case	Mfg.
23	16 13	08	4	4 36	O N	FC LD

PICTURE READING CARD

Picture No.	Date	Time	I_C/div (ma)	V_C/div (volts)	I_B/step	Load Resistor (megohms)	Fluence (electrons/cm^2)	Temperature (degrees absolute)
A1	07 27 65	14 56	2. 0	2. 0	0 .0 5	0 .0 00 1	0. 0	29 8. 5
A2	09 28 65	13 07	2. 0	2. 0	0 .0 5	0 .0 00 1	0. 0	29 8. 2
B	09 30 65	14 32	2. 0	2. 0	0 .0 5	0 .0 00 1	5. 04 E 14	29 9. 7
C	09 30 65	23 35	2. 0	2. 0	0 .2 0	0 .0 00 1	3. 64 E 15	29 8. 7
D	10 01 65	10 53	2. 0	2. 0	0 .5 0	0 .0 00 1	1. 82 E 16	29 8. 2

fluence, were taken of each of the 10 transistor types plus the continuous bias transistor. Identification numbers of transistors exposed in the three electron tests are given in Figures 27, 28, and 29.

2.6 PRELIMINARY ANALYSIS OF TEST DATA

A preliminary analysis was performed on the effects of electron irradiation on transistor parameters. The data which were analyzed included values of those radiation-sensitive parameters measured by use of the Fairchild Series 500 Semiconductor Tester as well as oscillograms of transistor common-emitter characteristic curves made from the display of the Tektronix 575 Curve Tracer. The results of this study are presented mainly as an indication of the direction in which the program is proceeding. Included is an example of the effectiveness of radiation-control parameters in normalizing the degradation of common-emitter current gain. Preliminary correlation of radiation damage with the energy of electron radiation is also given.

In the contract final report considerably more data will be reduced. A greater emphasis will be placed on the correlation between the radiation-induced changes observed and the theory of transistor behavior. Extensive data taken from the oscillograms of characteristic curves will be computer analyzed before valid radiation equivalences are presented.

2.6.1 Fairchild Series 500 Semiconductor Tester Data

Selected values of radiation-sensitive transistor parameters, which were measured using the Fairchild Series 500 Semiconductor Tester (breakdown voltage, d.c. common-emitter current gain, saturation voltages, leakage current, and base turn-on voltage), have been analyzed. This was done in order to investigate the dependence of those parameters on electron fluence and energy. In addition it will provide insight into both the role of radiation interactions in inducing significant effects in various regions of the transistor and into the means of predicting or controlling these effects.

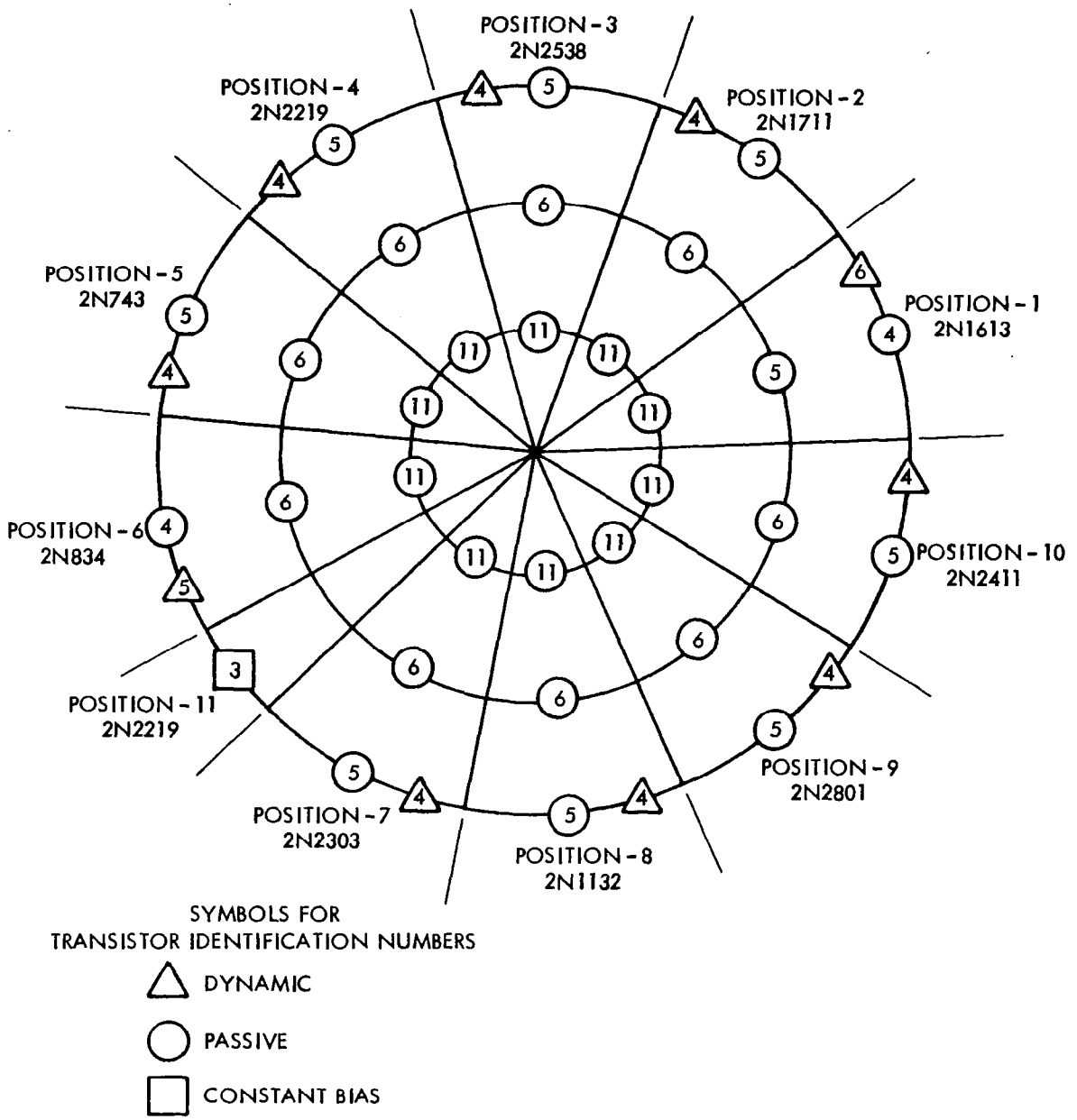

Figure 27. Transistor Array for 2.0-Mev Test

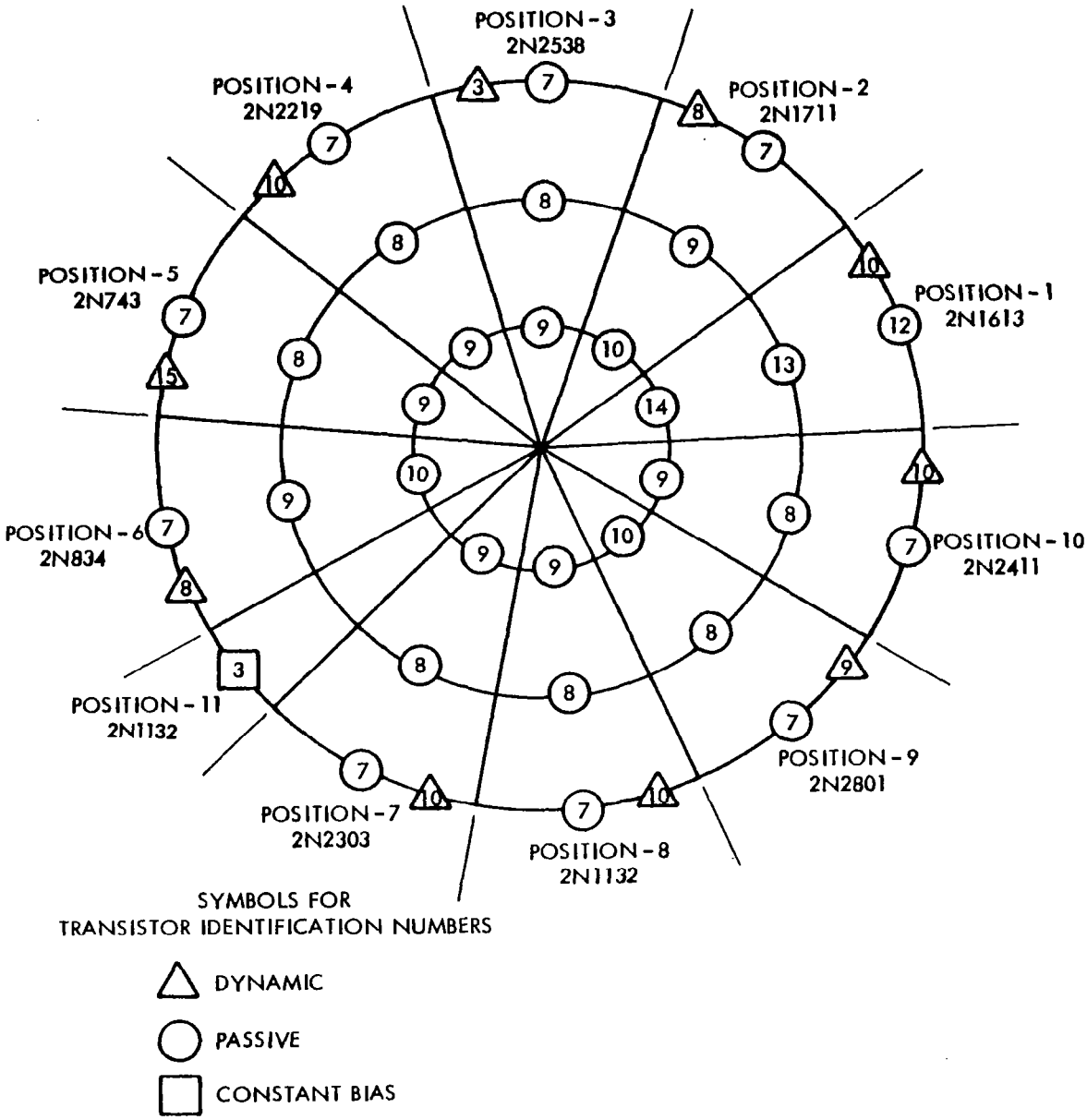

Figure 28. Transistor Array for 1.3-Mev Test

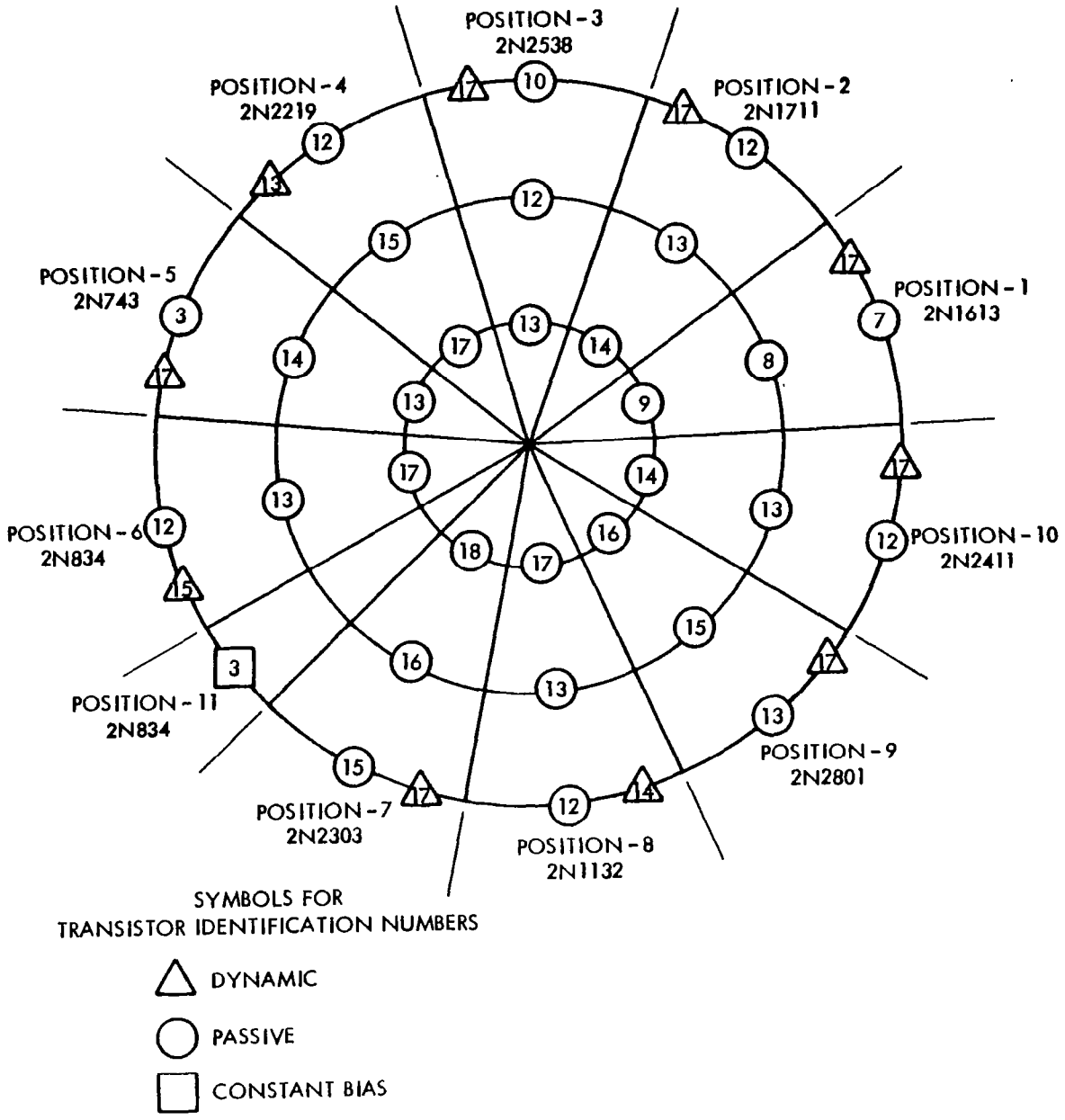

Figure 29. Transistor Array for 0.53-Mev Test

The least radiation sensitive of the parameters which were studied was the breakdown voltage, BV_{CBO} (measured at a collector current of 100 μa). Even after extensive electron irradiation (over 10^{16} electrons/cm^2) only small changes were observed for all of the 10 transistor types. An average of those values of the percentage of change in BV_{CBO} is shown in Table 15 for each of the three electron tests. Most of the transistor types either showed no significant change (within the limits of precision) or showed an increase in breakdown voltage which does not appear to be a function of electron fluence (over the range of approximately 4×10^{15} to 4×10^{16} electrons/cm^2). Only a few of the devices appeared to show any dependence on electron fluence. Both of the npn epitaxial mesa transistors, 2N743 and 2N834, as well as transistor 2N2538, showed an apparent decrease of BV_{CBO} with increased fluence. Both pnp epitaxial planar devices, 2N2801 and 2N2411, showed an apparent increase in BV_{CBO}. Changes in breakdown voltage for those transistors of types 2N2411 and 2N2538 are plotted in Figure 30 for each of the electron tests. A dotted line is used to compare the 2N2411 data with a linear dependence on fluence. Accuracy of the electron fluence measurement is approximately 15 percent. The accuracy of the BV_{CBO} measurement from the Fairchild Series 500 is only about ±1 percent, which almost renders these values of small change useless. However, only relative values are important for comparison purposes and the precision, as determined by repeatability of measurements, is approximately ±0.2 percent. Thus, Figure 30, due to its consistent dependence on energy, may possibly be an indication of the relative order of effectiveness of electron energy (1.8, 1.1, and 0.5 Mev) for changes in BV_{CBO}.

Saturation voltage, $V_{CE}(sat)$, measured at a current gain of 2 for collector currents of 2 and 10 ma, respectively, increased by over 100 percent for many of the exposed transistors. Table 16 lists the observed changes in both h_{FE} and $V_{CE}(sat)$ for those transistors of each type which were exposed passively during the 1-Mev electron test. Analysis of the changes of h_{FE} will be discussed in detail for the data reduced from oscillograms of common-emitter characteristic curves. The strong dependence of the changes of both h_{FE} and $V_{CE}(sat)$ on electron fluence is apparent. The changes in $V_{CE}(sat)$ for the npn transistors exposed in the 1-Mev electron

Table 15. Electron-Induced Changes in BV_{CBO}

Device Type	BV_{CBO} at 100 μa of Control Transistor No. 1 (volts)	Average $\Delta(BV_{CBO})$ in Percentage for the Electron Tests			Apparent Change with Increased Fluence
		0.53 Mev	1 Mev	2 Mev	
2N1613	118	7	10	9	None
2N1711	135	8	7	7	None
2N2538	100	0 to -12	-1 to -17	1 to -25	Possible decrease
2N2219	82.7	1	6	8	None
2N743	63.9	0 to -10	0 to -5	0 to -8	Possible decrease
2N834	81.2	1	-4	-1	Possible decrease
2N303	70.8	0	7	2	None
2N1132	82.9	12	9	9	None
2N2801	57.9	0 to 3	0 to 8	3	Possible increase
2N2411	57.7	0 to 6	0 to 4	2 to 7	Possible increase

test are shown in Figure 31. The data for pnp transistors are presented in Figure 32. A dependence on electron energy is also apparent and is shown in Figure 33 for the npn epitaxial mesa devices 2N743 and 2N834. The dotted lines are used to compare these data with a linear dependence on fluence. Changes in $V_{CE}(sat)$ for the other transistor types also show a strong dependence on fluence and, in general, a similar relative dependence on electron energy. This dependence is somewhat similar to the possible energy dependence observed for changes in BV_{CBO}. It can be noted that the relative effectiveness of electron energy is in the same order as the cross section for electron displacements in silicon (Reference 15). Furthermore, the effectiveness of electrons is not consistent with the relative rates of ionization in silicon for these energies (Reference 16).

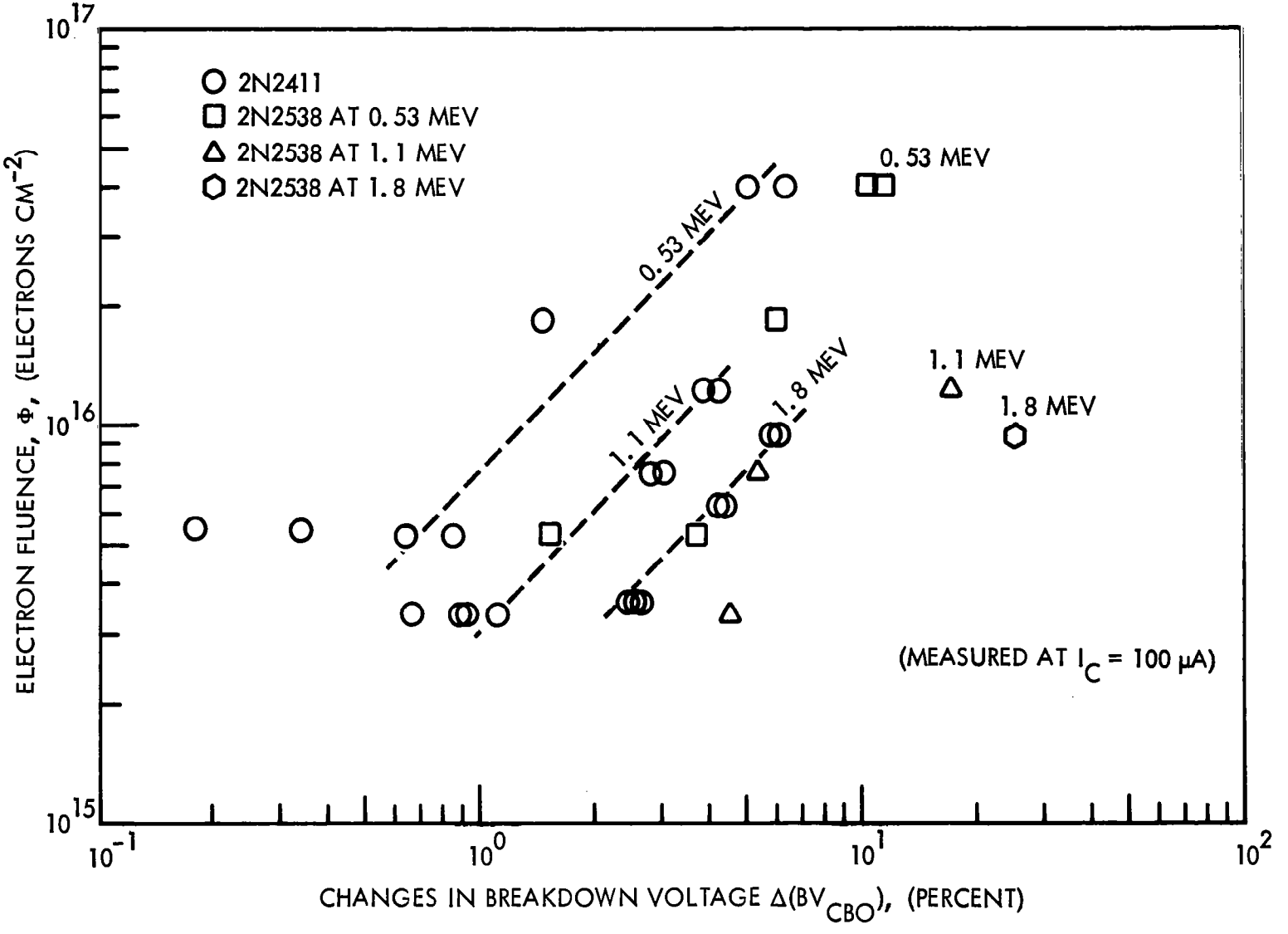

Figure 30. Dependence of $\Delta(BV_{CBO})$ on Electron Fluence

Table 16. Electron-Induced Changes in V_{CE}(sat) (Passive Transistors in the 1-Mev Test)

Transistor Type	Exposure	$\Phi = 3.36 \times 10^{15}$ e/cm^2 Device No.	h_{FE} 2 ma	h_{FE} 10 ma	V_{CE}(sat) (volts) 2 ma	V_{CE}(sat) (volts) 10 ma	$\Phi = 7.56 \times 10^{15}$ e/cm^2 Device No.	h_{FE} 2 ma	h_{FE} 10 ma	V_{CE}(sat) (volts) 2 ma	V_{CE}(sat) (volts) 10 ma	$\Phi = 1.22 \times 10^{16}$ e/cm^2 Device No.	h_{FE} 2 ma	h_{FE} 10 ma	V_{CE}(sat) (volts) 2 ma	V_{CE}(sat) (volts) 10 ma
2N1613	Before	12	51.4	58.7	0.065	0.090	13	46.4	56.8	0.063	0.092	14	54.7	61.1	0.068	0.094
	After		9.7	10.9	0.125	0.178		6.2	6.6	0.143	0.208		2.2	2.4	---	---
2N1711	Before	7	183	215	0.052	0.093	9	179	202	0.048	0.087	10	167	213	0.047	0.085
	After		28.3	33.3	0.099	0.183		14.9	16.5	0.115	0.203		9.2	9.7	0.130	0.228
2N2538	Before	7	73.8	102	0.102	0.094	8	229	291	0.102	0.094	9	136	186	0.103	0.095
	After		25.9	36.0	0.111	0.115		27.5	34.2	0.118	0.130		19.9	23.6	0.122	0.138
2N2219	Before	7	145	180	0.008	0.018	8	131	163	0.009	0.018	9	139	163	0.011	0.022
	After		44.8	63.8	0.054	0.060		33.6	43.7	0.070	0.084		24.3	29.2	0.095	0.121
2N743	Before	7	30.0	35.1	0.084	0.093	8	41.2	51.2	0.090	0.096	9	33.0	43.2	0.115	0.115
	After		14.0	17.5	0.102	0.118		13.1	15.3	0.116	0.137		9.0	8.8	0.152	0.180
2N834	Before	8	152	157	0.134	0.139	9	64.9	72.0	0.135	0.133	10	92.4	103	0.121	0.116
	After		18.9	23.7	0.149	0.165		6.9	7.9	0.170	0.192		7.0	8.9	0.152	0.163
2N2303	Before	7	117	113	0.048	0.091	8	149	141	0.062	0.146	9	119	115	0.052	0.105
	After		6.4	7.0	0.115	0.160		4.0	4.2	0.152	0.232		1.89	1.99	---	---
2N1132	Before	7	67.2	68.4	0.026	0.031	8	26.0	41.7	0.026	0.032	9	58.4	59.4	0.027	0.033
	After		6.6	7.8	0.100	0.108		3.0	3.7	0.154	0.155		2.0	2.2	---	---
2N2801	Before	7	80.9	92.2	0.055	0.066	8	92.3	97.5	0.046	0.057	10	78.5	83.0	0.063	0.068
	After		10.9	14.9	0.09	0.112		4.8	6.6	0.123	0.154		3.0	4.0	0.169	0.186
2N2411	Before	7	142	135	0.085	0.107	8	150	146	0.088	0.123	9	85.8	85.8	0.051	0.080
	After		27.1	30.7	0.108	0.145		16.1	18.2	0.127	0.192		8.5	9.0	0.136	0.219

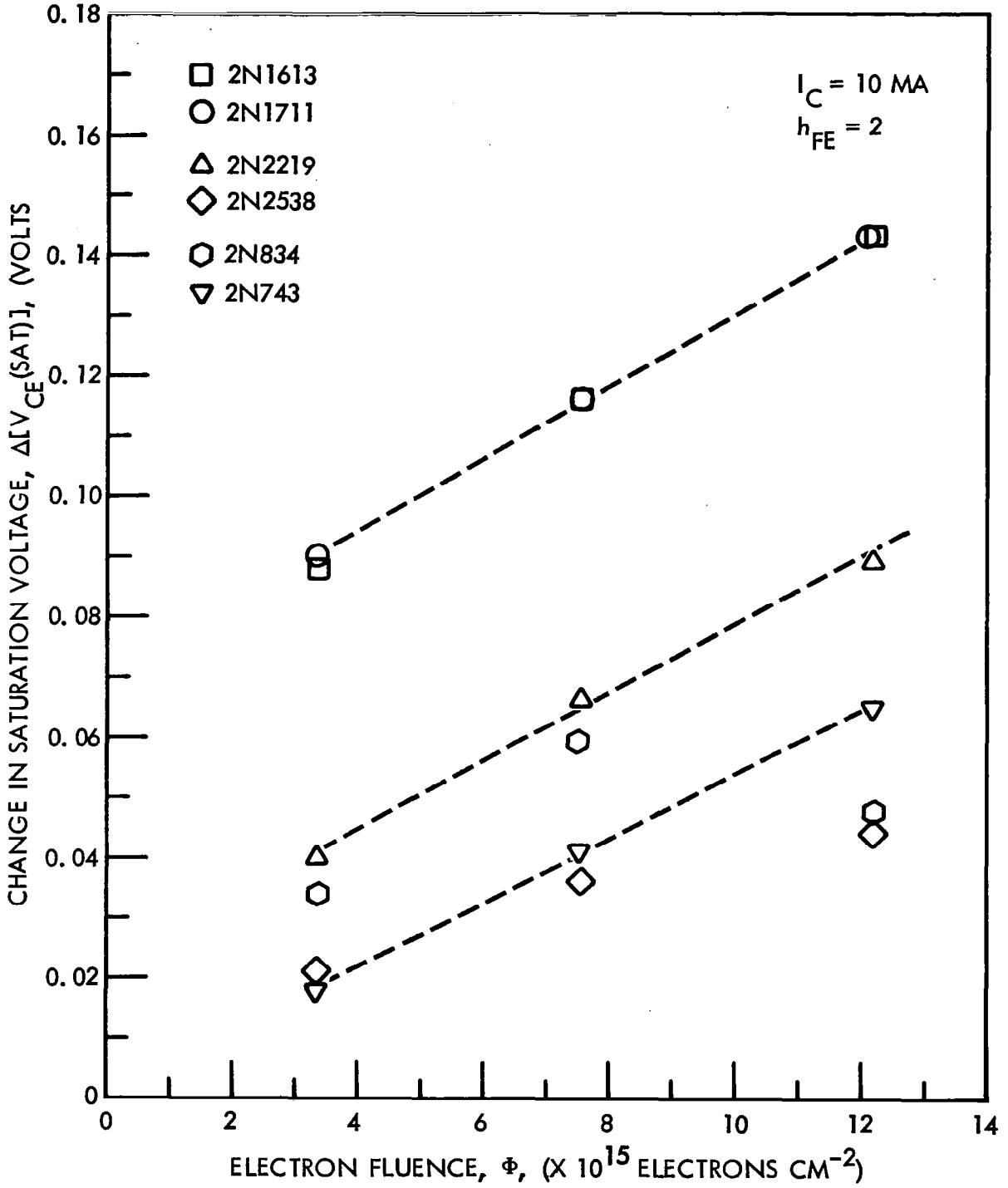

Figure 31. $\Delta[V_{CE}$ (sat)] of npn Transistors for 1-Mev Electrons

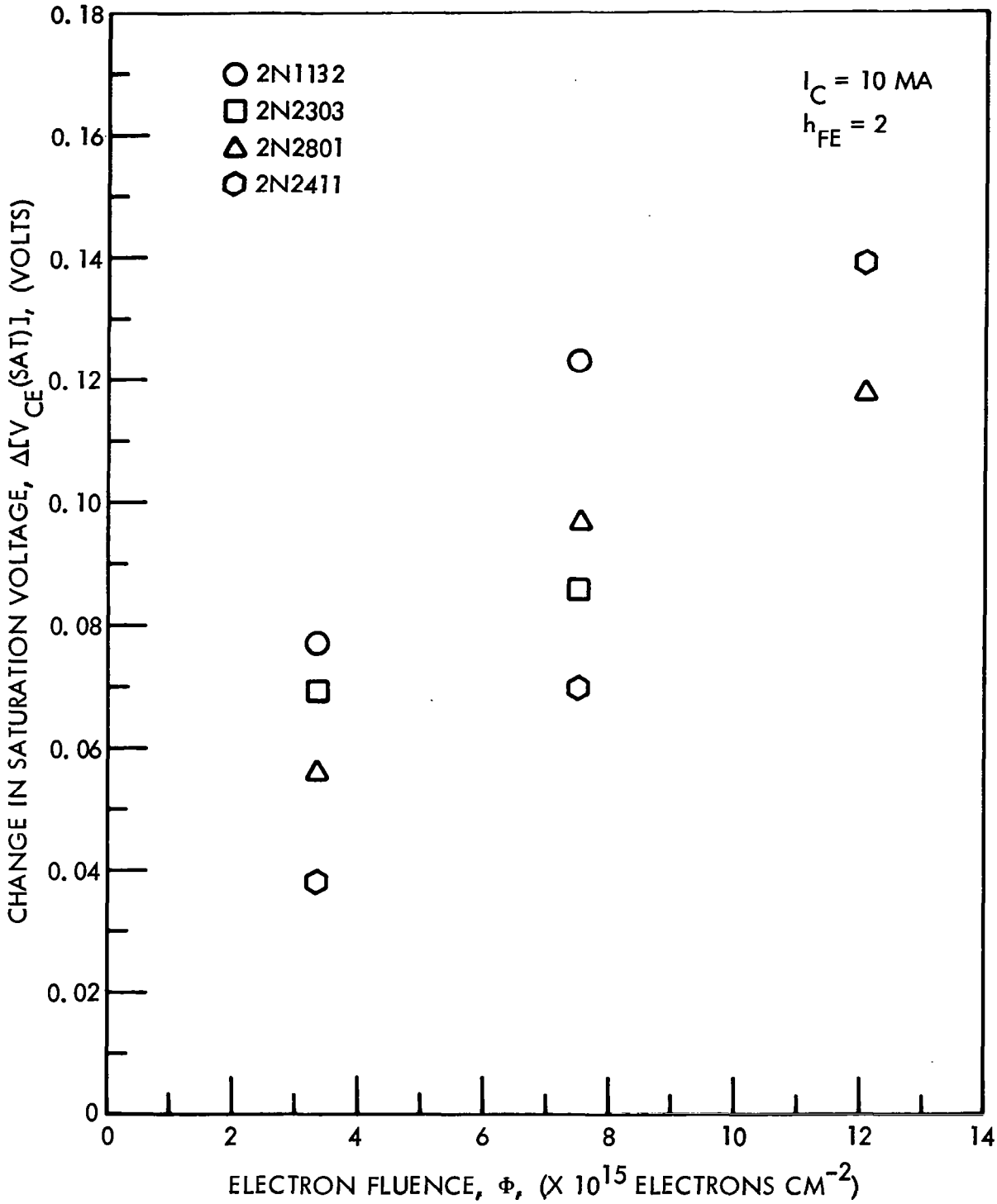

Figure 32. $\Delta[V_{CE}$ (sat)] of pnp Transistors for 1-Mev Electrons

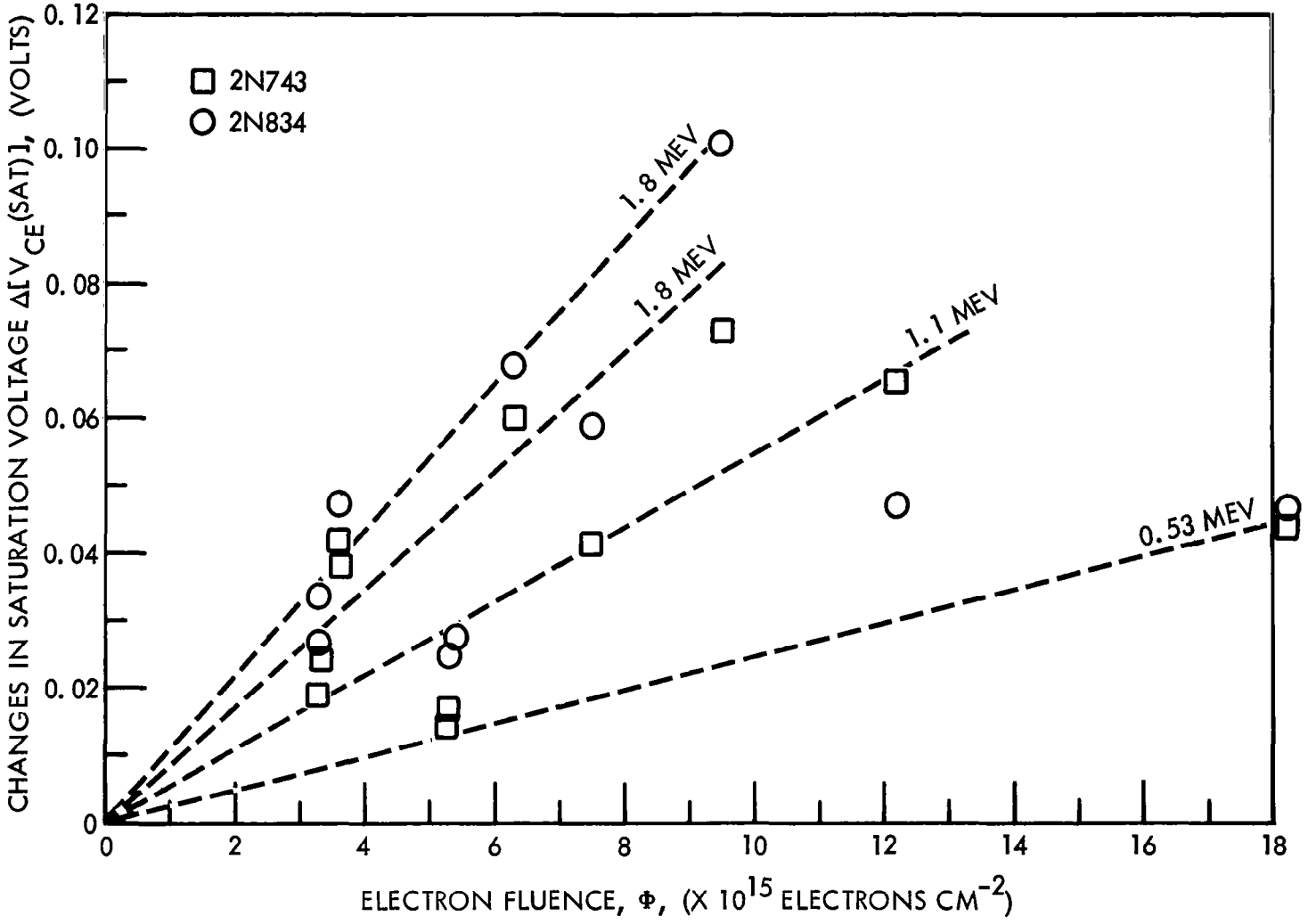

Figure 33. Dependence of $\Delta[V_{CE}(sat)]$ on Electron Energy

The changes in saturation voltage, $V_{BE}(sat)$, were, in general, much smaller than those of $V_{CE}(sat)$. However, $\Delta V_{BE}(sat)$ also shows the strong dependence on electron fluence. Values of changes in $V_{BE}(sat)$ after the 0.52-Mev electron test are presented in Table 17 for transistor types 2N743 and 2N834.

Table 17. Electron-Induced Changes in $V_{BE}(sat)$

Device Type	$\Delta[V_{BE}(sat)]$ (volts) for 0.53-Mev Test		
	$\Phi_1 = 4.94 \times 10^{15}$ e/cm^2	$\Phi_2 = 1.6 \times 10^{16}$ e/cm^2	$\Phi_3 = 4.03 \times 10^{16}$ e/cm^2
2N743	0.006	0.016	0.034
2N834	0.011	0.031	0.067

Leakage current, I_{CBO} (measured at a collector voltage of 10 volts), was observed to permanently increase for transistors exposed to electrons. Test data for the effects on I_{CBO}, in general, showed no evidence of a dependence on electron fluence (over the range of exposures). Figure 34 shows a comparison of initial- and final-leakage currents for the 2N2303 transistors irradiated in the electron tests. The diagonal line represents values for no change. This transistor comes the closest to showing any dependence on the amount of radiation exposure, but it also is the only transistor that shows such a wide variation in both initial and final values of leakage current. Furthermore, these tests provide no evidence of a dependence on particle energy that would indicate whether it is ionization or displacement damage which was the important factor for these permanent changes in leakage current. Five other transistor types (2N1132, 2N1613, 2N1711, 2N2219, and 2N2801) also showed large changes in leakage current changes but no dependence on electron energy. Data on these devices are shown in Figure 35, with the exception of the 2N1613 whose data point grouping was the same as the 2N1711. These devices, with the exception of the 2N1132, had very little dispersion in either the initial or final values of I_{CBO}. The 2N1132 showed the same increase in I_{CBO} independent of initial value, which would indicate greater percentage

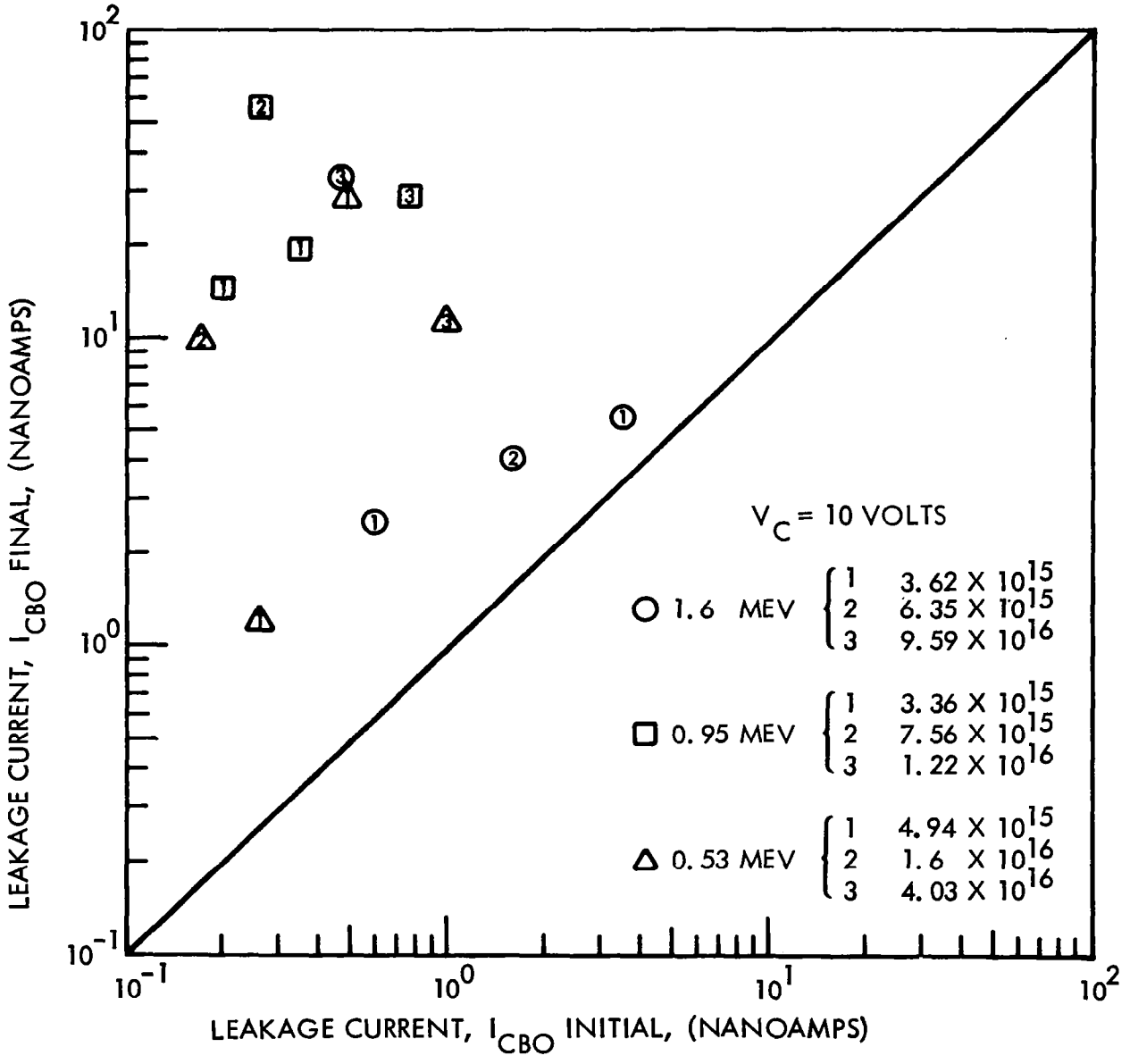

Figure 34. Changes of I_{CBO} for the 2N2303

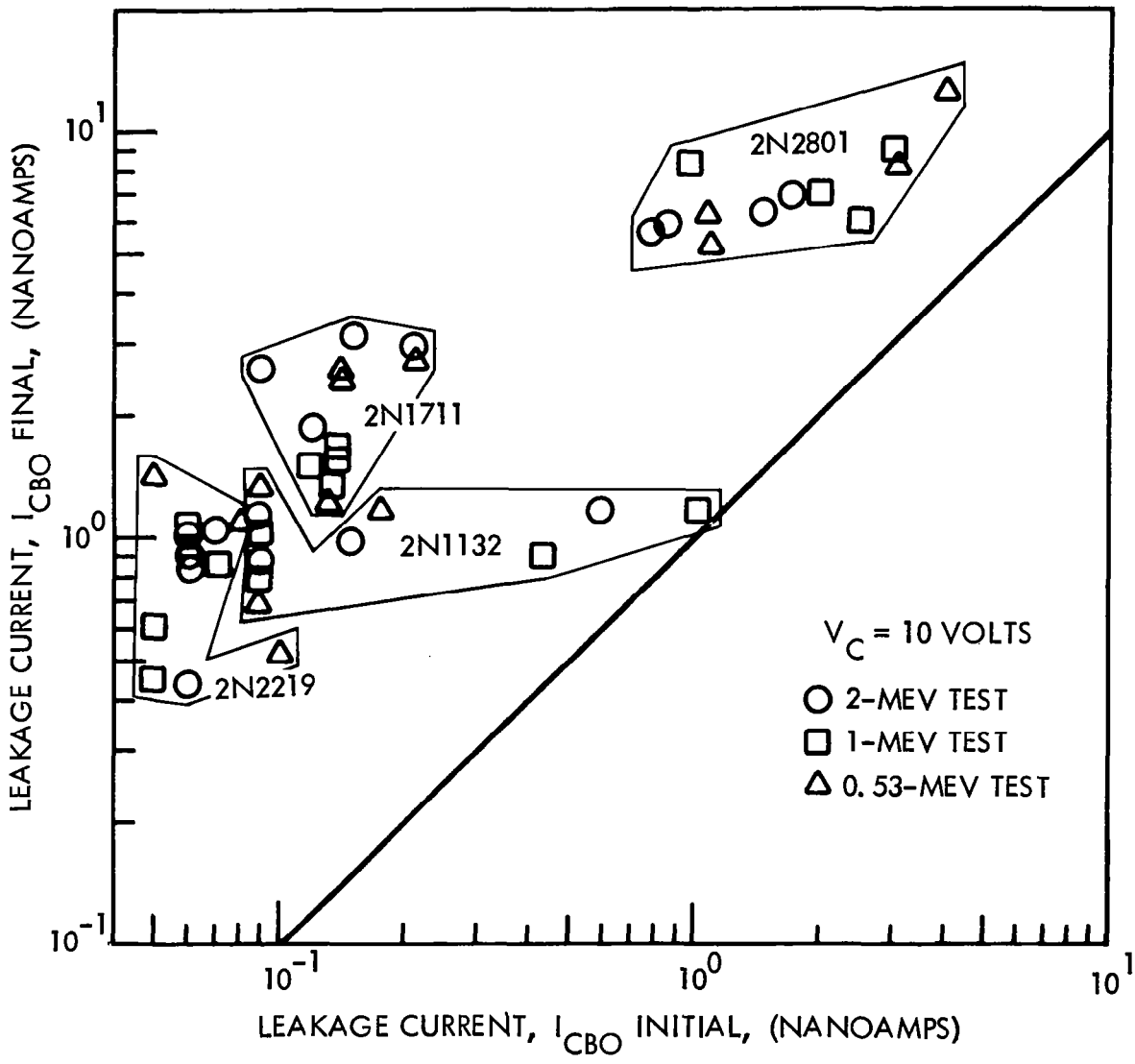

Figure 35. Transistor of Large Percentage of ΔI_{CBO}

increases for those of lower-initial leakage current. The remaining transistor types (2N743, 2N834, 2N2411, and 2N2538) are shown in Figure 36. These devices showed only small percentage increases in leakage current. This percentage increase, however, is approximately a constant over 2 orders of magnitude of initial I_{CBO}. This dependence of the radiation sensitivity of transistor I_{CBO} on its initial value was observed in earlier neutron-irradiation tests (Reference 17). The individual groupings of Figure 35 also would indicate that, in general, transistors of higher-initial-leakage current have higher-leakage current following irradiation.

Curves of I_C versus V_{BE} were plotted from data obtained on the Fairchild Series 500. Two such curves are shown in Figures 37 and 38 for a pnp device, 2N2303, and an npn device, 2N2219, respectively. These curves should appear as straight lines on a semi-log plot if the typical diode equation is valid.

$$I_C = I_o[\exp(qV_{BE}/kT) - 1] \qquad (23)$$

The I_C curves, however, showed a deviation from linear, which was even more pronounced after irradiation. Such increased deviations have been attributed by Goben (Reference 3) to a slight increase in base sheet resistance and an increased I_B. Some of the analyzed data (e.g., Figure 38) also showed an apparent increase in I_C as a function of V_{BE}. According to the analysis of Easley (Reference 18) and Goben (Reference 3), one would expect I_C to decrease as the base-transport factor decreases. In order to test the validity of this data and extend the range of current measurements, the circuit described in Section 2.2 was assembled. Typical curves were obtained from measurements using this circuit. Figures 39 and 40 show data for two different types (2N1613 and 2N2303), respectively. Analysis of the 2N1613 data revealed three distinct components of base current having reciprocal slopes of approximately $2\frac{kT}{q}$, $1.5\frac{kT}{q}$, and $\frac{kT}{q}$ which have been attributed to bulk recombination-generation in the transition (space-charge) region, to surface recombination-generation in the transition (space-charge) region, and to bulk recombination-generation or ideal diffusion current, respectively (Reference 3). Goben found that after neutron irradiation a component of I_B appeared having a reciprocal

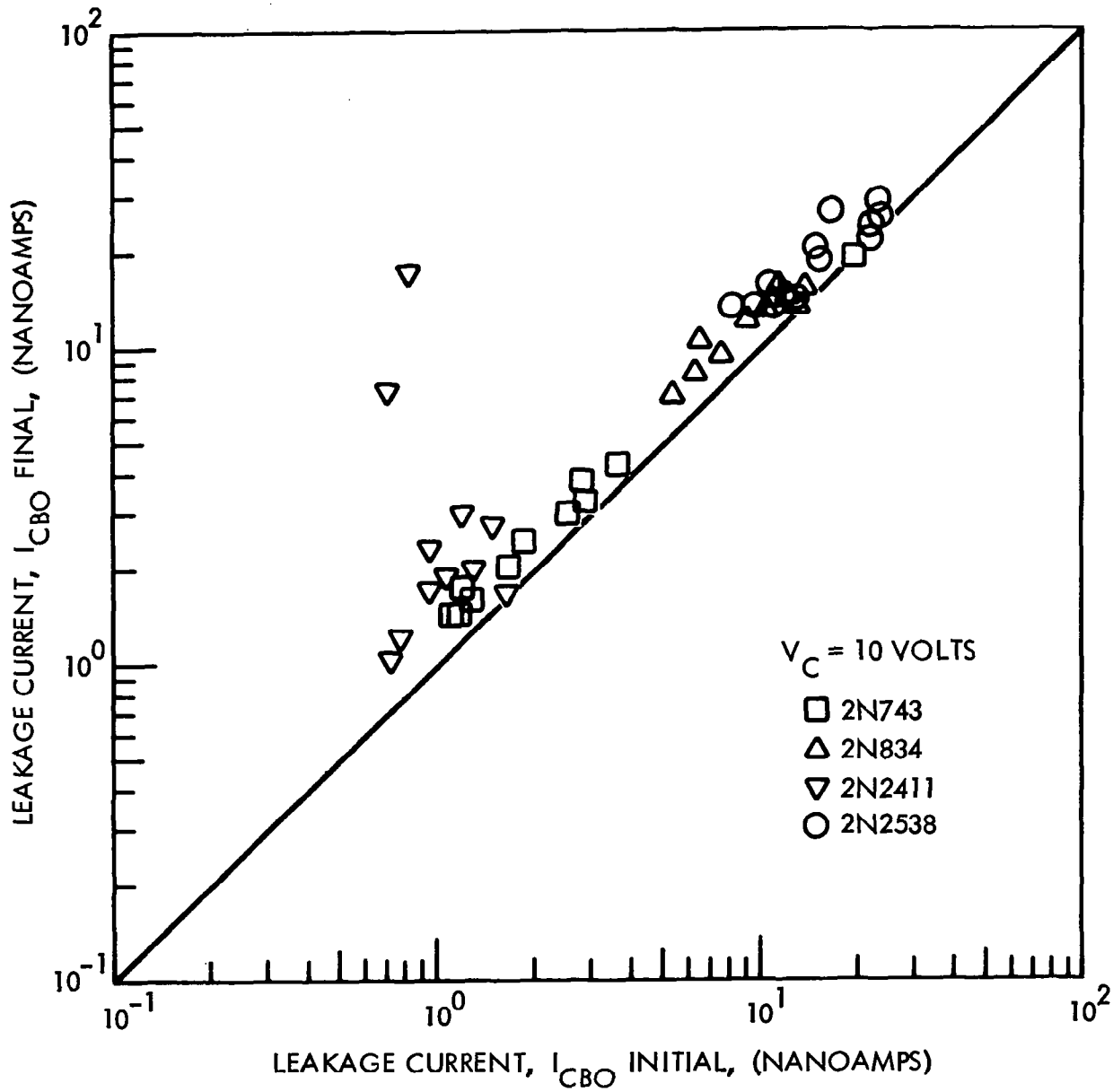

Figure 36. Transistors of Small Percentage of ΔI_{CBO}

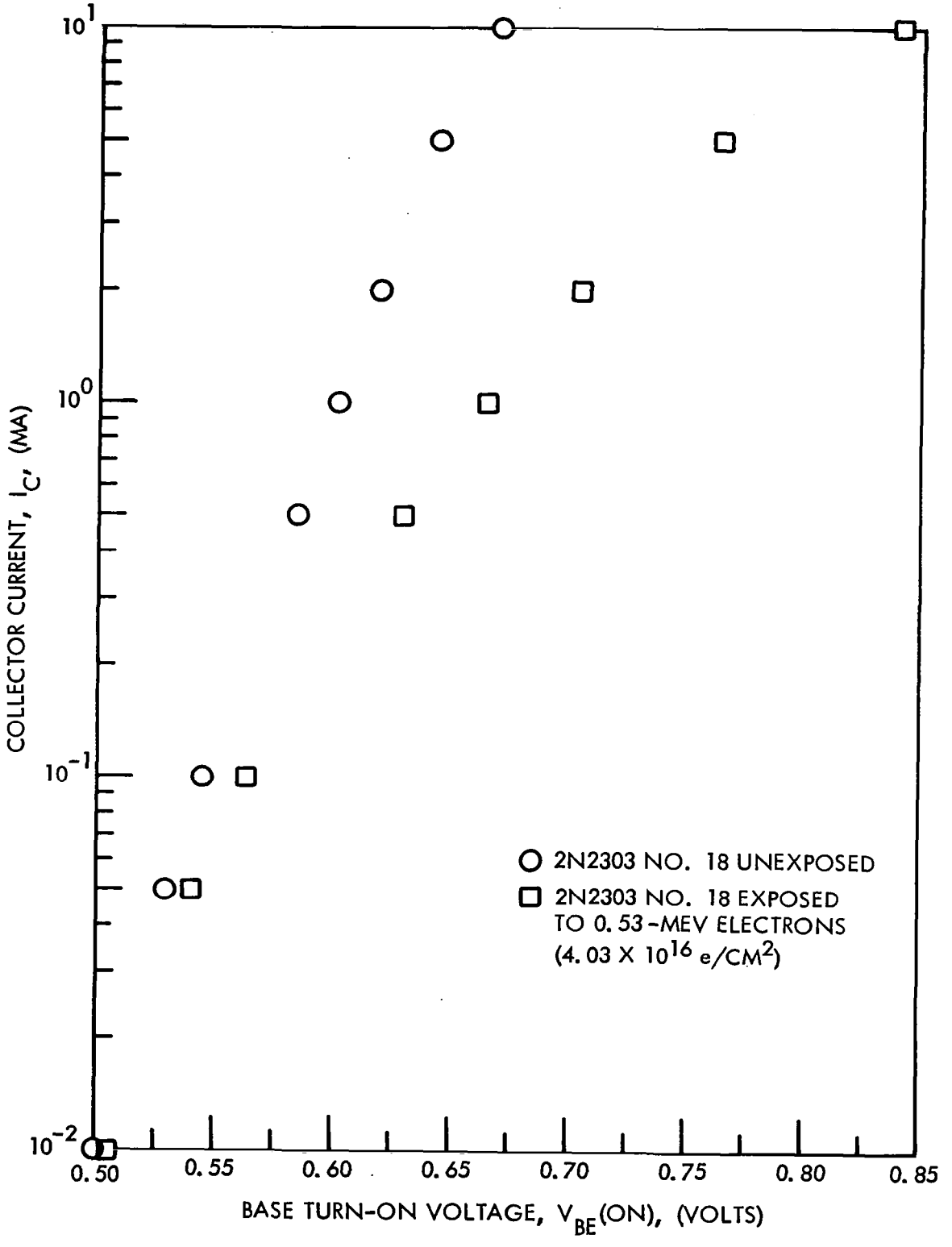

Figure 37. I_C Versus V_{BE}(on) for 2N2303

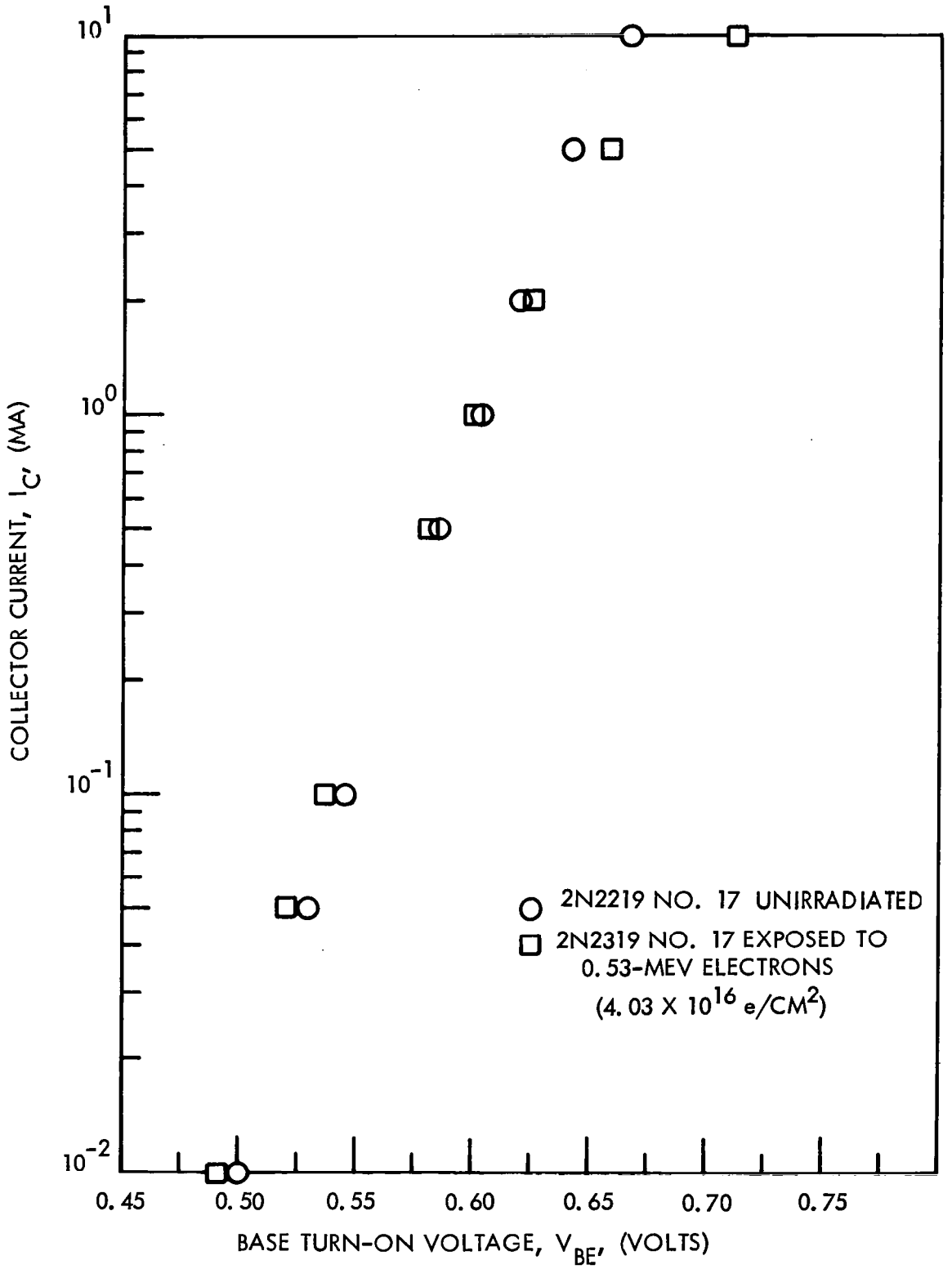

Figure 38. I_C Versus V_{BE}(on) for 2N2219

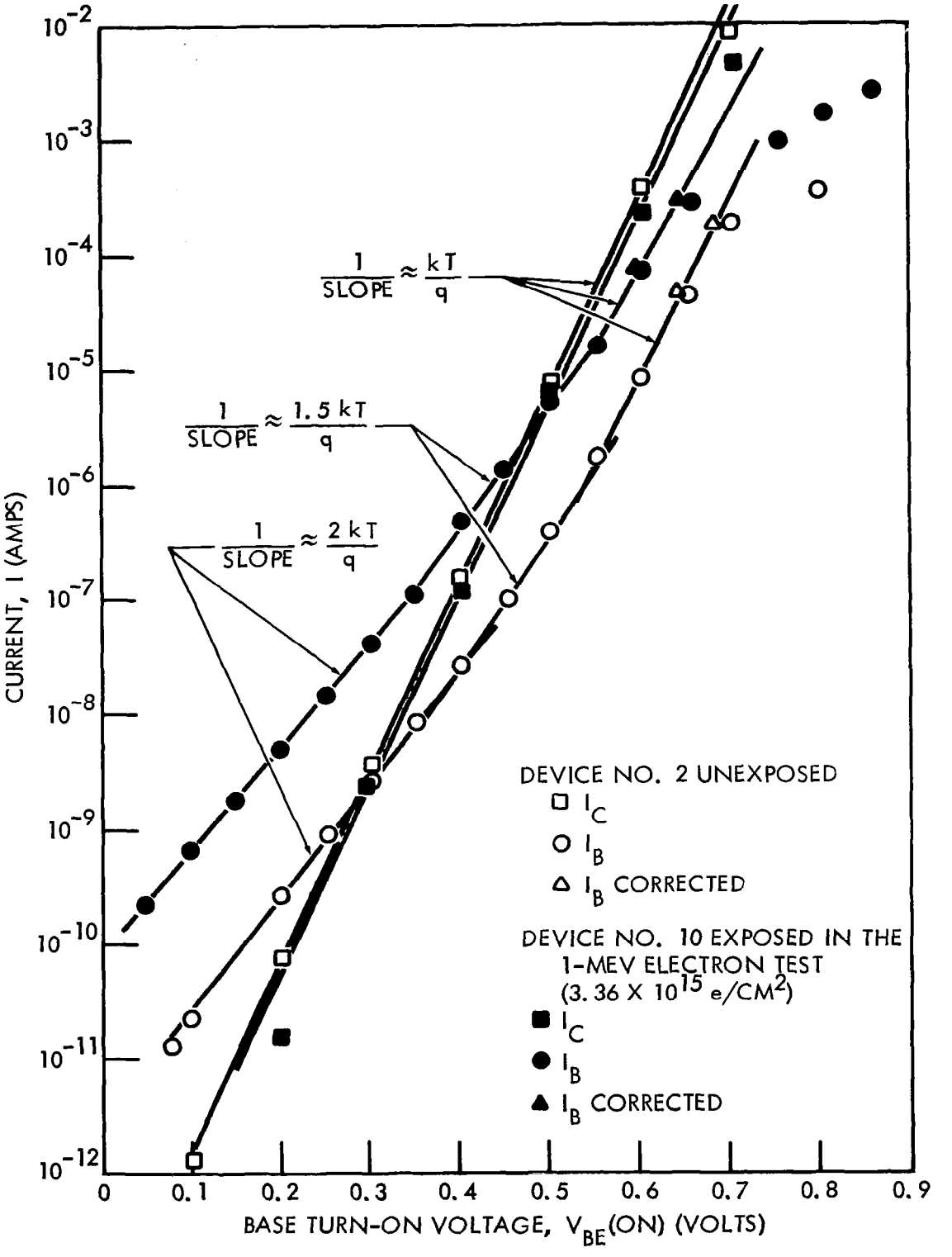

Figure 39. I_C and I_B Versus V_{BE}(on) for 2N1613

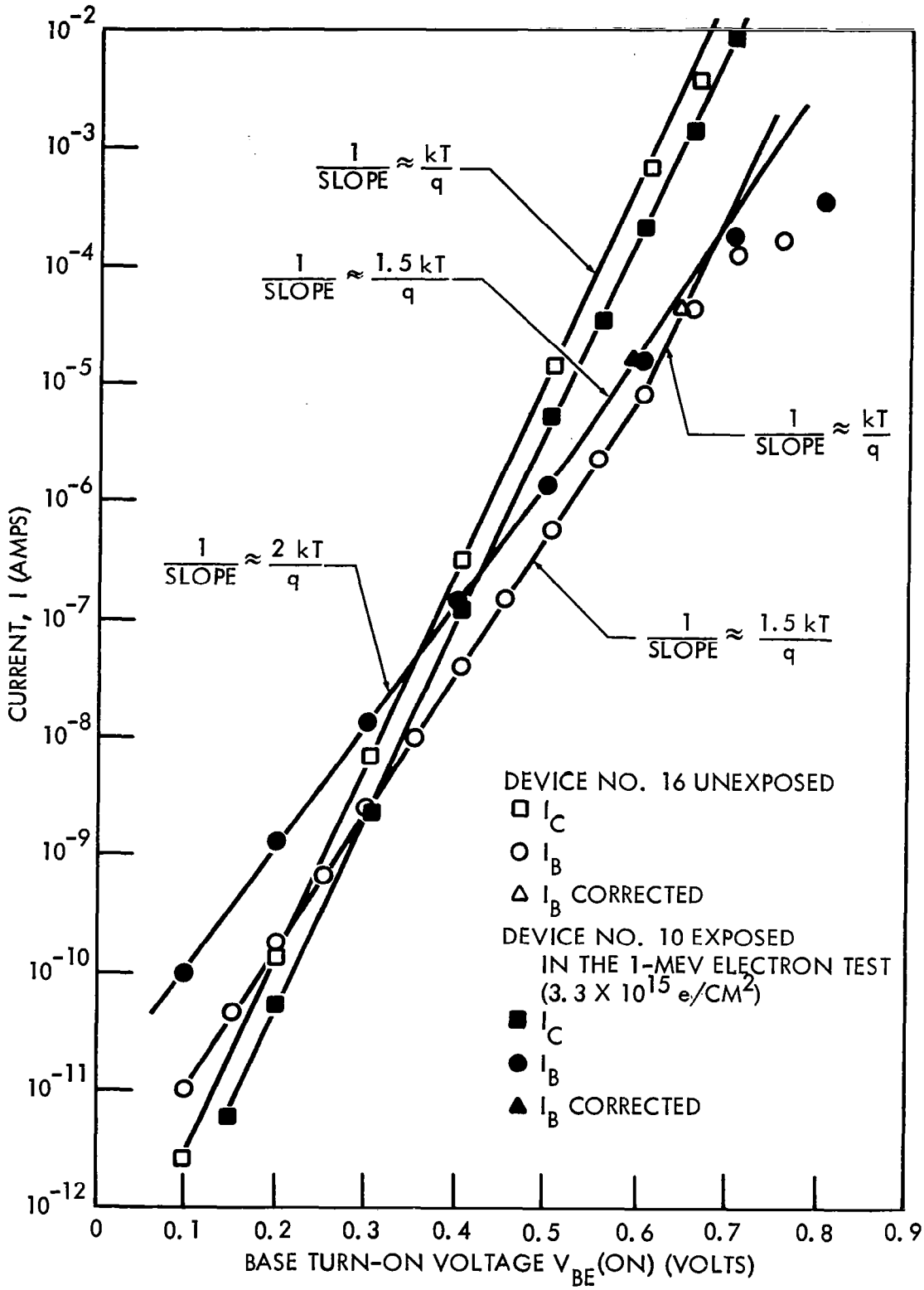

Figure 40. I_C and I_B Versus V_{BE}(on) for 2N2219

slope of $1.5\frac{kT}{q}$ but originating in the bulk space-charge or transition region, and it tended to dominate the base current over a large range. In Figure 39 for the 2N1613 the "$1.5\frac{kT}{q}$ component" of I_B has increased after irradiation but does not seem to be dominant over a significantly greater current range than is the surface "$1.5\frac{kT}{q}$ component" in the unirradiated device. It is of further interest to note that for the unirradiated 2N2219 device there is no "$2\frac{kT}{q}$ component"; however, in the irradiated device such a component appears and dominates I_B over a large range.

It is hoped that further tests and analysis will: (1) show whether I_C does in fact increase with V_{BE} as a function of irradiation in certain devices, and (2) provide information as to the effects on current-gain degradation of the different regions of the transistor.

2.6.2 Common-Emitter Characteristic Curves

Data was reduced from oscillograms of transistor d. c. characteristics taken from the display of a Tektronix 575 Curve Tracer. In analyzing changes in current gain of the transistors exposed in the three electron tests, it was consistently observed that current gain degraded initially in a rapid fashion not predictable by atomic-displacement theory. However, after extensive exposure, this effect tended to saturate and the gain degradation was predictable on the basis of changes in base minority-carrier lifetime.

Initial-minority-carrier lifetime in the base region of a transistor, τ_{b_i}, is expected to be inversely proportional to the initial density, N_i, of carrier recombination centers (Reference 19):

$$1/\tau_{b_i} = cN_i \qquad (24)$$

Electron-induced atomic displacements would form new recombination centers. The density of these centers should be proportional to the radiation exposure and will cause a decrease in minority-carrier lifetime (Reference 20); therefore,

$$1/\tau_b = cN_i + K\Phi \tag{25}$$

and

$$\Delta(1/\tau_b) = 1/\tau_b - 1/\tau_{b_i} = K\Phi \tag{26}$$

where Φ is the electron fluence. The common-emitter current gain of a minority-carrier injection-type transistor can be related to the base lifetime by the following equation (Reference 21):

$$1/h_{FE} = SA_s W/A_c D_b + \sigma_b W/\sigma_e L_e + W^2/2D_b\tau_b \tag{27}$$

where S = surface recombination velocity

A_s = effective area for surface recombination

W = effective width of the base region

A_c = area of the conduction path

D_b = minority-carrier diffusion constant in the base

σ_b, σ_e = conductivities of the base and emitter regions, respectively

L_e = emitter diffusion length

The following relation, which was reported by Easley (Reference 22) in 1958, expresses the dependence of changes in gain on neutron fluence:

$$\Delta(h_{FE}^{-1}) = K_d\Phi \tag{28}$$

where K_d is the displacement-induced transistor damage constant. The "linear" dependence on fluence has consistently been observed for transistors irradiated in a neutron environment. However, analysis of the d.c. common-emitter characteristics obtained from the recent irradiation tests show that Equation 28 is not valid for electron effects on transistors except for large values of fluence, for which gain degradation is severe. The "nonlinear" effects are also more pronounced at reduced

currents where the first term in Equation 27 has its greatest influence on current gain. Thus nonlinear effects which were observed for electron damage could arise from alterations of the surface recombination velocity. The surface recombination velocity can be effected by chemical treatment of a transistor surface; and this treatment which can greatly alter the common-emitter current gain is saturable (Reference 23). Thus, it is conceivable that ionization may also induce changes in surface recombination velocity which would saturate with heavy exposure to ionizing radiation. Earlier tests using X rays of energies below the silicon displacement threshold indicated that permanent "nonlinear" damage is probably caused by ionization effects (Reference 4). Furthermore, this type of effect has only been observed for charged-particle damage and, generally, only at low levels of exposure (References 4 and 24). It is thus possible that ionizing radiation causes permanent changes in surface recombination velocity (surface lifetime) and that these changes dominate transistor gain degradation for low operating currents and small values of electron fluence, while displacement damage dominates for heavy electron exposure.

If ionization of the surface is the cause of the initial electron effects on current gain and if these effects are saturable, then it would seem reasonable to suggest that there may be a limited number of prospective surface sites, N_{s_i}. As these sites are acted upon their number should decrease resulting in eventual saturation of the effect. The conversion or rate of change of the prospective sites, N_s, with electron fluence would be expected to be proportional to the number available.

$$dN_s/d\Phi = K_I N_s \tag{29}$$

K_I of Equation 29 would be the energy-dependent ionization-damage constant, since it would include the ionization rate of the incident electron. Then integration of Equation 29 and application of the initial conditions ($\Phi_i = 0$, $N_s = N_{s_i}$) would lead to a relation for the growth of ionization-induced surface recombination sites, N_I, as a function of electron fluence.

$$N_I = N_{s_i} \left[1 - \exp(-K_I \Phi)\right] \tag{30}$$

Applying Equation 30 to the observed degradation of current gain would modify Equation 28.

$$\Delta(h_{FE}^{-1}) = C_s N_{s_i} \left[1 - \exp(-K_I \Phi)\right] + K_d \Phi \tag{31}$$

where C_s is a constant which includes, in part, the constants in the first term on the right of Equation 27.

Values of the constants in Equation 31 were calculated from curves of experimental data on current gain degradation. Figure 41 depicts gain degradation resulting from the 0.53-Mev electron test. The experimental data points have been corrected for ambient temperature [$\Delta(h_{FE}^{-1})$ of 0.0008/°C]. The surface term of Equation 31 represents well the observed initial degradation of gain. The linear region of the curve of Figure 41 was extrapolated back and subtracted from the experimental curve in order to separate the postulated displacement and ionization damage. The dashed line which represents this nonlinear damage has indeed the shape of a saturation curve. With the constants evaluated, Equation 31, represented by the solid line, fits the experimental data of Figure 41.

Assuming that the so-called ionization-induced damage sites are a result of surface-fabrication processes and ambient conditions at the time of fabrication, it seems reasonable that the number of defect sites per-unit-surface area would be similar for devices produced under similar conditions. If the above assumption is valid, the total number of defect sites in different transistors of a given type should differ only to the extent that their effective-surface areas differ. Further tests and analysis are expected to provide insight on whether the nonlinear effect is truly due to surface ionization. If it is indeed surface-ionization damage then further analysis will be performed to see if values of N_{s_i} can be predicted, and if K_I is relatively constant for transistors of a given type.

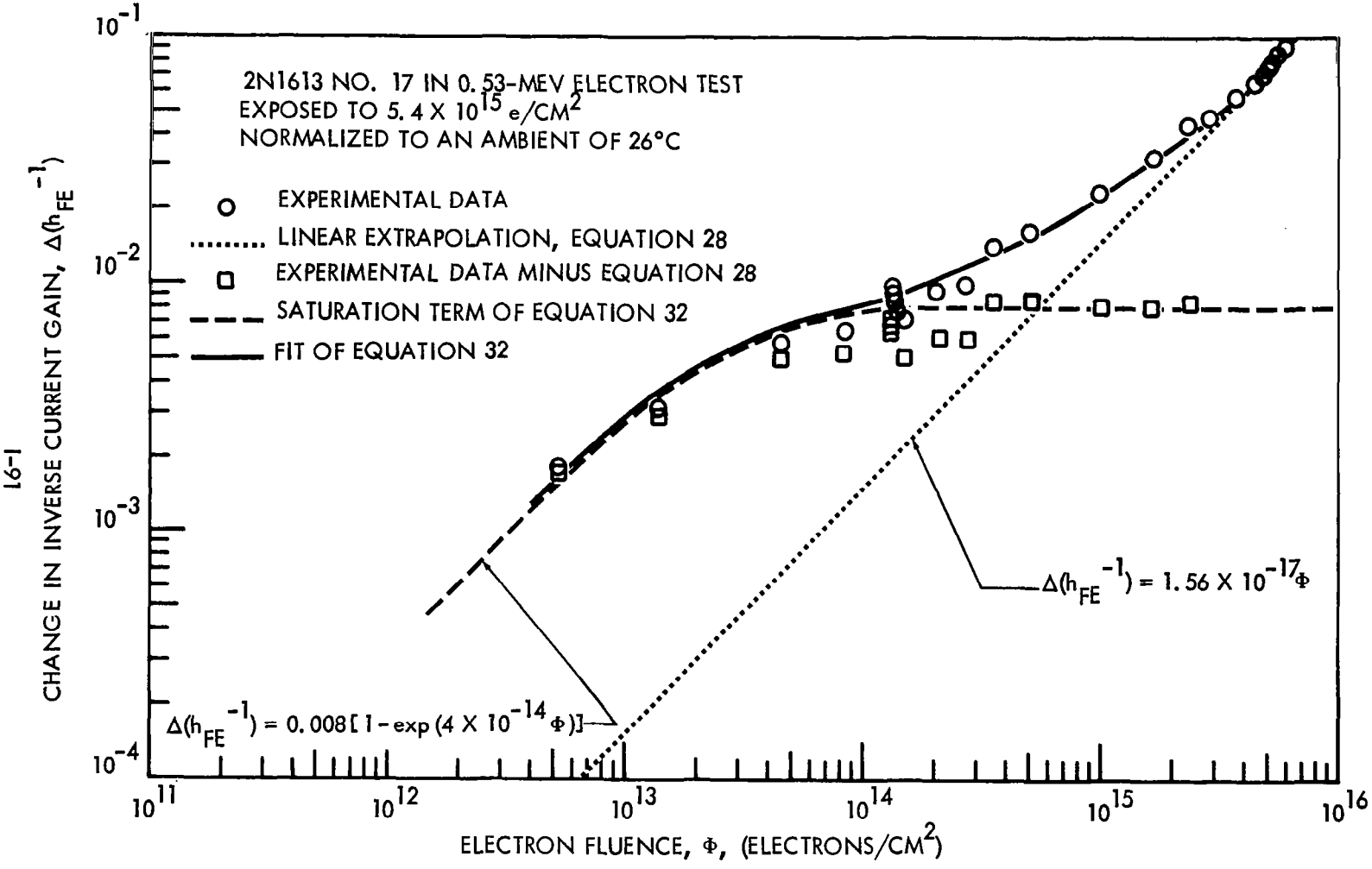

Figure 41. Separation of Electron Effects on h_{FE}

2.6.3 Radiation Equivalences

The results of additional data, a very preliminary analysis of curve tracer oscillograms, are now presented to indicate the process used to eventually arrive at values of radiation equivalences. The validity of radiation equivalences for permanent degradation of common-emitter current gain will depend both on the validity of the assumed dependence of degradation on fluence and on the effectiveness of the methods used for normalizing this degradation.

This study of radiation equivalences is presently limited to conditions where either Equation 28 is valid or where a separation can be made of the terms in Equation 31. For this reason exposure of transistors in the electron tests was continued until "linear" damage was observed. Measurements of f_T and base-transit time were then used to normalize the degradation of common-emitter current gain in the linear-damage region. The techniques used for obtaining normalization parameters were described in Section 2.2.3. Figure 42 shows the unnormalized current gain data of four transistors of type 2N1613 which were exposed during the 1-Mev electron test. The data shown is primarily for high-fluence exposure and the dispersion between devices is shown by the two linear-fit lines. This same data after normalization to a value of base-transit time that is typical of the 2N1613 transistors is then shown in Figure 43. Normalization by use of values of base-transit time appears to be effective in reducing the dispersion between devices of the same type. Figure 42 also shows the relative-damage sensitivity of npn transistors of two different types. The higher frequency type, 2N743, is significantly more radiation resistant, as would be expected from Equations 1 and 18 if W^2/D_b is a damage-control factor. In Figure 43, devices of each of the two transistor types are normalized to a value of base-transit time that is typical of each type, respectively. In Figure 44, data for both transistor types were normalized to a common value of base-transit time (1×10^{-9} sec) and the difference in radiation sensitivity decreased significantly. The difference between the linear regions of the curves for the 2N1613 and 2N743 (factor of approximately 0.88) appears to be due to the fact that the t_b values used to normalize the 2N1613 transistors are

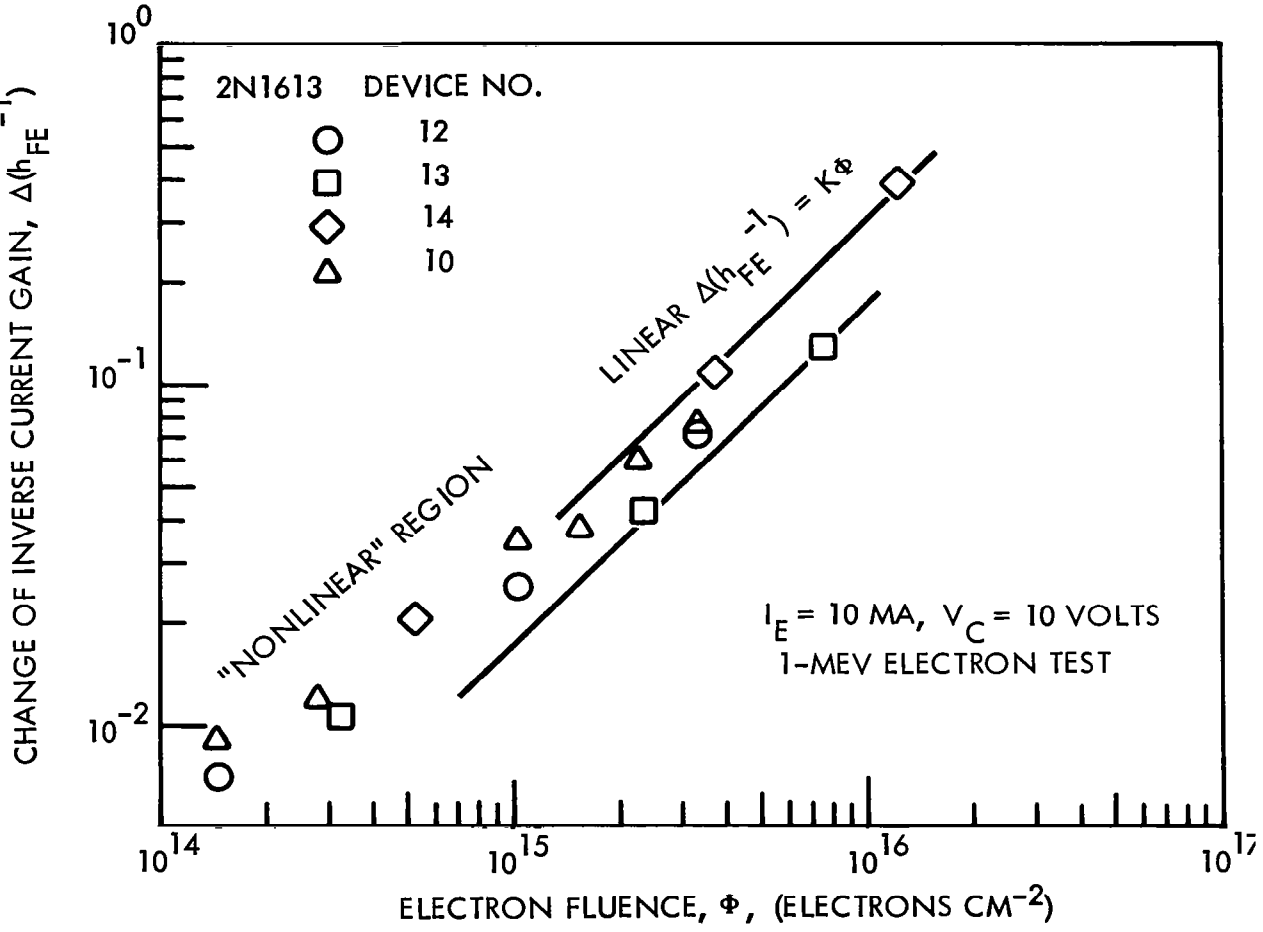

Figure 42. Unnormalized Gain Degradation of 2N1613's

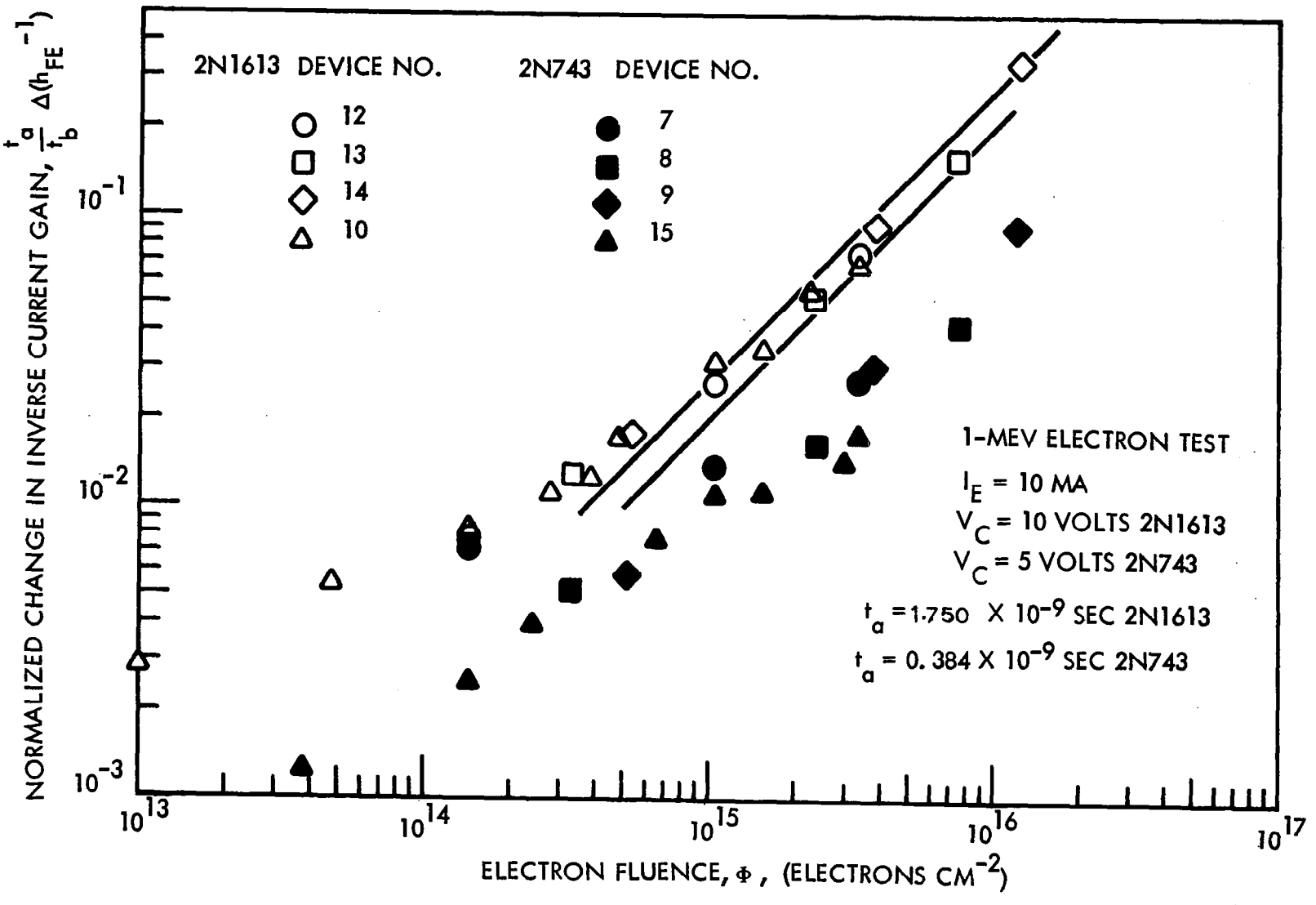

Figure 43. npn Transistors Normalized to a Typical t_b

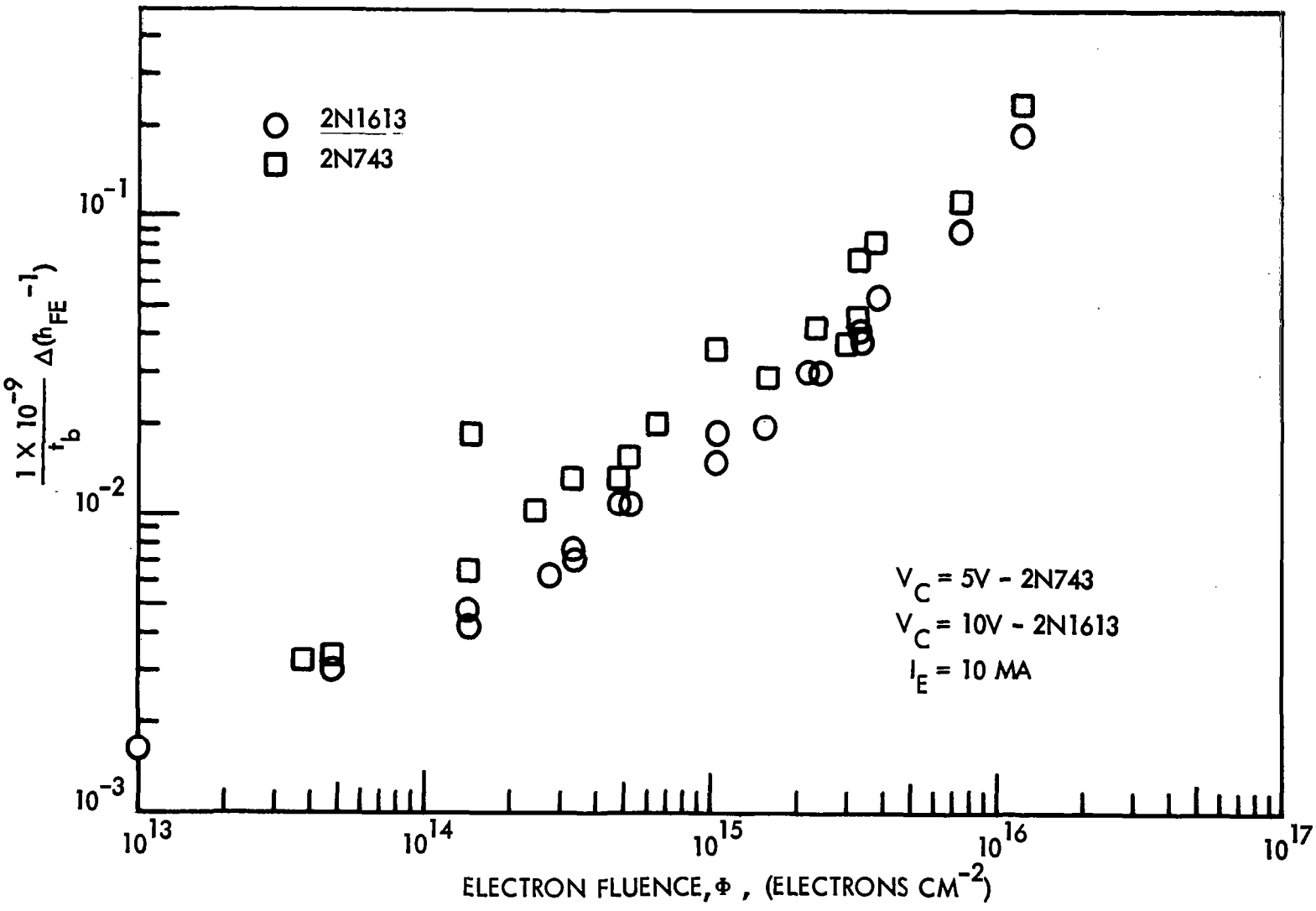

Figure 44. npn Transistors Normalized to Unit t_b

actually values of the base-transit time while values of t_b used for the G. R. bridge still contain the constant $\alpha_o K_\theta$. Figure 44 indicates that there is a good prospect that a common value for radiation equivalence may be obtained for npn silicon transistors can be made from data plotted in Figure 45. However, final values await more detailed analysis of all available data. The fact that nonlinear damage is far more pronounced for the 0.53-Mev electron test is a further indication of ionization effects, since the ratio of ionization production rate to displacement cross section was far greater for the 0.53-Mev test than for the 1- or 2-Mev tests.

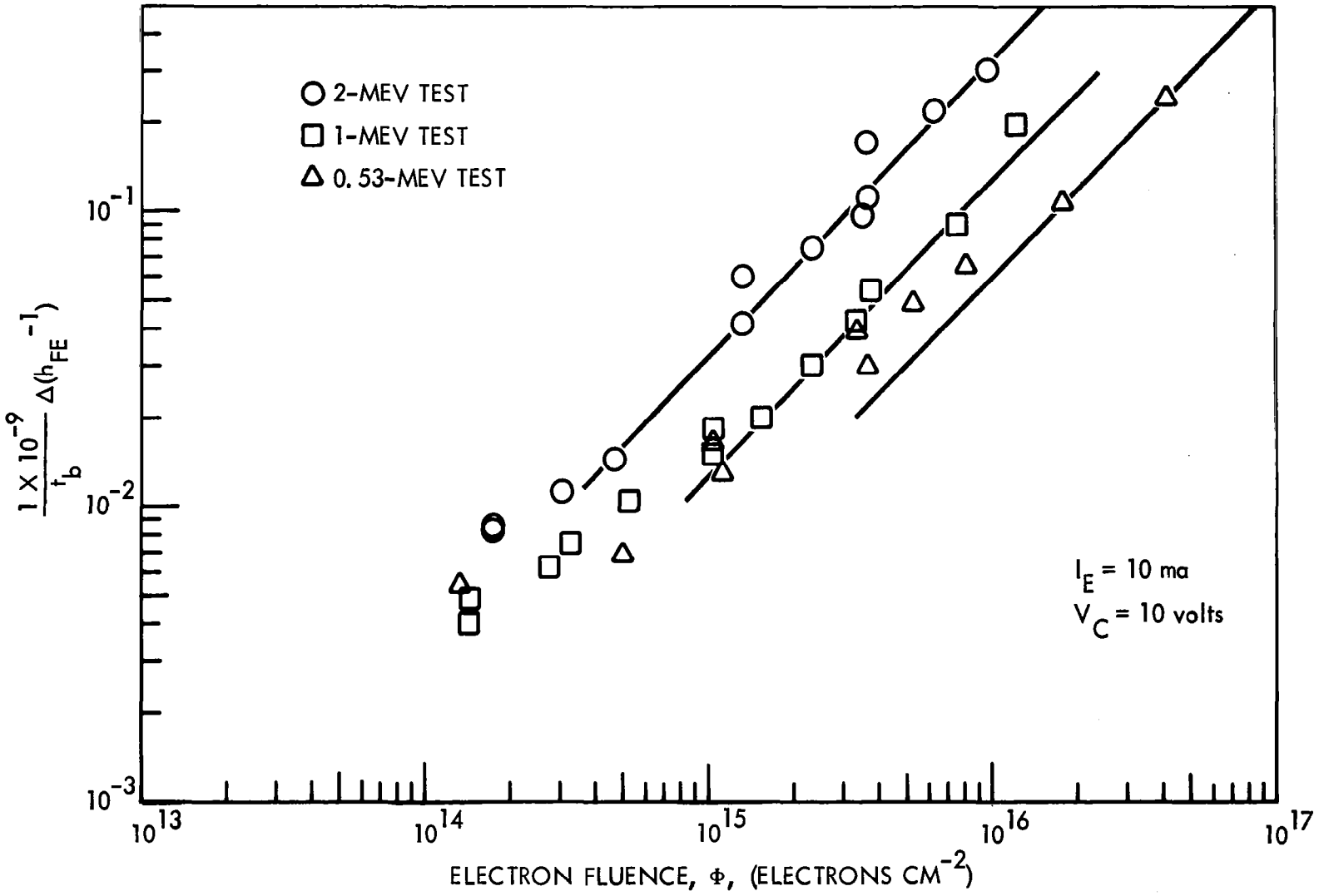

Figure 45. Energy Dependence of Electron Effects (2N1613)

3.0 NEW TECHNOLOGY

The research work performed on this contract has been reviewed. To the best of our knowledge there is no new technology to report to date.

4.0 PROGRAM FOR NEXT REPORTING INTERVAL

The next major reporting interval will be approximately 6 months from this time. By then, all irradiation tests on transistors will have been completed. Data will be computer analyzed and radiation equivalences established.

The 1-Mev-proton test has already been performed. The final proton tests, 20 and 100 Mev, are scheduled for approximately January and March, respectively. In addition a gamma-ray irradiation test, scheduled for December, will be conducted to provide information on the feasibility of using cobalt-60 facilities for simulating space radiation effects.

A computer code has been developed at Boeing that will aid significantly in the analysis of data on all transistor-current-gain degradation tests (Reference 14). Data taken from oscillograms of photographs of transistor curve traces, using an oscillogram reader, will be directly punched on IBM cards and analyzed by an SRU 1107 computer.

Radiation-equivalence values will be presented, relative to unity damage for the most damaging test (1-Mev protons). Comparison will be made between pnp and npn transistors, including not only the 10 transistor types and 7 radiation tests of this program, but also selected transistors from past tests (2- and 10-Mev protons; 0.8-, 2-, 5-, 10-, and 25-Mev electrons; reactor and fast-fission neutrons; and 5-Mev alpha particles).

Curves showing the dependence of transistor damage on particle type and energy will also be presented and will include selected results from previous tests.

A correlation between the displacement effects of cobalt-60 gamma rays and charged particles will be made to determine the range of validity of cobalt-60 gamma-ray simulation of space-radiation damage.

Data, in general, will be in a form which will allow a design engineer to evaluate actual changes in transistor gain caused by space radiation.

5.0 CONCLUSIONS AND RECOMMENDATIONS

5.1 CONCLUSIONS

Progress of the research program has been encouraging. To date four of the seven irradiation tests have been completed (including the 1-Mev proton test). Preliminary analysis of the electron tests has been completed and a number of conclusions are evident. Only small changes of BV_{CBO} were observed for these tests and only limited evidence of a fluence dependence was observed. A strong dependence of $V_{CE}(sat)$ on electron fluence has been observed. The apparent dependence of this effect on the relative energy of the electron indicates that these changes are probably due to atomic displacement rather than ionization. $V_{BE}(sat)$ was also observed to increase with electron fluence. Values of I_{CBO} of the transistors tested, in general, increased but showed no dependence of ΔI_{CBO} on electron fluence for exposures from 4×10^{15} to 4×10^{16} electrons/cm^2.

All transistor types display an initial degradation of current gain (over a significant electron exposure) which appears to be attributable to the effect of ionization on the surface recombination velocity. Techniques have been successfully used to separate this "nonlinear" damage from damage attributable to displacements. Preliminary analysis indicates that values of base-transit time can be used effectively to normalize the degradation of transistor current gain when displacement effects in the transistor base dominate damage.

The data also indicate that the energy dependence of electrons damage should be readily separable and should provide useful equivalence information.

5.2 RECOMMENDATIONS

It is recommended that more effort be directed to determining how better data can be obtained for transistor damage normalization. This effort should include both study of the General Radio Transfer Function and Immittance Bridge to determine why transistor measurements near unity gain deviate from the expected behavior, and a correlation of the normalization data obtained by different methods.

Further, studies should be made involving large numbers of transistors of the same type in a given test to examine the statistical variation of normalized damage constants.

Since for electron and gamma irradiation the transistor gain degradation is nonlinear over a large range of fluence, an effort should be made to more fully understand this type of damage. A study of the dependence of I_B on V_{BE} as a function of fluence seems promising as a possible method of correlating the initial nonlinear gain degradation with damage in a given region of the transistor. Also, further efforts to separate the linear and saturable damage components may indicate methods by which the initial nonlinear damage may be predicted.

6.0 BIBLIOGRAPHY

1. "Series 500 Semiconductor Tester Technical Manual with Electrical Specification No. 606886," Fairchild Semiconductor, December 1963.

2. "Type 575 Transistor Curve Tracer Instruction Manual," Tektronix, Inc., 1959.

3. Goben, C. A., and Smits, F. M., "Anomalous Base Current Component in Neutron Irradiated Transistors," Sandia Corporation Reprint SC-R-64-195, July 1964.

4. Brown, R. R., "Proton and Electron Permanent Damage in Silicon Semiconductor Devices," a paper presented at the joint ANS and ASTM Conference: Radiation Effects on Electronics, Nuclear News, ANS-7, 8, p. 43, August 1964.

5. "Operating Instructions Type 1607A Transfer Function and Immittance Bridge," Form 1607-0100-E, General Radio Company, West Concord, Massachusetts, July 1963.

6. Phillips, A. B., Transistor Engineering and Introduction to Integrated Semiconductor Circuits, New York, McGraw-Hill Book Co., 1962.

7. "Type RM 567 Readout Oscilloscope Instruction Manual," Tektronix, Inc.

8. "Instruction Book Model 74C-S8 Capacitance Bridge," Boonton Electronics Corporation, Morris Plains, New Jersey.

9. Ashar, K. G., "Transit Time in High-Speed Switching Transistors," Solid State Design, 5, 24-26, 1964.

10. Thomas, D. E., and Moll, J. L., "Junction Transistor Short-circuit Current Gain and Phase Determination," Proceedings IRE, Vol. 46, pp. 1177-1184, June 1958.

11. Bethe, H. A., "Moliere's Theory of Multiple Scattering, Phys. Rev., 89, 1256, 1953.

12. Personal communication with technical representatives of Fairchild Semiconductor, Motorola, Raytheon, and Texas Instruments, Inc.

13. "Reference Data for Radio Engineers," Federal Telephone and Radio Corporation.

14. Rooney, J. A., "Transistor Damage Plotting Program," Boeing Document AS 1706, March 1964.

15. Cahn, J. H., "Irradiation Damage in Germanium and Silicon Due to Electrons and Gamma Rays," Jour. of Applied Phys., 30, 8, 1310, 1959.

16. Nelms, A. T., "Energy Loss and Range of Electrons and Positrons," N. B. S. Circular 577, July 26, 1956.

17. Brown, R. R., "Identification of Radiation Preferred Electronics," Record of the 1965 International Space Electronics Symposium, Institute of Electrical and Electronic Engineers, Inc., New York, N. Y., 1965.

18. Easley, J. W., and Dooley, J. A., "On the Neutron Bombardment Reduction of Transistor Current Gain," Jour. of Applied Phys., 31, 6, 1960.

19. Shockley, W., Electrons and Holes in Semiconductors, D. Van Nostrand Publishing Co., New York, N. Y., 1950.

20. Messenger, G. C., and Spratt, J. P., "The Effects of Neutron Irradiation on Germanium and Silicon," Proc. IRE, Vol. 46, No. 6, pp. 1038-1044, June 1958

21. Webster, W. M., "On the Variation of Junction Transistor Current Amplification Factor with Emitter Current," Proc. IRE, Vol. 42, No. 6, pp. 914-920, June 1954.

22. Easley, J. W., "Comparison of Neutron Damage in Germanium and Silicon Transistors," Proceedings Third Semiannual Radiation Effects Symposium, Vol. 4, October 28-30, 1958.

23. Moore, A. R., and Pankove, J. I., "The Effect of Junction Shape and Surface Recombination on Transistor Current Gain," Proc. IRE, Vol. 42, 6, pp. 907-913, 1954.

24. Frank, M., Larin, F., and Niehaus, D. J., "A Generalized Approach to Transistor Damage by Radiation," Bendix Corporation, Research Laboratories Division, Southfield, Michigan, Nucleonics, 22, 9, 1964.

7.0 GLOSSARY

A	Indicator of the transfer function and immittance bridge (real part current)
A_c	Area of conduction path
A_s	Effective area for surface recombination
a	The grade constant in atoms/cm^2 in the transistor base region
B	Indicator (imaginary part of current)
BV_{CBO}	Collector-base breakdown voltage
C_T	Transition capacitance
C_{Tc}	Collector transition capacitance
C_{Te}	Emitter transition capacitance
C_x	Variable capacitance of the base-transit-time circuit
D_b	Minority carrier diffusion constant in the base
D_{pb}	Hole diffusion constant in the base
E_f	Electron energy loss in foil
f_T	Gain-bandwidth frequency
f_a	Alpha cut-off frequency
h_{FE}	d. c. common-emitter current gain
h_{fe}	a. c. common-emitter current gain
I_B	d. c. base current
I_{B1}	Turn-on base current
I_C	d. c. collector current
I_{CBO}	Collector-base reverse current

I_E	d. c. emitter current
I_o	Leakage current of ideal diode
K	Damage constant
K_d	Displacement-induced transistor damage constant
K_I	Energy dependent ionization damage constant
K_θ	The excess phase constant
K_ϵ	Dielectric constant
k	Boltzmann's constant
L_e	Emitter diffusion length
M	Magnitude of the base drive current (multiplier)
$N_{B'}$	Base impurity concentration at emitter junction
N_{BC}	Background impurity concentration
N_I	Ionization-induced surface damage recombination sites
N_i	Initial density of carrier-recombination centers
N_s	Prospective surface-damage sites
N_{s_i}	Initial density of prospective surface-damage sites
q	Electronic charge
R_c	Collector resistance in base-transit-time circuit
R_e	Emitter resistance
R_L	Load resistance
R_{sc}	Collector series resistance
R_x	Variable resistance of base-transit-time circuit
S	Surface recombination velocity

T	Absolute temperature
T_r	Rise time
t	Thickness of scattering foil
t_b	Base-transit time
t_c	Collector-delay time
t_e	Emitter-delay time
t_x	Emitter-delay time plus collector-delay time
$V_{BE}(sat)$	Base to emitter saturation voltage (grounded emitter)
V_C	Collector voltage
V_{CB}	Collector-base voltage
$V_{CE}(sat)$	Collector to emitter saturation voltage (grounded emitter)
V_o	External applied bias
V_{sc}	Scattering limited velocity
V_T	Contact potential
W	Effective base width
X_m	Collector depletion layer thickness
α_o	The grounded emitter current gain (low frequency)
$\frac{dE}{dX}$	The rate of energy loss
ρ	Density of the scattering foil
θ	Scattering angle
λ	Wavelength
τ_b	Minority carrier lifetime in the base region

τ_{b_i}	Initial minority carrier lifetime in the base region
Φ	Charged particle fluence
ω_T	Angular gain-bandwidth frequency
ω_α	Angular alpha cut-off frequency
σ_b	Conductivity of base region
σ_e	Conductivity of emitter region